VIBRATIONAL SUM-FREQUENCY SPECTROSCOPY: TOWARDS UNDERSTANDING ADSORBATE BEHAVIOUR ON SUBSTRATES RELEVANT TO THE NUCLEAR FUEL CYCLE

A thesis submitted to The University of Manchester for the degree of
PhD Corrosion & Protection
in the Faculty of Engineering and Physical Sciences

2013

FRANCIS PETER LYDIATT

SCHOOL OF MATERIALS

Contents

Chapter 3. Principles of VSFS & Other Experimental Techniques

Chapter 4. VSFS Implementation

Chapter 5. TiO2-adsorbate Systems Studied via VSFS

Chapter 6. The Metal-water Interface Studied via VSFS

Abstract

The primary goal of this thesis was to commission an instrument for vibrational sum frequency spectroscopy (VSFS), and exploit it for the study of solid/gas interfaces; of ultimate interest is characterisation of substrate surfaces in humid environments. Such effort is motivated by interest in understanding the potential for atmospheric corrosion in dry storage facilities of spent nuclear fuels or other nuclear-related wastes.

VSFS is a non-linear, interface specific, vibrational spectroscopy, in which two photons of different energies (infrared (IR) and visible (VIS)) impinge upon a surface at the same point at the same time, leading to the generation of a third (*sum-frequency generation* (SFG)) photon. Features in VSFS spectra can be assigned to vibrational modes of interfacial species, and so enable details of interfacial structure and chemistry to be elucidated. An instrument for such measurements has been developed using laser facilitates located in the Photon Science Institute (PSI) of The University of Manchester. More specifically, an ultra-fast (femtosecond) laser has been employed as a light source, enabling acquisition of spectra ($\sim$250 cm^{-1} in width at a resolution of $\sim$11 cm^{-1}) without the need for scanning the energy of either IR or VIS beams, i.e. so called broad-band VSFS. To test performance, data have been acquired from self-assembled monolayers of alkanethiols (octadecanethiol) on gold substrates, which demonstrate the utility of the instrument.

Subsequent to commissioning, the VSFS instrument was initially exploited to study the interaction of two organic molecules, acetonitrile and acetic acid, with a single crystal TiO_2(110) substrate; measurements were performed with the sample exposed to the vapour of each organic species under ambient conditions. Surface adsorption was identified through the appearance of the CH_3 symmetric stretch. Furthermore, spectra as a function of light (IR/VIS/SFG) polarization combinations have been recorded to explore adsorbate angular geometry.

Finally, VSFS measurements have been undertaken from a number of substrates (GaAs, Au, Zn, Fe, Cr, stainless steel), as a function of relative humidity; D_2O was employed to overcome the issue of loss of IR beam intensity due to interaction with atmospheric H_2O. Signal quality varies significantly with substrate, with the most insight being gained for the interaction of D_2O with polycrystalline Zn. Clear vibrational resonances due to both hydroxyls (OD) and molecular water (D_2O) are observed, which vary with relative humidity, indicating that there are significant changes in interface structure with relative humidity.

Declaration

No portion of the work referred to in the thesis has been submitted in support of an application for another degree or qualification of this or any other university or other institute of learning.

Copyright Statement

i. The author of this thesis (including any appendices and/or schedules to this thesis) owns certain copyright or related rights in it (the "Copyright") and s/he has given The University of Manchester certain rights to use such Copyright, including for administrative purposes.

ii. Copies of this thesis, either in full or in extracts and whether in hard or electronic copy, may be made only in accordance with the Copyright, Designs and Patents Act 1988 (as amended) and regulations issued under it or, where appropriate, in accordance with licensing agreements which the University has from time to time. This page must form part of any such copies made.

iii. The ownership of certain Copyright, patents, designs, trade marks and other intellectual property (the "Intellectual Property") and any reproductions of copyright works in the thesis, for example graphs and tables ("Reproductions"), which may be described in this thesis, may not be owned by the author and may be owned by third parties. Such Intellectual Property and Reproductions cannot and must not be made available for use without the prior written permission of the owner(s) of the relevant Intellectual Property and/or Reproductions.

iv. Further information on the conditions under which disclosure, publication and commercialisation of this thesis, the Copyright and any Intellectual Property and/or Reproductions described in it may take place is available in the University IP Policy (see http://documents.manchester.ac.uk/DocuInfo.aspx?DocID=487), in any relevant Thesis restriction declarations deposited in the University Library, The University Library's regulations (see http://www.manchester.ac.uk/library/aboutus/regulations) and in The University's policy on Presentation of Theses.

Acknowledgement

I would like to thank everybody who has helped me both academically and spiritually over the course of my PhD studies. The all-important support staff who have patiently interpreted all my vague and sketchy requests; Steve and Simon in Corrosion Stores, Malcolm in the workshop, John Walton for all his straight-talking direction with XPS and AFM, Paul Jordan for always being around when you need him, Med and Alasdair for their unique brands of assistance in the PSI, and the many more whose names I desperately tried to remember for four years but who now must unfortunately remain anonymous.

I'd also like to thank James, John, Perla, Carino, Mahmoud, Matt, Gaurav, Chloe, Sam, and all the other post-grads and post-docs who offered up genuine advice, solid banter, and just generally tolerated my presence.

Special thanks to Heike and Sergio in Liverpool for essentially teaching me SFG from scratch, to Joon Hee and Steve in Houston for reminding me I still knew almost nothing about it, to Chris for stealing/long-term-lending me thousands of pounds worth of unused apparatus, and Olwen for generally being incredibly nice and helpful.

And now for the big thanks, Steve, Tom, Dimitri, and most of all Rob, without whose collective assistance, steering, advice and metered enthusiasm I'd have probably failed a long time ago! Joking aside, I'm genuinely grateful for the time and effort you have all put into me and my studies, thank you deeply.

Also my family and my long-suffering partner, can't forget them (I'll get in trouble otherwise).

Special financial acknowledgement goes to The National Nuclear Laboratory (NNL) and the Engineering and Physical Sciences Research Council (EPSRC), who funded this investigation.

Chapter 1. General Introduction

1.1 Introduction

Given the ubiquitous nature of water vapour in the atmosphere, there is a distinct lack of nanoscale mechanistic understanding into its interaction with metallic surfaces, something key to the onset of atmospheric corrosion. Such understanding would allow for better predictive models and thus preventative measures for the initiation of atmospheric corrosion at low relative humidities.[1] This research project will seek to gain an insight into the interaction of water with metal and metal oxide substrates using a variety of complimentary surface analysis techniques.

1.2 Context of Research

1.2.1 Nuclear storage applications

Currently around one eighth of the UK's total power consumption is generated through nuclear fission.[3] There are nine nuclear power stations still operational, of which one is a legacy Magnox reactor built in the early 1970s, seven are Advanced Gas-cooled Reactors (AGRs) built in the late 1970s and 80s, and one is a Pressurised Water Reactor commissioned in the mid-1990s.[3] Power from these is generated through the fission of heavy radioactive isotopes such as ^{235}U into smaller fission products via a controlled chain reaction. After some time, the decreased amount of fissile isotope coupled with the often reaction-moderating properties of the fission products means that a particular fuel element is no longer capable of maintaining a chain reaction, and the fuel is no longer efficient in terms of its neutron economy. This 'spent' fuel element is no longer usable in the reactor but still contains a large quantity of fissile material and other radioactive elements with long decay times.

In the UK the majority of this spent nuclear fuel (SNF) is sent to the Sellafield site in Cumbria for reprocessing at the Thermal Oxide Reprocessing Plant (THORP), where fissile materials are separated from the fission products and can go on to be used again. Like the nuclear power stations themselves, THORP was built and designed with a finite lifespan and there are currently no plans for a new-build reprocessing plant beyond the planned 2018 THORP closure date, so future projections show a significant amount of SNF with no UK reprocessing options.[1]

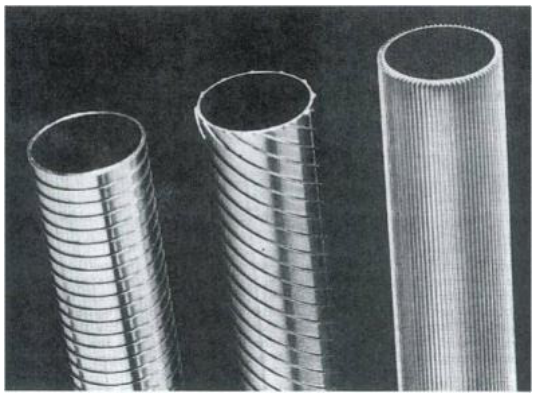

Figure 1.1. Images of the 20Cr/25Ni/Nb stainless steel cladding which encases the fuel pellets for use in an AGR reactor. A number of detailed design variants have arisen over some 30 years of operations.

Figure 1.2. Photograph and diagram of the AGR fuel element's graphite sleeve inside which can be seen the stainless steel fuel pins.

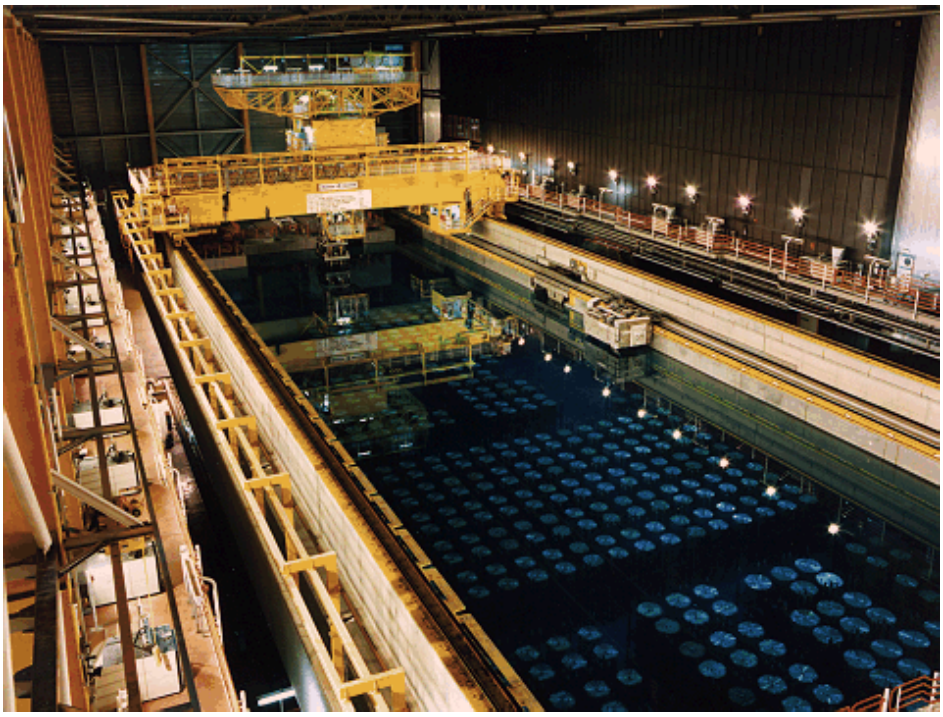

Figure 1.3. Photograph of the storage/cooling pool at Sellafield's THORP facility

As the UK's nuclear industry is privatised it also must respond to market pressures, and the relatively low price of purchasing its primary fuel Uranium compared to the cost-per-unit of reprocessing means that the latter option is no longer economically viable.

Whilst geological disposal — sealed storage underground with no intent of retrieval — of high-level SNF is planned by the UK Government,[4] there remains a likely interval of several decades before the geological disposal facility (GDF) is available, and it may be some further decades before the spent fuel is transferred to the GDF. During this entire period the fuel must be safely stored, in a monitored retrievable storage arrangement. Strategic options on how to do so are required, this will include the option to dry store the fuel (possibly for several decades) and in any event the fuel will ultimately be placed in dry containers for disposal in the GDF and it will be important to understand fuel performance in the early years of disposal, before the GDF is sealed off.

The current arrangement is that the spent fuel elements undergo a process of immersion in a water-filled cooling pond until their heat and radiation emissions reach an acceptable level; long term pond storage remains one option. If the option was taken to subsequently dry store the fuel, considerable efforts would be made to reduce the presence of moisture in the vapour phase to a minimum. However, some graphite components of the fuel elements and the deposited carbon are partially porous and even after intense baking and vacuum drying the elements have been shown to retain water.[1] The fuel elements could be dismantled (as they are at present, prior to pond storage) to remove the graphite components, but the deposited carbon on the fuel surface is a persistent feature. Moreover baking may not be practicable: the possibility exists of creep of the stainless steel cladding tubes if heated sufficiently and that is a disincentive to forcefully dry the fuel. If the transfer to dry storage took place some decades into the future, the radiogenic heat production normally associated with SNF would by that time have decayed to insignificance, so the fuel might not be self-drying.

Whilst the amount of water expected to be carried over with the fuel into a dry store is still minimal in terms of regular atmospheric corrosion, it becomes significant over long timescales especially when a requirement of the storage system is retrievability. It is the possibility of a corrosion mechanism operating at low relative humidities that is of interest, and the reason this research project is industrially funded by the National Nuclear Laboratory (NNL).

1.2.2 Storage conditions

The AGR fuel pins illustrated in Figure 1.1 are the main fuel element currently used in the UK, and each one consists of 64 enriched uranium oxide (UO_2) fuel pellets stacked inside a 20Cr/25Ni/Nb austenitic stainless steel cladding to form the 'pin', shown separately in Figure 1.2. A complete AGR fuel element comprises 36 of these fuel pins encased in a 1 metre long graphite sleeve, with stainless steel grids at the centre and ends to maintain pin geometry.[5] Once the fuel pins are spent, the whole fuel element is transferred to the station cooling ponds. These are borated – boron is an effective neutron moderator – and the pH is then controller to be neutral using LiOH. The pond water may also contain trace levels of chloride (Cl^-) ions present from sea salt particle deposition.[2] Once the heat and radioactivity have fallen sufficiently the assembly is removed from the reactor station pond and transported to the reprocessing plant at Sellafield. At the reprocessing plant, the assemblies are disassembled, and the individual fuel pins are loaded into slotted cans and placed in large storage ponds such as that illustrated in Figure 1.3.[1]

The approach towards the dry storage of spent nuclear fuel (SNF) can vary considerably between nations, as can the materials and technologies involved. Due to the privatised nature of the UK nuclear industry the majority of research and literature relevant to the UK approach is carried out and published by the industry itself. In the mid-1990s a research programme was undertaken into the corrosion of AGR fuel in dry storage conditions, which had a number of key findings.[6]

Primarily, the key to corrosion onset was found to be the presence of an adsorbed water layer sufficiently thick to form an electrolyte. The adsorption of water on metals is known to be dependent on temperature, humidity and the presence of oxides.[7] Importantly, a step change was identified in the corrosion rate of mild steel as a function of humidity, and this change, illustrated in Figure 1.4, was linked to the availability of adsorbed surface water layers. This step change was observed at a humidity of around 35% RH, significantly below the normally acknowledged threshold of around 65% RH for atmospheric corrosion.[2]

There are two additional contributions to metallic corrosion identified, both of these resulting from the radioactive environment. The first is Radiation-Induced Sensitisation (RIS), which alters the chemistry of the metal alloy at grain boundaries on the surface of the AGR cladding, involving chromium migration into the metal grains in balance to the outward migration of vacancies formed by neutron irradiation, known as the Inverse-Kirkendall effect. This chromium depletion at the grain boundaries increases susceptibility to corrosion and intergranular stress corrosion cracking.[8] The second major contribution to corrosion identified is the production of acidic species due to radiolysis of the dry storage gas phase if it contains trace air and water vapour

presence. Due to the presence of high energy gamma rays, water, oxygen and nitrogen in particular can lead to the formation of NOx species and the particularly problematic nitrous- and nitric acid compunds.[9]

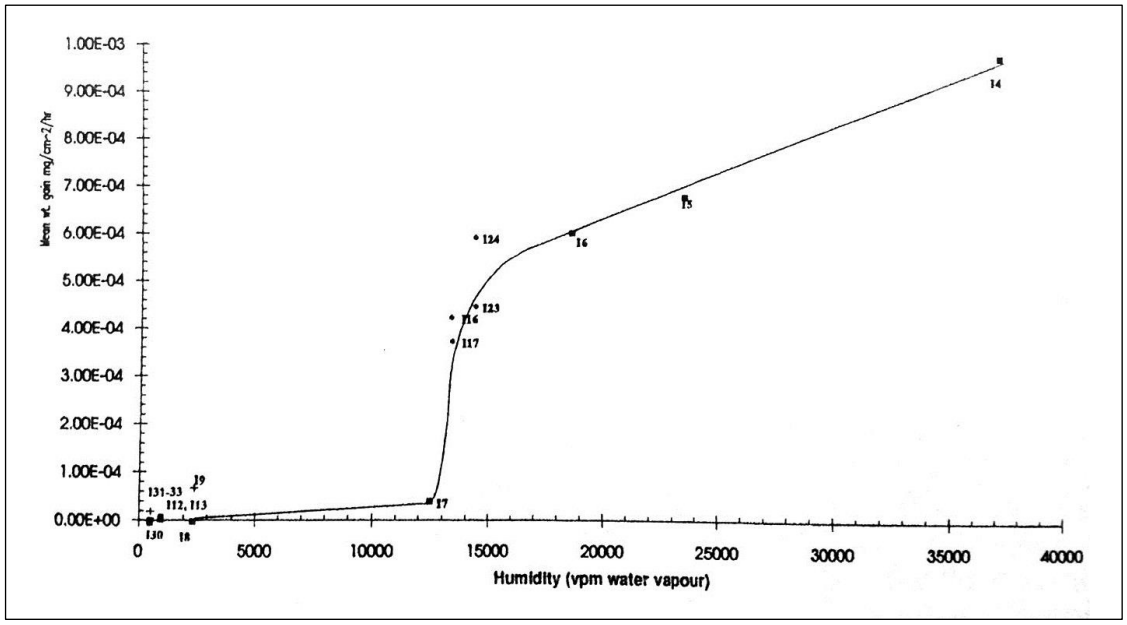

Figure 1.4 A plot showing normalised corrosion rates of irradiated mild steel samples as a function of moisture acquired via weight-change measurements. The sharp step-change is the critical onset humidity, and is at 13000 vpm (parts per million by volume, the ratio between water vapour and total gas pressures) which is around 35% Relative Humidity at 20°C.[2]

1.2.3 Carbonaceous Deposition

The carbonaceous deposits often present on irradiated AGR fuel pins have been investigated and characterised in a number of industrial projects.[1, 2, 10] Two main deposition mechanisms were identified, with each resulting in different amounts and structures of carbon deposit. The radiolysis of the principal reactor coolant, CO_2, produces various radiolysis products such as CO and oxygen radicals. The oxygen radical in turn interacts with the graphite core of the reactor and forms more CO (thus removing carbon from the core). At the fuel cladding surface, CO molecules may interact, releasing C atoms as a deposit and re-forming CO_2. Thus the process restarts and continually carbon is being removed from the core moderator and deposited on the fuel. There are also other minor species in the coolant, such as CH_4, ethene and ethane, and some of these further influence the carbon redistribution processes. . The carbon formed through this pathway possesses a complex structure, often filamentary or columnar in nature, with effective thicknesses of over 150 µm although generally between 100-150 µm. The amount and structure of carbonaceous deposition on the SNF pins is found to be mainly dependent on the reactor it was

irradiated in, the length of time the fuel had been in the reactor and the fuel pin's physical position in the reactor. The carbon build-up is a problem for the industry as it shields heat when in the reactor and retains moisture after pond storage, increasing the chances of pins corroding in long term dry storage.

1.3 Research Programme Overview

Aqueous and atmospheric corrosion of metals is a huge and unavoidable issue in our modern industrial society. It is estimated that roughly 3% of the world GDP overall is spent on corrosion issues, and this percentage is even greater in the more developed nations.[11] The underlying theory of atmospheric corrosion is accordingly well developed, and models based on empirical observations allow for successful corrosion mitigation measures to be regularly employed in the production and maintenance of the various infrastructure, engineering, and construction projects for which it will be a necessary consideration.

Due to the complexity of the systems involved and the large impact of metallic degradation, efforts are predominantly focussed on environments where moisture and contaminants (the key driving influences on corrosion rates) are minimally controlled.[12] In these environments, materials consideration, surface coatings and modification techniques go hand-in-hand with the more practical maintenance and repair needed in order to preserve the functionality of all key metallic systems. The electrochemical corrosion reactions are highly pronounced and thus industrially significant in scenarios where the ready availability of moisture allows for its electrolytic action, but there a key lack of understanding of the physical processes involved in metallic degradation at lower humidities, where corrosion rates are minimal but degradation is seen nonetheless to progress. This nanoscale corrosion action is important in the case of sensitive systems and applications, and those metallic systems which must maintain their integrity over long timescales.

This research project is driven by concerns regarding the long-term storage of spent nuclear fuel and other nuclear-related wastes, and aims to examine the behaviour of adsorbed surface water on industrially relevant substrates via sensitive surface characterisation techniques. A key feature of the project is the development of a non-destructive optical spectroscopy technique called vibrational sum-frequency spectroscopy (VSFS) which allows for high-sensitivity chemical and conformational measurements to be taken from surface adsorbates in a controlled laboratory setting.[13] A number of model sample systems will be examined to test the efficacy and

capabilities of the VSFS technique, and measurements of adsorbed surface water on metallic substrates will be presented and analysed.

Also under investigation is the rutile TiO_2(110) surface, pictured in Figure 1.5, for which a novel in-air preparation and cleaning procedure has been developed and investigated. TiO_2(110) is to-date the most studied TiO_2 surface and is frequently used as the model metal oxide surface for fundamental scientific studies, but titanium dioxide itself is a highly relevant material with wide applications in photovoltaics, corrosion control, catalysis and medical implantation.[14] Here, the VSFS technique will be used to characterise TiO_2 surface chemistry, and an investigation will also be conducted into the adsorption on TiO_2 of the volatile organic molecules acetonitrile and acetic acid.[15]

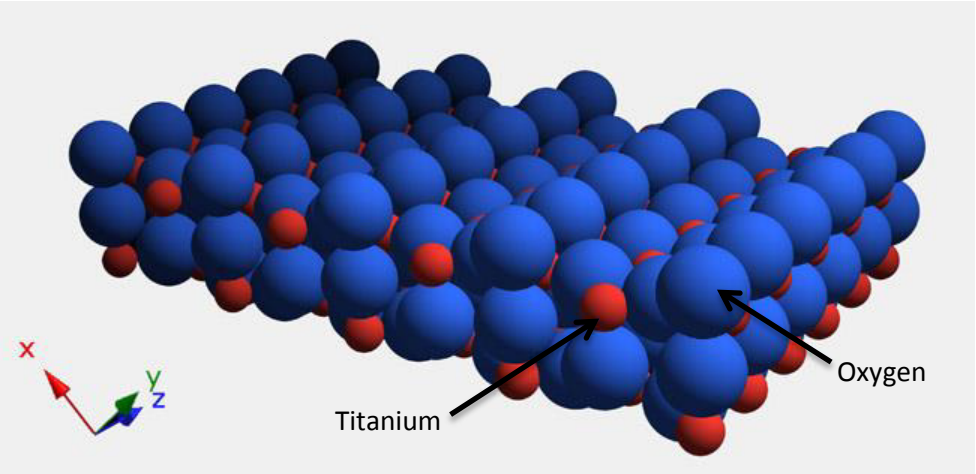

Figure 1.5. The TiO_2(110) surface, with crystallographic axes shown for clarity.

1.4 References

1. Walters WS. Current State of UK Nuclear Fuel Cycle (personal communication). In: Lydiatt F (ed), 2012.
2. Walters WS. Review of the Experimental Data on AGR Cladding Corrosion under Dry Storage Conditions. In: Hands B (ed): National Nuclear Laboratory, 2009.
3. MacKay D, *Sustainable Energy-without the hot air*. 2008: UIT Cambridge.
4. Pickard WF. Finessing the fuel: Revisiting the challenge of radioactive waste disposal. *Energy Policy*. 2010; **38:** 709-14.
5. Steer AG. AGR core design, operation and safety functions. *SPECIAL PUBLICATION-ROYAL SOCIETY OF CHEMISTRY*. 2007; **309:** 11.
6. Walters WS, Paintin PD. Radiolytic corrosion of stainless steel AGR fuel element cladding under conditions relevant to the proposed SNL modular vault dry store. In: Perkins R (ed) Atomic Energy Authority, 1994.
7. Schweitzer PA, *Fundamentals of metallic corrosion: atmospheric and media corrosion of metals*. 2006: CRC press.
8. Busby J, Was G, Kenik E. Isolating the effect of radiation-induced segregation in irradiation-assisted stress corrosion cracking of austenitic stainless steels. *Journal of nuclear materials*. 2002; **302:** 20-40.
9. Nesic S, Sun W, Richardson T, Cottis B, Lindsay R, Lyon S, Scantlebury D, Stott H, Graham M. Corrosion in acid gas solutions. *Shreir's Corrosion*. 2010; **2:** 1270-98.
10. Sykes M, Edwards I, Thomas K. Metal carbonyl decomposition and carbon deposition in the advanced gas-cooled nuclear reactor. *Carbon*. 1993; **31:** 467-72.
11. Revie RW, *Corrosion and corrosion control*. 2008: John Wiley & Sons.
12. Cottis RASLL, *Shreir's corrosion*. 2010, Amsterdam; London: Elsevier.
13. Jayathilake H, *Vibrational Sum Frequency Generation Spectroscopy: Basics, Concepts, Method Development & Applications*. Vol. 1. 2010, Saarbrücken, Germany: VDM Verlag. 212.
14. Pang CL, Lindsay R, Thornton G. Chemical reactions on rutile TiO2 (110). *Chemical Society Reviews*. 2008; **37:** 2328-53.
15. Jang JH, Lydiatt F, Lindsay R, Baldelli S. Quantitative Orientation Analysis by Sum Frequency Generation in the Presence of Near-Resonant Background Signal: Acetonitrile on Rutile TiO2 (110). *Journal of Physical Chemistry A*. 2013; **117:** 6288-302.

Chapter 2. Atmospheric Corrosion & the Interaction of Water with Surfaces

2.1 Introduction

Metallic corrosion ultimately involves the chemical redistribution of metal atoms from exposed surfaces, which on a macroscopic scale may result in the functional or structural failure of components e.g. rust damage. This component degradation is the driving force behind the ultimate need for better corrosion understanding and control. The aqueous corrosion which occurs on environmentally exposed metals depends upon surface water, which is the focus of this research programme.

To interpret any data related to water on metal surfaces will require a better understanding of corrosion processes and prior experimental approaches. This chapter will introduce the background behind atmospheric corrosion, and also present a general overview of current thinking regarding water adsorption behaviour.

2.2 Basics of Aqueous Corrosion

Aqueous corrosion as depicted in Figure 2.1 is an electrochemical process that occurs in a corrosion cell, which in order to function must have several key components. A dissolving metal anode must be connected to a non-dissolving cathode via both a conducting metallic pathway and a conductive electrolyte capable of transferring electric charge through ion diffusion. The driving force for this reaction is a potential difference, which can be present either due to physical or chemical inhomogeneities in the metal or alternatively due to local differences in the concentration of oxygen (the primary oxidising agent) dissolved in the electrolyte. Whilst aqueous corrosion of this nature is thermodynamically favourable, in many metals the process is significantly limited by the rapid formation of a surface metal oxide layer.[1] The oxide layer acts to limit chemical diffusion and may effectively passivate the metal surface, although in actuality the oxides can be easily disrupted by impurities or difference in microstructure and so corrosion is allowed to continue, albeit at a slower rate. This passivation is the reason for the characteristic shape of corrosion rate-humidity plots such as in Figure 1.4, with a sudden sharp increase in the corrosion rate at the onset humidity which quickly levels out to a much shallower gradient as surface oxides are formed.

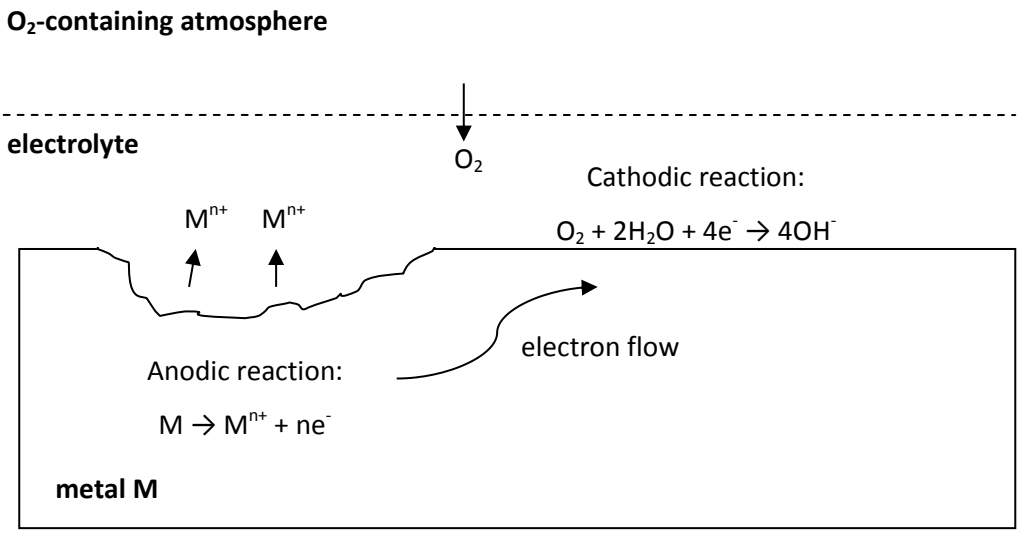

Figure 2.1. A schematic of a typical aqueous corrosion reaction

Oxidation occurs spontaneously on most metals in the absence of moisture due to reaction with physisorbed O_2 from the gas phase. The metal oxide initially forms at nucleation points and spreads across the surface, and it fairly quickly becomes stable due to it forming a sufficient barrier between the bare metal and the atmosphere. Oxides formed via this dry oxidation mechanism tend to have good coverage and may reduce the rate of aqueous corrosion on the metal surface more efficiently when compared to metal oxides formed in the presence of water.[2]

2.3 Atmospheric Corrosion

2.3.1 Overview

Atmospheric corrosion of metals occurs when adsorbed water layers due to humidity in the air are present on the surface, often in conjunction with atmospheric impurities. The presence of surface water alone is sufficient for the onset of aqueous corrosion provided enough is present to allow mass transport and act as an electrolyte.[2]

If water vapour is present in the air surrounding a metallic surface, depending on the chemical and thermodynamic environment it is likely that water molecules will become adsorbed at chemically favourable sites. Assuming the environment to be closed or in a relatively steady state, this reversible water adsorption process will eventually reach an equilibrium. The amount of water on the surface at equilibrium will depend on several variables such as pre-existing oxides,

surface contaminants and surface structure[3], but the key variables are temperature and the availability of water in the vapour phase, both of which factor into a Relative Humidity (RH) measurement.

The Relative Humidity of a gas-water vapour mixture is the ratio between the water vapour density and the saturation vapour density at a specific temperature and pressure. When these two vapour densities are equal, the RH is 100%, and liquid water will condense directly out of the gas phase – this is called the Dew Point. As previously mentioned, in a 'damp' corrosion regime, corrosion will become significant when there is enough surface water to act as an electrolyte for ionic transport, and the necessary humidity for this to occur is often well below 100% RH. Table 2.1 shows estimates for the number of adsorbed monolayers of surface H_2O for a standard temperature and pressure, and thus initial work in this area suggests that only between 1-2 water monolayers are necessary before the critical onset humidity. These values have been deduced from quartz crystal microbalance measurements taken of a number of metals in varying humidities, where the mass of the adsorbed water has been acquired.[4]

Approximate number of water surface monolayers adsorbed on metals vs. Relative Humidty	
Relative Humidty	**Number of Monolayers**
20	1
40	1.5-2
60	2-5
80	3-10

Table 2.1. Humidity versus adsorbed water monolayers metals, with data compiled from several weight change experiments.[2]

It should be noted that as these data were taken via weight change measurements, the surface distribution of water has been assumed homogeneous although this is not necessarily the situation.

Outside of this idealised model of aqueous degradation, atmospheric impurities (most commonly nitrogen- or sulphur-containing compounds, oxidising agents, aerosol particles, or organic acids) may affect the corrosion process in several ways; by increasing the amount of surface water, by

altering the pH of the surface film, or by affecting the amount of metallic surface oxides.[3] In a complex environment, these impurities are a result of biological, chemical and human factors, and as such cannot feasibly be controlled or militated against.

2.3.2 Humidity effects

Previous studies on atmospheric corrosion of metals, both in general and specifically related to steel, have helped to characterise the key controlling factors and the various chemical reactants and their products. Early work done by Vernon revealed low atmospheric corrosion rates of metal samples even at 100% RH when measurements were performed in purified air, void of significant electrolyte content.[5] Small weight increases are seen but reach a steady state rapidly, corresponding to the creation of a passivating layer via surface oxidation.[3] The critical humidity level required for sufficient water adsorption onto a real-world metal surface actually depends on several variables; the nature of the metal surface, the presence of atmospheric pollutants and the hygroscopic nature of any surface deposits or contaminants.[6]

2.3.3 Impurity effects

The introduction of trace impurities such as NaCl, NH_3, NOx or SOx significantly increases corrosion rates at all humidities, and sharp step changes appear, generally between 50-80% RH.[5, 7, 8] Further studies have since linked the presence of these trace impurities with an increased pH of the adsorbed water layers, which has the effect of accelerating the dissolution of the protective oxide.[3] Aerosol particles also commonly affect surface pH, having accumulated nitrates and sulphates from the atmosphere. These are also often hygroscopic, so promoting further water adsorption.[4] A review by Roberge of several atmospheric corrosivity models indeed cites the deposition rate of pollutants and aerosols as the primary factor influencing metal corrosion rates.[8]

The periodic nature of atmospheric conditions can lead to repeated wetting and drying of metallic surfaces. This compounds the effects of impurities as they remain after drying, resulting in high localised concentrations.[7, 9]

Also of note is the production of nitrogen oxy-acids and other acidic or cathodic reduction species in the presence of radiation as studied by Byalobzheskii in the 1950s, which was found to both reduce the critical onset humidity and increase the overall weight change due to corrosion compared to the equivalent non-irradiated metal samples.[10]

2.4 Introduction to Water Interaction with Surfaces

2.4.1 Overview

Until fairly recently the accepted model of water adsorption on metal surfaces has been of an ice bilayer structure, made up of intact molecules with a long range ordering and only marginally distorted from the bulk ice structure to accommodate for surface topography, reactive species or surface defects.[11] Poor agreement with previous data and new emerging studies have led to the revision of this model to a far more complex situation, depending heavily on the specific water-surface interactions and the bonding between the water molecules.[12]

2.4.2 Experimental approaches

When determining the chemistry and structure of molecular and thin film water at interfaces, experimental approaches must be chosen that do not interfere significantly with the system. X-ray Photoelectron Spectroscopy (XPS) and other similar photoemission techniques (e.g. Auger Electron Spectroscopy) are used to identify surface species; low X-ray fluxes are employed along with scanning of the samples, due to the high electron sensitivity of water films.[13]

Crystallographic probes such as Low Energy Electron Diffraction (LEED) will return structural information from ordered surface structures in the form of complex diffraction patterns, but again low exposures must be used. X-rays, neutrons and helium nuclei may also be used as probes for surface elastic scattering/diffraction measurements, as their different scattering properties return complementary structural information and may offer additional benefits. Helium scattering for example is a non-destructive technique and avoids the complications of multiple scattering events.[12] Electron Energy Loss Spectroscopy (EELS) and its high-resolution version HREELS harness inelastic electron scattering, and the energy loss of scattered electrons has been used to infer electronic and vibrational states of adsorbed water.[14]

Scanning Tunnelling Microscopy (STM) is a high-resolution surface imaging technique capable of resolving individual atoms, and is used extensively to image the initial structure and behaviour of water clusters and overlayers.[15] When combined with computational techniques utilising density functional theory (DFT) to calculate molecular structures, STM has been highly instrumental in developing many of the currently accepted models for initial water adsorption.[16, 17] Atomic Force Microscopy (AFM) is an alternative topographical imaging technique which can be used to evaluate film and droplet morphology, and may also be used to identify liquid surface layers via surface adhesion measurements.

The bonding energies of adsorbed water or hydroxyls can be examined using a technique called Temperature Programmed Desorption (TPD). In TPD, samples are heated at a steady rate and species desorbed from the surface are analysed by a mass spectrometer; the temperature can then be correlated with adsorption energies. Another desorption technique known as Electron Stimulated Desorption in Ion Angular Distributions (ESDIAD) bombards adsorbates with electrons and measure emitted ions as a function of angle, this allows direct determination of adsorbate bond strengths and orientation.[18]

Finally, vibrational spectroscopies such as reflection-absorption infrared spectroscopy (RAIRS, IRAS) or vibrational sum-frequency spectroscopy (VSFS) will give information on the various bonding structures present in adsorbed water through optical excitation, although accurate ascription of spectral features to specific chemical bonds requires a good physical model acquired through additional complementary techniques e.g. STM, DFT.

Fundamental studies of water adsorption behaviour are often performed at low temperatures to ensure the system under investigation is a static one, and additionally many of the above experimental techniques require UHV conditions due the finite mean free path of probe or emission molecules. As such there is still a knowledge gap to bridge between fundamental molecular models and real-world applicability, and in response to this a number of high-pressure or ambient condition analogues to the techniques formerly described have been recently developed. Aside from purely optical spectroscopic techniques which are mostly invariant in/out of vacuum conditions, High Pressure XPS or Ambient Pressure Photo-Electron Spectroscopy (APPES) will now allow chemical photoemission spectra to be acquired for samples in pressures of up to 25 mbar.

2.4.3 Water adsorption behaviour

Water is a nonlinear molecule with a net polarity owing to the strong electronegativity of the oxygen's lone pair electrons. This means neighbouring water molecules will align and bond with one another in an arrangement called a hydrogen bond or H-bond, which is key to many of the unique properties of water. An H-bond is intermediate between ionic/covalent and Van der Waals bonding where the hydrogen acts as a proton donor for the lone electron pair of the adjacent water molecules' oxygen, and whilst it is a relatively weak effect it leads in bulk water to large-scale ordering of H_2O in an H-bonded network.[19]

In terms of water adsorption, fundamental studies on single crystal metals under UHV have observed and modelled a variety of initial structures for low concentrations, varying in size from

basic water dimers[20] (two H_2O molecules), to the stable ice building block the cyclic hexamer[21, 22] (a ring of six H_2O), up to chains[23] and large clusters with many multiple component water molecules. All of these have been observed via STM and modelled using DFT, which predicts the various bond orientations relative to the surface.[16, 17, 24, 25]

Such clustering occurs when the intermolecular water-water interactions are of greater strength than water-surface interactions, such as is the case on noble metals.[22, 26, 27] Water adsorption on all substrates has been found to be highly dependent on this balance between H-bonding and surface/substrate effects, and the structure and binding strength of the initial deposition state then governs that of subsequent adlayers.[12] Two other regimes have been classified based on this principle, and each are associated with their own water adsorption mechanisms. When the water-water interactions are smaller in strength than water-surface interactions, this will result in a surface layer in a state of partial dissociation with some molecular water adsorption and some dissociation of H_2O into OH/H.[28, 29] Only when water surface interactions dominate the intermolecular energies will one observe full dissociation, as is also observed locally on many metal surfaces at defect sites,[30, 31] oxygen vacancies and step edges.[29] Importantly for this study, there have been numerous UHV investigations of water adsorption on model metal oxides which have seen significant dissociation and thus surface hydroxylation from the surface termination other than solely at select defect sites.[30, 32, 33]

Surface hydroxyls are strong H-bond acceptors,[34] and the availability of so called 'dangling' OH such as surface hydroxyls and free O-H (the O-H bond of adsorbed water that does not participate in H-bonding) heavily influences surface wetting behaviour, as these strong acceptors act as adlayer nucleation sites.[35, 36] The stability of any associated hydrogen bonded network that might develop is however found to be dependent on the quality of the H-bonds rather than the number, and this often relates back to the initial surface adsorption structure as governed again by surface effects such as chemistry, temperature and crystal coordination.[12, 37] For example, some surface geometries lead to a multilayer ordered ice structure,[38] whilst some result in amorphous structures.[39]

A review of findings concerning water adsorption on metal oxides and non-UHV measurements of surface water will be presented in Chapter 6, which begins to examine water adsorption on various metallic substrates via the VSFS technique.

2.5 References

1. Ahmad Z, *Principles of corrosion engineering and corrosion control*. 2006: Butterworth-Heinemann.
2. Schweitzer PA, *Fundamentals of metallic corrosion: atmospheric and media corrosion of metals*. 2006: CRC press.
3. Cottis RASLL, *Shreir's corrosion*. 2010, Amsterdam; London: Elsevier.
4. Leygraf C, *Atmospheric corrosion*. 2000: Wiley Online Library.
5. Vernon W. A laboratory study of the atmospheric corrosion of metals. Part II.—Iron: the primary oxide film. Part III.—The secondary product or rust (influence of sulphur dioxide, carbon dioxide, and suspended particles on the rusting of iron). *Transactions of the Faraday Society*. 1935; **31:** 1668-700.
6. Roberge PR, *Handbook of corrosion engineering*. Vol. 1128. 2000: McGraw-Hill New York.
7. Graedel TE, Frankenthal RP. CORROSION MECHANISMS FOR IRON AND LOW-ALLOY STEELS EXPOSED TO THE ATMOSPHERE. *Journal of the Electrochemical Society*. 1990; **137:** 2385-94.
8. Roberge PR, Klassen RD, Haberecht PW. Atmospheric corrosivity modeling - a review. *Materials & Design*. 2002; **23:** 321-30.
9. Zhu F, Zhang XY, Persson D, Thierry D. In situ infrared reflection absorption spectroscopy studies of confined zinc surfaces exposed under periodic wet-dry conditions. *Electrochemical and Solid State Letters*. 2001; **4:** B19-B22.
10. Ab B. THE EFFECT OF IONIZING RADIATION ON THE CORROSION OF METALS UNDER ATMOSPHERIC CONDITIONS. *ZHURNAL FIZICHESKOI KHIMII*.
11. Menzel D. Surface science - Water on a metal surface. *Science*. 2002; **295:** 58-9.
12. Hodgson A, Haq S. Water adsorption and the wetting of metal surfaces. *Surface Science Reports*. 2009; **64:** 381-451.
13. Henderson MA. The interaction of water with solid surfaces: fundamental aspects revisited. *Surf. Sci. Rep.* 2002; **46:** 5-308.
14. Wu M-C, Estrada CA, Goodman DW. New approach to high-resolution electron-energy-loss spectroscopy of polar materials: Studies of water and methanol adsorption on ultrathin MgO (100) films. *Physical review letters*. 1991; **67:** 2910.
15. Okuyama H, Hamada I. Hydrogen-bond imaging and engineering with a scanning tunnelling microscope. *Journal of Physics D: Applied Physics*. 2011; **44:** 464004.
16. Meng S, Wang EG, Gao S. Water adsorption on metal surfaces: A general picture from density functional theory studies. *Physical Review B*. 2004; **69:** 195404.
17. Schaub R, Thostrup P, Lopez N, Lægsgaard E, Stensgaard I, Nørskov JK, Besenbacher F. Oxygen vacancies as active sites for water dissociation on rutile TiO 2 (110). *Physical Review Letters*. 2001; **87:** 266104.
18. Doering DL, Madey TE. The adsorption of water on clean and oxygen-dosed Ru (011). *Surface Science*. 1982; **123:** 305-37.
19. Ludwig R. Water: from clusters to the bulk. *Angewandte Chemie International Edition*. 2001; **40:** 1808-27.
20. Motobayashi K, Matsumoto C, Kim Y, Kawai M. Vibrational study of water dimers on Pt (111) using a scanning tunneling microscope. *Surface Science*. 2008; **602:** 3136-9.
21. Xantheas SS. Cooperativity and hydrogen bonding network in water clusters. *Chemical Physics*. 2000; **258:** 225-31.
22. Gregory JK, Clary DC, Liu K, Brown MG, Saykally RJ. The water dipole moment in water clusters. *Science*. 1997; **275:** 814-7.
23. Yamada T, Tamamori S, Okuyama H, Aruga T. Anisotropic water chain growth on Cu (110) observed with scanning tunneling microscopy. *Physical review letters*. 2006; **96:** 036105.
24. Wehling TO, Lichtenstein AI, Katsnelson MI. First-principles studies of water adsorption on graphene: The role of the substrate. *Applied Physics Letters*. 2008; **93:** 202110.

25. Michaelides A, Morgenstern K. Ice nanoclusters at hydrophobic metal surfaces. *Nature Materials*. 2007; **6:** 597-601.
26. Liu K, Cruzan JD, Saykally RJ. Water clusters. *SCIENCE-NEW YORK THEN WASHINGTON-*. 1996**:** 929-32.
27. Henderson MA. The interaction of water with solid surfaces: fundamental aspects revisited. *Surface Science Reports*. 2002; **46:** 1-308.
28. Stirniman MJ, Huang C, Smith RS, Joyce SA, Kay BD. The adsorption and desorption of water on single crystal MgO (100): The role of surface defects. *The Journal of chemical physics*. 1996; **105:** 1295-8.
29. Giordano L, Goniakowski J, Suzanne J. Partial dissociation of water molecules in the (3× 2) water monolayer deposited on the MgO (100) surface. *Physical review letters*. 1998; **81:** 1271.
30. Bikondoa O, Pang CL, Ithnin R, Muryn CA, Onishi H, Thornton G. Direct visualization of defect-mediated dissociation of water on TiO2 (110). *Nature materials*. 2006; **5:** 189-92.
31. Smyth DM. The defect chemistry of metal oxides. *The Defect Chemistry of Metal Oxides, by DM Smyth, pp. 304. Foreword by DM Smyth. Oxford University Press, Jun 2000. ISBN-10: 0195110145. ISBN-13: 9780195110142*. 2000; **1**.
32. Brookes IM, Muryn CA, Thornton G. Imaging water dissociation on TiO 2 (110). *Physical review letters*. 2001; **87:** 266103.
33. Raymand D, van Duin ACT, Goddard Iii WA, Hermansson K, Spångberg D. Hydroxylation Structure and Proton Transfer Reactivity at the Zinc Oxide− Water Interface. *The Journal of Physical Chemistry C*. 2011; **115:** 8573-9.
34. Michaelides A, Hu P. A density functional theory study of hydroxyl and the intermediate in the water formation reaction on Pt. *The Journal of Chemical Physics*. 2001; **114:** 513-9.
35. Salmeron M, Bluhm H, Tatarkhanov M, Ketteler G, Shimizu TK, Mugarza A, Deng X, Herranz T, Yamamoto S, Nilsson A. Water growth on metals and oxides: binding, dissociation and role of hydroxyl groups. *Faraday discussions*. 2009; **141:** 221-9.
36. Karlberg GS, Olsson FE, Persson M, Wahnström G. Energetics, vibrational spectrum, and scanning tunneling microscopy images for the intermediate in water production reaction on Pt (111) from density functional calculations. *The Journal of chemical physics*. 2003; **119:** 4865-72.
37. Liu K, Brown MG, Carter C, Saykally RJ, Gregory JK, Clary DC. Characterization of a cage form of the water hexamer. *Nature*. 1996; **381:** 501-3.
38. Feibelman PJ, Bartelt NC, Nie S, Thürmer K. Interpretation of high-resolution images of the best-bound wetting layers on Pt (111). *The Journal of chemical physics*. 2010; **133:** 154703.
39. Angell CA. Amorphous water. *Annu. Rev. Phys. Chem.* 2004; **55:** 559-83.

Chapter 3. Principles of VSFS & Other Experimental Techniques

3.1 Introduction

Traditionally, atmospheric corrosion research was limited to weight-change or stress-failure experiments of test coupons left outside or in controlled lab atmospheres[2], but the introduction of electrochemical techniques meant instantaneous corrosion rates could be measured in controlled environments.[3] Chemical or molecular analysis was necessarily performed ex situ via X ray Photoelectron Spectroscopy (XPS), Low Energy Electron Diffraction (LEED), Scanning Electron Microscopy (SEM) or Secondary Ion Mass Spectrometry (SIMS)[4], but more recently, surface-specific techniques that do not require vacuum conditions are being employed. Now a more holistic approach can be taken towards understanding atmospheric corrosion at a molecular scale, utilising complimentary techniques such as Atomic Force Microscopy (AFM), Infrared Reflection-Absorption Spectroscopy (IRAS) and Vibrational Sum Frequency Spectroscopy (VSFS) to characterise surface species and structures in situ.[4-8] Through using such complimentary techniques for example, Leygraf managed to identify the importance of the solid-liquid over the liquid-gas interfacial processes in the acidic corrosion of Cu and Zn.[9]

This chapter will focus on the principles governing the experimental techniques used; primarily the science behind optical spectroscopies and VSFS, and then also the complimentary surface characterisation techniques of contact angle analysis, AFM and XPS.

3.2 Vibrational sum-Frequency Spectroscopy

3.2.1 History of VSFS

Investigating the vibrational modes of molecules can provide a wealth of information for any given scenario, and has been used successfully in scientific investigations for many years. Herschel discovered the existence of infrared radiation in 1800, and after a brief period of inactivity it was finally used to measure the first infrared absorption spectra around the start of the 20th century, first notably by Abney and Festing[10] and then in great depth by Coblentz[11]. It was recognised through this early work that compounds and some of their constituent chemical groups possessed characteristic absorption bands, due to vibrational excitations of the constituent molecular bonds. Absorption bands may also arise as a result of electronic excitation, but these are typically at higher energies corresponding to shorter wavelengths of light.

Raman was the first person to observe the inelastic light scattering processes which now bear his name, and the significant work of Placzek in the 1930s enabled the development of techniques which would allow chemical vibrational information to be acquired with a single monochromatic light source. The development and introduction of lasers in 1960 allowed much more detailed information to be gathered via optical spectroscopy methods due to their greater peak powers and coherence length – this is sometimes referred to as the 'birth of modern spectroscopy'.

Whilst still used extensively in surface science, infrared absorption and Raman spectroscopies lack any inherent surface specificity, meaning it can be problematic to separate surface signals from bulk response. The first appearance of surface-specific optical spectroscopy was the development of Second Harmonic Generation (SHG) spectroscopy through the 1960s and 70s, and the 1980s saw a large interest in utilising nonlinear optical effects experimentally; this is when the majority of these techniques were pioneered, notably by Shen's research group which published the first sum-frequency generated spectra.[12]

3.2.2 Theory

Surface Spectroscopy

There are a variety of optical mechanisms by which surface adsorbates may be probed. All of these are a result of the interaction between the adsorbate molecules and an incident electromagnetic field $\boldsymbol{E}$. The simplest and most well-established of these is via infrared (IR) absorption, where an electromagnetic field at infrared wavelengths $\boldsymbol{E}_{IR}$ effects a change in the transition dipole moment μ along a vibrational coordinate Q. The intensity $\boldsymbol{I}_{IR}$ of the transition is proportional to both the strength of the dipole moment and of the electromagnetic field, so that

$$\boldsymbol{I}_{IR} \propto \left(\frac{\partial \mu}{\partial Q}\right)^2 |\boldsymbol{E}_{IR}|^2$$

(Eq 1.)

Concerning surface studies, Reflection Absorption Infrared Spectroscopy (RAIRS) is a common technique associated with this induced transition, along with IR Attenuated Total Reflectance (IR-ATR) modification which utilises an aspect of total internal reflectance to minimise the effective IR sampling depth. This IR light is incident on a surface and the reflected light is collected and analysed – where a vibrational transition has occurred there is a typically notable loss in the reflected intensity, which can be used to identify chemical resonances.[13] The energy level diagram for a basic ground-state IR excitation is shown in Figure 3.2.

Another optical surface transition which is relevant to VSFS is the Raman scattering transition, which is sensitive to electromagnetic fields in the visible region $\boldsymbol{E}_{VIS}$. Raman-active wavelengths – which can be in the visible, near-IR or ultraviolet range – are absorbed at a surface and then re-emitted instantaneously by scattering.[14] The electromagnetic field interacts with molecular vibrations or other system excitations, which results in a shift in the emitted light away from the excitation wavelength. The Raman shift can be positive or negative; when energy is absorbed by the molecule (and thus there is a decrease in the emitted photon energy) it is called a Stokes shift, and when the molecule loses energy (resulting in an increase in emitted photon energy) this is an anti-Stokes shift as shown also in Figure 3.2. Effectively, the field $\boldsymbol{E}_{VIS}$ induces a dipole moment and the intensity $\boldsymbol{I}_{VIS}$ of scattered light shifted by the vibrational energy is related to the change in molecular polarisability α along the vibrational coordinate Q such that

$$\boldsymbol{I}_{VIS} \propto \left(\frac{\partial \alpha}{\partial Q}\right)^2 |\boldsymbol{E}_{VIS}|^2$$

(Eq 2.)

Sum-Frequency Generation is a two stage nonlinear optical process that can occur through a coherent combination of both infrared and Raman transitions. For it to take place the molecular vibration under investigation must be both infrared- and Raman-active, which depends on specific geometries and selection rules. For a mode to be IR-active, there must be a change in the overall dipole moment μ during the normal vibration along Q, otherwise Equation 1 gives zero intensity. On metal surfaces the added effect of an induced image dipole on the conductive surface renders certain vibrational modes IR-inactive, as illustrated by the flat-lying CO molecule in Figure 3.1.

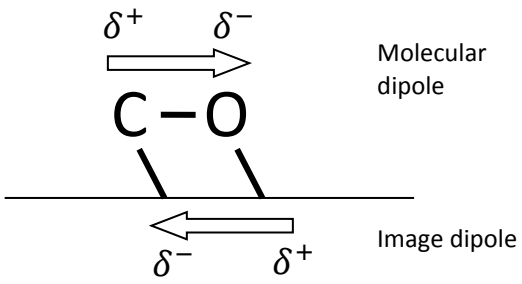

Figure 3.1. An example of vibrational mode that is non IR-active due to a metallic image dipole.[15]

For a mode to be Raman-active it must experience a change in molecular polarisability α during the normal vibration, which physically corresponds to a slight molecular distortion under an incident EM field.

The intensity of the sum-frequency response $\boldsymbol{I}_{SFG}$ can then be described by

$$\boldsymbol{I}_{SFG} \propto \left(\frac{\partial \mu}{\partial Q}\right)^2 \left(\frac{\partial \alpha}{\partial Q}\right)^2 |\boldsymbol{E}_{IR}|^2 |\boldsymbol{E}_{VIS}|^2$$

(Eq 3.)

Energy-level Interpretation

It is equally valid to describe the various processes of IR absorption, Raman scattering and sum-frequency generation in terms of potential and vibrational energy levels. Assuming the probed molecule to be in a resting ground state, excitation with an IR photon of appropriate energy will promote the system from the $\upsilon = 0$ to the first vibrational mode $\upsilon = 1$. Subsequent excitation by a higher-energy visible photon will promote the system up into a virtual electronic state, and the natural ground state is then returned to via the emission of an SFG photon. This alternative interpretation of sum-frequency generation is illustrated in Figure 3.2, which shows all three transitions and demonstrates how the total photon energy is conserved.

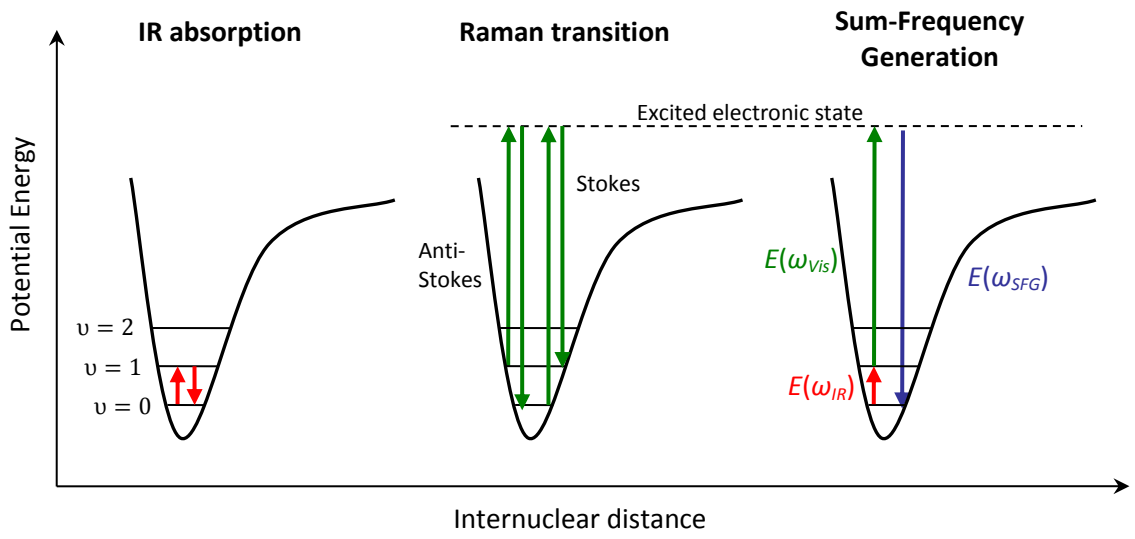

Figure 3.2. A potential energy diagram showing the energy level transitions of IR absorption, Raman, and SFG processes.

Nonlinear Optics

To better understand some of the physical principles involved in the light generation and interaction processes in VSFS, it will help to briefly illustrate the theory behind nonlinear optical effects. All electromagnetic (EM) radiation can be described mathematically in terms of a complex electric field vector with phase and time dependencies, and the propagation of light can be accurately described via Maxwell's equations.[16] To solve Maxwell's equations for light in a medium, the induced polarisation term must be included which contains within it the effect of the medium. For a simplified wave travelling through a medium in the z-direction, the solution to Maxwell's equations can be written as

$$\frac{\partial^2 E}{\partial x^2} - \frac{1}{c^2}\frac{\partial^2 E}{\partial t^2} = \mu_0 \frac{\partial^2 P}{\partial t^2}$$

(Eq 4.)

where E is the electric field, c is the speed of light, μ_0 is the permeability of free space and P is the polarisation term. This is the inhomogeneous wave equation. The polarisation vector $\boldsymbol{P}$ is related to the electric field vector $\boldsymbol{E}$ by

$$\boldsymbol{P} = \varepsilon_0 \chi \boldsymbol{E}$$

(Eq 5.)

where ε_0 is the emissivity of free space and χ is the macroscopic susceptibility term. In linear optics this corresponds to a basic medium interaction whereby a light wave acting on a molecule causes the molecule to vibrate and emit its own light wave which in turn interferes with the first.

When the incident power or irradiance of the EM wave is high enough however, higher order terms must be taken into account, in which case the polarisation term can then be approximated by

$$P = \varepsilon_0\left[\chi^{(1)}E + \chi^{(2)}E^2 + \chi^{(3)}E^3 + \cdots\right]$$

(Eq 6.)

where $\chi^{(n)}$ are the nth-order susceptibilities.

The effects of these additional higher order terms mean that interactions that are classically forbidden such as those between two waves of different frequency are now possible, albeit with a significantly reduced probability of occurrence. In the time-domain, an EM wave can be approximated by

$$E(t) \propto E\exp(i\omega t) + E^*\exp(-i\omega t)$$

(Eq 7.)

where E and E^* are the real and imaginary field amplitudes and ω is related to the wave frequency f by $\omega = 2\pi f$. If we consider the interaction of two EM waves with the different colours ω_1 and ω_2, and then expand for the 2nd order (E^2) term, one can begin to see the physical basis for several well-known optical nonlinear transitions:

$$E(t) \propto [E_1\exp(i\omega_1 t) + E_1^*\exp(-i\omega_1 t)] + [E_2\exp(i\omega_2 t) + E_2^*\exp(-i\omega_2 t)]$$

$$\begin{aligned}
E(t)^2 \propto\ & E_1^2\exp(2i\omega_1 t) + E_1^{*2}\exp(-2i\omega_1 t) && \textbf{a)}\ \omega_1\ 2^{nd}\text{ Harmonic Generation}\\
& + E_2^2\exp(2i\omega_2 t) + E_2^{*2}\exp(-2i\omega_2 t) && \textbf{b)}\ \omega_2\ 2^{nd}\text{ Harmonic Generation}\\
& + 2E_1E_2\exp[i(\omega_1+\omega_2)t] + 2E_1^*E_2^*\exp[-i(\omega_1+\omega_2)t] && \textbf{c)}\ \text{Sum-Frequency Generation}\\
& + 2E_1E_2^*\exp[i(\omega_1-\omega_2)t] + 2E_1^*E_2\exp[-i(\omega_1-\omega_2)t] && \textbf{d)}\ \text{Difference-Freq Generation}\\
& + 2|E_1|^2 + 2|E_2|^2 && \textbf{e)}\ \text{Electro-Optic DC Rectification}
\end{aligned}$$

(Eq 8.)

This description forms the basis of both VSFS and the operation and mechanisms behind the various laser amplifiers used for the VSFS technique.

Vibrational Sum-Frequency Spectroscopy

The generation of a sum-frequency signal results from the interaction between two coincident photons ω_1 and ω_2 at a surface or interface, which then results in the generation of a third photon. The photon frequency is conserved, such that the frequency (and consequently energy, as $E = \hbar\omega$) of the generated photon is the sum of the coincident photon frequencies. An

illustration of this principle is shown in Figure 3.3, which in terms of E-fields corresponds with the term in Equation 8a).

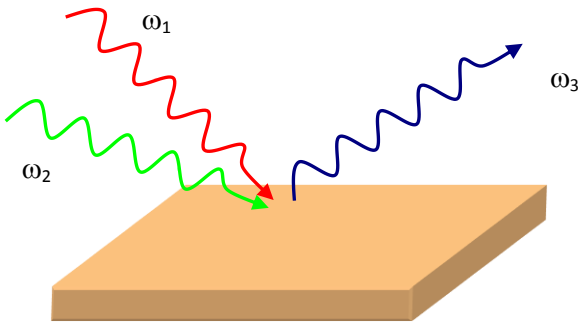

$$\omega_3 = \omega_1 + \omega_2$$

$$\therefore E(\omega_3) = E(\omega_1) + E(\omega_2)$$

Figure 3.3. Diagram showing the basic principles of sum-frequency generation off a surface.

SFG with two incident light sources such as this is referred to as a three-wave mixing process (two waves in, one wave out) and these processes can only occur at interfaces, where a lack of inversion symmetry results in an inherent dipole moment. An interface in this respect could be between two different materials, at a solid-liquid, solid-gas, or liquid-gas interface, essentially at any point where there is a discontinuity in the local optical environment. Typically, VSFS setups involve a tuneable infrared (IR) coherent light source and a fixed visible (VIS) coherent light source. When properly aligned at an SFG-active interface both spatially and temporally, a non-resonant SFG signal will be detected at the incident photons' sum-frequency, in a direction consistent with the conservation of momentum. The non-resonant SFG signal is electronic in origin, and as such is independent of the incident wavelengths. To then probe for chemical species, the infrared frequency ω_{IR} can be set to correspond to the energy of an expected molecular vibrational or electronic transition. If there are transitions present at that energy and the associated bonds have a net polar orientation, there will be an additional resonant element to the SFG signal, which will interfere with the non-resonant contribution and result in a change in SFG intensity.

Electromagnetic Field Interpretation

In terms of the electromagnetic fields, the property of a medium which is probed by VSFS is the macroscopic nonlinear susceptibility $\chi^{(2)}$ which describes the material-light interaction. As previously described, the polarisation of a medium can be described by the following electric dipole approximation

$$P = \left(\chi^{(1)}E + \chi^{(2)}E^2 + \chi^{(3)}E^3 + \cdots\right)$$

(Eq 9.)

where again P is the dielectric polarisation, E is the applied electric field and $\chi^{(n)}$ are the n^{th}-order nonlinear susceptibilities (for simplicity, tensor values will be treated here as scalars). For any three-wave mixing processes in non-centrosymmetric regions (those lacking the inversion symmetry of molecular bulk media) it can be shown mathematically that $\chi^{(2)}$ is the only non-zero term.[17]

Qualitatively, we can write the induced second-order polarisation as a product of $\chi^{(2)}$ and the two incident electric fields, thus

$$P^{(2)}(\omega_2 + \omega_2) = \chi^{(2)}E(\omega_1)E(\omega_2)$$

(Eq 10.)

where $P^{(2)}$ is the induced second-order polarisation or dipole per unit volume. In a medium possessing inversion symmetry, axis reversal leads to a change in the direction of the polarisation and electric field vectors, which can only be satisfied if $\chi^2 = 0$. At an interface or in chiral media however this is not the case, and therein lies the innate surface sensitivity of the SFG transition.

The intensity of the SFG signal is proportional to the absolute square of the second-order susceptibility and the visible and IR intensities such that

$$I_{SFG} \propto \left|\chi^{(2)}\right|^2 I(\omega_{IR})I(\omega_{VIS})$$

(Eq 11.)

Where I_{SFG}, $I(\omega_{IR})$ and $I(\omega_{VIS})$ are the intensities of the SFG, infrared and visible signals respectively.[18] The further relationship

$$\left|\chi^{(2)}\right| = \left|\chi^{(2)}_{\text{nR}} + \sum_q \chi^{(2)}_q\right|$$

(Eq 12.)

describes the second-order susceptibility in terms of the non-resonant contribution $\chi_{nR}^{(2)}$ and the resonant terms $\chi_q^{(2)}$ resulting from q vibrational modes.

The magnitude of the resonant susceptibility term for the q^{th} vibrational mode and also the means with which to calculate molecular orientation is given by the equation

$$\chi_q^{(2)} = N \sum_{abc} \langle \mu_{xyz \cdot abc} \rangle \beta_q^{abc}$$

(Eq 13.)

where *N* is the number density of excitable species at the surface, $\langle \mu_{xyz \cdot abc} \rangle$ is the orientationally-averaged Euler transformation to allow translation of lab coordinates (xyz) into molecular coordinates (abc), and β_q^{abc} is the molecular hyperpolarisability of the q^{th} mode (see Section 5.4.2). Thus the square root of the measured SFG intensity is shown to be sensitive to both the number density and the orientation of molecular species at the interface.

From Equation 13 can be derived a fundamental relationship between the resonant susceptibility term and the frequency of the incident infrared, namely that

$$\chi_{\text{eff}}^{(2)} \propto \frac{A}{\omega_q - \omega_{IR} - i\Gamma}$$

(Eq 14.)

where ω_q is the central frequency of the vibrational transition q and Γ is a damping factor that defines the half-width half-maximum of the transition. As ω_{IR} tends towards ω_q, the denominator tends toward zero and the resonant behaviour is amplified. The term A represents the magnitude of the transition moment which is a product of both the IR transition moment and the Raman polarisability tensor, meaning that only transitions which are both IR and Raman active will give a resonant SFG contribution. This theory is expanded upon in Chapter 5, which will attempt to model molecular orientations.

Narrowband vs. Broadband VSFS

Typically, surface science work via VSFS has been done using a 'narrowband' or scanning SFG setup.[19] In this arrangement, the overlapped IR and visible light sources are both spectrally narrow pulses, and the frequency of the IR light is scanned in steps whilst the visible light frequency is kept constant. This allows an SFG intensity measurement to be taken at each IR value, which when plotted yields an SFG emission spectrum with an effectively flat non-resonant baseline response (after correcting for any non-linearity in the emission spectrum of the IR

generation optics). The advantage of this technique is that the resulting spectra are more easily interpreted visually, and the laser technology for the generation of the spectrally narrow light sources is well established and relatively stable.[19] The technique can however be a time-consuming one, and often changing the IR wavelength will affect the steering of the beam and consequently the SFG overlap. Scanning VSFS setups are also problematic in that the longer duration of spectral acquisitions does not permit investigations into short timescale phenomena. Similarly, due to the inherent relationship between spectral width and pulse duration the narrowband technique is incapable of resolving molecular dynamics which occur over even shorter timescales.

Due to the advancements in pulsed laser technology, it is now possible to use commercial amplifiers to generate ultrafast, high peak intensity laser pulses with durations of the order of femtoseconds. The effects of this can be shown through the following derivation of the Heisenberg Uncertainty Principle,

$$\Delta E \Delta t \geq \frac{\hbar}{2}$$

(Eq 15.)

where ΔE and Δt are uncertainties in energy and time respectively, and $\hbar$ is Plank's constant divided by 2π. As the energy of a photon can be expressed as $E = \hbar\omega$, it then follows that there is a fundamental uncertainty relationship between the pulse width Δt and the spectral bandwidth $\Delta\omega$. Thus as light pulses become shorter, the spectrum of frequencies they contain becomes broader. This effect can be utilised by the IR light source in VSFS and means one can effectively survey a wide range of IR frequencies/wavelengths in a single acquisition, with no need to scan the centre wavelength of the generated infrared light.[20] This significantly saves on acquisition times and also has the added benefit of being able to resolve and identify chemical process and molecular dynamics that happen over increasingly short timescales[21] – atomic and molecular processes generally occur over femtosecond or picosecond timescales due to the short distances involved.

One disadvantage of VSFS spectra taken using ultrafast broadband laser sources is that due to the inherent Gaussian spectral profile of a properly generated ultrafast pulse, the sum-frequency spectral information appears over a Gaussian background (remembering that the non-resonant surface response is only dependent on incident powers and not wavelength) and is thus more difficult to interpret. Equally, ultrafast laser pulses are more prone to spatial and spectral distortion after interacting with optical components, and so the technique can be harder to align and optimise.[22]

Pulse shaping

Assuming ultrafast lasers are to be utilised for broadband VSFS, the resulting frequency spread of the generated sum-frequency spectrum will be a product of the various frequencies of all the interacting infrared and visible excitation photons. To resolve any IR-resonant features in the sample environment, it is necessary to convolute the broadband IR pulse with a fixed visible pulse that has been spectrally narrowed. As the SFG spectrum is a product of two interacting spectral distributions, the overall spectral resolution is by-definition governed by the width of the narrowest source, in this case the visible. A spectrally narrow visible pulse is thus highly desirable, and there are various means of pulse shaping by which to achieve this whilst minimising dispersion or distortion. It should be mentioned that due to the Heisenberg relationship it is equally valid to describe spectral-narrowing in terms of time-stretching; which description to use is purely conventional.

A pulse shaper is anything that specifically changes a pulse's intensity or phase in either the time or frequency domain. The simplest pulse shaping arrangement consists of a double grating-lens pair with an intermediate phase/amplitude mask or a spatial modulator, as shown in Figure 3.4.[23] The first grating translates wavelength into angular dispersion, and a corrective cylindrical lens collimates this so that wavelength information is dispersed spatially. The mask or spatial modulator is placed in the optical Fourier transform plane, and transmitted pulse then passes through a second cylindrical lens and grating pair which correct for the spatio-temporal distortions.

For the purposes of broadband VSFS, spectral narrowing can be achieved by introducing a variable slit as the spatial modulator. As wavelength is distributed spatially, a basic adjustable slit will allow only a small range of wavelengths to pass through, resulting in a spectrally narrowed/time-stretched pulse.

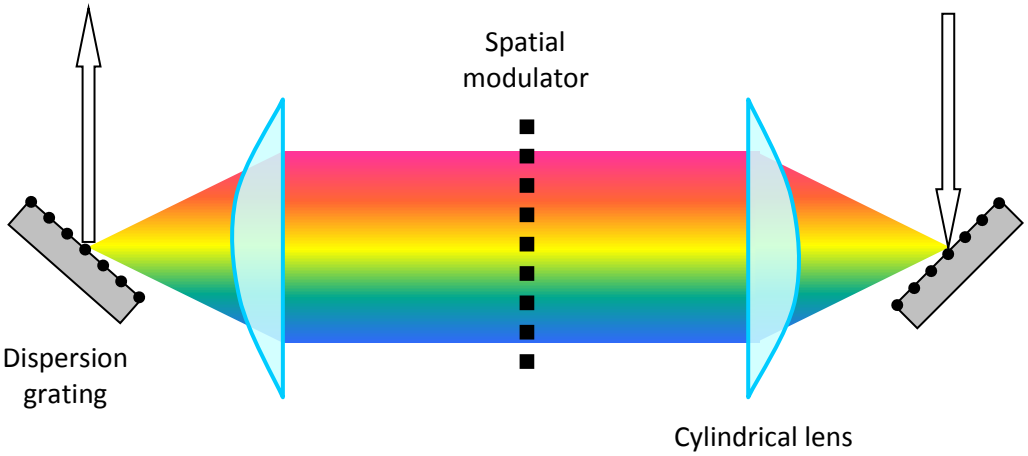

Figure 3.4. Diagram depicting a grating-based pulse shaper for tailored modulation of a pulse's characteristics

An alternative method of pulse shaping which offers several advantages over a grating arrangement involves the use of a Fabry-Pérot interferometer or etalon. This optical device illustrated in Figure 3.5 consists of two parallel mirrors or partially-reflecting surfaces separated by a small distance d. An incident broadband pulse will experience multiple reflections, transmitting a small fraction of the pulse at each reflection. The resulting train of offset pulses self-interferes due to the additional path length/phase difference incurred after each reflection, and for highly reflective surfaces with an appropriate incidence angle θ and mirror spacing d the resulting pulse is both spectrally-narrowed and time-asymmetric.

In the etalon output, multiple rays are emitted with a constant incremental phase difference δ governed by

$$\delta = (2\pi/\lambda)2nd\cos\alpha$$

(Eq 16.)

where $\boldsymbol{\lambda}$ is the wavelength of incident light, and n and α are the refractive index and angle of the beam inside the etalon cavity.[18, 24] Figure 3.5 assumes an air cavity of equal refractive index to the laboratory environment: in this situation the internal and external angles would be equivalent($\theta \sim \alpha$).

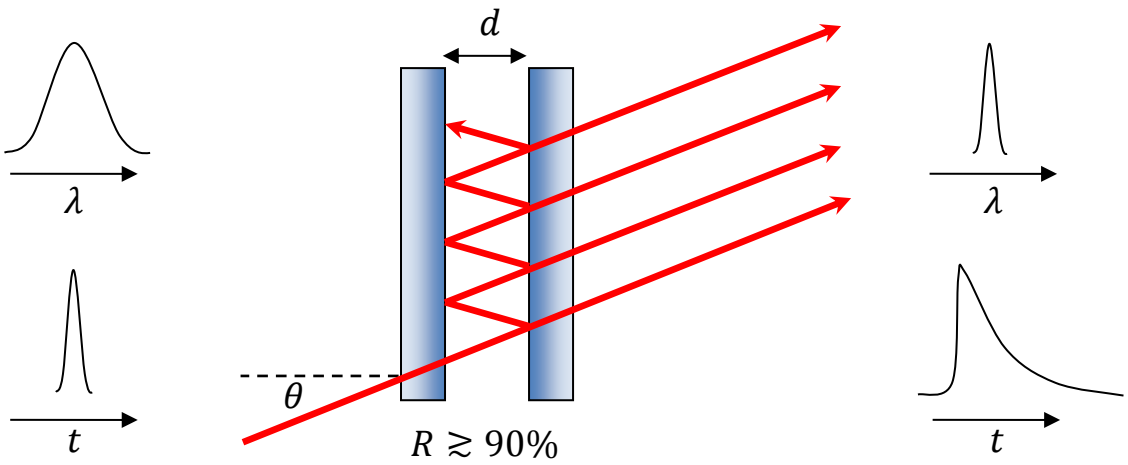

Figure 3.5. The basic operating principle of a Fabry-Perot interferometer etalon. Also shown are the effects on a pulse's wavelength and temporal profile

Assuming there are no power losses in the interaction and that the two mirrors have the same reflectivity coefficient R, the transmitted light intensity I_t as a function of the incident light intensity I_i is described by the equation

$$\frac{I_t}{I_i} = \frac{(1-R)^2}{(1-R)^2 + 4R\sin^2(\delta/2)}$$

(Eq 17.)

This relationship can be simplified by defining a parameter called the coefficient of finesse which is solely related to the reflectivity by

$$F = \frac{4R}{(1-R)^2}$$

(Eq 18.)

which then simplifies equation 17 into the Fabry-Perot interferometer Airy Function equation

$$\frac{I_t}{I_i} = \frac{1}{1 + F\sin^2(\delta/2)}$$

(Eq 19.)

From this relationship, also plotted in Figure 3.6, one can see that for phase differences which are multiples of 2π, the transmitted intensity is at a maximum independent of F. For etalons with high reflectivity and F values, the transmitted intensity is essentially zero unless phase conditions are satisfied. Thus from the derivation of δ one can show that the key variables governing the output of a highly reflective air-spaced Fabry-Perot interferometer are the wavelength of the

incident light, the cavity spacing, and the incidence angle of the input beam. The high sensitivity of a high-F etalon to the phase change δ means that in both phase space and consequently frequency space, the bandwidth of the output pulse will be significantly narrowed, as shown in Figure 3.6.

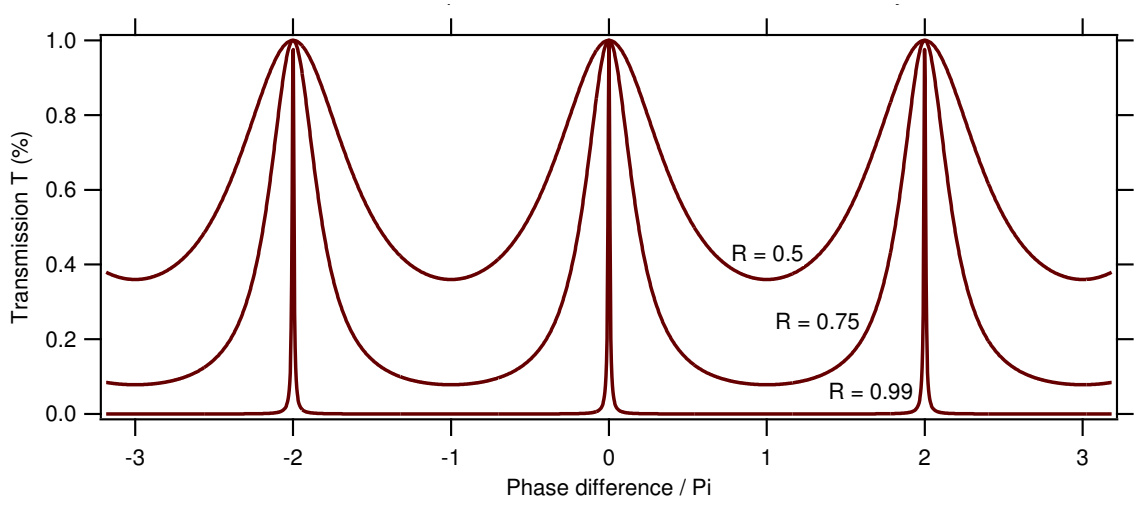

Figure 3.6. Etalon transmission vs. phase difference for various internal reflectivity values

As it is often a single optical component, an etalon is essentially plug-and-play and thus avoids many of the difficulties involved in thoroughly aligning a grating-lens pulse shaper.[24] It also effectively applies a selective band-pass filter over the wavelength distribution of the input pulse, which means that selectively rotating the input angle changes the centre-frequency of the output pulse.

3.2.3 General Broadband VSFS Experimental Setup

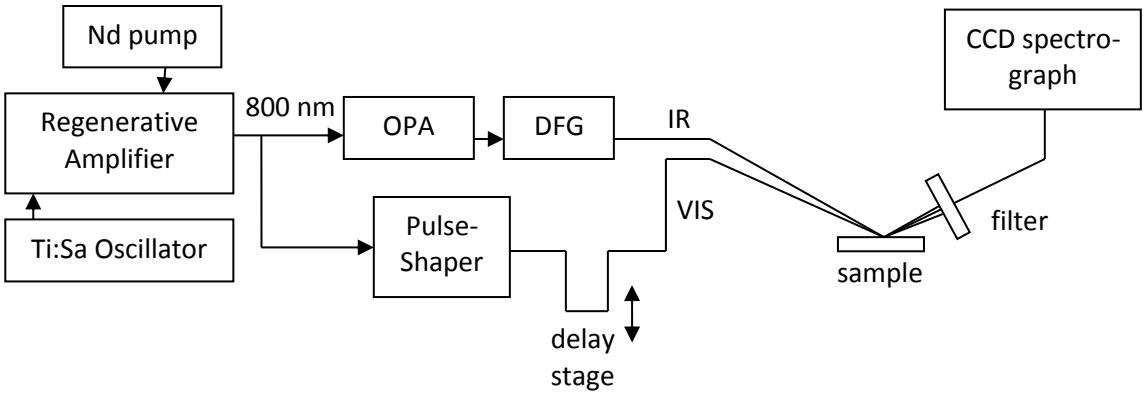

Figure 3.7. The basic elements involved in broadband VSFS including light generation and detection stages

A schematic for a generic broadband VSFS experimental rig is shown in Figure 3.7. Typically a regenerative Ti:Sapphire amplifier is used to generate 800 nm ultrafast pulsed light.[20] Part of this is pulse-shaped and used as the 'visible' SFG probe whilst another part is amplified and converted non-linearly via difference-frequency generation into the broadband infrared SFG probe. Path lengths are matched via the use of a delay stage and are spatially and temporally overlapped on an interface of interest. A bandpass filter allows only the generated SFG wavelengths past and the signal is finally collected via a spectrograph and CCD pair. For a scanning or narrowband system the setup is very much similar; the key differences being the mechanism and gain medium of the pulse generation, the lack of a pulse shaper, and the utilisation of a monochromator and photo-multiplier tube as SFG detection optics.[25]

Ultrafast Light Generation

For further understanding, it is useful to briefly describe the physics behind the generation of ultrafast pulsed laser light – ultrafast usually refers to pulse durations of the order of femtoseconds (10^{-15} s). Typical lasers operate via the mechanism of stimulated emission, that is, a photon impinging on a excited molecule in a 'gain medium' can result in the emission of multiple photons of the same energy. The gain medium is a solid or gas that has been specially selected for its energy level structure, and is said to 'lase' when the gain threshold is achieved and the gain in light intensity is greater than losses from absorption or scattering etc. In a laser cavity the gain medium is enclosed by two partially reflecting mirrors, meaning the majority of the light experiences multiple trips before it is emitted. To obtain ultrafast pulsed laser light, one must include an additional component in the resonator system capable of bringing into phase the many

longitudinal laser modes in a process called mode-locking.[26] This component can be passive such as a saturable absorber where only the high intensity spikes 'burn' through, or it can be an active element capable of periodically modulating the phase or losses of the resonating laser modes and thus bring them into phase as illustrated in Figure 3.8. The greater the number of longitudinal modes within the resonator, the shorter and more intense the output pulse.

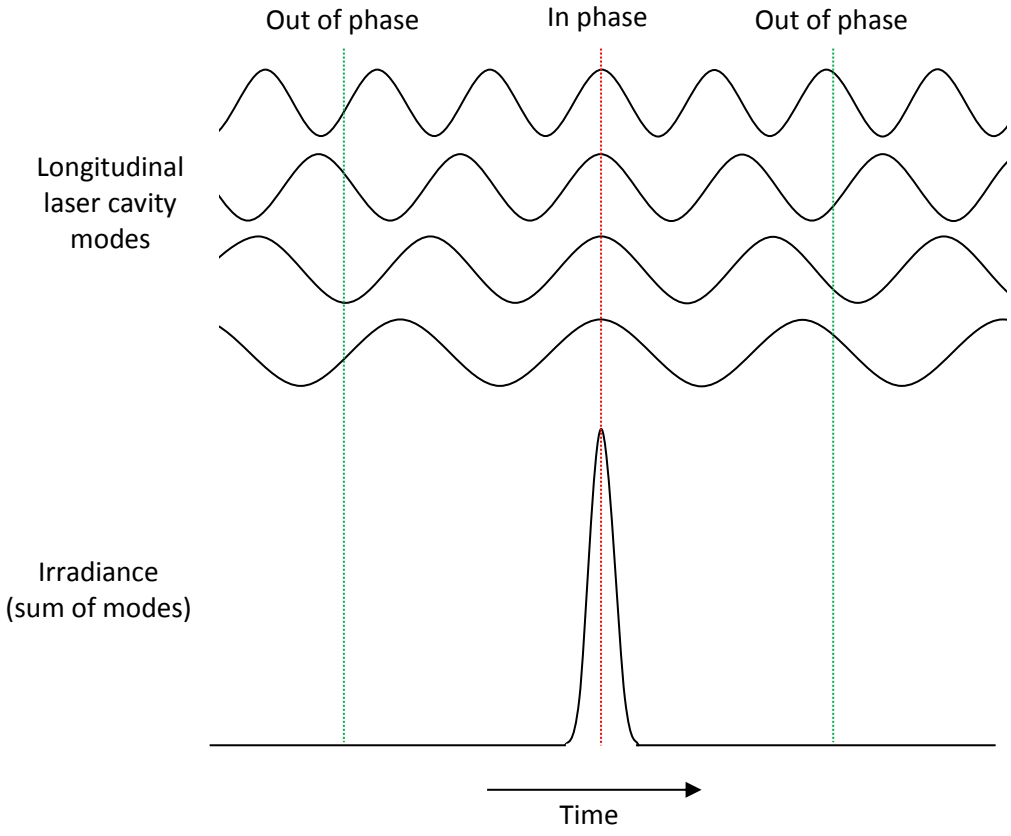

Figure 3.8. Illustration of the basic principles of mode-locked ultrashort light pulse generation.

Additionally, in generating ultrashort pulses with accordingly large bandwidths the pulses are highly prone to dispersion and distortion effects, as different wavelengths propagate through and interact with components and optics differently, even within the resonator. Thus the lasing system requires dispersion compensation which is achieved using a series of prism pairs.

Pulse Amplification

For many experimental purposes where high peak intensities are required it is necessary to amplify ultrafast pulses. In a fashion analogous to laser light generation, amplification requires an appropriate gain medium, and an additional light source to supply the extra energy. The light source to be amplified is known as the 'seed' laser whereas the energy-supplying source is known as the 'pump' laser.

An essential optical element for this purpose is the Pockels cell which is a switchable optical gate. Applying a voltage rapidly turns a Pockels cell into a polariser which will only allow a specific polarisation of light to pass through, and this can be done electronically with specific timings. These allow an ultrafast pulse to enter the gain medium and undergo multiple passes through it, extracting as much energy as possible before being allowed to escape at the output again by the action of a Pockels cell.

IR Generation

Using a secondary light source for the IR probe in VSFS would invoke complications with the differing pulse characteristics and difficulty in synchronisation. Instead, a portion of the broadband amplifier output is taken and converted via nonlinear processes into the desired wavelengths as shown in Figure 3.7. Nonlinear crystals, so called because their dielectric polarisation varies non-linearly with the incident electric field, allow for various nonlinear processes to occur as illustrated by Equation 8 provided they are illuminated with high enough peak intensities. This is achieved via an Optical Parametric Amplifier (OPA), the operation of which will be briefly outlined.[27]

A portion of the OPA input beam is passed through a series of nonlinear optics which generate a wavelength-tuneable pulse. This pulse becomes the seed for amplification in further nonlinear optics, where it is mixed collinearly with the majority of the original pump input beam – this is the optical parametric amplification stage. This amplified pulse is passed through an additional nonlinear crystal, where each photon is split into two photons of equivalent sum-energy, which is varied by minutely adjusting the crystal incidence angle.

The two outputs of this process are called the signal and idler beams, and to produce the necessary IR wavelengths these are finally combined non-collinearly in the nonlinear mixing crystal which operates via Difference-Frequency Generation (DFG), a process similar to SFG.

3.2.4 Instrumentation

The equipment used for VSFS acquisition will be described in detail in the following chapter, as the implementation of the technique constituted a significant portion of the experimental project.

3.3 Complementary Surface Characterisation Techniques

A number of alternative surface characterisation techniques have been utilised to investigate sample preparation and cleanliness. The most important of these will be briefly outlined in the following section.

3.3.1 Contact Angle Analysis

Contact angle goniometry is a means of ascertaining aspects of surface chemistry using a macroscopically observable system. It is utilised in this study as a complimentary technique capable of indicating differences between varying chemical systems.

Theory

A macroscopic contact angle is defined as a boundary condition in a solid-liquid-vapour system for the differential equation governing the shape of the liquid-vapour interface.[28] Essentially, for a liquid droplet on an idealised homogeneous surface, the contact angle is dictated by the equilibrium between opposing interfacial tensions, and is described by the Young-Dupré equation:

$$\cos\theta = \frac{\gamma_{SV} - \gamma_{SL}}{\gamma_{LV}}$$

(Eq 20.)

where θ is the contact angle and γ_{SV}, γ_{SL} and γ_{LV} are the interfacial energies for the solid-vapour, solid-liquid and liquid-vapour interfaces respectively as illustrated in Figure 3.9.

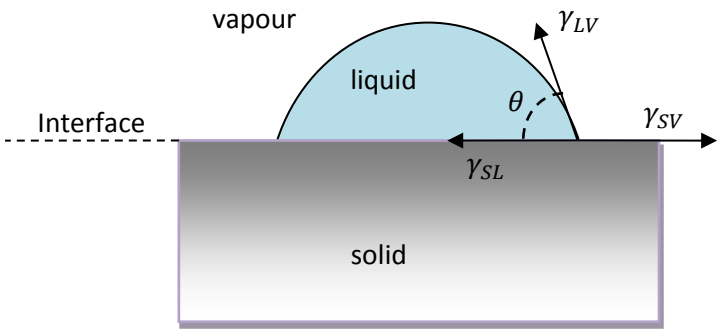

Figure 3.9. Illustration of the origin of parameters in the Young-Dupre equation for a liquid droplet on a solid surface. The arrows represent the interfacial energy vectors.

When taking contact angle measurements, heterogeneities and local interactions may result in significant hysteresis effects, and so for any real surface a range of contact angles will be experienced. These will range from a maximum value known as the advancing or 'recently advanced' contact angle, to a minimum value known as the retreating or 'recently retreated'

contact angle. To fully characterise a surface in this respect then one must obtain both these values.[29]

Measurement Technique

Several methods are frequently reported for the acquisition of contact angle data, although a number of these introduce extraneous forces into the system or fail to report both advancing and retreating values. The technique used in this study is the 'captive needle' technique.

First a droplet of deionised water is dispensed onto the sample surface using a fine micrometer syringe. The syringe tip is then lowered towards the sample such that the needle is captive within the droplet. The micrometer syringe is carefully turned to enable a slow, steady flow of water into the droplet, causing the droplet to grow in volume and advance radially outwards. When the drop has reached an appreciable size (generally the width of the camera's field of view) this is stopped and reversed so the droplet is made to retreat slowly toward its centre. 'Snapshot' measurements are automatically taken throughout, and a frame-by-frame analysis allows the corresponding angles to be plotted and maxima and minima ascertained. Typical images taken using this technique are shown in Figure 3.10.

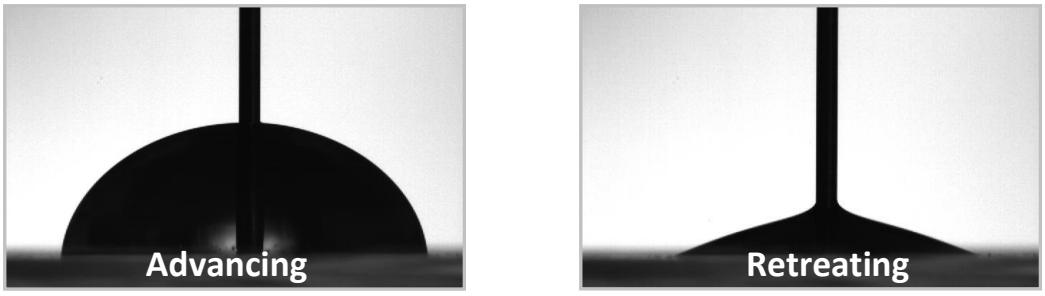

Figure 3.10. Typical images of advancing and retreating contact angles using the captive-needle technique.

Instrumentation

The equipment used for detailed contact angle work is the FTÅ188 Contact Angle and Surface Tension Analyser (First Ten Angstroms Inc., Portsmouth VA). Images are taken with a mounted CCD camera, and are analysed semi-automatically, where the user defines the droplet baseline and the software picks out the droplet radius of curvature and interpolates out the contact angles, provided exposure and focus settings are optimal.

More commonly however, this technique was used as a macroscopic check for sample cleanliness, in which case a droplet of water was introduced to the sample using a syringe or pipette and it was visually ascertained whether or not the sample exhibited wetting (hydrophilic) behaviour.

3.3.2 Atomic Force Microscopy

Atomic Force Microscopy (AFM) is a form of scanning probe microscopy (SPM), able to resolve topographical surface details on a sub-nanometre scale. In AFM, an atomically sharp semiconductor tip on the end of a cantilever is scanned along a surface, and a feedback/detection system allows the local height of the surface to be inferred at any particular point. Raster-scanning the tip back and forth then allows the creation of a three-dimensional terrain map of the surface being investigated. A basic schematic of an atomic force microscope assembly is shown in Figure 3.11, which depicts the more common method of cantilever displacement detection involving a laser and photodiode array.[1]

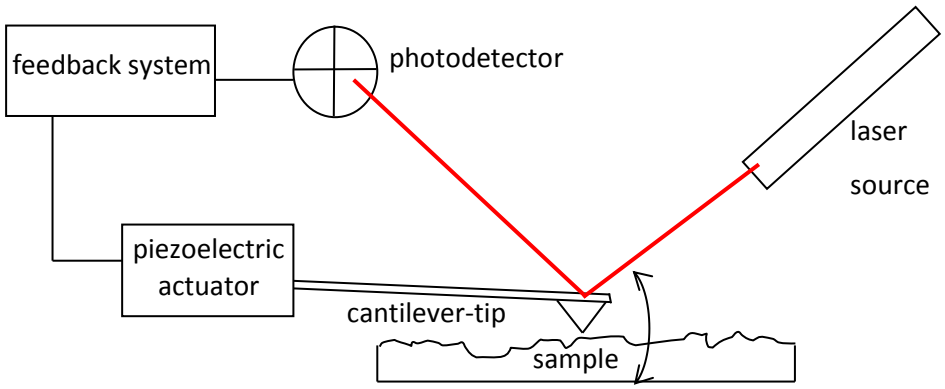

Figure 3.11. A schematic diagram showing the main operating principles of an atomic force microscope

AFM Modes

Several different modes of AFM operation exist, each with differing feedback mechanisms.

In *contact mode* AFM, the tip-cantilever assembly is held close to the surface such that it experiences a repulsive force, corresponding to a specific cantilever deflection. As the tip and sample are scanned relative to one another, any changes in local height result in an altered cantilever deflection. This altered deflection is detected and a feedback mechanism, in conjunction with a piezoelectric element, alters the height of the sample relative to the tip in

order to restore the original cantilever deflection. The amount of this restorative feedback required at any point can then be directly used to infer the local height.

Non-contact mode AFM operates on a similar principle to contact mode, except the tip is maintained a certain distance away from the sample surface and the forces experienced are attractive. Due to the weaker nature of these attractive forces, the piezoelectric element is operated using an alternating current, vibrating the cantilever assembly. Thus, an incrementally altered force between tip and sample, resulting from a change in local height, manifests itself as a more-readily detectable change in the frequency of oscillation.

The mode used in this study is known as '*tapping mode*' or *dynamic contact mode* AFM and involves piezoelectrically driving the tip at or around its resonant frequency so that it passes over a large oscillation amplitude through both the attractive and repulsive regimes illustrated in Figure 3.12. Changes in local height lead to changes in the oscillation amplitude, which are registered and corrected for by the feedback system, which adjusts the tip-to-sample distance until the initial amplitude is restored. This mode of AFM minimises the sample/tip degradation associated with typical contact-mode AFM, and also avoids issues relating to viscosities of vapour and gas layers present on surfaces under ambient conditions.[30] The high driving frequencies (50 – 500 kHz) also mean that the tip is able to overcome tip-sample adhesion forces.

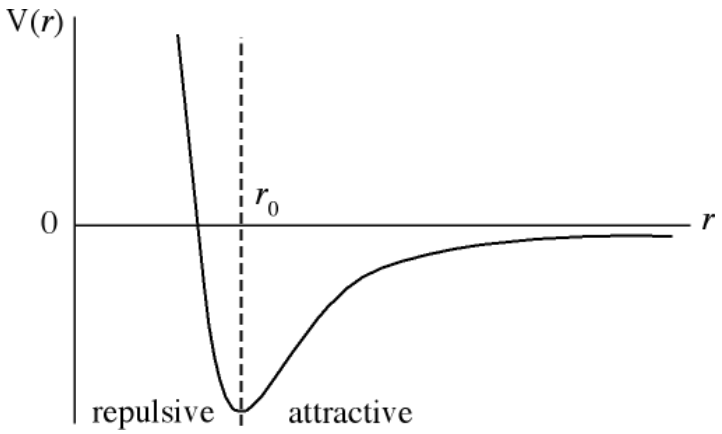

Figure 3.12. Diagram of the interatomic potential energy between two atoms, showing the transition from repulsive (contact mode) to attractive (non-contact mode) regimes. Reproduced from Vickerman.[1]

Instrumentation

The instrument used for this study is a Veeco Nanoscope Multimode SPM. Due to the instrument's high sensitivity, it is mounted on an active vibration isolation table.

The cantilever tips are TESPA units (Veeco Probes) and are made of antimony (n) doped silicon with resonant frequencies between 280 – 350 kHz. The AFM software 'tunes' the cantilever controller to the resonant frequency of each tip inserted, and the optimum tip-sample distance is computer controlled. Through the acquisition software one can then input desired variables such as scan size, scanning speed and z-sensitivity. The cantilever, laser and detector assembly is suspended stationary above the sample stage, which itself is translated by computer-controlled piezoelectric elements for the x-y (horizontal translation) and z (tip-sample distance adjustment) axes.

3.3.3 X-ray Photoelectron Spectroscopy (XPS)

X-ray Photoelectron Spectroscopy (XPS), also known as Electron Spectroscopy for Chemical Analysis (ESCA), is a technique used to get quantitative elemental and chemical information on the composition of the first few atomic layers of any surface under investigation. It is a common characterisation technique for surface science as it is highly surface specific and can detect concentrations in the parts-per-thousand range.[31]

In standard XPS, a sample is irradiated under ultra-high vacuum conditions with a beam of monochromatic X-rays. Electrons ejected through the photoelectric effect are collected by an electron analyser and detector, and the number of detected photoelectrons can be plotted as a function of their kinetic energy in the form of an XPS spectrum.

Theory

When a photon of energy $h\nu$ is incident on an atom, it may be absorbed by a core-level electron and induce an excited electronic state. If the energy of the photon is sufficiently high, as is the case in Figure 3.13, the electron will be able to escape, and it is these 'photoelectrons' that are detected and used to plot XPS spectra.

The key relationship between the energies involved in the photoelectric effect and which allows chemical identification can be described by the Einstein equation:

$$E_B = h\nu - E_K$$

(Eq 20.)

where E_B is the binding energy of the bound electron *in the atom*, $h\nu$ is the energy of the absorbed photon, and E_K is the kinetic energy of the ejected photoelectron.

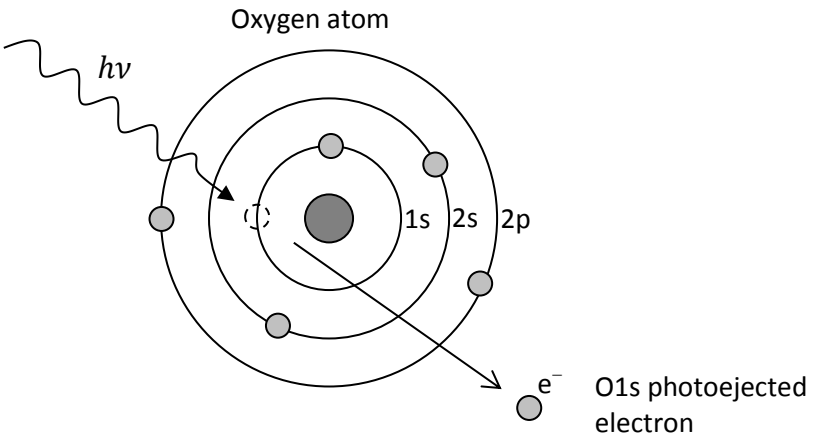

Figure 3.13. The basic photoelectric mechanism involved in XPS. If unaffected by inelastic interactions with neighbouring atoms the ejected electron would go on to contribute to the O1s peak.

Every chemical element possesses characteristic binding energies for each of its electronic states, so using the above equation with a known monochromatic photon source allows photoelectrons to be plotted as a function of binding energy and thus elements and indeed chemical states to be identified from their characteristic peaks.

Sample XPS Spectrum

A typical XPS spectrum such as that shown in Figure 3.14 plots the number of electrons detected versus electron binding energy. Figure 3.14 contains two XPS scans of the same carbon-contaminated TiO_2 sample and possesses a number of features typical to XPS.

Core-level Photoemission Peaks

The majority of labelled peaks in the figure correspond to specific elemental core-level photoelectrons, ejected directly from electronic orbitals via the mechanism illustrated in Figure 3.13. Due to variations in the size and distribution of charge within atoms, the electronic binding energies are at different values for each core-level orbital of each element. Thus spectral peaks may be identified by cross-referencing their peak energies with tables containing known binding energy values — the peak in 3.14 with the greatest intensity for example has been identified as originating from the 1s orbital of oxygen atoms and so has been labelled O 1s.

The width of core-level peaks is a combined result of the lifetime of the corresponding core holes as described by the Heisenberg uncertainty principle and also instrumental effects relating to the X-ray source and electron analyser[32]. When treating spectra quantitatively it is the background-subtracted peak areas that are relevant.

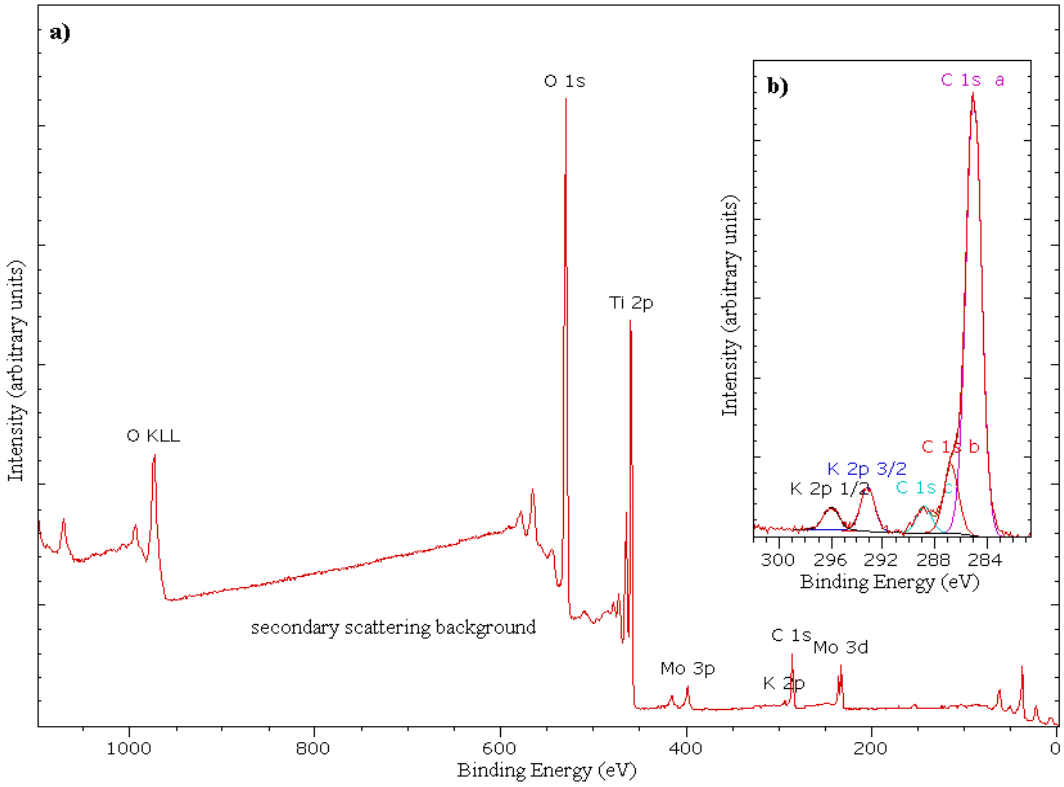

Figure 3.14. a) A 'wide-scan' XPS spectrum of a surface-contaminated TiO2 crystal sample prepared via wet chemical methods. Figure 3.14b) shows a 'narrow-scan' expanded view of the C 1s and K 2p region, with sub-peaks fitted and labelled.

Auger Peaks

Certain peaks, such as that labelled O KLL in Figure 3.14a), are not directly due to photoemission but are instead due to Auger electron emission. When an inner shell electron is ejected from an atom via photoemission, the 'hole' it leaves behind has a finite lifetime as electrons from outer shells will preferably drop down to the vacant lower-energy state. The excess energy can then be shed either through fluorescence or by ejection of an electron from a higher-energy shell. This second process is Auger emission, and is independent of the original X-ray energy. As such, although it appears to have a high binding energy this is only due to its less-energetic emission process. Consequently it cannot be treated in the same way as standard XPS peaks, and will not factor into quantitative analysis.

Secondary scattering background

The significant background seen in Figure 3.14a) is a result of photoelectrons undergoing inelastic collisions with other atoms and electrons in the sample, and losing energy as a result. The distance an electron may travel in a specific environment without losing energy is dictated by the Inelastic Mean Free Path (IMFP) which is an energy-dependent property and varies between

materials. Inelastic scattering is the basis of the surface-specificity of XPS, as the IMFP of typically-energetic photoelectrons in a solid is of the order of ~10 nm. Photoelectrons emitted more than 10 nm from the sample surface have a limited probability of escape without energy loss, so meaningful data can only be gathered from this thin layer.[32] Inelastic scattering necessitates the ultra-high vacuum requirements of an XPS chamber, as the irradiated sample is often up to a metre from the electron lens/analyser.

Energy Shifts

The binding energy of an atomic electron is strongly dictated by the charges present in the nucleus i.e. the specific chemical element, but many other environmental factors will induce shifts in E_B which provide more detailed information useful for surface characterisation.[33] Significantly, the formal oxidation state of an atom alters an orbital electron's binding energy such that the chemical state of the probed atom may be inferred. Increased oxidation states result in higher binding energies, and quantitative chemical data can be arrived at through decomposing peaks via peak-fitting procedures as illustrated by the multiple carbon peaks in Figure 3.14b). This effect is known as a chemical shift.

Also apparent in Figure 3.14 are the multiple-peak structures associated with Ti 2p, Mo 3p, K 2p and Mo 3d due to an effect called spin-orbit coupling. All orbitals whose principle quantum number *n* is greater than 0 (all except s shells) may contain pairs of degenerate electrons with the same energy but opposing spin values. In these open shells, a magnetic coupling of the electrons' orbital angular momenta l and spin angular momenta s can lead to a splitting of the degenerate state into two components of different energy, giving rise to two separate peaks. This is the origin of the K $2p_{1/2}$ and K $2p_{3/2}$ features visible in Fig 3.14b), where the number in subscript is the *j* quantum number ($j = |l + s|$where $l = 0, 1, 2 \ldots$ and $s = \pm 1/2$). The intensity ratio of these two peaks can be calculated from the degeneracy $2j + 1$, which is a useful tool for peak-fitting.

Instrumentation

A typical XPS system as illustrated in Figure 3.15 consists of an X-ray source/sources, a series of electron lensing components, an electron analyser and a means of electron detection. The analyser system is a Concentric Hemispherical Analyser, and the electrons are detected by an electron multiplier. The majority of the acquisition process is computer controlled. The X-ray Photoelectron Spectroscopy equipment used in this study is the Kratos Axis ULTRA (Kratos Analytical Ltd, Manchester UK) which has been previously well-described and characterised in a number of publications.[34-36]

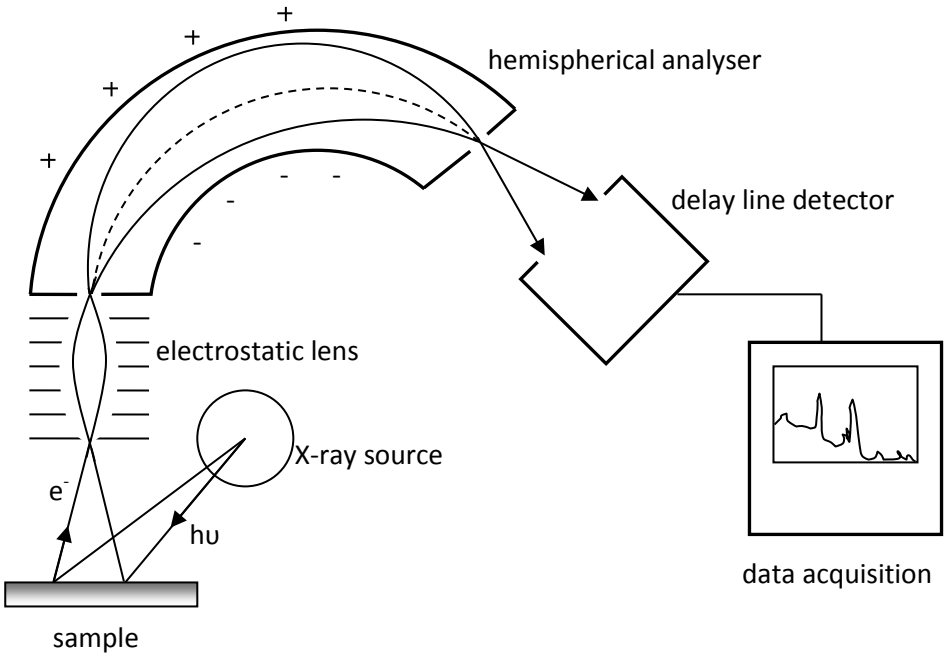

Figure 3.15. A schematic diagram of a typical XPS setup, with key components labelled

3.4 References

1. Vickerman JC, Gilmore IS, *Surface analysis: the principal techniques*. Vol. 2. 2009: Wiley Online Library.
2. Leygraf C, *Atmospheric corrosion*. 2000: Wiley Online Library.
3. Gonzalez JA. DETERMINATION OF INSTANTANEOUS RATE OF ATMOSPHERIC CORROSION. *Werkstoffe Und Korrosion-Materials and Corrosion*. 1978; **29:** 456-60.
4. Aastrup T, Leygraf C. Simultaneous infrared reflection absorption spectroscopy and quartz crystal microbalance measurements for in situ studies of the metal/atmosphere interface. *Journal of the Electrochemical Society*. 1997; **144:** 2986-90.
5. Zhu XD, Suhr H, Shen YR. SURFACE VIBRATIONAL SPECTROSCOPY BY INFRARED-VISIBLE SUM FREQUENCY GENERATION. *Physical Review B*. 1987; **35:** 3047-50.
6. Cimatu K, Baldelli S. Chemical imaging of corrosion: Sum frequency generation imaging microscopy of cyanide on gold at the solid-liquid interface. *Journal of the American Chemical Society*. 2008; **130:** 8030-7.
7. Hedberg J, Baldelli S, Leygraf C. Initial Atmospheric Corrosion of Zn: Influence of Humidity on the Adsorption of Formic Acid Studied by Vibrational Sum Frequency Spectroscopy. *Journal of Physical Chemistry C*. 2009; **113:** 6169-73.
8. Kleber C, Hilfrich U, Schreiner M. In situ QCM and TM-AFM investigations of the early stages of degradation of silver and copper surfaces. *Applied surface science*. 2007; **253:** 3712-21.
9. Leygraf C, Hedberg J, Qiu P, Gil H, Henriquez J, Johnson CM. 2007 WR Whitney Award Lecture: Molecular in situ studies of atmospheric corrosion. *Corrosion*. 2007; **63:** 715-21.
10. Abney C. On the influence of the atomic grouping in the molecules of organic bodies on their absorption in the infra-red region of the spectrum. *Philosophical Transactions of the Royal Society of London*. 1881; **172:** 887-918.
11. Coblentz WW, *Investigations of infra-red spectra*. Vol. 1. 1905: Carnegie institution of Washington.
12. Shen YR. Surface properties probed by second-harmonic and sum-frequency generation. 1989; **337:** 519-25.
13. Raval R. Probing the nature of molecular chemisorption using RAIRS. *Surface science*. 1995; **331:** 1-10.
14. Campion A, Kambhampati P. Surface-enhanced Raman scattering. *Chem. Soc. Rev.* 1998; **27:** 241-50.
15. Rey NG. Interaction of a Copper Surface with Light: Plasmons, Electrons & Molecular Vibrations. *Department of Chemistry*. Vol. Doctor of Philosophy Surface Science Research Centre: University of Liverpool, 2011.
16. Shen Y-R. The principles of nonlinear optics. *New York, Wiley-Interscience, 1984, 575 p.* 1984; **1**.
17. Lambert A, Davies P, Neivandt D. Implementing the theory of sum frequency generation vibrational spectroscopy: A tutorial review. *Applied Spectroscopy Reviews*. 2005; **40:** 103-45.
18. Born M, Wolf E, *Principles of optics: electromagnetic theory of propagation, interference and diffraction of light*. 1999: CUP Archive.
19. Smith JP, Hinson-Smith V. Product review: SFG coming of age. *Analytical Chemistry*. 2004; **76:** 287 A-90 A.
20. Richter LJ, Petralli-Mallow TP, Stephenson JC. Vibrationally resolved sum-frequency generation with broad-bandwidth infrared pulses. *Optics Letters*. 1998; **23:** 1594-6.
21. Arnolds H, Bonn M. Ultrafast surface vibrational dynamics. *Surface Science Reports*. 2010; **65:** 45-66.
22. Akturk S, Gu X, Gabolde P, Trebino R. The general theory of first-order spatio-temporal distortions of Gaussian pulses and beams. *Proc. of SPIE Vol*. Vol. 6108, 2005. 61080E-1.
23. Trebino R, *FROG*. 2000: Springer.

24. Hernández G, *Fabry-Perot Interferometers*. Vol. 3. 1988: Cambridge University Press.
25. Bain CD. Sum-frequency vibrational spectroscopy of the solid/liquid interface. *Journal of the Chemical Society, Faraday Transactions*. 1995; **91:** 1281-96.
26. Hooker SWCE, *Laser physics*. 2010, Oxford; New York: Oxford University Press.
27. Ross I. Optical Parametric Amplification Techniques. In: Brabec T (ed). *Strong Field Laser Physics*. Vol. 134: Springer New York, 2009. 35-59.
28. Good RJ. CONTACT-ANGLE, WETTING, AND ADHESION - A CRITICAL-REVIEW. *Journal of Adhesion Science and Technology*. 1992; **6:** 1269-302.
29. Krishnan A, Liu YH, Cha P, Woodward R, Allara D, Vogler EA, Hematology Biomater Inter Res G. An evaluation of methods for contact angle measurement. *Colloids and Surfaces B-Biointerfaces*. 2005; **43:** 95-8.
30. James PJ, Antognozzi M, Tamayo J, McMaster TJ, Newton JM, Miles MJ. Interpretation of contrast in tapping mode AFM and shear force microscopy. A study of nafion. *Langmuir*. 2001; **17:** 349-60.
31. Tilinin IS, Jablonski A, Werner WSM. Quantitative surface analysis by Auger and x-ray photoelectron spectroscopy. *Progress in Surface Science*. 1996; **52:** 193-335.
32. Watts JF, Wolstenholme J, *An Introduction to Surface Analysis by XPS and AES* 2nd ed. 2003: Wiley-Blackwell.
33. Fairley N, Carrick A, *The Casa Cookbook: Recipes for XPS Data Processing, Pt. 1*. 2005, Knutsford: Acolyte Science. 390.
34. Walton J, Fairley N. Characterisation of the Kratos Axis Ultra with spherical mirror analyser for XPS imaging. *Surface and Interface Analysis*. 2006; **38:** 1230-5.
35. Walton J, Fairley N. Data scaling for quantitative imaging XPS. *Surface and Interface Analysis*. 2009; **41:** 114-8.
36. Walton J, Wincott P, Fairley N, Carrick A. Peak Fitting with CasaXPS: A Casa Pocket Book. 2010.

Chapter 4. VSFS Implementation

4.1 Introduction

A considerable part of the project has involved the development of the experimental apparatus for Vibrational Sum-Frequency Spectroscopy, or VSFS. The completed broadband VSFS experiment is one of only two operating in the UK, and its gas-flow capability (explored in further detail in Chapter 5) makes it a unique facility, nationally. This chapter describes the implementation in Manchester's Photon Science Institute (PSI) of the VSFS apparatus, exploring the practicalities of Sum-Frequency Generation (SFG) along with the various issues encountered and the steps taken to rectify and improve upon them.

4.2 Experimental Apparatus

The experimental setup is installed in the ground floor laser laboratory of the Alan Turing Photon Science Institute building at Manchester University. The ground floor lab was designed and built with stringent low-vibration specifications, so as to reduce and dampen ambient structural vibrations for sensitive laser-based experiments. The ultrafast pulsed laser system UF4 and spectroscopy setup are assembled over three joined RS-Series optical tables (Newport Corporation, Irvine USA) which allow for pneumatic decoupling if required.

Over the course of the project there have been several iterations of the VSFS apparatus. Changes were often incremental to improve the efficacy and efficiency of the system, but several complete rebuilds were also undertaken for both technical and logistical reasons. The thing that has changed the least over this time is the means of light generation and so this is a good starting point to begin the experimental description.

4.2.1 Light Generation

To generate the appropriate ultrashort pulses requires multiple optical steps, each with numerous light mixing stages. Importantly, the main Ti:Sapphire amplifier has dedicated seed and pump lasers which must be combined with the aid of timing and compensation controls in order to generate the usable light for VSFS experimentation

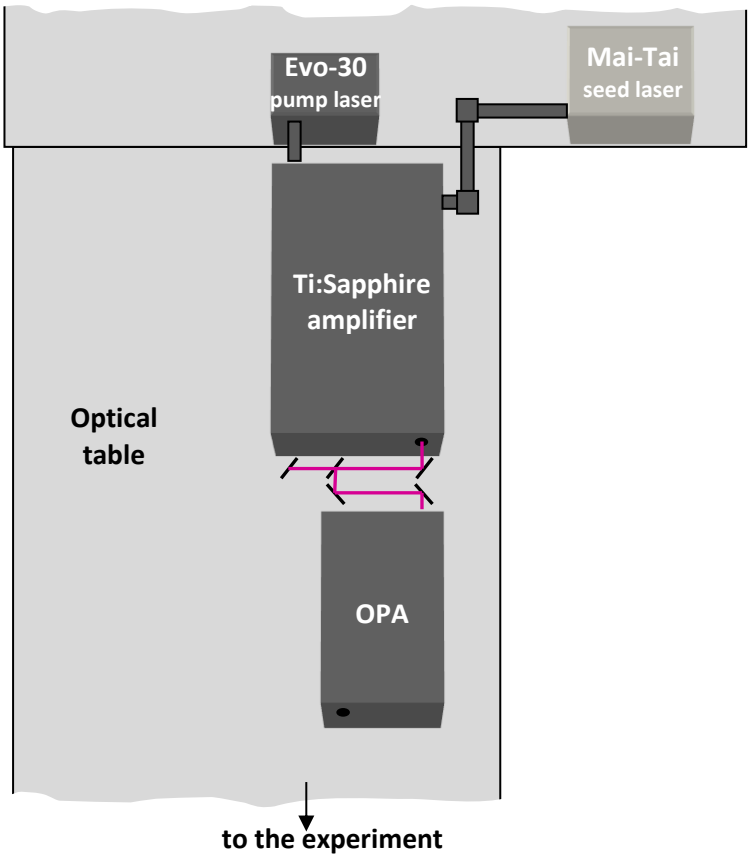

Figure 4.1. A top-down view of the light generation and amplification setup in the PSI.

Figure 4.1 illustrates the layout of the light generation section of the experiment, the underlying theory of which has been outlined in Section 3.2.3. The femtosecond seed pulse for the amplification process comes from a Broadband Mai Tai mode-locked Ti:Sapphire laser (Spectra-Physics) which outputs 803 nm pulses at a frequency of 78.9 MHz and with <100 fs duration (itself internally pumped by a continuous wave Nd:YVO4 laser at 532 nm). The amplifier pump source which provides the amplification energy is a Positive Light (Spectra-Physics) Evolution-30 Nd:YLF laser which emits 1kHz pulsed green light at 527 nm, with a pulse duration of 100-250 ns and a standard working power of ~23 W.

The two inputs are steered into the amplifier which is a Ti:Sapphire Legend Elite F-HE (Coherent), and the timing of pulse injection and ejection from the cavity is controlled by a synchronisation and delay generator. This main amplifier emits ~120 femtosecond duration pulses at a wavelength of 802 nm, a rate of 1 kHz and a typical average power of 3.2 W, and constitutes the useable output for the VSFS experiment.

A 50:50 beamsplitter sends half of the amplifier output to an optical parametric amplifier (Coherent OPerA SOLO, Coherent Inc. USA) which is converted into tuneable IR pulses via non-collinear difference frequency generation. This optical parametric amplifier (OPA) is controlled via a laptop computer, which allows wavelength tuning from 1100 nm to 20 µm, as well as facilitating control over several variables which can improve output efficiency. The IR is output via one of the OPA's exit ports, and from there is steered to the spectrometer setup.

The visible (VIS) light probe for VSFS is the ultrafast 802 nm pulse train from the amplifier. Due to space constraints, the visible VSFS light was originally taken from the 'dump port' of the OPA which exhausts a significant proportion of the pump power left over after IR-generation, but this was later changed to take the VIS directly from the main amplifier – see Section 4.5.3.

Initially, the VSFS setup was installed with the aid of Dr. Heike Arnolds of Liverpool University. Her group is the only other in the UK performing broadband VSFS, but that system employs a 10 Hz pulsed femtosecond laser with lower average powers[1] and so the development at Manchester formed part of a collaborative feasibility study for the investigation of less SFG-responsive sample systems. The schematic for the experiment is shown in Figure 4.2.

All illustrated optical components and mounts were obtained through Newport (Newport Corporation, Irvine USA) or Edmund Optics (Edmund Optics Ltd, York UK) and are firmly attached to the optical table breadboard. All mirrors and lenses are optimised and anti-reflection coated for their specific wavelengths (IR and 802 nm) and are mounted in precision kinematic mounts for height and angular adjustment.

Notably, this iteration uses a grating pulse shaper to time-stretch the visible pulse, the layout of which can be seen in Figure 4.3. To more accurately correct for the pulse shaper's spatio-temporal distortions and to economise on components, a mirror was used at the Fourier transform plane, allowing the same cylindrical lens and grating to correct any dispersion on the pulse's return trip. Another key feature was that the visible beam was taken from the OPA's dump port where the majority of the pump beam is sent after parametric amplification.

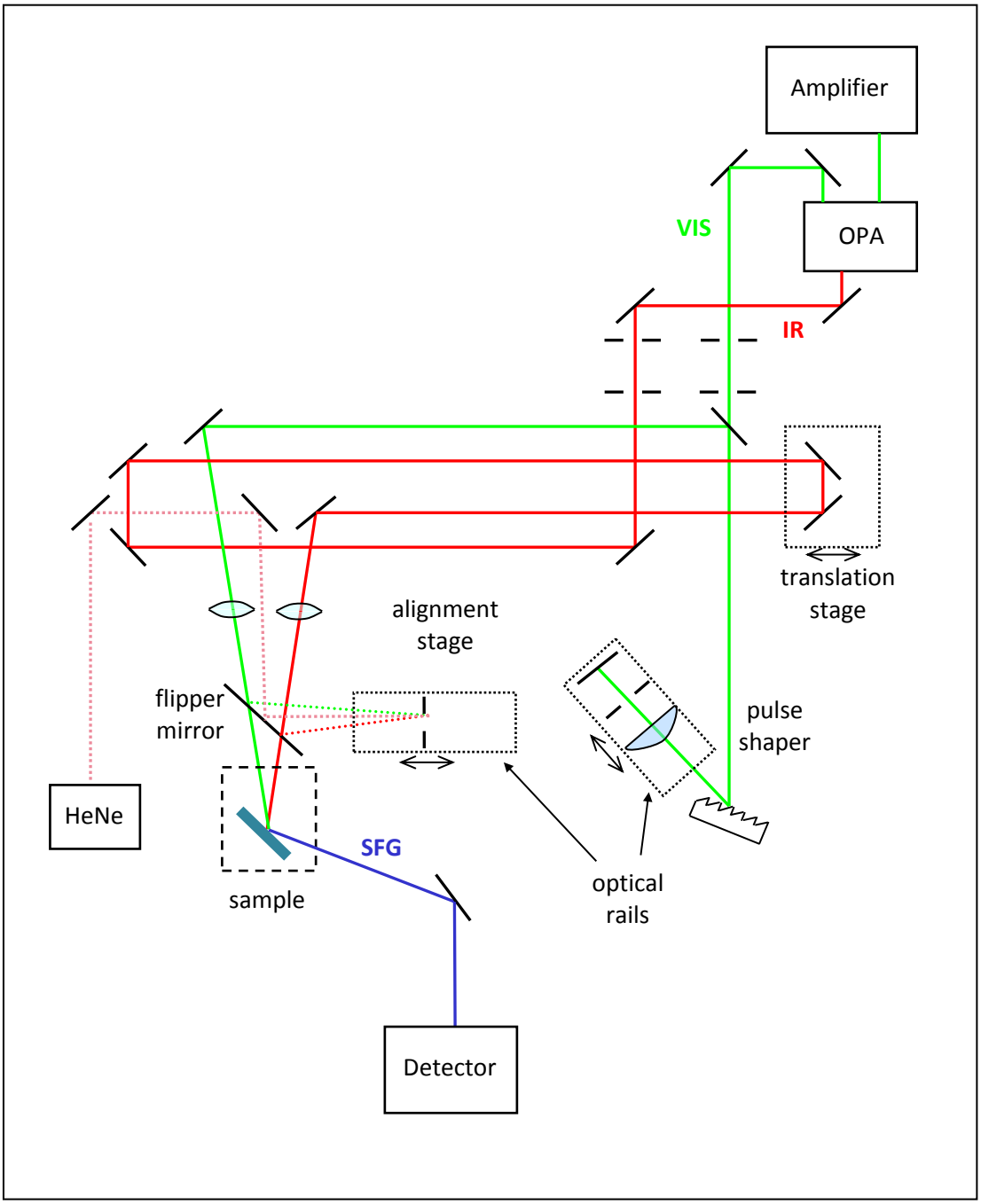

Figure 4.2. The initial experimental layout of the VSFS setup utilised for alignment purposes and for preliminary spectral acquisitions..

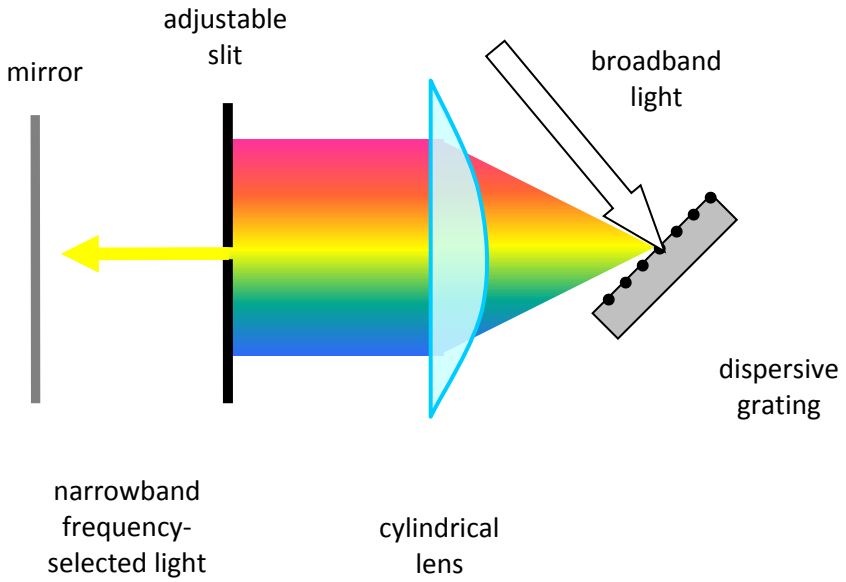

Figure 4.3. A representation of the grating pulse shaper initially employed for time-stretching the visible pulse. For simplicity the light's return journey is not shown.

4.3 Practical SFG detection

4.3.1 Overlap

It is essential for the creation of an SFG signal that the input probes are both spatially and temporally overlapped. Spatial overlap is achieved when the maximum power from both IR and visible beams is incident at the same spot on the sample, and is accomplished first visually with laser alignment cards and more precisely with a power meter and pinhole incorporated into the *Alignment Stage* through which the beams are redirected using a flipper mirror as shown in Fig 4.2. Whilst the alignment stage is not necessary, an accurately placed pinhole/iris provides an analogue of the sample position and significantly aids the initial overlap procedure. Both beams are focused using wavelength-specific lenses; common practice is to tightly focus the infrared spot onto the sample whilst maintaining a softer focus with the visible, as in terms of power the infrared is the limiting factor. A softer focus on the visible beam should be exaggerated when examining samples with low damage thresholds as even at relatively low powers it is possible to cause significant beam damage (as determined empirically).

Temporal overlap is satisfied when the IR and visible pulses overlap sufficiently in time, and is achieved by ensuring the two beams have matching pathlengths i.e. that each beam travels for

the same amount of time after the point at which they split. Beta-barium borate (BBO) is a nonlinear crystal which is particularly SFG-active, and can thus be used to test for temporal alignment.[2] A thin BBO crystal is placed in a holder at the alignment stage, and the delay stage is gradually adjusted. When good temporal alignment is achieved a bright visible sum-frequency spot can be observed, provided phase matching conditions have been met in the crystal. Zinc selenide (ZnSe)[3] is another nonlinear crystal which can be used to give a visible SFG spot to indicate temporal alignment. However, whilst this substrate does not necessitate phase matching, the resulting SFG spot tends to be dimmer and less well defined. The entire alignment process including both spatial and temporal overlap and initial steering in the detector is outlined in Figure 4.4.

Whilst taking SFG data certain variables may need to be changed such as the time-delay between pulses, the light polarisation, or the IR wavelength, and it is important that overlap is maintained during any such alteration. The delay stage for example must be very carefully aligned so that the incoming and outgoing rays are parallel. If they are not parallel, altering the position of the delay stage will spatially translate the focussed spot on the sample and lose spatial overlap.

Adjusting the IR wavelength through the OPA is computer controlled and is achieved by actuated movement of delay stages and rotation of nonlinear crystal angles. If the complex internal alignment of the OPA is not optimised, it is possible that the IR beam steering (direction) will alter when the wavelength is changed, which would also result in loss of spatial and potentially temporal overlap.[4] Other unwanted effects can come about through incorrect OPA alignment, and these will be discussed later in the chapter.

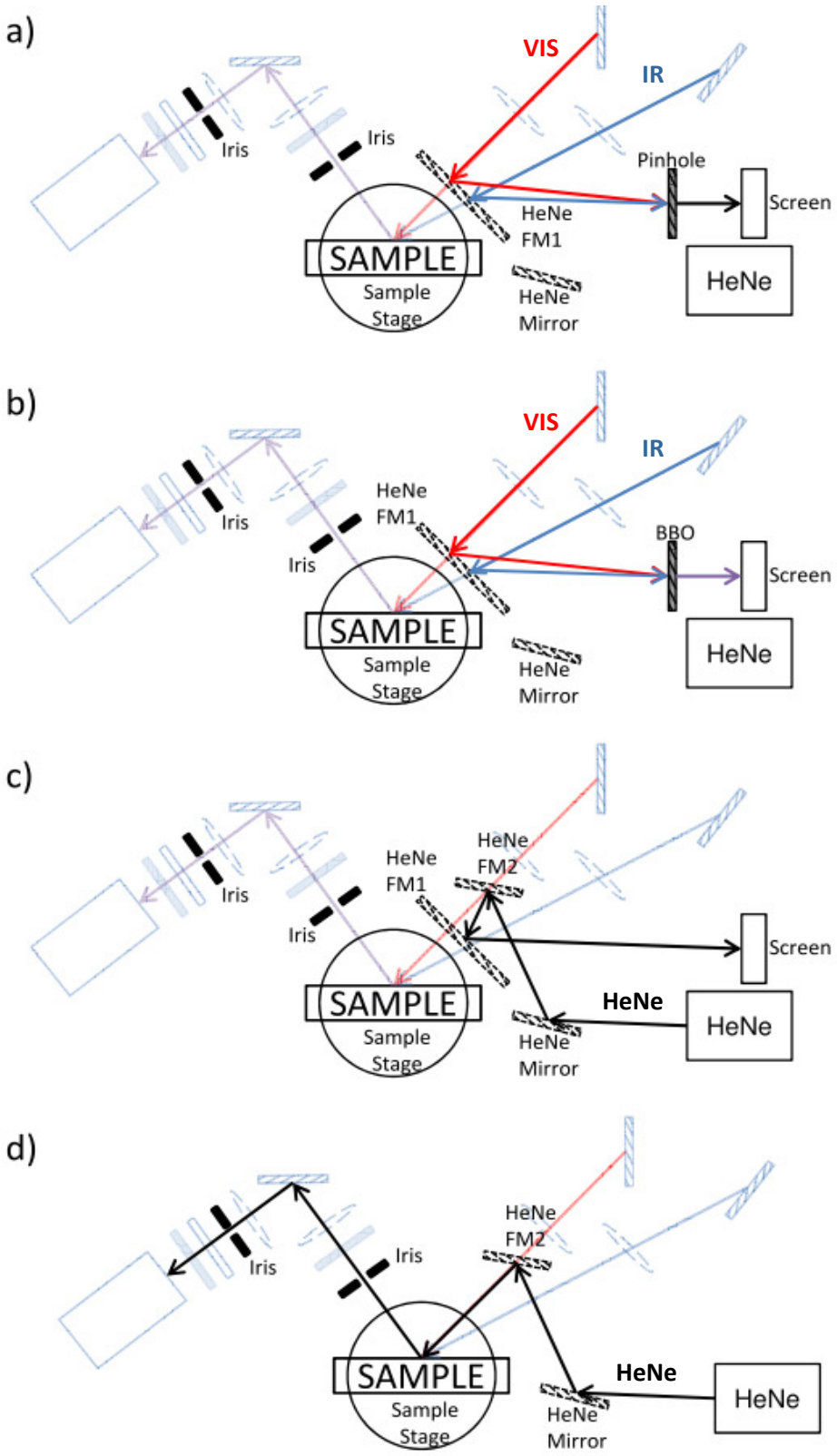

Figure 4.4. A representation showing the standard technique for achieving spatial and temporal overlap. In a) both visible and infrared beams are first steered through a fixed pinhole in the alignment stage. In b) the pinhole is replaced by an SFG-active crystal and the time delay on the delay stage is adjusted until a visible SFG signal is observed on the screen. In c) and d) the path of the visible SFG signal is traced by an alignment HeNe laser and subsequently steered into the detector. FM1 and FM2 denote flipper mirrors, which can be manually brought into and out of the beam paths without affecting their steering.[31]

4.3.2 Light Detection

With a narrowband VSFS arrangement, it is sufficient to use a monochromator and photo-multiplier tube as the SFG emission is also narrowband and thus essentially monochromatic at each IR wavelength acquisition point. For broadband VSFS, due to the spread of wavelengths it is necessary to employ a spectrometer in conjunction with an imaging Charge-Coupled Device (CCD) detector and so this is the arrangement used in this project. The spectrograph is a Shamrock 163 Czerny-Turner spectrograph (Andor Technology) and the detector is an iStar ICCD DH734 intensified-CCD camera (Andor Technology).

After generation at an interface, the SFG signal must first be collimated with a corrective lens before passing through a series of polarisation and filter optics which allow only the desired wavelengths and polarisations of light through. A final lens focuses the light onto the spectrograph entrance aperture.

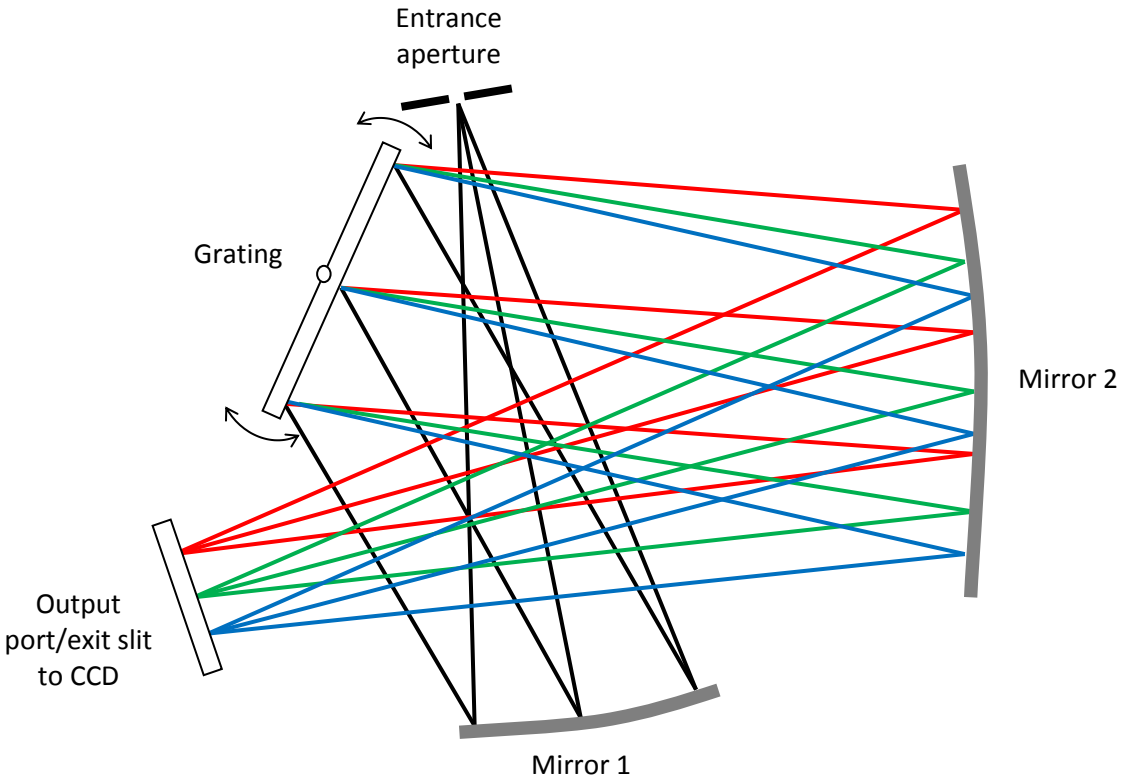

Figure 4.5. A ray diagram illustrating the operation of the off-axis Czerny-Turner spectrograph utilised in the detector.

For our purposes, the entrance aperture is an adjustable slit. The slit width physically limits the overall spectrograph resolution, so a value must be chosen which is low enough to allow high resolution spectra but does not also significantly limit the transmitted signal intensity.[5] Inside the spectrograph the light is collimated and then dispersed by a grating, after which it is focussed onto an output port/exit slit coupled to the ICCD/detector, see Fig. 4.5. The grating has a 500 nm blaze which increases the dispersion efficiency around that wavelength, meaning the SF signal which on our system typically occurs around 650 nm is optimally and linearly dispersed for detection. The centre-wavelength of the light entering the output port is controlled by precise rotation of the grating which is adjusted via a factory-calibrated micrometer screw gauge.

4.3.3 The Intensified Charge-Coupled Device (ICCD) Camera

The operation of the camera is a multistage process involving photon detection, amplification, imaging, and gating steps.[6] A diagram of the detector used is shown in Figure 4.6.

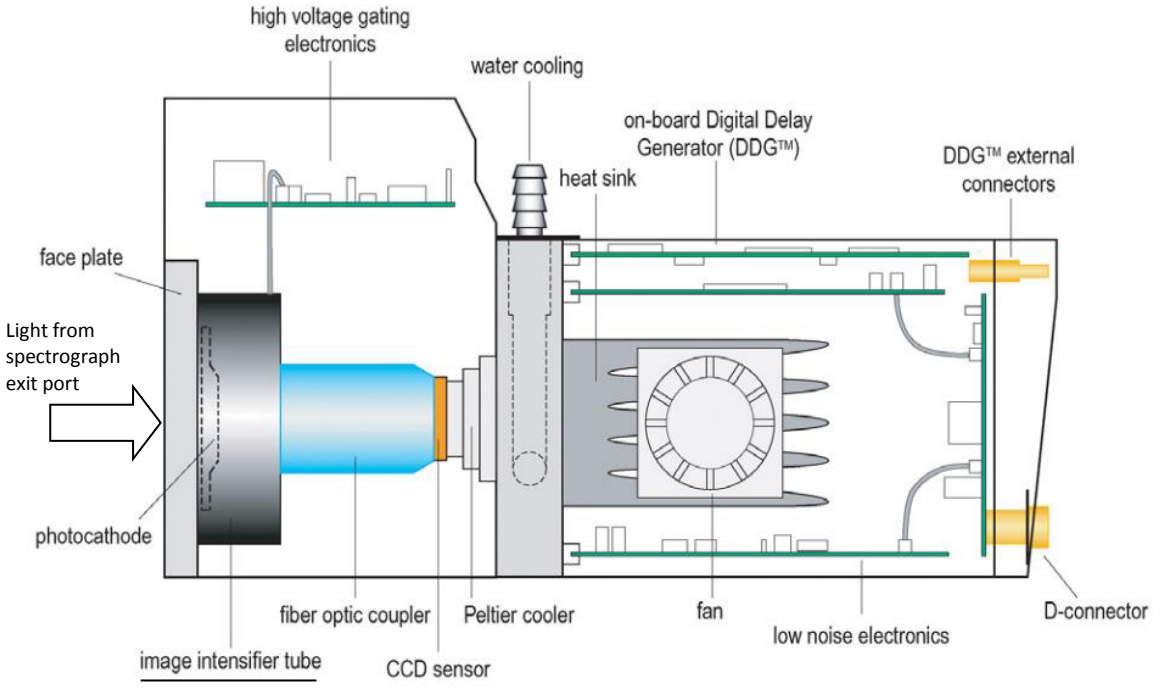

Figure 4.6. A cross-sectional schematic of the ICCD camera unit and its various constituent parts. The camera unit is coupled directly to the spectrograph and its operation is fully software-controlled. An expanded view of the image intensifier tube is shown in Fig 4.7.[6]

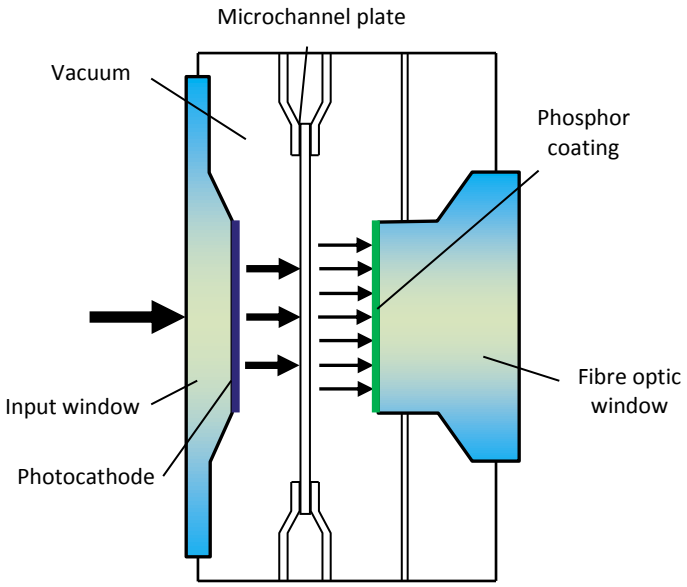

Figure 4.7. A close up cross-section of the evacuated image intensifier tube. The arrows indicate the direction of the electro-optic signal and show the various stages of detection/amplification.

The spectrograph is directly coupled to the ICCD camera, so when a photon passes the spectrograph output port it passes through a window and impinges directly on the intensifier tube. In the intensifier tube, pictured in Figure 4.7, the photon passes through a quartz input window and arrives at the photocathode, which is an alkali-metal-based coating on the rear face of the quartz. This coating may emit a photoelectron as governed by the material's quantum efficiency (QE), which is around 10% for the photocathode material at typical SFG wavelengths – this means that roughly 10% of impinging photons will generate an electron. Generated electrons are then passed through a multi-channel plate which is a thin disc of honeycombed glass with a high voltage applied to it that acts like a photomultiplier tube array. When an electron passes down one of the honeycomb channels, it creates a cascade of secondary electrons via impact ionisation, the magnitude of which can be varied by changing the applied voltage; this is the system's *gain*. This amplified photoelectronic signal finally reaches the exit window which has a specific phosphorescent coating (Gd_2O_2S:Tb) that generates visible light at 545 nm, capable of being detected by the CCD. The exit window is fibre optic and directly couples to the CCD sensor, meaning spatial (imaging) information can be preserved and translated by the camera and software.

The CCD sensor is a semiconductor chip possessing 1024 × 1024 pixels, each of which acts as an individual photo-sensor. Photons generate electronic charge in the potential well of a pixel where it remains until sequentially read out and converted into a binary value by an analogue-to-digital converter. The CCD possesses a high QE (~45 %) and linearity (number of counts versus the

actual signal) and as such the more limiting factor of the ICCD system is the QE of the intensifier photocathode.

4.3.4 Signal Gating

Due to the weak second-order nature of the SFG process it is common during data acquisition to need to detect single photon events. In this case efforts must be taken to reduce background counts, whether instrumental or environmental in origin, to a minimum. As SFG obeys momentum conservation it is a highly directional process and thus careful steering and spectral filtering will reduce a significant amount of spurious environmental counts. Additionally, due to having been generated with fast laser pulses the SFG signal is highly time-localised, typically of the order of picoseconds. With fast signal gating it is possible to isolate the SF generation time window and miss any background counts during the 99.9 % of the time the laser intensities are zero. Whilst no shutters exist that will operate on these timescales, the major advantage of the image intensifier tube is that in conjunction with an onboard digital delay generator (DDG) both it and the CCD can be gated simultaneously via rapid voltage application.[6]

A trigger pulse from the Ti:Sapphire amplifier is fed into the ICCD unit and with *external triggering* mode enabled the camera software allows for adjustment of timing variables. A specified time (Trigger Delay) after receiving the trigger pulse, the gate is 'opened' for a predefined window of time (TTL/Gate Width) down to a minimum of 2 ns. The exact values can be determined experimentally where the emphasis is on defining the narrowest time window which still allows the maximum SFG throughput. Unless a change is made to the timings on the Ti:Sapphire amplifier's synchronisation and delay generator (the rack unit which controls pulse injection and ejection from the amplifier cavity) these timings once ascertained will change very little.

4.4 Model SFG substrates & Preliminary Spectra

In order to properly align and characterise the VSFS experiment, several model substrates were frequently utilised. For visual spatial/temporal alignment checks using the alignment stage, one requires materials that will generate a visible SFG spot in a transmission geometry. As previously mentioned the two materials used in this stage are Beta barium borate (BBO) and zinc selenide, as both are transparent in the visible and near-IR and possess a high nonlinear responsiveness.

Once this alignment has been achieved an SFG signal must be generated off a surface at the sample stage, and then be properly filtered and focussed into the ICCD. Due to the large number of variables and degrees of freedom of the optics this can be aided with an (visible-HeNe) alignment laser which is set to trace the SFG beam path from the BBO (see Figure 4.4). At the sample stage, the alignment laser is reflected off an SFG-active sample and carefully steered into the detector; if done accurately enough a non-resonant SFG background signal should be seen by the ICCD once the flipper mirrors are disengaged and the visible and IR beams reintroduced.

GaAs is a direct band gap semiconductor material commonly used in solar cells, LEDs and laser diodes.[7] It is also highly useful for SFG alignment procedures as it produces a non-resonant surface sum-frequency signal significantly greater than other materials currently probed on the PSI system. It is indeed possible to saturate the ICCD camera with an SFG signal from very low incident powers.

As the non-resonant signal originates from surface electronic effects, metals are also highly useful for alignment and pulse characterisation, provided they are clean and do not have a significant thickness of surface oxide. As such, gold is frequently used which has been deposited on a silicon or glass substrate by chemical vapour deposition. When coated in such a way, gold has been shown to reproducibly form a preferentially Au(111) oriented surface.[8] Typical non-resonant spectra from both GaAs and Au are shown in Figure 4.8.

The spectra in Figure 4.8 were taken prior to x-axis calibration but the spectrograph pixel number corresponds to wavelength. The spectral profile of the pulse-shaper output (which governs spectral resolution) has been shown also for comparison, although with an x-axis offset. The two non-resonant spectra were both taken with an OPA output setting of 3450 nm, which corresponds to a central SFG wavelength of 649 nm. As seen from the figure, both GaAs and Au spectra are spectrally broad with approximately Gaussian distributions, suggesting firstly no major pulse distortions in the frequency-domain and secondly the lack of any significant vibrational resonances, assuming a functioning experimental setup. Whilst these were taken prior to x-axis

calibration, an approximate estimate for the spectral width (Full Width Half Maximum (FWHM)) via the use of a spectrograph calculator is 100-200 cm^{-1} at this point in the implementation.

In addition to these two substrates, single crystal TiO_2(110) was also frequently used during alignment as this is a well understood metal oxide that would be used latterly for further studies. This material will be discussed in more detail in Chapter 5, but was used in these early alignment stages of development as it exhibits a significantly weaker SFG response and so requires more accurate alignment to detect.

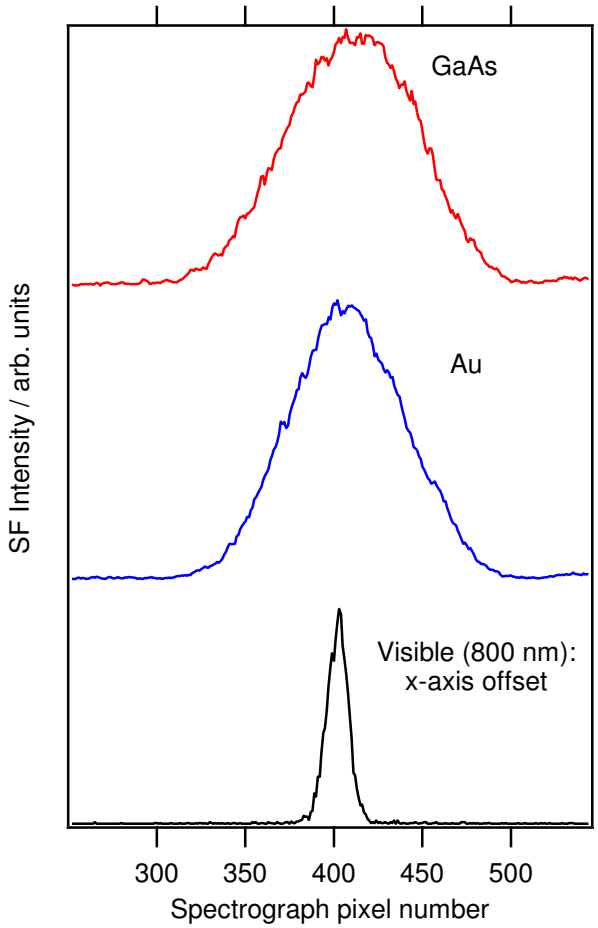

Figure 4.8. Non-resonant SFG spectra from Au and GaAs substrates. The visible signal is from the pulse shaper output and has been horizontally offset so it can appear on the same plot – the width of the visible is the resolution limiting-factor.

For more detailed system optimisation it is also useful to have a model system capable of exhibiting adsorbate related vibrational resonances through SFG. A model system commonly used for this purpose is a self-assembled monolayer (SAM) of octadecane-thiol (ODT) molecules.[9-

[11] This molecule, the formula and diagram of which can be seen in Figure 4.9, has been shown to form a well-ordered monolayer when dissolved in ethanol and exposed to bare silver or gold substrates. The hydrocarbon chains tend to align relative to the surface normal, and as VSFS is sensitive to surface ordering this results in strong identifiable resonance peaks in the C-H stretching region.

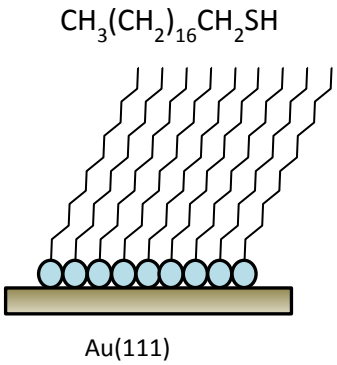

Figure 4.9. A representation of an ODT self-assembled monolayer on the Au(111) surface. The formula of ODT is also shown

4.4.1 Spectral Convention

As VSFS probes vibrational resonances traditionally investigated via IR spectroscopy, detected spectra are often plotted as function of 'equivalent IR wavelength', where the visible wavelength contribution has been subtracted. To further follow conventions in infrared vibrational spectroscopies, the wavelength scale is converted to 'wavenumber', equivalent to $1/\lambda$ or the inverse wavelength and quoted in units of cm^{-1}. The reason for using wavenumber is that it is directly proportional to photon energy, thus making it easier to identify molecular vibrational modes of specific known energy through the use of a simple scaling factor.

Infrared spectroscopy looks at molecular vibrations or rotations, and the energies of the fundamental modes of most common chemical bonds occurs between 4000-400 cm^{-1}, which is equivalent to an IR wavelength range of 2.5-25 μm.[12]

4.5 Experimental Optimisation

4.5.1 Introduction

Over the course of setting up the experiment, numerous scans were taken from the model substrates (GaAs and Au), which were used to identify any faults or issues, and measures were then taken to improve matters. This section will detail the various improvements in approximate chronological order, including descriptions of any relevant theoretical or technical background.

4.5.2 Pulse Characterisation

Early scans taken from gallium arsenide are shown in Figure 4.10, from which several observations may be made. Firstly, it is apparent that the overall signal intensity decreases significantly with increasing IR(λ). This was discovered to result from a number of factors, namely the SFG directional change consistent with momentum conservation (SFG emission angle fundamentally varies with IR photon energy), and a variation in the IR pulse properties originating from the OPA. With a less-than-ideal OPA alignment, a change in the output wavelength may result in a reduced/increased output power, a steering change, or a change in the IR pulse quality or its spatial/temporal profile. These IR property variations are illustrated further in Section 4.5.3. All of these factors can contribute to a significant variation in SF signal strength.

A second identifiable feature is the consistently asymmetric spectral shape. An optimally aligned broadband VSFS setup collecting data from a molecule-free substrate should yield a non-resonant signal only, and this signal is a convolution between the Gaussian spectral distribution of the OPA out and the Lorentzian spectral distribution of the pulse-shaper/etalon as predicted theoretically[13] and suggested by Figure 4.8. As such the resulting NR spectrum should be roughly Gaussian after taking into account the visible pulse's narrowed bandwidth. The asymmetric peak shape of the scans in Figure 4.10 could partially be the result of adsorbed surface species, but the consistency in shape suggests otherwise.

The additional 'hump' feature on each scan at higher wavelengths was a particular cause for concern and led to a more in-depth characterisation of the two input probe pulses, as it suggested either a particularly irregular IR pulse spectrum (NR SFG can be used to infer the infrared pulse spectrum) or the presence of an additional visible pulse at an alternate wavelength which was also participating in SFG upconversion.

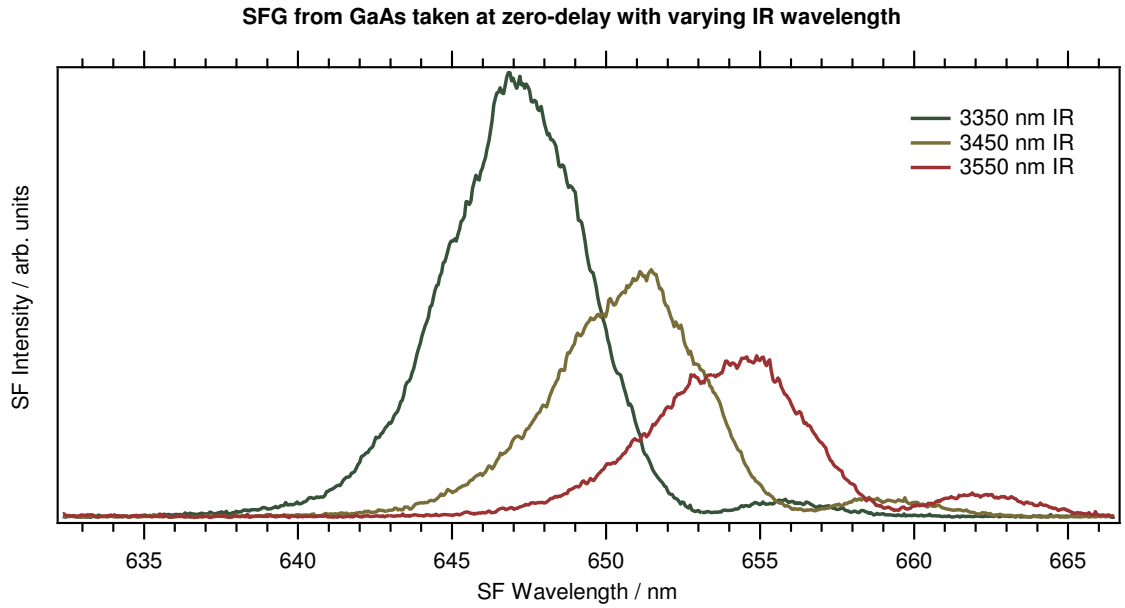

Figure 4.10. Preliminary NR SFG spectra taken off gallium arsenide at three different IR centre-wavelengths

4.5.3 Input Probe Characterisation

As well as the ICCD spectrograph, a calibrated USB fibre-coupled spectrometer was used to ascertain spectral profiles of the various visible/near-IR emissions. This spectrometer is not useable for wavelengths above 1.1 µm, and so to measure the OPA output spectral profile requires upconversion (photon mixing) via SFG with the narrow visible pulse. If the visible probe is sufficiently narrow, the SFG spectrum will closely resemble the spectral profile of the IR pulse, and deconvolution allows both IR wavelength and bandwidth to be inferred.[14, 15]

The initial setup took the visible (802 nm) beam from the OPA dump port, so this was investigated for quality. By observing it reflected off a white card, it was apparent that the pulse profile was spatially non-Gaussian in intensity, and certain areas of different wavelength were also identified. Spectral profiles of the 802 nm beam at various locations within the OPA are shown in Figure 4.11, from which it can be seen that the wavelength distribution is also non-Gaussian/non-Lorentzian after interaction with OPA optics. From this it was decided that a better quality visible pulse would be required to obtain meaningful data, and so a portion of the beam directly from the Ti:Sapphire amplifier was then considered for use as a spectrally 'cleaner' VIS probe pulse source.

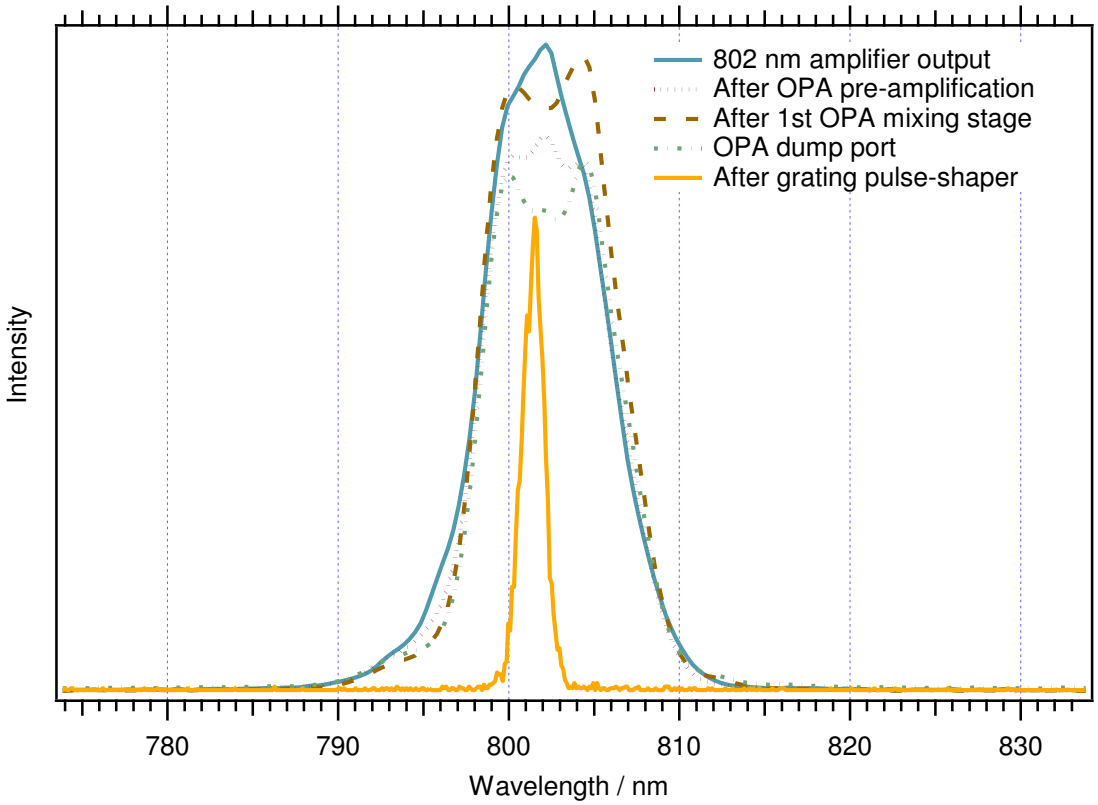

Figure 4.11. The spectral profile of the visible (802 nm) beam at various points between the amplifier output and grating pulse-shaper. The irregular spectral profiles post-OPA interaction is a result of losses from the OPA mixing stages.

To determine the quality of the visible probe pulse, further characterisation was sought. The measurement in the time-domain of an ultrafast pulse is theoretically problematic as to measure anything temporally requires something shorter to measure it against. This issue can be overcome through the use of autocorrelation, where a pulse is split in an interferometer-type arrangement and through the use of a variable delay is interacted with itself. As the emitted intensity is a product of two identical pulse time-profiles as depicted in Figure 4.13 a), temporal pulse data can be extracted from it.[16] One device used for this measurement was a commercial PulseCheck autocorrelator (APE, Berlin) and whilst the data from it was not recorded the temporal pulse shape of the 802 nm beam is shown in Figure 4.12 with a pulse width of ~150 fs. An additional Grenouille (Swamp Optics) autocorrelator was also used to characterise the short visible pulse and in addition to temporal information this is capable of resolving the pulse spectrum and beam spatial profile, as well as diagnosing any spatio-temporal distortions such as chirp or pulse-front tilt (see below for details). The beam from the amplifier was found to have an acceptably Gaussian spatial and spectral profile, free from any major distortions, and so it was

decided to utilise a portion of this for the visible SFG probe. Due to limitations with the computer used for Grenouille autocorrelation, it was not possible to record this data.

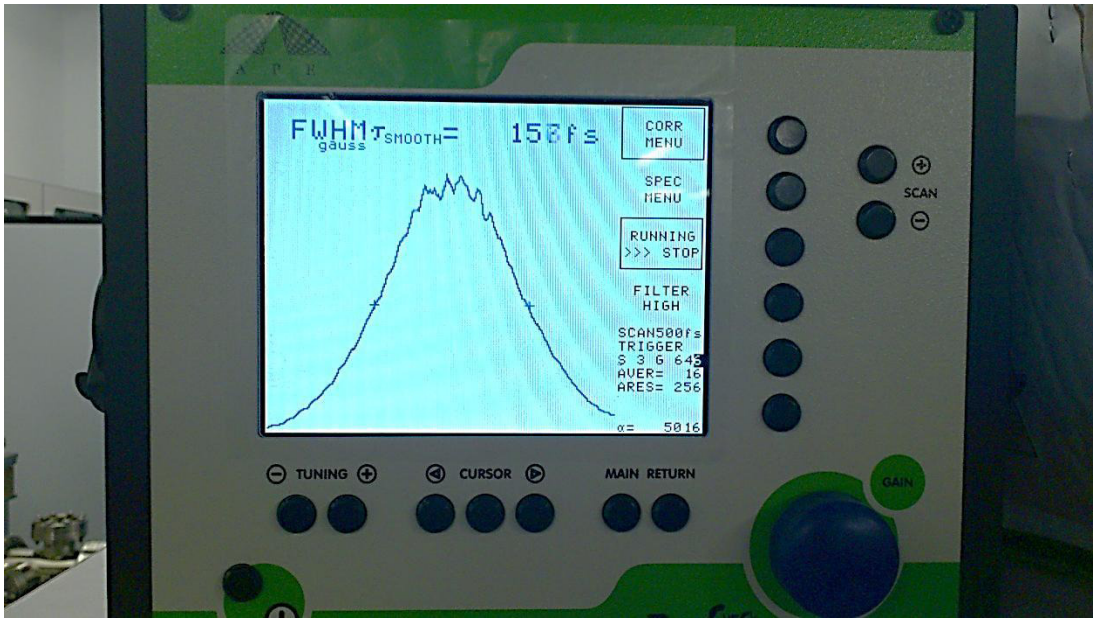

Figure 4.12. The temporal profile of the 802 nm pulse as measured by the APE autocorrelation unit.

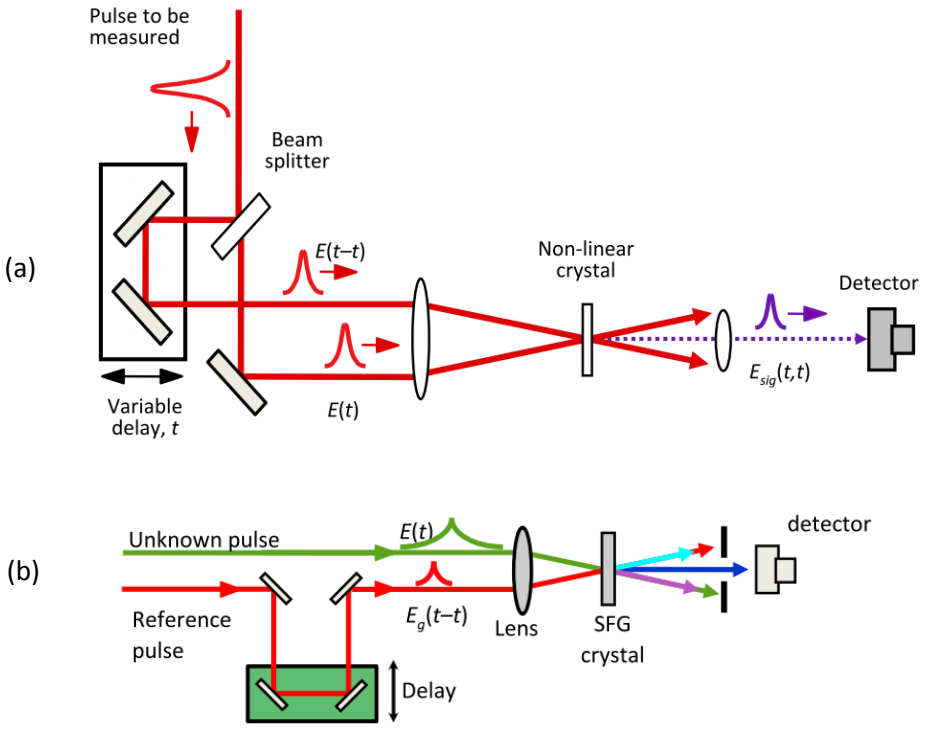

Figure 4.13. Schematic representations of both the a) autocorrelation and b) cross-correlation pulse characterisation techniques. Commercial autocorrelation units are typically designed for a particular wavelength, but have an otherwise high tolerance for various input parameters, and are becoming increasingly compact.

Concerning IR pulse characterisation, a similar correlation technique is required. However, few detectors function well over the infrared spectrum, so IR pulse autocorrelation was not possible with the detectors and optics available. Alternatively, as previously touched upon, the generation of a SFG signal from a broadband IR source and a spectrally narrowed visible source allows for the analysis of the IR spectral characteristics. If the same arrangement is used with the introduction of a variable delay line as in Figure 4.13 (b), spectral information can be plotted in the time-domain and used to derive time profiles of the pulses.[17] This technique is also able to diagnose distortions in the IR pulse, assuming that the visible pulse has been checked to be free of chirp or tilt.

Figure 4.14 shows cross-correlation data taken off a gold substrate with no pulse-shaping of the visible component both before and after OPA optimisation. The asymmetric profile of the first plot implies that there is temporal chirp present in the IR pulse, meaning different wavelengths arrive at the interface at different times. After careful alignment of beams and optics within the OPA, this asymmetry is sufficiently negated.

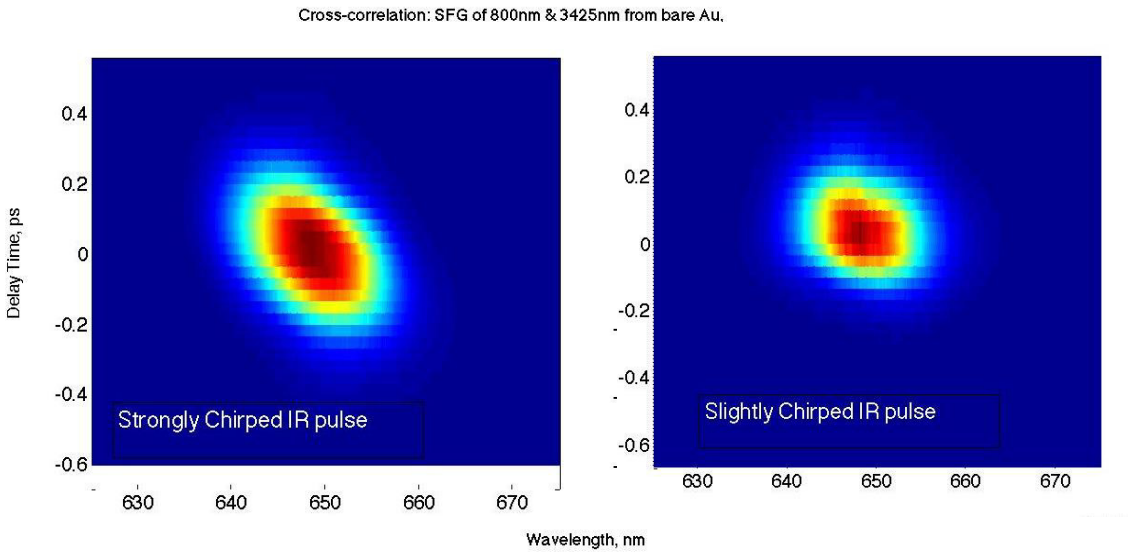

Figure 4.14. Cross-correlation scans taken from a gold substrate without any pulse shaping on the visible light. The IR OPA was thoroughly re-aligned in between the two scans, resulting in a significant decrease in the observed tilt. The time profile of the scan is a product of the temporal profiles of both ultrafast pulses, and so in conjunction with visible autocorrelation each can be accurately inferred.

Spatio-temporal Pulse Distortions

Pulse distortions can be either temporal or spatial in nature. The term 'chirp' was initially applied to wave patterns whose instantaneous frequency varies with time, analogous to the audible chirp

a bird makes. This effect known as temporal chirp can be described by a complex phase factor in the electric field, and is caused when pulses pass through various window, lens or crystal materials.[18] Depending on the medium, chromatic dispersion may occur where different frequencies propagate through at different velocities, and nonlinear crystals such as those in the OPA also inherently interact with EM waves nonlinearly with respect to frequency/wavelength; both these processes can result in temporal chirp.

The two major spatial pulse distortions are spatial chirp and pulse-front tilt. A pulse which is spatially chirped possesses a distribution of wavelengths across the pulse front as illustrated in Figure 4.15, and in broadband VSFS this will negatively affect the system's spectral reliability – certain IR colours may preferentially interact with the visible light whereas other may not.[17] Pulse-front tilt, also illustrated in Figure 4.15, is when the pulse-front normal is at an angle to the direction of propagation. This can significantly decrease the SFG interaction cross-section, meaning lower signal strengths, and it also impacts on data quality.

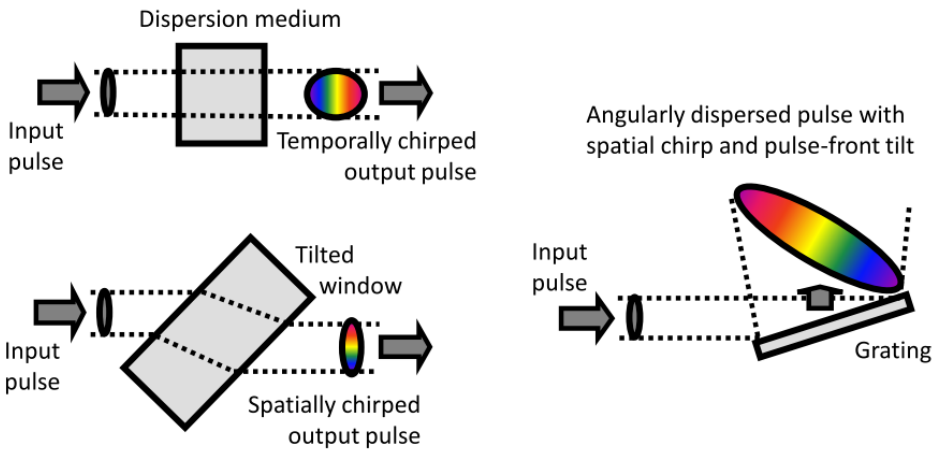

Figure 4.15. Diagram showing examples of the major spatio-temporal pulse distortions which may affect VSFS measurements.

4.5.4 Acquisition Parameters

The Andor ICCD spectrograph has numerous variables which can be manually- or software-controlled depending on the experimental conditions. It was necessary to experiment with each of these in order to better understand their effects and maximise the detector response and spectral quality for any given sample scenario.

Optimising Spectrograph Collection Efficiency

The spectrograph is a non-active arrangement of optics which imposes fundamental limits on its throughput and resolution,[19] and so for our purposes the entire series of optics from sample to spectrograph exit slit can be considered a single optical system, outlined in Figure 4.16.

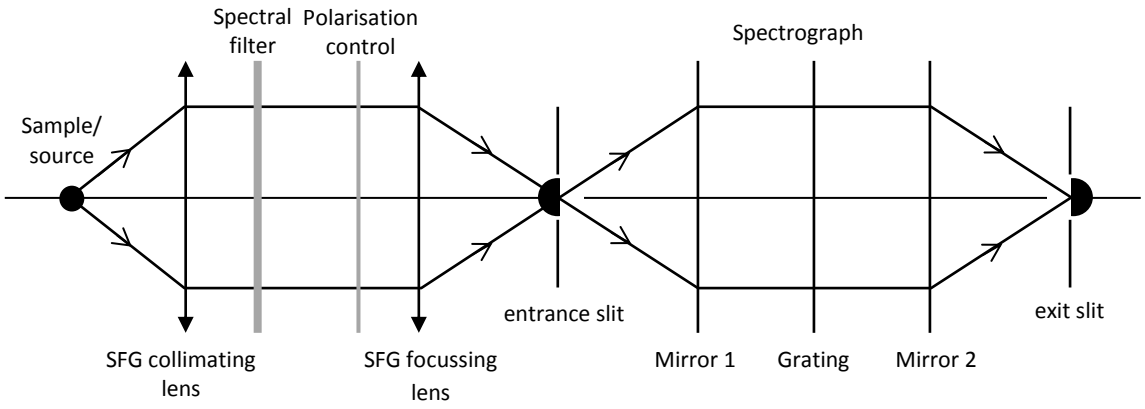

Figure 4.16. A linear representation of the collection, steering and light-tailoring optics between the SFG source and spectrograph output.

The first optic after the sample stage is a lens of roughly the same focal length as the visible and IR probe focussing lenses – as the SFG signal is generated by two focussed beams the resulting signal is divergent and requires collimation. There are two spectral filters utilised in the setup which act to reject photons of unwanted wavelength; the first blocks the high-power 802 nm reflected beam and the second is a band pass filter which only allows the transmission of SFG wavelengths (650 nm centre, 80 nm bandwidth). The polarisation optics are primarily a polarising beamsplitter to transmit only light of a specific set polarisation, but the grating in the spectrograph also has a wavelength and polarisation-dependent reflection efficiency and thus additional optics are necessary depending on the experimental conditions. If a fixed SFG polarisation is needed, a half-wave plate will rotate the linear polarisation axis until the signal intensity is maximised on the ICCD. For situations requiring multiple SFG polarisations a quarter-wave plate will convert a linear to a circular polarisation, effectively averaging out the polarisation of light incident on the grating and ensuring minimal instrumental effects on the signal intensities for different polarisations.

In coupling the SFG signal to the spectrograph, the intention is for a maximum amount of signal to pass through the entrance slit and illuminate the grating over as large an area as possible.

Considerations must also be made towards the overall resolution of the optical system in Figure 4.16, which is controlled and fundamentally limited by a number of system variables.

The *entendue* of an optical system describes its ability to accept light, and is a constant determined by internal geometric constraints. In a multi-stage system such as the one illustrated in Figure 4.16, the overall entendue is determined by the least optimised component[5] and so once values have been calculated efforts must be taken to improve the limiting factors. As the SFG signal is collimated it can be considered optically as an extended light source (as opposed to a point- or narrow fibre light source) and as such the spectrograph entendue is orders of magnitude lower and is the overall limiting component for system throughput. It can be shown mathematically[19] that the light-gathering ability of a spectrograph is proportional to its grating specifications (area, diffraction order, groove density) and entrance slit parameters (height, width and focal length). As the grating and entrance slit height are both fixed, the main throughput variable in the VSFS setup is the entrance slit width which is directly proportional to entendue/throughput.

For maximum throughput the slit width should be as large as possible, but the overall bandpass or spectral resolution of the spectrograph is inversely proportional to the entrance slit width, and so a compromise must be arrived at. Other factors affecting spectral resolution are the exit slit size, CCD pixel size, and diffraction/aberration phenomena introduced by the grating and mirrors, but again all these are fixed in the system and only affected initial detector purchasing choices. Optimum slit widths for data acquisition depended on the SFG focussing lens's focal length but were found to give the best resolution-throughput compromise at a width of 50-80 μm. During alignment when resolution was less important, widths of 200-1000 μm could be used as they made for much easier initial SFG detection.

To illustrate the spectral effects of varying the entrance slit width, a series of resonant spectra taken from ODT on gold substrates is shown in Figure 4.17. Note how overall intensities decrease with slit width but also especially how the two central features separate and fully resolve between a slit width of 40-80 μm.

These spectra were taken with 'background suppression' techniques (see Section 4.5.7), but clearly resolve the three CH_3 vibrational resonances. In the case of an older gold/ODT sample such as this particular one, changes in the surface ordering over time means the long hydrocarbon chains distort and two additional resonances may appear due to CH_2 vibrations becoming SFG-active, hence the four identifiable molecular resonances.[11] Direct assignation of peaks is difficult

as spectra were taken without x-axis calibration, but all peaks are present at the expected C-H stretch wavenumber range according to the reported OPA IR emission wavelength ($\sim 3300\ \mathrm{nm} = 3030\ \mathrm{cm}^{-1}$)

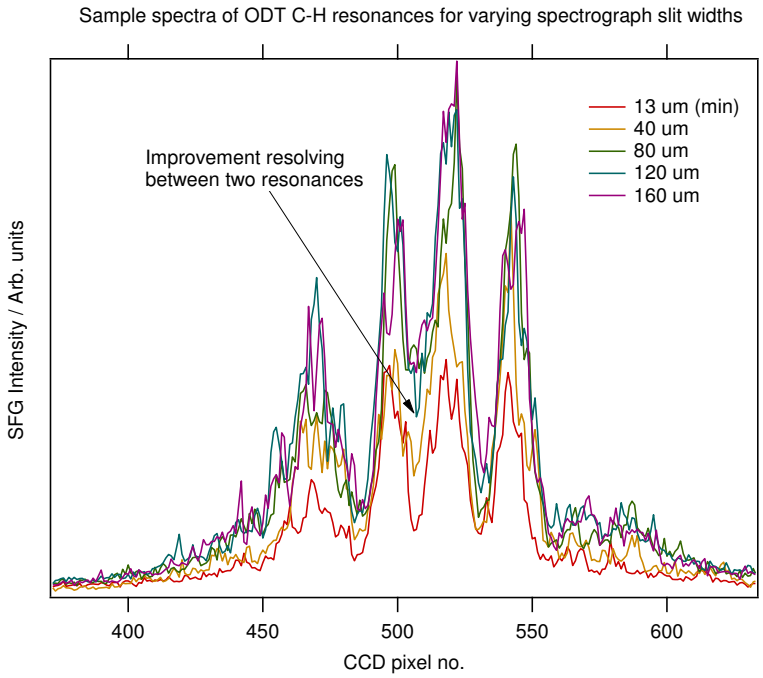

Figure 4.17. SFG spectra (background suppressed – see Section 4.5.7) of the CH stretch resonances from ODT molecules on a gold substrate. The plots shows the effect of a varying spectrograph entrance slit width when all other variables are kept constant.

ICCD Settings Optimisation

The ICCD detector has a plethora of variables that are adjustable within the accompanying Andor Solis software. These will be discussed, and their effects on the output spectra examined.

The timing variables affect the gating of the intensifier similar in effect to a high speed mechanical shutter. A trigger pulse from the Ti:Sapphire amplifier is sent to the detector head, and the user can define the time-delay in between the trigger pulse and a voltage being applied to the intensifier, and additionally define the duration/width of each gate exposure. Optimal values were arrived at empirically. The system was temporally and spatially aligned and a non-resonant SFG signal generated off a GaAs substrate. The gate width was set to a high value (0.5 s) and the TTL delay adjusted until the highest signal was detected. The gate width was then incrementally lowered and the delay changed so as to maintain the same signal strength, and this was done iteratively down to a minimum gate width of 25-30 ns.

CCD operation

To explain certain other variables related to spectral acquisition will require a brief explanation of the operation of the CCD chip. The CCD chip is a 1024 × 1024 pixel array of individual semiconductor photodetectors. When a photon impinges on a pixel it generates a charge which remains until it is read out; this means charge is able accumulate on the chip. In a read-out, the charge from each pixel in a column is shifted downwards one by one into a non-photoactive row of pixels called the shift register, whereupon their voltages are measured and sent to the computer as a per-pixel intensity value. To shorten acquisition times it is possible to specify smaller regions on the CCD for read out, and the most commonly used mode for this technique is *Single Track Mode* which integrates the charge from a set number of pixel rows. A comparison between this and *Image Mode* which reads an entire CCD image is shown in Figure 4.18. Additionally the *Full Vertical Binning* mode bins the information from each column of pixels on the CCD, and is highly useful in alignment procedures as it treats each column as an individual datapoint and integrates information from the whole CCD chip.

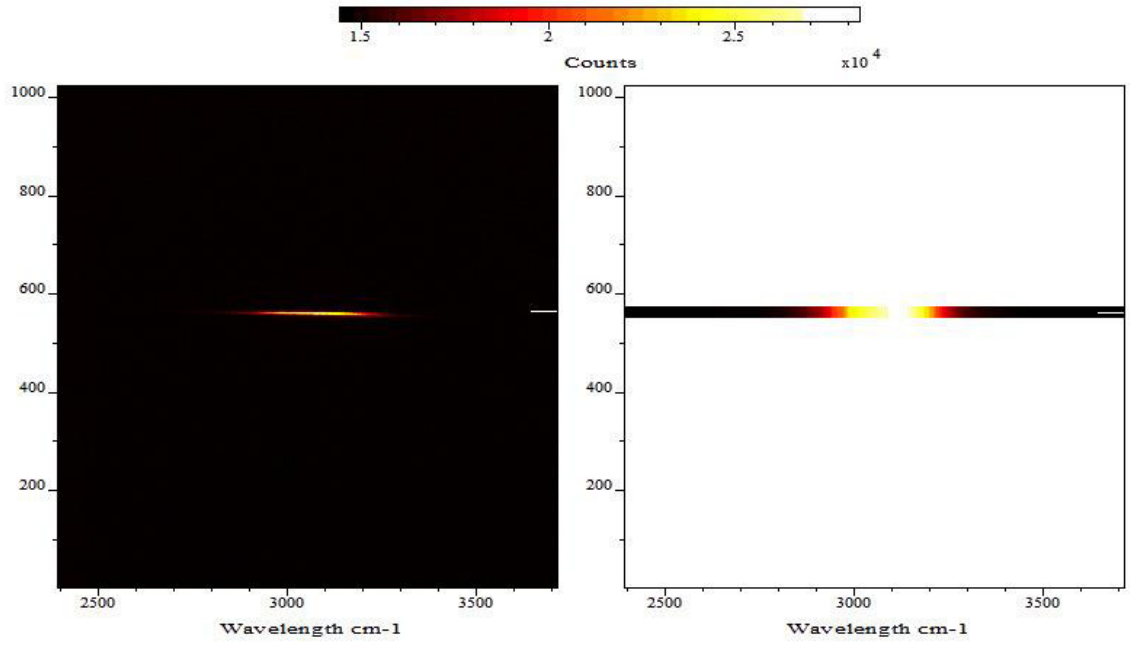

Figure 4.18. A comparison between the active areas of the CCD chip for *image mode* (left) and *single track mode* (right) when looking at a strong non-resonant SFG response from Au. As well as shorter acquisition times, using the *single track mode* nullifies any potential noise or erroneous counts from the non-active areas of the CCD.

The *integrate-on-chip* function (IOC) takes advantage of the fact that charge can build up and remain on the CCD, and so makes it possible to collect the signal from multiple gated pulses in a

single exposure. The exposure time setting specifies the interval of time between each CCD readout, and can be anything from 2 ms to hundreds of seconds. Without a gate this would limit the refresh rate of the camera but in conjunction with a properly timed trigger pulse means as many SFG pulses can be detected as possible whilst negating any undesired photon counts from the 'dead' time between pulses.

The *pixel readout time* parameter refers to the time the camera allocates for reading out charge from each pixel on the shift register. A faster pixel readout time decreases the overall acquisition time but due to physical limitations from the fast electronics introduces a higher amount of noise in the data, so a compromise must be made regarding these two factors.

It is often necessary to tailor the acquisition parameters to the sample under investigation, as it was found that different settings recorded higher signals with lower signal-to-noise (S/N) ratios depending on the magnitude of the samples' SFG activity. For situations with minimal SFG emissions the detector at a high gain is able to register single-photon events. Whilst it is possible to accumulate spectra from these, each photon undergoes a random amplification cascade in the intensifier meaning the measured charge value for a single photon can vary greatly. Thus spectra gathered in this way may have features that are under or over exaggerated, unless extremely long accumulation times are used to average out the charge randomness. The camera comes equipped with a photon-counting (PC) functionality, which will register any CCD voltage value above a predefined threshold level as a single count – this solves the issue of the random electron cascade, with the caveat that any multiple photon events on the same pixel in an exposure would only generate a single count. For situations with higher SFG signal strengths where multiple photon events are probable it then makes sense to disable the photon counting function, and the mode in which spectra were acquired in this project were determined according to the level of their SFG response (number of counts) as observed in real-time.

The various effects of changing these parameters were determined experimentally, and Figure 4.19 shows an example of the spectral variability that can be achieved from the same sample over a set acquisition time by varying only the exposure time, pixel read out time, and whether the IOC function is enabled. These were taken for a situation with a relatively low number of photon counts. The variety in S/N ratios is immediately apparent from the overall photon counts and spectral shapes. It was found that the greatest detection efficiency utilised a moderately long (in terms of minimum gate response times) exposure time, high pixel readout time, and exploited the IOC function. A CCD readout takes a finite amount of time, during which signal will not be registered, and so a shorter exposure time results in more 'dead signal' unable

to be detected, as apparent from the plots in Fig 4.19 with the lower exposure times. Also apparent are large single-pixel spikes which have been significantly trimmed in the figure – these are due to the photon counting detection threshold registering non-random background noise from the detector. The spectra have been taken off a gold substrate with a time-delay on the visible pulse, and demonstrate the potential difficulties when examining surfaces with a low SFG signal count. Thus it is paramount that background counts are effectively minimised.

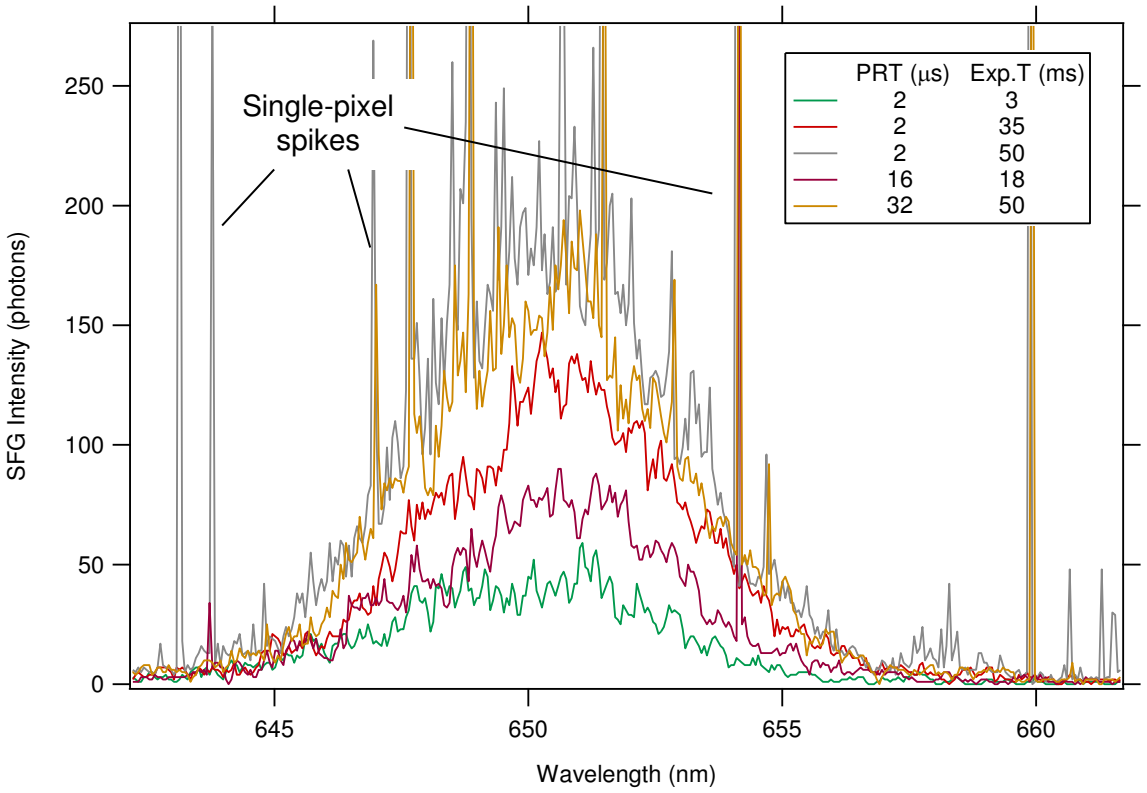

Figure 4.19. A plot of several SFG spectra taken of the same Au(111) sample over the same (multiple exposure) acquisition duration but with differing pixel readout time (PRT) and exposure times (Exp.T). This illustrates the importance of optimising these variables such that a minimum of the useful light signal is lost.

Background Noise & Noise Reduction

Background noise is an unavoidable factor when taking measurements of this type as it is necessarily introduced at various stages in the detection process. Whilst the alignment procedure and sensor gating can be used to eliminate spurious counts from non-SFG photons, noise will be present in the data from three major sources; the desired light signal, the dark signal, and the pixel readout process.[6, 20]

For the light and dark signal, noise values are essentially equivalent to the variation in intensity one would see from a single pixel if multiple identical measurements were made – a quoted noise value would be the root mean square of these variations. The light signal is a result of incident photons and must be maximised, but a standoff is introduced as the shot noise from the light signal is proportional to the signal itself. In the case of a strong light signal (multiple photon events per pixel per exposure) where photon counting would be disengaged the gain must then be set high enough to clearly minimise the effects of CCD background noise on the signal (maximising the S/N), but not so high as to introduce irregularities at the signal peak intensities. Long acquisition times with numerous multiple exposures will also serve to average out light signal noise.

The pixel readout noise is a constant of the system and is only dependent on the time taken for each pixel charge to read out from the CCD shift register. This timing variable is adjustable via the detector software, and whilst the longest values would give minimum noise levels they also drastically lengthen exposure and acquisition times and can fail to register a larger amount of 'dead signal' during readouts. A compromise value of 2 μs was chosen for the majority of this project.

The dark signal is the baseline signal level that is detected by the CCD regardless of incident light. It arises due to charge generated thermally in the CCD over time, and as such is dictated by CCD temperature and exposure time. The dark current level varies between pixels due to physical irregularities and its associated noise is also proportional to the (dark) signal level, so steps should be made to minimise this overall. The high inverse dependency of the dark signal on the CCD temperature means the most effective means of reducing it is to cool the sensor,[21] and so a circulating water chiller system was installed to supplement the camera's on-board thermoelectric cooler. Figure 4.20 shows a series of image mode acquisitions taken by the camera for a number of different CCD temperatures in the case of a closed spectrograph entrance where the only signal registered is due to the dark current. Each sub-image has been auto-scaled by its minima and maxima, and the given scaling values along with the apparent homogeneity of the images shows how effectively CCD cooling will reduce dark current and any irregularities between pixels. Whilst the presented images are sub-images of the CCD to highlight the presence and subsequent disappearance at low temperatures of unwanted thermal counts (lighter specks on the top three sub-images), the auto-scaling has been applied over the whole CCD area. What this shows is that as the temperature of the detector is lowered towards $-20℃$, thermal counts vanish, the overall average background level drops, and the standard deviation in measured

voltages of all CCD pixels from the average is also reduced (manifested by a lighter, more homogeneous sub-image). Such a reduction in the background and its variation leads to significant improvements in the S/N of low photon count rate spectra.

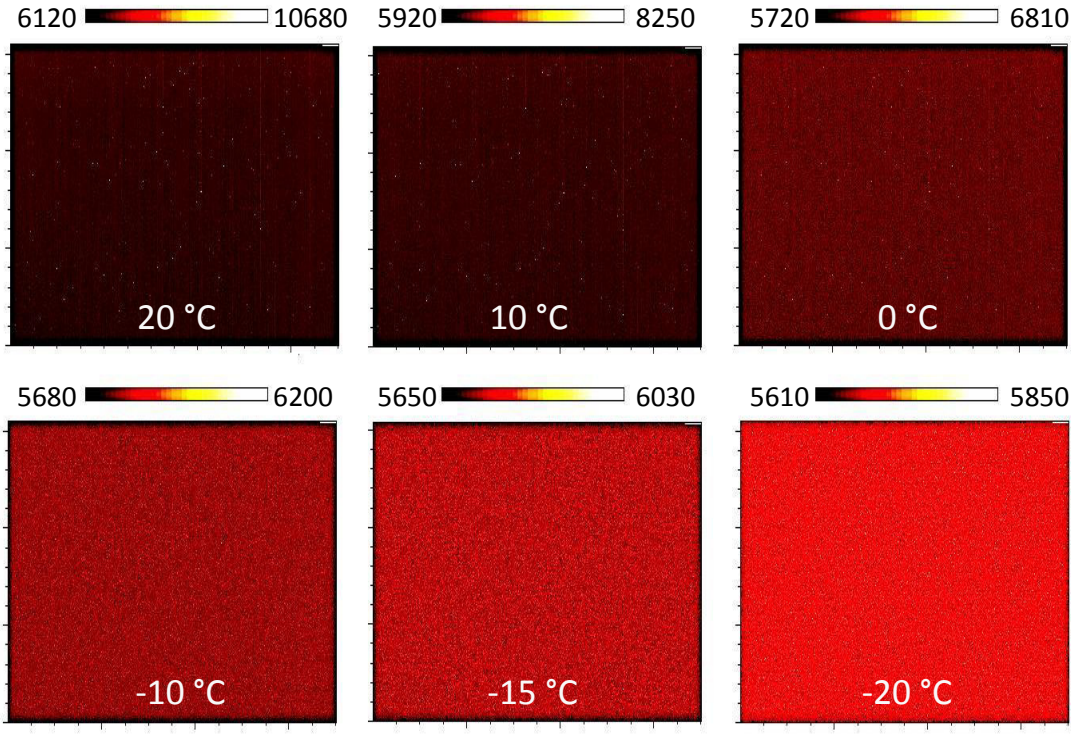

Figure 4.20. CCD sub-images taken of the camera's dark current response at varying CCD temperatures.

4.5.5 Spectral Calibration

The wavelength of the light read by the detector is calculable by the camera software, via reading off the micrometer screw on the spectrograph which has been factory calibrated. When tested with a known laser emission, it was accurate to within 1.5 nm. The issue is complicated however by the fact that the desirable signal is a product of the mixing of two different pulses, each with different spectral widths and centre-wavelengths. Assuming both centre wavelengths are known the expected centre-wavelength of the SFG emission is dictated by

$$\frac{1}{\lambda_{SFG}} = \frac{1}{\lambda_{IR}} + \frac{1}{\lambda_{VIS}}$$

where all variables are measured in nanometres. To obtain an accurate x-axis calibration from this requires an adjustment to the standard grating equation which factors in for spectrograph and camera dimensions, and gives you the wavelength range that will impinge on the CCD for any

given centre wavelength[19] (grating dispersion calculators are also available on several spectrograph manufacturers' websites) . This method requires accurate values of λ_{VIS} and λ_{IR} and whilst the former is easily ascertained with a standard spectrometer, there are very few spectrographs capable of detecting in the IR region – the best estimation of λ_{IR} on this VSFS is taken from the OPA calibration which must then be assumed accurate.

The visible wavelength is responsible for the Raman-upconversion of IR excitations but its value is not especially important; what is more useful on spectra is an accurate representation of the equivalent IR wavelength/wavenumber range and this can be found by correlating IR absorptions present in an SFG spectrum with the same absorptions as investigated by IRAS. Polystyrene was chosen for this purpose as it has a highly characteristic absorption spectrum in the areas of interest and is readily available in thin film form. A non-resonant SFG spectrum was taken off a clean gold substrate with a polystyrene film placed in the IR path prior to the surface, and the characteristic absorptions were then correlated with a reference IR absorption spectrum as shown in Figure 4.21.

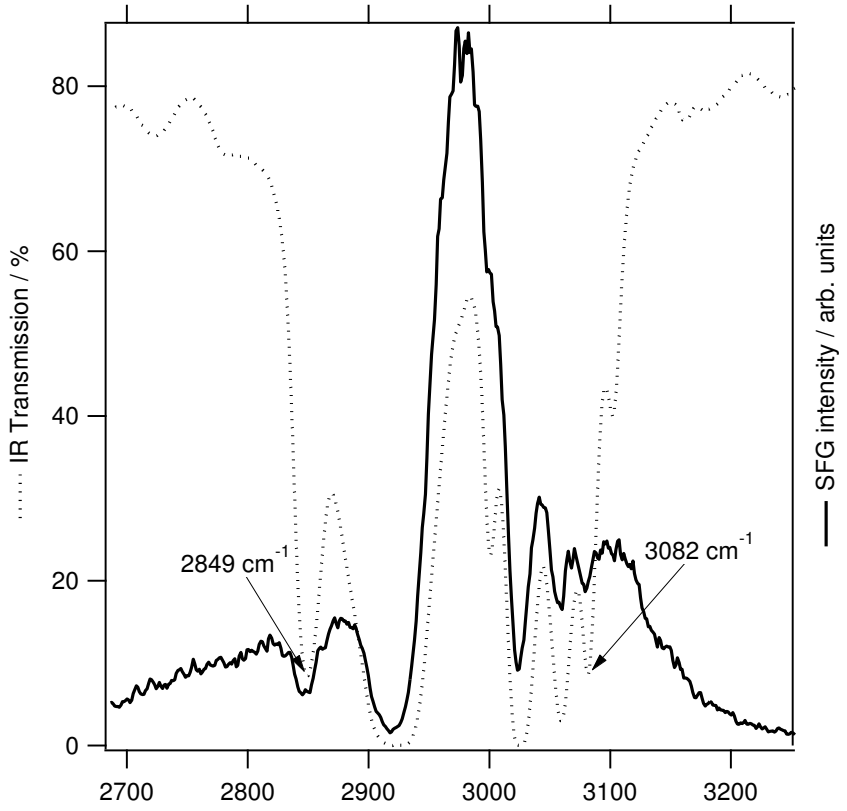

Figure 4.21. The solid black trace results from the SFG interaction of a polystyrene-transmitted broadband IR pulse with a time-stretched visible pulse on a clean gold substrate. The characteristic polystyrene absorptions were then correlated with a polystyrene IRAS reference spectrum (dotted black trace)[22] for the purposes of spectral calibration.

The two strong absorptions highlighted in Figure 4.21 were chosen for calibration which was performed manually on the spectrograph software, and notwithstanding any major setup changes the calibration remained fairly static accurate to within $\sim 3\ \mathrm{cm}^{-1}$. From this calibration technique it was discovered that the quoted IR emission wavelengths from the OPA controller software were up to 200 nm away from the measured values, due to an OPA software miscalibration.

4.5.6 System Rebuild

After initial testing and calibration, it was deemed necessary to engage in a complete system rebuild, during which many additional improvements were installed. The primary reason for the move was to minimise losses in the IR, as being the most power-limited component it was experiencing power losses after each mirror interaction. The eight protected gold mirrors with approximate reflectance of 96% at 3000 nm were reduced to two protected silver mirrors with reflectance 98% at 3000 nm, resulting in a not-insignificant increase in the IR power available for SFG mixing. Additionally, a significantly reduced pathlength of the IR beam from 4.74 - 0.37 cm meant that any IR absorption or distortion from water vapour and other species present in the laboratory air was also reduced.

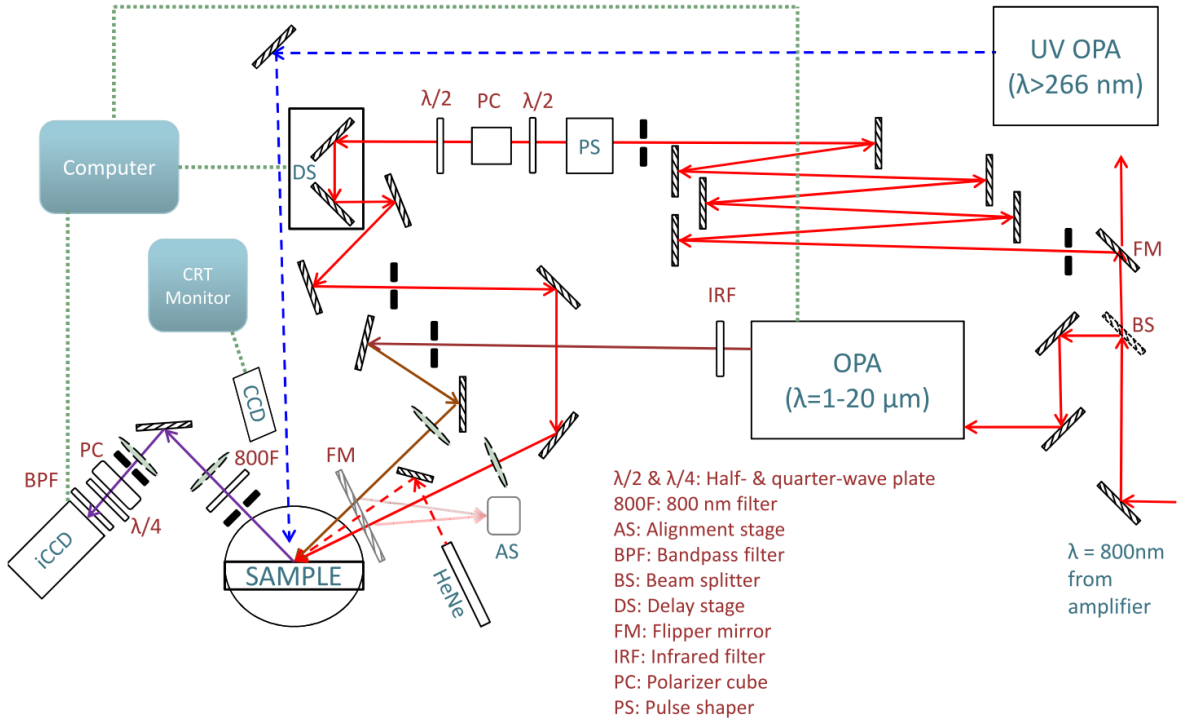

Figure 4.22. The VSFS experimental setup following a system rebuild, with key features and optics labelled.

A diagram of the updated VSFS experiment is shown in Figure 4.22, where a number of the additional elements for pulse control can be seen. In the visible path, a rotatable half-wave plate in conjunction with a polarising beamsplitter cube allows for fine control of the visible pulse power which is necessary to avoid sample damage. A second half-wave plate was installed to allow the polarisation of the visible EM wave to be rotated (see Sections 4.5.4 and 5.4.2 for more detail on polarisation control and theory). In the path of the generated SF signal an additional polariser cube selects which polarisation to pass, and a subsequent quarter-wave plate converts the linear polarised light into circularly polarised light. The cicularly polarised SFG signal effectively averages out the polarisation and negates the wavelength- and polarisation-dependence of the spectrometer grating's diffraction efficiency, which is illustrated in Figure 4.23. As can be seen from the intersection through the data, at the typical SFG wavelengths of around 0.65 µm the amount of light transmitted by the grating varies by 45% between s- and p-polarised light.

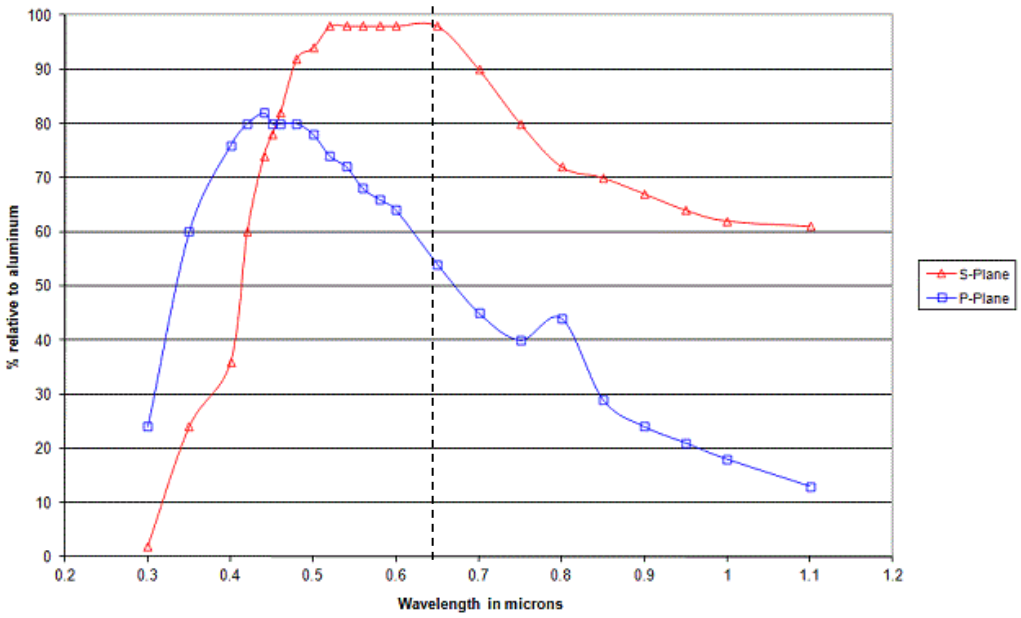

Figure 4.23. A plot showing the polarisation- and wavelength-dependence of the spectrograph grating as compared to the reflectance of an aluminium mirror.

The delay stage which was previously on the IR path and controlled by a manual micrometer screw gauge was instead installed on the visible path, and a motorised actuator drive fitted to permit finer control digitally via software. With this it became possible to perform cross-correlation measurements with an improved time-resolution (see Section 4.5.8).

Aside from several practical considerations such as an improved sample translation stage and a basic CCD camera and screen for better alignment and sample monitoring purposes, the major functional change in the setup was the introduction of a Fabry-Pérot etalon as a pulse shaper for the visible probe light.

4.5.7 Etalon Introduction

Whilst a well aligned grating pulse shaper is able to narrow a pulse's spectral bandwidth to a high degree, any inaccuracies in the alignment will have considerable pulse-broadening and distortion effects which can be difficult to rectify. This would limit the ultimate VSFS resonance bandwidth, and any distortions may induce additional spectral features which can be misinterpreted as vibrations. For this reason a Fabry-Pérot interferometer/etalon was constructed by SLS Optics for the specific wavelength of the amplifier output and installed during the system rebuild. With an internal reflectivity of 95.5% at 804 nm the air-spaced etalon is capable of transmitting a spectrally narrowed pulse over a range of ~30 nm depending on the specific tilt angle employed, and as an enclosed component will not suffer from the same alignment issues. As shown in Figure 4.24 which was taken using the USB spectrometer, the peak transmitted intensity was found experimentally to coincide with the narrowest pulse which follows a Lorentzian lineshape with a full width half maximum (FWHM) value of ~0.81 nm, giving a limiting VSFS spectral resolution of 12 cm^{-1}.

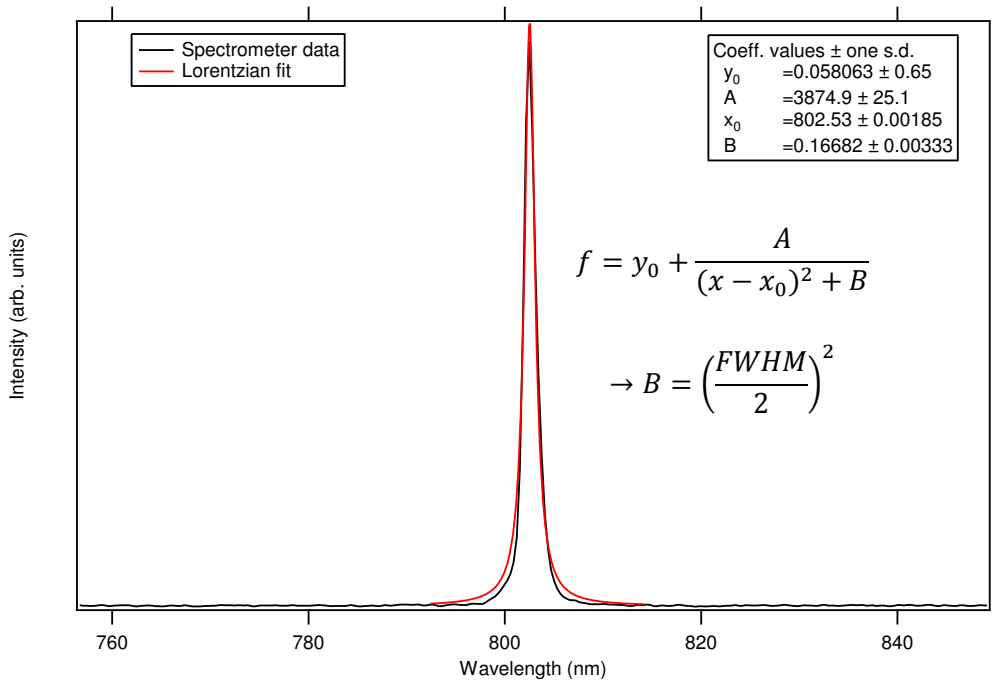

Figure 4.24. A spectrum taken of the etalon output pulse using the Avantes USB spectrometer, with a Lorentzian fit.

Background Suppression

Another advantage of using an etalon rather than grating pulse shaper deals with exploiting its time-asymmetric output pulse as reported by Dlott.[23] As seen in Figure 2.9 an etalon's output pulse is a result of multiple internal reflections and their self-interference, and if the etalon spacing is small compared to the laser pulse coherence length the temporal pulse profile has a sharp, sudden onset followed by an inverse exponential decay. SFG spectra taken in a *zero-delay* setting i.e. when the maxima of both visible and IR pulses are exactly temporally overlapped, will give the strongest overall SFG signal, but this will most often be a complex product of resonant and non-resonant components. Vibrational analysis would then require some post-processing in order to deconvolute and remove the unwanted surface response. Fortunately the time-dependent non-resonant SFG component $P^{IR}{}_{NR}(t)$ has a much shorter lifetime than induced molecular resonances $P^{IR}{}_{R}(t)$ as depicted in Figure 4.25, and if the now time-asymmetric visible pulse is set to arrive at the sample a short time after the IR pulse, the non-resonant background signal can be effectively suppressed.

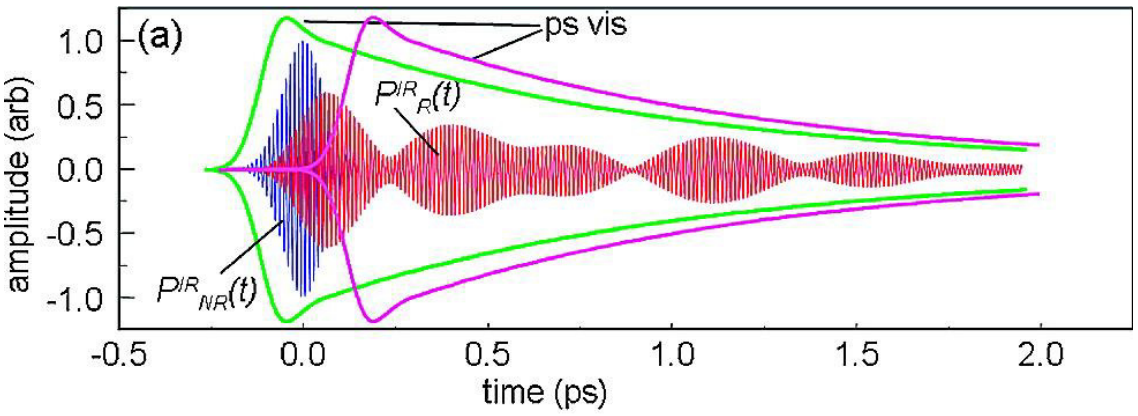

Figure 4.25. A comparison between the temporal characteristics of the resonant and non-resonant induced polarisations when performing VSFS with an etalon. The green envelope represents the temporal amplitude profile of the visible pulse at zero-delay and the pink envelope is the same with a 0.2 ps time delay. The blue non-resonant polarisation $P^{IR}_{nR}(t)$ has a much shorter decay time than the resonant polarisation $P^{IR}_{R}(t)$ (shown in red). Thus a delay on the visible pulse suppresses the non-resonant contribution to the overall detected SFG spectrum. Actual time characteristics and decay times were measured by Dlott,[23] and differ for different laser amplifiers and beam geometries.

This background (BG) suppression technique was tested using the model gold/ODT sample and initial data are shown in Figure 4.26. In the zero-delay setting, the CH resonances appear as three main dips in the NR surface response due to the ~180° phase difference between the two signals. As the delay on the visible pulse is increased the spectral shapes change until the Gaussian background diminishes and the resonances become positive features. In a confirmation of the

wavenumber calibration technique and the ability of the system to resolve molecular information, the three CH_3 features from the ODT response plotted in Figure 4.25 are consistent with those reported in the literature.[9-11, 24]

The vibrational lifetimes of the resonant and non-resonant SFG responses shown in Figure 4.25 have been reproduced from work done by Lagutchev et al.[23] and so the actual timescales are relative to their system's specific pulse durations and beam characteristics. To test the effect of a varying time-delay and ascertain an optimum delay for efficient BG suppression, scans were taken of a gold/ODT system at multiple time-delay intervals. Whilst the physical vibrational lifetimes should not differ greatly between samples in the case of an instantaneous excitation, different time profiles of the probe pulses and any spatial distortion would mean the molecules and surface are being optically excited for longer durations. The results of this experiment are summarised in Figure 4.26, where the transition from negative to positive resonant features is seen to occur suddenly between 600 fs and 800 fs.

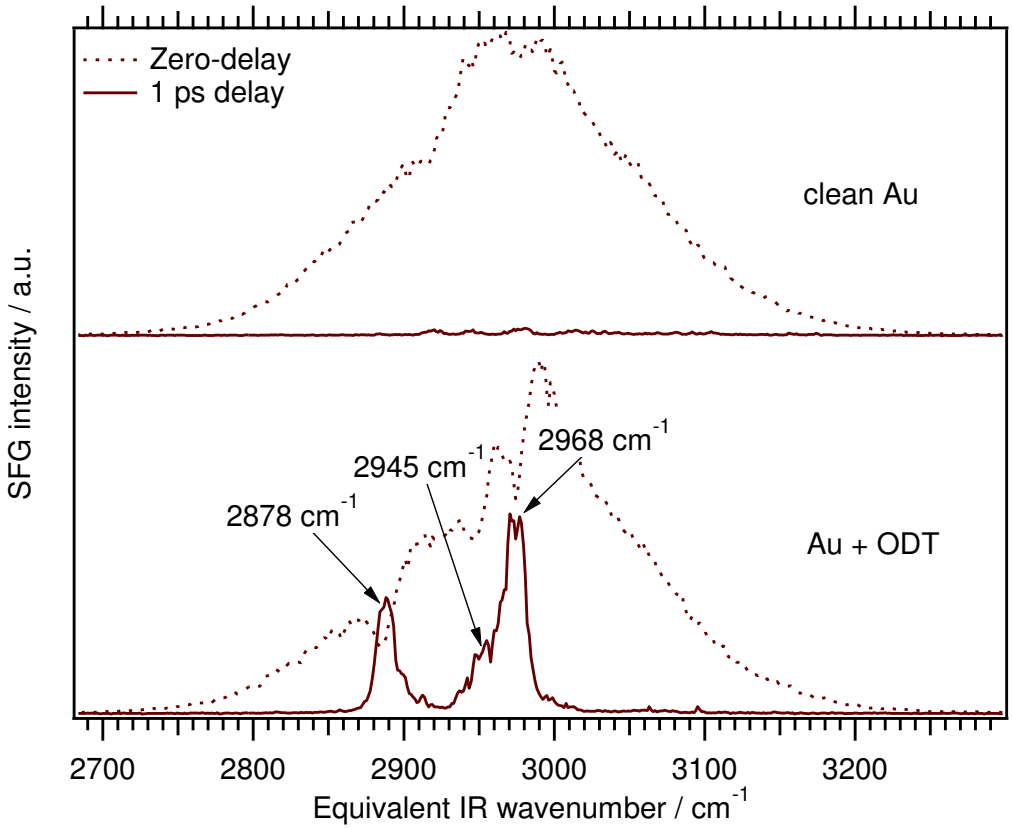

Figure 4.26. SFG spectra taken from UV-cleaned gold and gold with an ODT self-assembled monolayer, both shown with and without background suppression techniques.

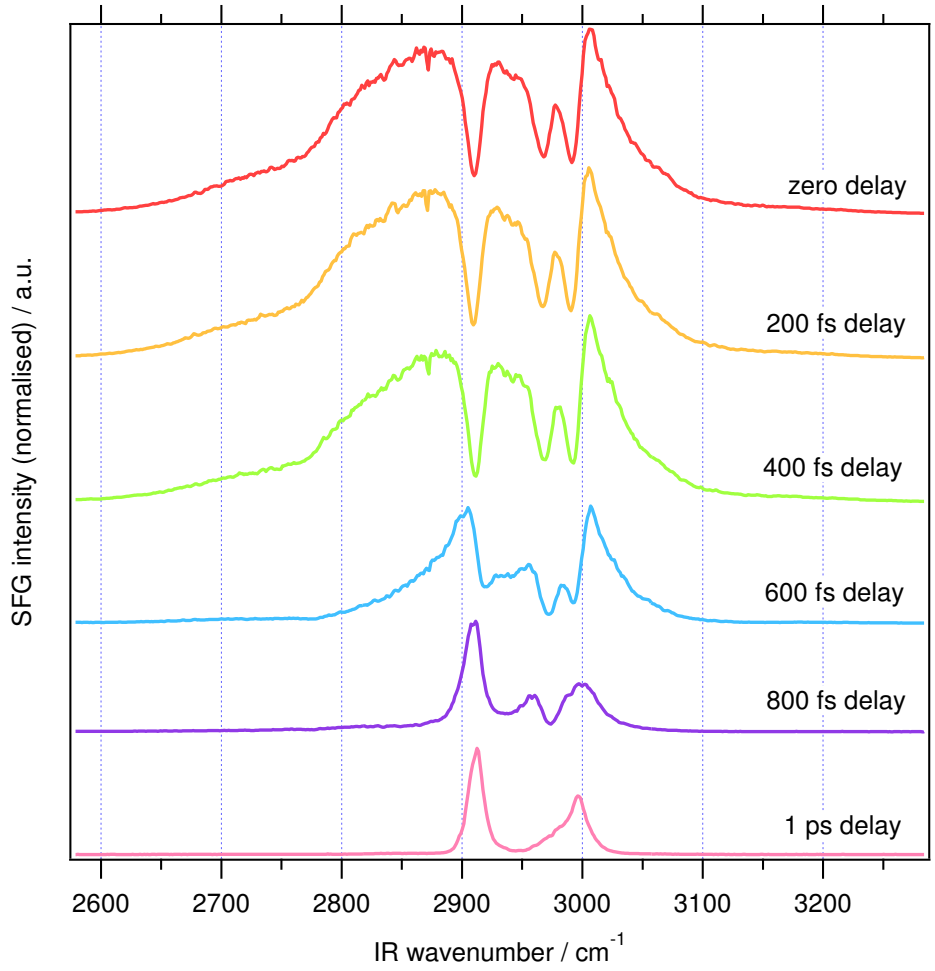

Figure 4.27. The effect of altering the visible pulse delay during VSFS measurements from an octadecanethiol self-assembled monolayer on Au(111).

The utility of this BG suppression technique allows IR transitions to be more easily identifiable, and has the added advantage of not requiring any data processing procedures meaning raw data can be published. Quantitatively there are however several disadvantages to BG suppression, the first and foremost of these being the significant reduction in signal intensity – from zero to 1 ps delay for example the maximum signal reduces to fifth of its intensity, and this is for Au/ODT where the high surface ordering generates resonant features orders of magnitude greater than in most other sample scenarios. Another disadvantage is the fact that relative peak intensities are seen to change depending on the time-delay employed, so whilst changes can be observed if a secondary parameter is varied (e.g. temperature, gas concentration, time-evolution) it is harder to develop quantitative models based on one arbitrarily set time-delay value. In addition to this molecular resonances can possess different decay times, so those with lifetimes comparable to the visible time-delay may be misrepresented or missed altogether. As an example Figure 4.27

shows the diminishing and eventual disappearance on the central CH_3 peak as a function of the time-delay. This peak is a Fermi resonance between the other two peaks and as such has a correspondingly shorter lifetime.[9]

Because of these factors it is understood that BG suppression is a valuable tool but when used its limitations should be considered. As different substrates and molecules will generate SFG signals of different relative sizes, the delay-time utilised for BG suppression should therefore be tailored for each sample under investigation. The delay chosen should enable resonances to be sufficiently prominent from the NR background, whilst maintaining as high as possible an overall signal strength for good S/N ratios over reasonable acquisition times.

4.5.8 Further Cross-correlation

The femtosecond amplifier including the seed and pump lasers is a complex multi-stage system requiring a high degree of precision in both alignment and timing parameters. Over time then it is common for alignment and timing over the various mixing stages and laser cavities to drift, resulting in a decrease in overall power and beam quality. Regular servicing is required for this and the corresponding shift in pulse characteristics and steering after each re-optimisation means it is necessary to frequently check these through auto- and cross-correlation.

With the improved utility of the actuated delay stage, a program was written in Matlab which allows for fast cross-correlation scans to be taken from a model sample surface with a high temporal resolution. Optimum acquisition parameters are first ascertained by taking an accumulation scan of the sample (typically gold or gallium arsenide) at zero-delay, and then manually scanning the delay stage in a real-time accumulation mode to evaluate the range of values over which a sum-frequency signal is generated. These parameters are transferred into the Matlab program which has been interfaced with the ICCD camera and thus can control it directly, and after a temporal step size has been decided upon the cross-correlation scan proceeds automatically. The Matlab program interface is shown in Figure 4.28 whilst Figure 4.29 shows an example cross-correlation scan of an Au/ODT system.

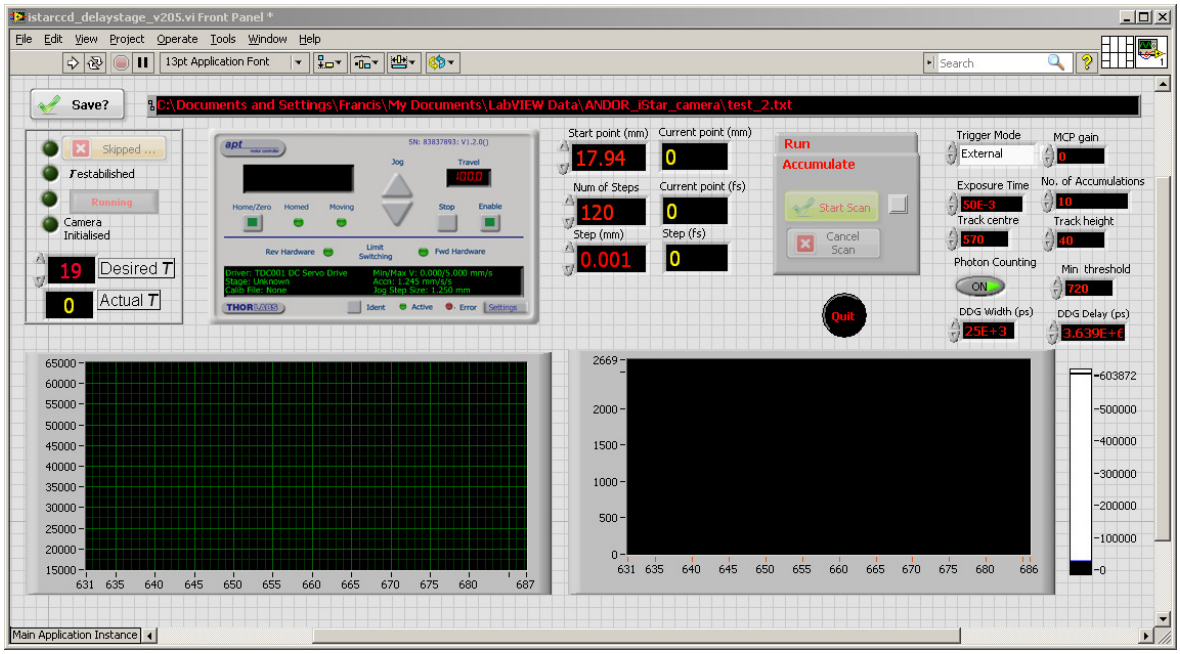

Figure 4.28. A screenshot of the Matlab program developed for fast cross-correlation measurements.

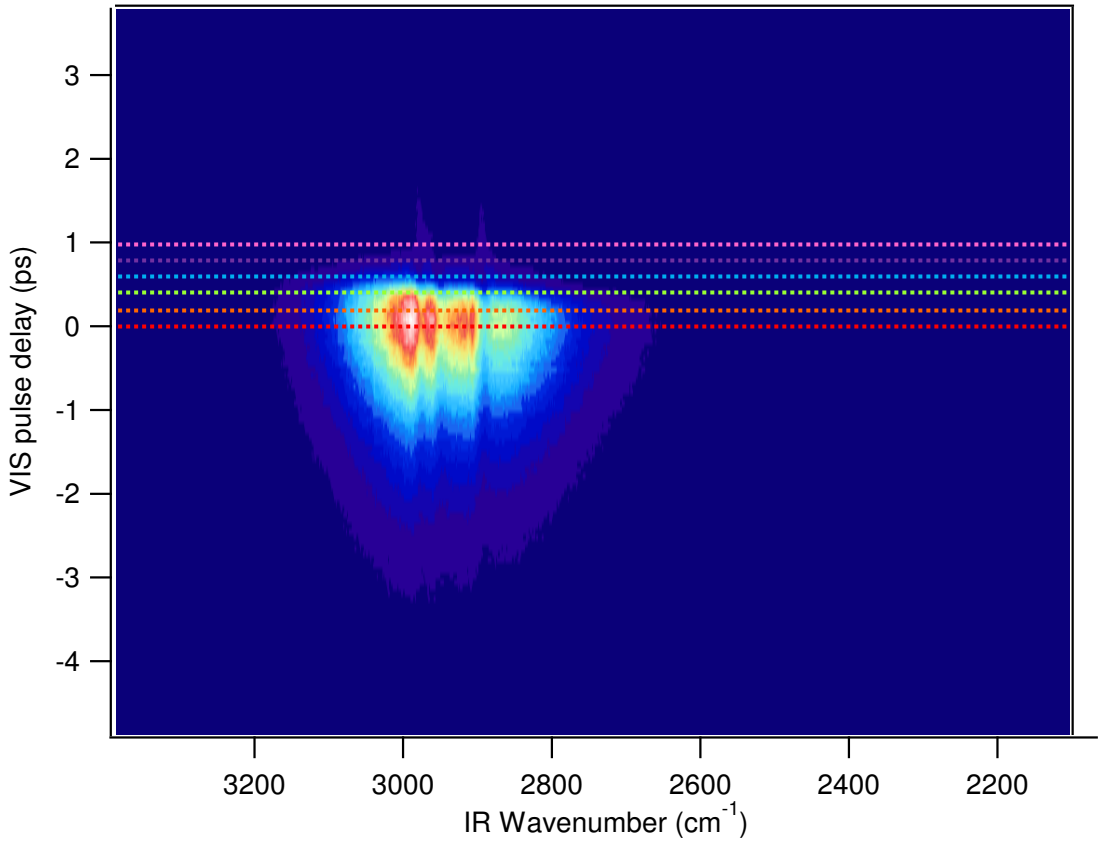

Figure 4.29. Cross-correlation plot taken off an Au/octadecanethiol sample system around the C-H stretching region. Cross-sectional spectra at each horizontal intersection can be compared directly to the varying-delay plots in Figure 4.27, with the exception that the wavenumber axis is reversed between the two.

The high resolution gold/ODT cross-correlation plot in Figure 4.29 helpfully illustrates several features and properties of the VSFS system which will be briefly discussed here. Firstly the central large SFG feature which is a result of predominantly non-resonant surface signal possesses a slight tilt, albeit to an acceptable degree. This could be a result of temporal chirp, presumably on the IR pulse as the visible was regularly investigated via auto-correlation, or alternatively spatial chirp along the pulse front combined with a pulse-front tilt would exhibit the same effects; indeed a tilted etalon will commonly result in a not insignificant pulse-front tilt.[25]

The three C-H resonances are apparent as three vertical discontinuities which are mostly subtractive due to phase effects. Fortunately the central wavenumber of each of these remains constant with varying delay time meaning the chirp would have minimal effects for any discrete delay, and this also renders spectra taken with different time delays directly comparable. The narrow spiked projections at the top of the central feature correspond to the background-suppressed signal, and the relative intensities of resonant and non-resonant spectra is well illustrated.

Compared to the cross correlation plot in Figure 4.14 which was taken with a grating pulse-shaper, there is a large temporal asymmetry in Figure 4.29 resulting from the time-stretched etalon output. The shape of this along the time axis implies both the time profile and duration of the visible pulse, which is estimated to be around 3 picoseconds. For clarity, a cross correlation plot taken off of gallium arsenide with a negligible resonant contribution is shown in Figure 4.30 which has been examined with two different time resolutions.

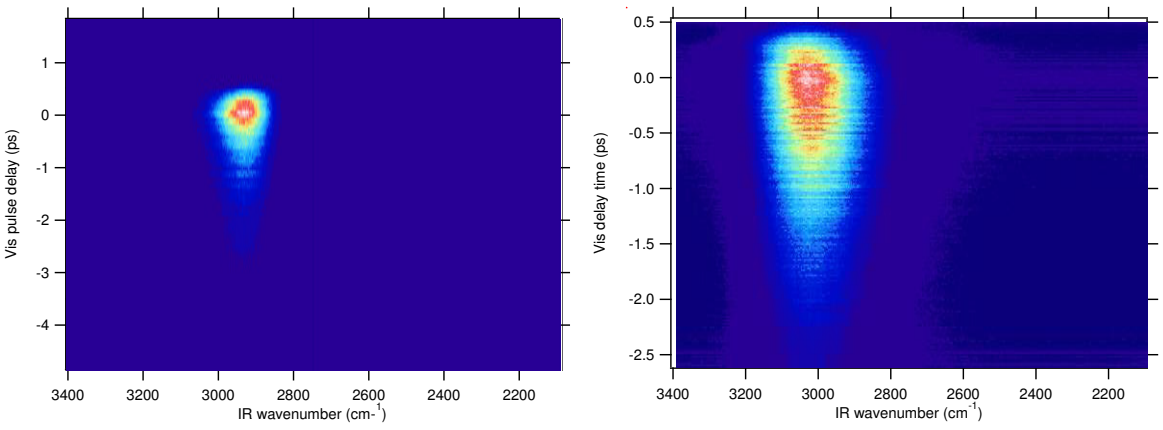

Figure 4.30. Two cross-correlation plots taken from GaAs both with a coarse (left) and finer (right) temporal resolution.

In these two figures the constancy of the central maxima for different time delays indiciates a low level of spatio-temporal or chromatic distortion. It should be noted that zero-delay here has been defined at the maximum SFG intensity, whereas in actuality due to the sharp temporal onset of the etalon output and the response time of the surface the two pulse maxima (visible and IR) are coincident a few hundred femtoseconds prior to this.

4.5.9 Sample Cell efficiency issues

The sum-frequency generation efficiency for any given sample is a function of probe pulse incidence angles, as well as the polarisation of the incoming light.[26] The theory has been described elsewhere and will be examined in further detail in Chapter 5 but essentially involves an examination of electric fields over interfaces and the nature of the polarisations they induce.[27] With foreknowledge of the wavelengths involved and the refractive indices of the materials on either side of the interface, optimum incidence angles can be calculated using the Fresnel equations.[18] Initially, the incidence angles chosen for the visible and IR beams were set at common intermediate values (~50-60°) which will illicit an SFG response from most metals in-air – these values were ascertained from similar experiments in the literature. [28-30]

Optimum angles for the TiO_2 substrate were later calculated (see Section 5.X) and set in the experiment design, but SF generation efficiency issues were encountered through the necessary introduction of a windowed sample cell for gas-dosing experiments. The initial sample cell design used a CaF_2 window which was oriented parallel to the sample, and ignoring any minor refraction effects, a significant amount of the incident light could be lost due to reflection off the window faces.

The reflectivity of an EM wave incident on a dielectric material is also governed by the Fresnel equations and thus also dependent on the refractive indices, incidence angles and light polarisation. These reflectivities, when plotted, tend to follow a characteristic shape as illustrated in Figure 4.31.[18] Variations in the relative refractive indices alter the slope gradient and points of intersection but the overall relationships still tend to follow the same shape. As the non-complex refractive index of CaF2 is n~1.45 at visible wavelengths and the laboratory air has n~1, the plot in Figure 4.31 with $n = 1.5$ is fairly representative. Whilst light incident at the Brewster angle would be fully transmitted through the window, the internal angle change due to refraction can mean that a significant portion of the light is reflected off the window's inside face. Also Brewster angle transmission only applies to p-polarised light.

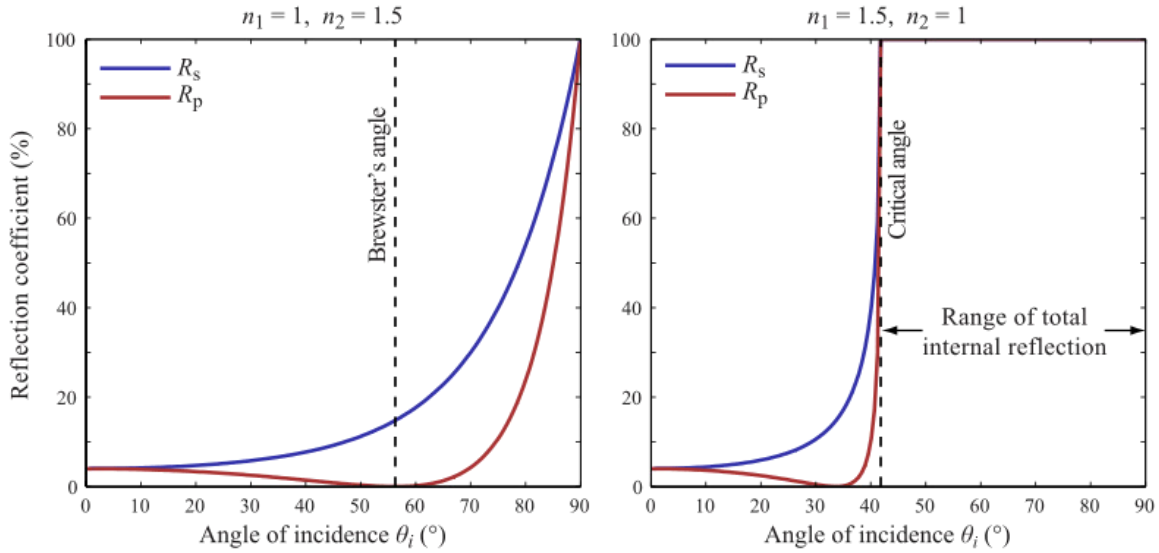

Figure 4.31. Plots of reflection versus incidence angle for an EM wave passing between materials with refractive indices of n=1 and n=1.5. Red and blue plots are for p-polarised and s-polarised light respectively.

To remove the discrepancies between s- and p-polarisations, the cell window was replaced with a CaF_2 prism (see Fig 4.33) which allowed external incidence angles to be close to 0°. Due to large refraction effects the plot in Figure 4.32 was created to relate incidence angles relative to the sample normal both before and after window interaction for common wavelengths of interest. The VSFS layout was altered to allow for the lower necessary external angles, and detected SFG signal intensities were seen to increase immediately after installation and realignment by a factor of roughly 20%.

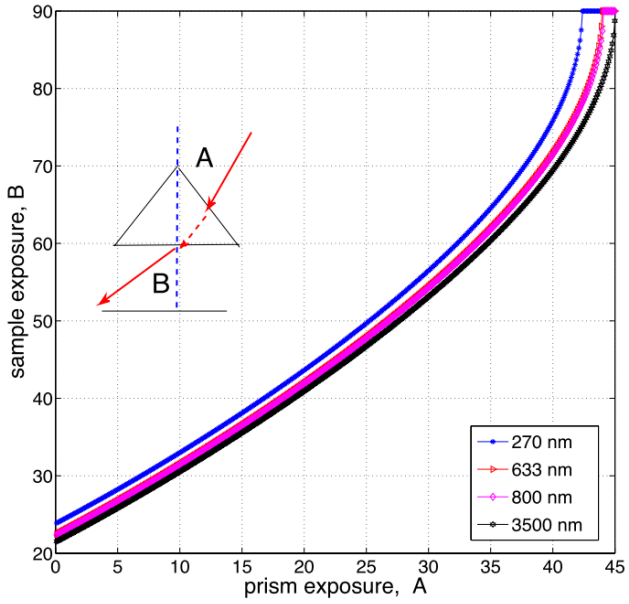

Figure 4.32. The relationship between input and transmission incidence angles for light passing from air through a 45° right-angled CaF_2 prism.

The original plane window cell and prism cell are both shown for reference in Figure 4.33, and the prism cell in particular will be presented further in the following chapter.

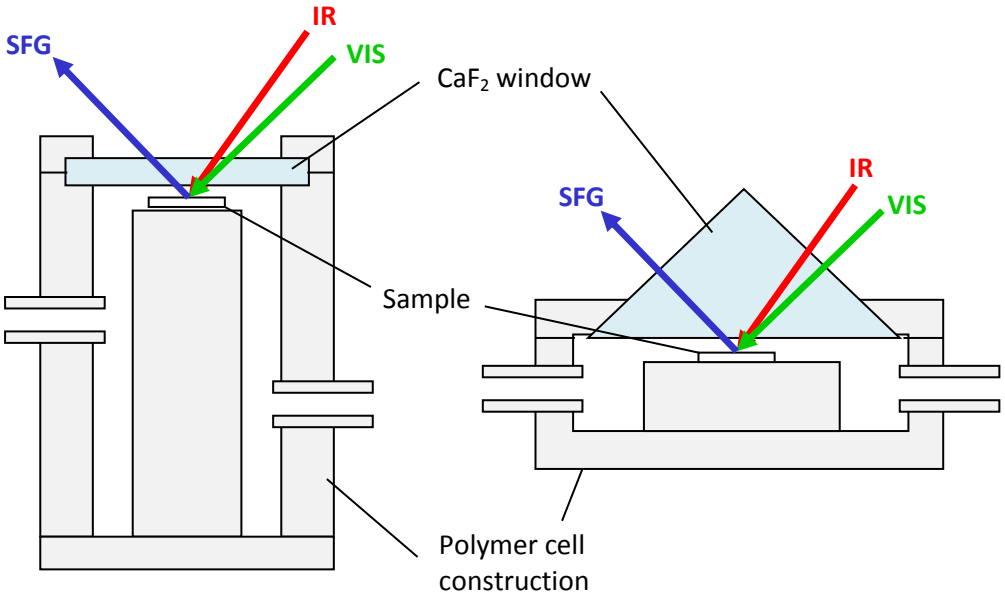

Figure 4.33. Cross sections showing the designs of the two sample cells utilised for vapour dosing experiments. The near-normal incidence of the IR and VIS beams on the outside face of the prism act to reduce back-reflection and power losses according to Figure 4.31.

4.6 References

1. Arnolds H, King DA, Lane IM. Inducing non-adiabatic effects through coadsorption: CO+NO on iridium. *Chemical Physics*. 2008; **350:** 94-103.
2. Nikogosyan D. Beta barium borate (BBO). *Applied Physics A*. 1991; **52:** 359-68.
3. Baudrier-Raybaut M, Haidar R, Kupecek P, Lemasson P, Rosencher E. Random quasi-phase-matching in bulk polycrystalline isotropic nonlinear materials. *Nature*. 2004; **432:** 374-6.
4. Ross I. Optical Parametric Amplification Techniques. In: Brabec T (ed). *Strong Field Laser Physics*. Vol. 134: Springer New York, 2009. 35-59.
5. Reader J. Optimizing Czerny-Turner spectrographs: a comparison between analytic theory and ray tracing. *JOSA*. 1969; **59:** 1189-94.
6. Koschuetzke O. ICCD Detectors - course notes. *http://www.lot-qd.de/files/downloads/andor/en/cc_notesiccd_deen.pdf* (2003). (Accessed 5th June 2013.)
7. Blakemore J. Semiconducting and other major properties of gallium arsenide. *Journal of Applied Physics*. 1982; **53:** R123-R81.
8. Barth J, Brune H, Ertl G, Behm R. Scanning tunneling microscopy observations on the reconstructed Au (111) surface: Atomic structure, long-range superstructure, rotational domains, and surface defects. *Physical Review B*. 1990; **42:** 9307.
9. Richter LJ, Petralli-Mallow TP, Stephenson JC. Vibrationally resolved sum-frequency generation with broad-bandwidth infrared pulses. *Optics Letters*. 1998; **23:** 1594-6.
10. Yeganeh M, Dougal S, Polizzotti R, Rabinowitz P. Interfacial atomic structure of a self-assembled alkyl thiol monolayer/Au (111): A sum-frequency generation study. *Physical review letters*. 1995; **74:** 1811.
11. Bain CD, Davies PB, Ong TH, Ward RN, Brown MA. QUANTITATIVE-ANALYSIS OF MONOLAYER COMPOSITION BY SUM-FREQUENCY VIBRATIONAL SPECTROSCOPY. *Langmuir*. 1991; **7:** 1563-6.
12. Raval R. Probing the nature of molecular chemisorption using RAIRS. *Surface science*. 1995; **331:** 1-10.
13. Rey NG. Interaction of a Copper Surface with Light: Plasmons, Electrons & Molecular Vibrations. *Department of Chemistry*. Vol. Doctor of Philosophy Surface Science Research Centre: University of Liverpool, 2011.
14. Dudley JM, Gu X, Xu L, Kimmel M, Zeek E, O'Shea P, Trebino R, Coen S, Windeler RS. Cross-correlation frequency resolved optical gating analysis of broadband continuum generation in photonic crystal fiber: simulations and experiments. *Opt. Express*. 2002; **10:** 1215-21.
15. Trebino R, *FROG*. 2000: Springer.
16. Trebino R, DeLong KW, Fittinghoff DN, Sweetser JN, Krumbugel MA, Richman BA, Kane DJ. Measuring ultrashort laser pulses in the time-frequency domain using frequency-resolved optical gating. *Review of Scientific Instruments*. 1997; **68:** 3277-95.
17. Arnolds H, Symonds JPR, Zhang VL, King DA. In situ characterization of ultrafast laser pulses for sum frequency surface studies. *Review of Scientific Instruments*. 2003; **74:** 3943-6.
18. Born M, Wolf E, *Principles of optics: electromagnetic theory of propagation, interference and diffraction of light*. 1999: CUP Archive.
19. Lerner JM, Thevenon A. Optics of Spectroscopy Tutorial Guide (website). *http://www.horiba.com/uk/scientific/products/optics-tutorial/* (2003). (Accessed 24th July 2013.)
20. Xu X-z, Li Z-t, Xue L-j. Analysis and processing of CCD noise. *Infrared and Laser Engineering*. 2004; **33:** 343-6.
21. Widenhorn R, Blouke MM, Weber A, Rest A, Bodegom E. Temperature dependence of dark current in a CCD. *Electronic Imaging 2002*: International Society for Optics and Photonics, 2002. 193-201.

22. Linstrom PJ, Mallard WGE. NIST Chemistry webbook; NIST standard reference database No. 69. 2001.
23. Lagutchev A, Lozano A, Mukherjee P, Hambir SA, Dlott DD. Compact broadband vibrational sum-frequency generation spectrometer with nonresonant suppression. *Spectrochimica Acta Part a-Molecular and Biomolecular Spectroscopy*. 2010; **75:** 1289-96.
24. Tanaka Y, Lin S, Aono M, Suzuki T. Sum-frequency vibrational spectroscopy of a monolayer self-assembled on gold: interference between resonant and nonresonant contributions of nonlinear polarization. *Applied Physics B: Lasers and Optics*. 1999; **68:** 713-8.
25. Bowlan P, Trebino R. Extreme pulse-front tilt from an etalon. *Journal of the Optical Society of America B-Optical Physics*. 2010; **27:** 2322-7.
26. Lambert A, Davies P, Neivandt D. Implementing the theory of sum frequency generation vibrational spectroscopy: A tutorial review. *Applied Spectroscopy Reviews*. 2005; **40:** 103-45.
27. Shen Y-R. The principles of nonlinear optics. *New York, Wiley-Interscience, 1984, 575 p.* 1984; **1**.
28. Noguchi H, Okada T, Uosaki K. SFG study on potential-dependent structure of water at Pt electrode/electrolyte solution interface. *Electrochimica Acta*. 2008; **53:** 6841-4.
29. Ye S, Osawa M. Molecular Structures on Solid Substrates Probed by Sum Frequency Generation (SFG) Vibration Spectroscopy. *Chemistry Letters*. 2009; **38:** 386-91.
30. Verreault D, Kurz V, Howell C, Koelsch P. Sample cells for probing solid/liquid interfaces with broadband sum-frequency-generation spectroscopy. *Review of Scientific Instruments*. 2010; **81:** 10
31. Holroyd C. 1st Year PhD Progress Report (via personal communication). 2013

Chapter 5. TiO_2-adsorbate Systems Studied via VSFS

5.1. Introduction

Titanium dioxide (TiO_2) is a technologically significant metallic oxide material. Due to its relative availability and low cost the rutile form is commonly used as a substrate for fundamental studies into metal oxide surface behaviour.[1] In addition, the crystal is a direct band gap material and as such is photoactive, meaning TiO_2 is also frequently investigated in relation to industrial applications involving e.g. catalysis and light energy conversion.[2] Whilst some work has been done previously involving SFG techniques with TiO_2 surfaces,[3-7] the following chapter will explore the application of VSFS to TiO_2 adsorbate systems, including the development of a novel in-air surface preparation and cleaning method and investigation into the adsorption of some simple organic molecules. Combined with parallel experimental work performed at the University of Houston, this investigation will also help to confirm the efficacy of the Manchester setup relative to other SFG systems.

5.2. Titanium Dioxide Background

In nature, TiO_2 is most commonly found in the rutile crystal conformation, which possesses the body-centred tetragonal unit cell shown in Figure 5.1a). Two other major polymorphs are known to exist naturally, anatase and brookite.[8] The rutile phase itself possesses a high degree of structural and chemical stability and, like its analogues, exhibits several physical properties which heavily influence its scientific and industrial application.

5.2.1. Applications

A key characteristic of TiO_2 is that it is a wide band gap semiconductor, and illumination with a photon of sufficient energy ($\gtrsim$ 3 eV depending on phase, doping and local chemical environment) may create an electron-hole pair or exciton.[9] If this migrates to the surface, it has the potential to react with any surface adsorbates, creating radical species via photocatalysis or generating transferrable charge. For this reason TiO_2 has been researched heavily with regards to application in the fields of fuel cells,[10] organic contaminant removal (e.g. self-cleaning windows or system sterilisation)[11], gas sensing and light-energy conversion, although in the latter dye molecules are often required to overcome the relatively low conversion efficiencies in the visible region of the electromagnetic spectrum.[12]

In addition to photoactivity, TiO_2 in all its forms has a particularly high refractive index, and coupled with its low relative cost and high availability this makes it an attractive material for use in visual/optical applications. It is used extensively as a pigment in everything from paints to foodstuffs,[13] and more recently has been utilised in optical coatings for mirrors, filters, and lenses.[9] At this point it is useful to note that the asymmetry in crystal structure of all TiO_2 polymorphs leads to it possessing birefringence; different refractive indices are experienced subject to the direction of radiation propagation relative to the crystal axes, thus light will interact with the material differently depending on its orientation.

5.2.2. Crystal Structure and Chemistry

Due to its high number of applications, TiO_2 is one of the best studied and characterised metal oxides, and the high level of interest and understanding encourages a feedback mechanism whereby it becomes a highly favourable system for any fundamental studies into metal oxides and metal oxide surfaces. The most studied TiO_2 crystal surface is the rutile TiO_2(110) interface illustrated in Figure 5.1b), and this is one that will be primarily investigated in this research.

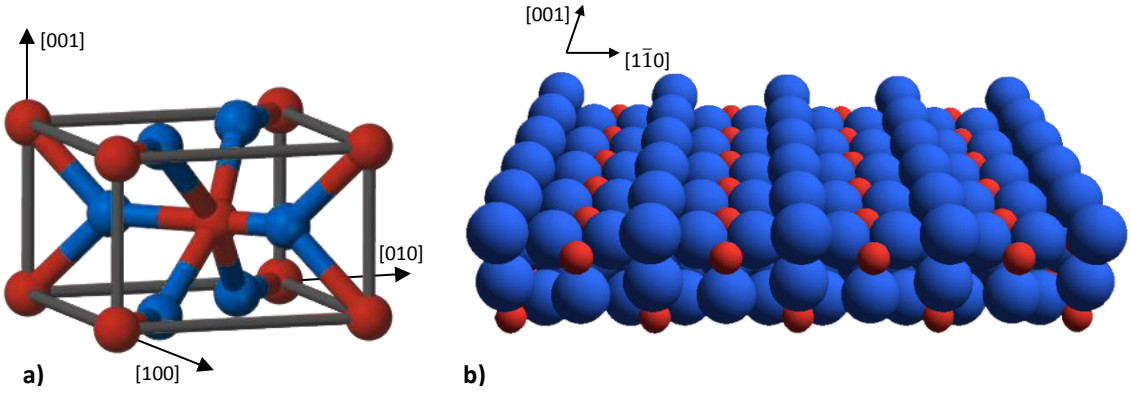

Figure 5.1. Rutile TiO_2 represented by a) a ball-and-stick depiction of its standard crystalline unit cell and b) a space-filling model of the rutile (110) surface, both with crystallographic axes labelled. Red and blue indicate titanium and oxygen atoms respectively.

In bulk rutile, the basic arrangement is a repeating pattern consisting of a titanium atom surrounded by six oxygen atoms, as illustrated by the unit cell in Figure 5.1a). This structure stacks to form the bulk crystalline structure, in which each oxygen atom is bonded to three titanium atoms; the oxygen is said to possess threefold coordination. As mentioned, the rutile (110) surface has been studied extensively via theoretical and experimental means, and the (1×1) termination shown in Figure 5.1b) – with fivefold coordinated surface Ti atoms and protruding rows of 'bridging oxygens' possessing twofold coordination – is thought to most closely resemble the surface structure exhibited by rutile (110) prepared via standard laboratory techniques.[14] The (1×1) termination has been predicted to be the most thermodynamically

stable scenario by Density Functional Theory (DFT) calculations, and examination of the surface structure with scanning probe microscopy and X-ray/electron scattering and diffraction techniques confirm this.[15, 16]

The reason for the wide body of literature examining the crystallographic surface structure is the large extent to which this influences surface chemistry. For example, defects such as atomic vacancies or substitutions are common and the local variations in oxidation states may act to preferentially promote or deter molecular surface interactions.[1] Bulk defects may also act to affect surface chemistry if they are sufficient enough to alter the electronic structure at the surface. On a larger scale, unless the extended surface under investigation is atomically flat with respect to the crystal face, there will necessarily be discontinuities at the 'step points' between atomic terraces. These discontinuities will result in atoms with differing coordination and thus 'free bonds,' giving rise to areas of the surface of lower or higher surface energy.[17] A model of a monatomic step on the rutile (110) surface is shown in Figure 5.2, and will be imaged via AFM in Section 5.3.2.

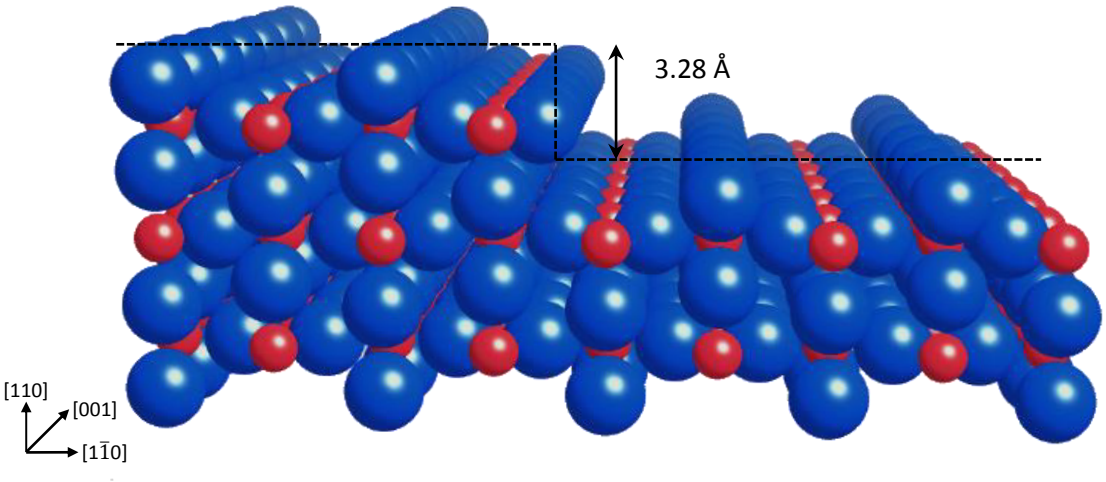

Figure 5.2. A space-filling model of the predicted atomic step seen on the TiO_2(110) surface, with crystal axes and step height indicated.

These various factors have been shown to have notable macroscopic effects during fundamental studies on single crystal substrates (chemical reactivity or wetting behaviour for example),[1] and whilst real-world systems would be further complicated by the presence of significant surface contamination and complex polycrystalline topographies, for such fundamental investigations this serves to illustrate the importance of a well prepared and characterised model substrate.

5.3. TiO_2(110) Surface Preparation

5.3.1. Ultra High Vacuum (UHV) Regime

For pure fundamental surface analysis of metals and their oxides samples are commonly prepared and examined under controlled UHV conditions; high resolution surface measurement techniques such as Scanning Tunnelling Microscopy (STM) and those involving electron/ion emission or diffraction require a vacuum to avoid complications arising from gas-phase molecular interactions (although low-vacuum and in air analogues have made promising developments).[18] Such conditions allow for much greater control over experimental variables and thus permit more fundamental characterisation, but difficulties may arise when attempting to apply these findings to vastly more complex real-world scenarios.

Standard UHV preparation techniques for creating flat, well-ordered crystal substrates free from contamination and are regularly adopted for surface studies into TiO_2(110). Depending on the exact history of the sample under investigation, various cleaving, etching, or polishing procedures may be employed prior to situating in a vacuum chamber and 'pumping down' to high vacuum conditions. Once a sufficient vacuum is achieved the substrate, either in the main chamber or an adjoining sample preparation chamber, is subjected to alternating cycles of high temperature annealing and sputtering with high energy ions (typically Argon). Bombarding the surface with chemically inert atoms at a high energy imparts enough energy to the surface atoms to allow them to be removed according to momentum conservation. Subsequent annealing with a heating element, provided it is at the correct temperature for the substrate material, will give the surface atoms some mobility, and upon cooling they will have reordered into their preferred lowest energy configuration. The temperatures utilised for successful ordering of TiO_2(110) via this method vary between research groups but are typically between 900-1100 K.[19-21]

TiO_2(110) prepared with standard UHV techniques has been shown to result in a (1×1) ordered surface termination, although annealing without oxygen will easily reduce (remove oxygen from) both surface and bulk, altering the crystal's electronic and optical properties e.g. eventually resulting in a (1×2) termination.[22] Similarly, ion bombardment has been shown to reduce the surface oxygen prevalence.[9] For certain analysis techniques bulk reduced TiO_2(110) is advantageous as it increases conductivity and thus prevents charging (this is an additional reason TiO_2 is the standard for fundamental metal oxide research), but a reduced surface with its associated oxygen vacancies will affect surface chemistry so should be characterised and accounted for in any development of scientific models.

5.3.2. Non-UHV Wet Chemical Regime

Introduction

Whilst it is possible to perform VSFS measurements on samples in vacuum provided appropriate chamber window materials are employed, at present the VSFS setup implemented by this author is optimised for in-air or gas flow cell-based operation. Rather than using UHV-prepared samples for in-air experiments it was decided that non-UHV wet chemical techniques would be explored as a more representative and accessible alternative for fundamental surface investigation – surface science as a whole is becoming increasingly interested in more complex systems that more closely approximate real-world environments.[23]

Non-UHV preparation of TiO_2(110) has been reported by several publications, most of which involve a combination of in-air annealing and wet chemical cleaning procedures.[24-26] Following on from previous work performed in the Corrosion and Protection Centre in Manchester,[27] a novel wet chemical TiO_2 preparation technique has been developed and characterised by several complementary surface techniques. Notably, this procedure negates the use of the particularly toxic hydrofluoric acid (HF) as the primary cleaning agent, which is otherwise employed in the majority of similar preparation regimes.

Methodology

The preparation of a contaminant-free, flat, and well-ordered rutile (110) crystal is achieved via a four stage process, as illustrated in Figure 5.3. The TiO_2 crystal substrates (PI-KEM Ltd, Staffordshire UK) measure $10 \times 10 \times 1$ mm and have been cut $\leq 1°$ from the (110) crystal face, before being EPI-polished to a high degree of surface flatness. The as-received samples were initially examined via AFM. Topologically, the surfaces exhibited no consistent small-scale surface ordering with variations in height of the order of 300-400 nm.

The first stage of the preparation procedure involves three consecutive 15 minute sonication cycles where the crystal sample is immersed first in acetone, then ethanol, and finally in deionised water. This stage will clean from the surface any macroscopic dirt or contaminants, as well as hydrocarbon contaminants such as oils or grease. After the final sonication in deionised water the samples are removed and dried under a nitrogen stream.

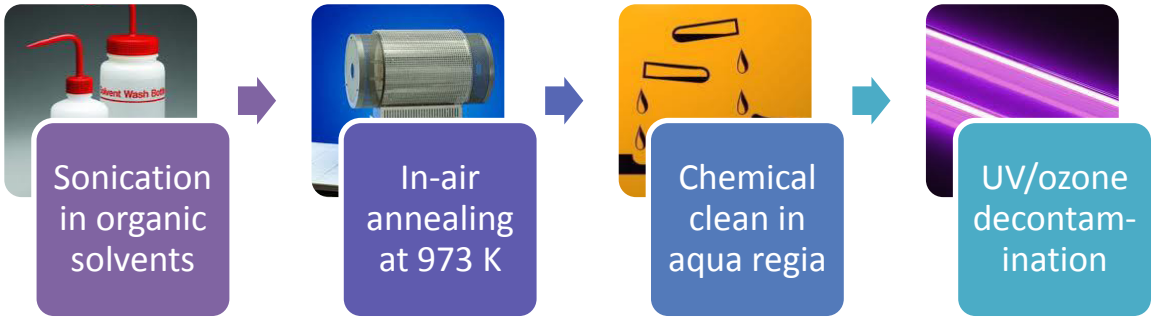

Figure 5.3. A basic flowchart illustrating the four stages involved in the TiO_2(110) non-UHV preparation procedure.

The second step is the annealing stage where the samples are placed in an alumina sample boat and heated in a furnace at 973 K (700°C) for a period of ~ 90 minutes. To avoid issues with rapid thermal expansion or contraction, the sample boat is present in the furnace for the warming and cooling periods also, which for a small tube furnace is between 15-45 minutes each; for larger furnaces this time can be much longer. As in the UHV preparation technique, this step gives the atoms at the surface of the crystal sufficient mobility to allow them to reorder into a preferential configuration.

The third step is a chemical clean in concentrated aqua regia to dissociate and remove metallic and organic surface contaminants either missed by the sonication stage or introduced during annealing. The annealed substrate, once cooled, is submerged in a concentrated solution of the acidic reagent 'aqua regia' which is a 3:1 mix of hydrochloric and nitric acids. Either acid is capable of breaking down all but the most stable of compounds, but when used in combination the two molecules interact and can facilitate the dissolution of precious metals. After immersion samples are thoroughly rinsed in deionised water and again dried in a nitrogen stream.

The final step involves the use of a UV/ozone decontamination unit (Novascan Technologies, Indiana USA). Samples placed in this enclosed unit are exposed to a high intensity ultraviolet light source, which has the dual effect of exciting organic molecules on the substrate surface and generating ozone (O_3) from the splitting of diatomic oxygen in the gas phase, which reacts with and removes the surface organics. As a minimum, samples were irradiated under the UV source for 15 minutes, and then left to react with the generated ozone for a further 30 minutes. For surfaces found to be particularly carbonaceous (through VSFS, Auger or XPS techniques), ozone in the UV chamber is vented with fresh laboratory air and the whole 45 minute cycle repeated.

Atomic Force Microscopy Results & Discussion

The particular methodology outlined in the previous section was arrived at empirically. The annealing stage was investigated at various temperatures and over several time durations; 90 minutes at 973 K was found to give the best surface images via AFM. A well-ordered TiO_2(110) surface scan is shown in Figure 5.4a), where the characteristic step-and-terrace structure is apparent. These terraces, analysed further in Fig 5.5, are ~ 50-300 µm wide depending on the exact angle the crystal has been cut at relative to the (110) plane, with straight edges and step heights of ~ 0.3 nm consistent with the monatomic step edges predicted theoretically[28] and illustrated in Figure 5.2. At temperatures 50-100 K either side of this value, the surface ordering becomes distorted: terrace widths become less consistent and step edges significantly less straight as seen in Figure 5.4b).

As for annealing durations, less than 90 minutes was found to be insufficient for complete surface reordering, and durations over 90 minutes were found to achieve no additional improvement on ordering effects. The history of the sample does play a role however, with previously unprepared substrates benefitting from slightly longer annealing durations, and recently prepared substrates maintaining their surface ordering and thus requiring shorter re-annealing times – whilst non-systematic in terms of sample reproducibility some results suggest the re-annealing of a previously non-UHV prepared sample can be skipped altogether.

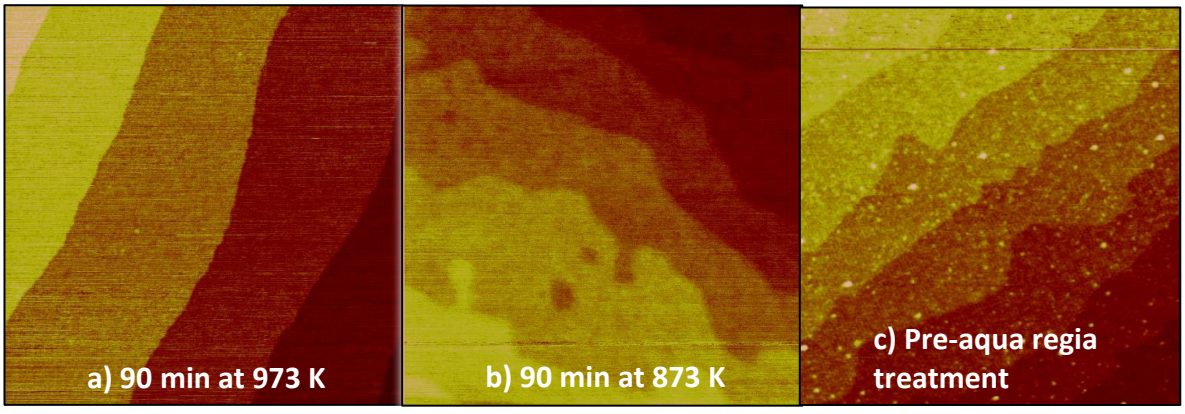

Figure 5.4. AFM images of rutile (110) showing the effects of annealing and chemical cleaning. All scans are 1×1 µm, and a) and b) have been acquired post immersion in aqua regia.

The AFM images in Figure 5.4 a) and b) look to be entirely free of additional atomic-scale features but occasionally spots, mounds or a 'pockling' effect were identified in the surface topography as evidenced in Fig 5.4c). These features changed size and distribution under further annealing, but were effectively removed after immersion in the concentrated aqua regia. As such, these were

attributed to metallic surface contaminants, although they were not a cause for concern as their removal further confirmed the efficacy of the chemical cleaning step.

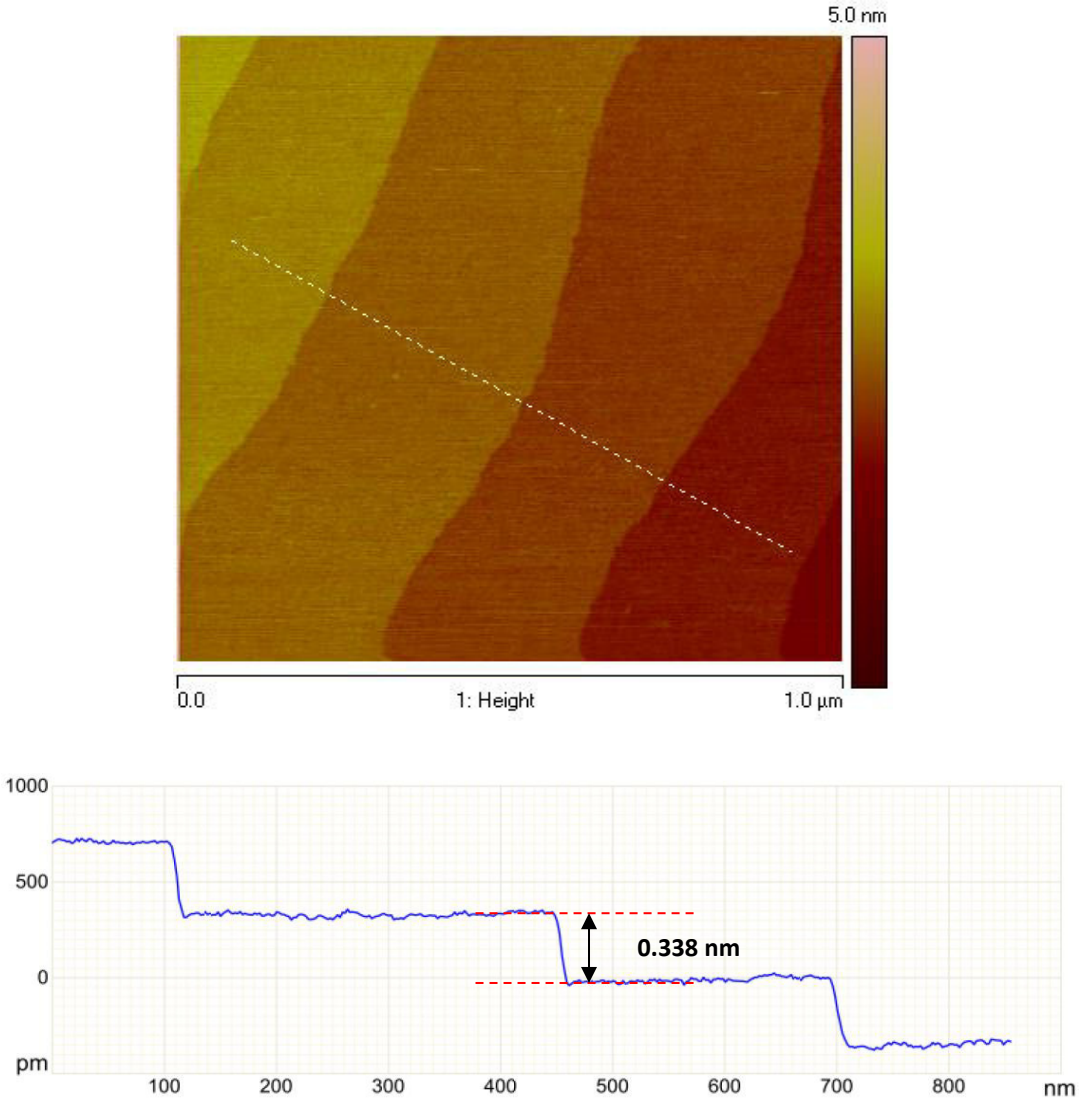

Figure 5.5. Cross-sectional AFM analysis of non-UHV prepared TiO_2(110). The cross sectional profile at the bottom of the figure corresponds to the white dashed line on the AFM image, and the calculated step height is indicated. This step height agrees well with the atomic step illustrated in Fig 5.2.

XPS Results & Discussion

Variations on the wet chemical technique were applied to rutile (110) samples which were subsequently examined via XPS (Kratos Axis Ultra). Several such wide scans (spectra covering a wide range of electron kinetic energies) are shown in Figure 5.6 which illustrates the effects of the aqua regia cleaning treatment. Emission peaks were identified belonging to titanium and oxygen, and carbon peaks from samples exposed to air are omnipresent in XPS due to the ubiquitous deposition of atmospheric carbon/organics. A small potassium peak is seen on any TiO_2 sample which has been annealed and has not undergone aqua regia treatment; this has been ascribed to surface segregation of trace amounts of potassium present in the bulk (from the crystal manufacture process) due to thermal diffusion.[29] Traces of molybdenum were also identified which, like the potassium, were seen to disappear after acid immersion – the presence of the relatively uncommon Mo was a cause for concern but was later identified as having originated from metallic contamination in the standard furnace used; all subsequent annealing was performed in a tube furnace with a dedicated quartz tube, and Auger spectra acquired by other members of the research group subsequent to this change detected no further Mo photoemission. Importantly, no emission peaks are present that would indicate chlorine or nitrogen left over from the aqua regia treatment.

Additional high resolution XPS spectra were also acquired from the rutile substrates to which peak-fitting procedures have been applied. These will be presented in further detail in Section 5.3.3, which will include contact angle and VSFS measurements to help characterise the nature of the adventitious carbon overlayer and its interaction with the UV cleaning process.

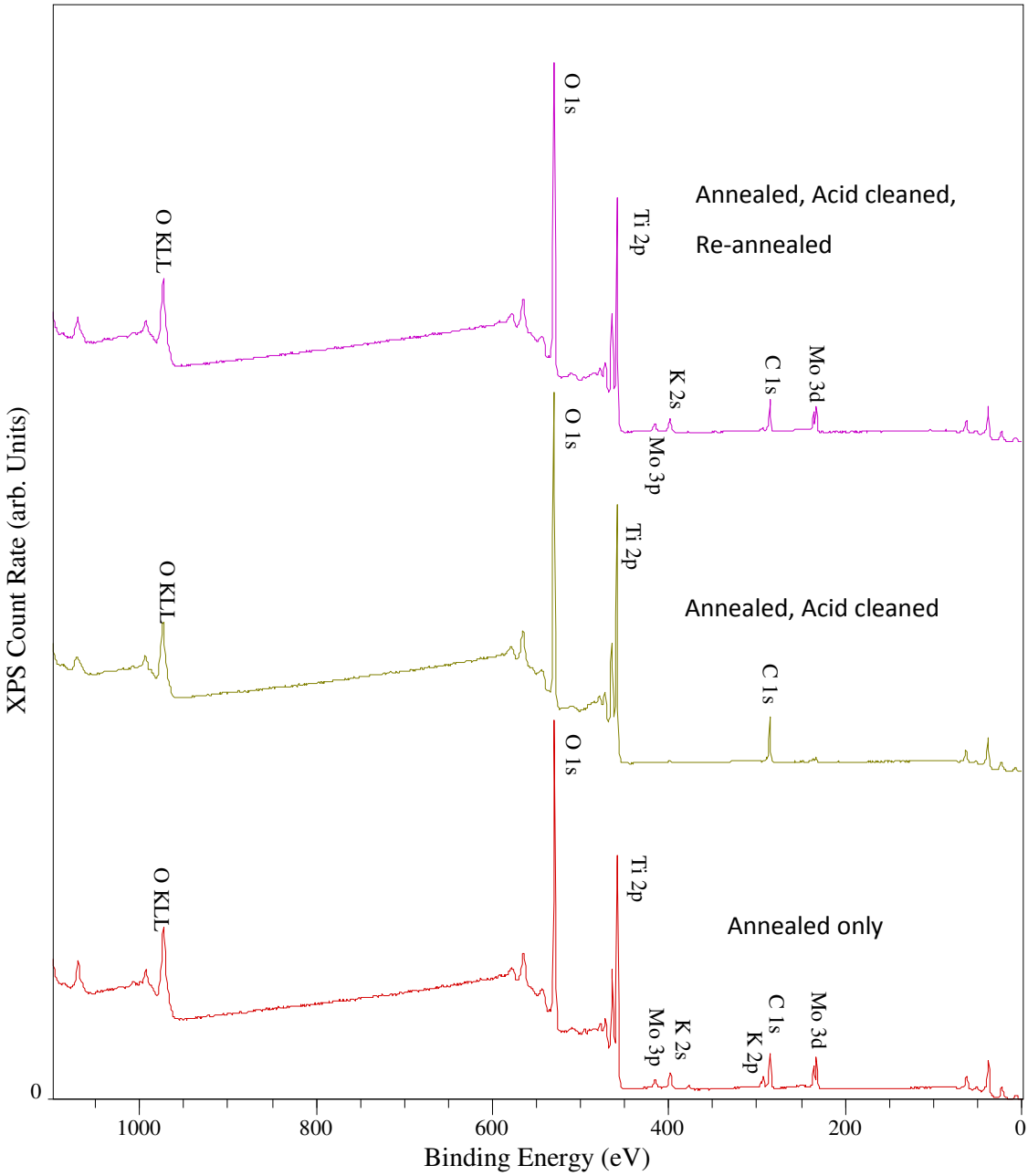

Figure 5.6. XPS wide-scan spectra of the TiO_2(110) surface under different preparation techniques. Spectra have been normalised around the O1s peak and prominent features have been labelled for convenience.

5.3.3. The Carbonaceous Overlayer on TiO_2(110)

Adventitious Carbon

Adventitious carbon is an ever present feature on surfaces in non-UHV environments and yet its origins and the mechanism of its deposition are surprisingly poorly understood. Small-scale deposits of organic complexes have been seen on practically every air-exposed inorganic surface, regardless of duration of exposure and surface reactivity.[30, 31] Even samples prepared under moderately high vacuum develop a carbonaceous overlayer and have to be periodically re-prepared[32] – this can be exploited in some experiments as the carbon 1s peak is commonly used as the binding energy calibration reference in photoelectron spectroscopies.

From a practical standpoint carbonaceous surface layers can negatively impact on the resolution and effectiveness of sensitive surface characterisation techniques.[33] More fundamentally however, the ubiquity of hydrocarbon species on all surfaces outside of ultra-high vacuum means that they are very likely to somehow mediate surface chemistry in a way not currently understood. Empirical observations of adventitious carbon have made several suggestions as to its behaviour and origins.[32, 33]

There are some practical issues with direct measurements *in situ* as sensitive chemical analysis often relies on vacuum conditions, but after cleaning the carbon species are seen to deposit over very short timescales (minutes) and reach a semi-stable equilibrium over a similarly short duration.[32] Typical estimated thicknesses are of the order of atomic monolayers, although surfaces left in-air for prolonged periods do continue to develop at a vastly slower rate.[30] Interestingly, metals left in-air for variable lengths of time will show a time-related development of the underlying surface oxide until the surface passivates, but the thickness of the overlying adventitious carbon remains more or less constant.[34] Whilst possessing a fairly uniform thickness, the surface distribution is not necessarily that of a homogeneous layer.

Rudimentary characterisation of the adventitious carbon tends to focus exclusively on the primary carbon 1s emission peak, but more involved chemical and vibrational analyses suggest that it consists of disordered hydrocarbon polymers (rather than the more ordered graphitic structures), and that they are usually physisorbed on the surface rather than chemically interacting with it in any way.[32] One explanation for this is that chemically, the more stable hydrocarbons are out-competed by the much more reactive O_2 and H_2O generally also present in the air.

Preliminary XPS Investigation

High resolution XPS spectra were acquired at several different emission angles over the Ti 2p, O 1s, and C 1s binding energy ranges for a freshly prepared TiO_2(110) substrate. XPS has an inherent surface sensitivity as a result of a finite photoelectron escape depth – X-rays can penetrate a few microns into the sample but the probability of an emitted photoelectron escaping the surface without undergoing an inelastic scattering event greatly decreases with emission depth – the depth is generally 2-3 nm depending on the electron kinetic energy and the sample being probed.[18] The finite electron escape depth can be used to estimate the thickness and makeup of surface films, as XPS scans taken at a grazing emission angle will be necessarily probing a shallower depth into the sample as illustrated in Figure 5.7.[35]

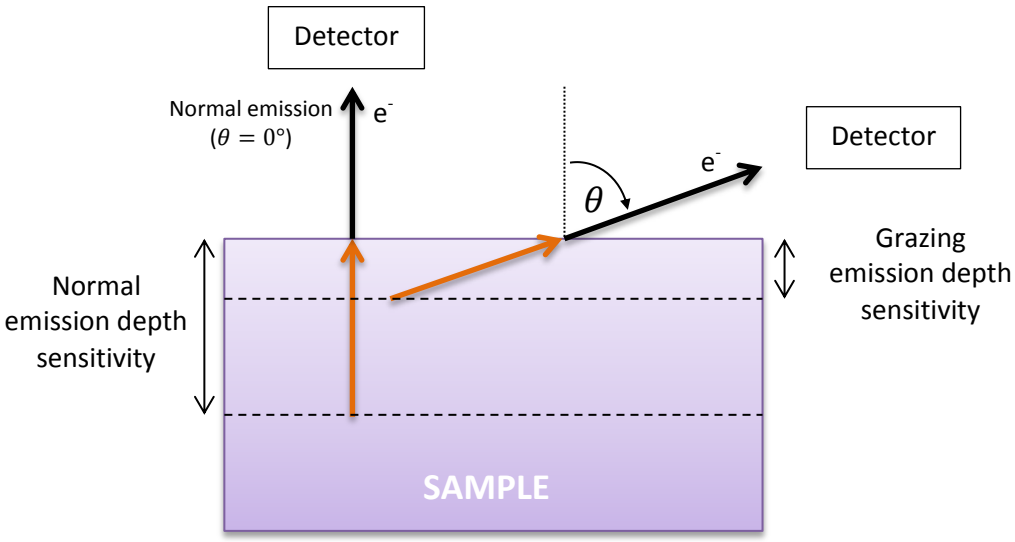

Figure 5.7. Diagram illustrating the variable depth sensitivity achieved with XPS by varying detection/ emission angle from normal. Emission angle θ from normal is shown, and the orange arrows represent the finite electron escape depth.

The high resolution spectra in Figure 5.8 have been background subtracted and peak-fitting procedures have also been applied. The purpose of this is to characterise the oxidation states of the detected elements. Only the carbon and oxygen results are displayed with the secondary scattering background subtracted, owing to the complexity of the Ti 2p feature and associated higher probability of errors in the peak fitting.[36] Different sub-peaks correspond to different oxidation and binding states of the elements, and suggest their local chemical environment.[37]

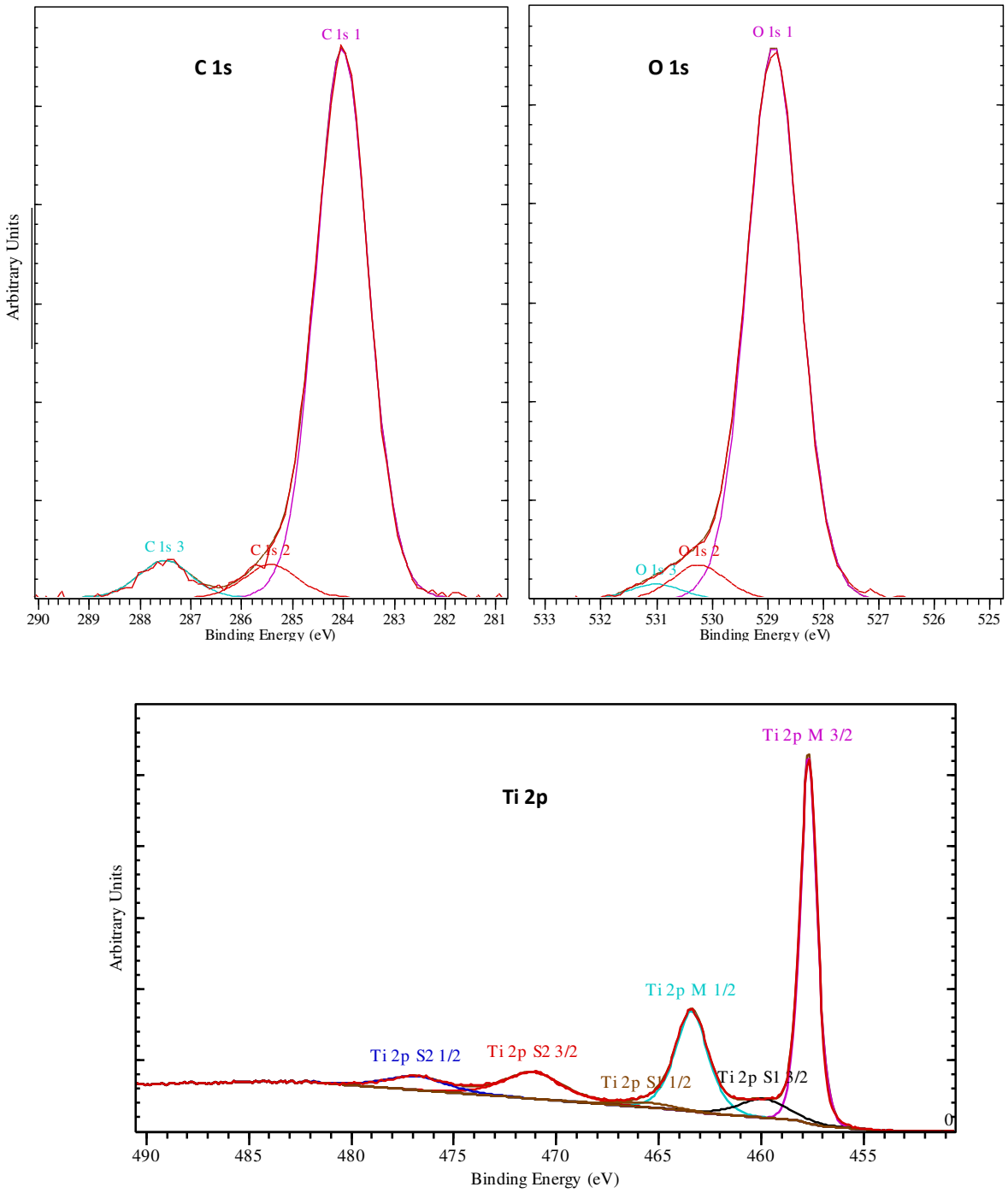

Figure 5.8. Peak-fitted high resolution XPS spectra of the C 1s, O 1s, and Ti 2p regions taken from a wet-chemically prepared TiO_2(110) substrate. The carbon and oxygen data have been background-subtracted. Some small relative changes were observed when the emission angle was varied, but the fitting models presented here (peak centre energies & widths) remained constant.

These data (Figure 5.8) in conjunction with the emission angle-dependent information in Figure 5.9 allow for a qualitative estimation of the distribution of carbon and oxygen at the surface of the cleaned rutile crystal, and support the expected model of the bulk TiO_2 covered by an overlayer of surface oxide and a 'layer' of adventitious carbon.

The central carbon peak labelled C 1s 1 shows a definite positive relationship between angle and intensity (whilst overall Ti and O contributions decrease – it is the relative changes in peak areas that implies a change in elemental concentrations), as do the two smaller sub peaks C1s 2 (ascribed to alcohol C-OH or ester C-O-C functionality) and C 1s 3 (assigned to C=O),[33] implying that all incidences of carbon are close to the surface. For the oxygen data, the inverse relationship between the large central peak (O 1s 1) and emission angle from normal suggests that this is due to the bulk oxide. The positive correlation between angle and the intensity of the second oxidation state (O 1s 2) relative to total O and Ti intensities implies that this species is surface-oriented, and is most likely due to the surface oxide or twofold coordinated oxygens at the bulk termination. This signal could alternatively be related to oxy-carbon species in the adventitious layer. These data also serve to illustrate the timescales involved in carbon deposition as these samples were placed in the XPS load-lock a maximum of 10 minutes post-UV/ozone cleaning.

The numerical intensities of the emissions are plotted for clarity in Figure 5.9. The standard Shirley background shape which works well for many photoemission peaks had to be modified for the Ti to avoid non-physical interpretations such as a negative count rate.[38] The two larger peaks labelled Ti 2p $M_{3/2}$ and Ti 2p $M_{1/2}$ comprise the main photoemission doublet, and the other four smaller peaks are satellite shake-up peaks resulting from electronic perturbations due to core-hole creation. Of key interest here is the lack of a lower energy Ti^{3+} feature which would indicate an oxygen-reduced surface.

After the initial XPS analysis, the samples were transferred to sample holders and left exposed to the laboratory atmosphere for a period of 14 days, after which they were loaded back into the XPS loading dock and normal emission measurements repeated. This second set of data may be used to evaluate the evolution of the carbon overlayer over time. The percentages shown in Table 5.1 correspond to the relative atomic concentrations at normal emission angle of detected elements, both initially after preparation and after 14 days atmospheric exposure. These data support the assertion that adventitious carbon deposition reaches a relatively steady state after a very short timescale, as only very minor relative concentration changes are recorded.

	Atomic percentage concentration from emission peak		
	Ti 2p	O 1s	C 1s
Immediately after preparation	24.8	48.2	26.6
After 14 days atmos. exposure	21.3	50.1	27.7

Table 5.1. Atomic concentrations of surface elements detected via normal emission XPS from a TiO2 crystal sample before and after significant atmospheric exposure. Figures calculated from wide-scan values.

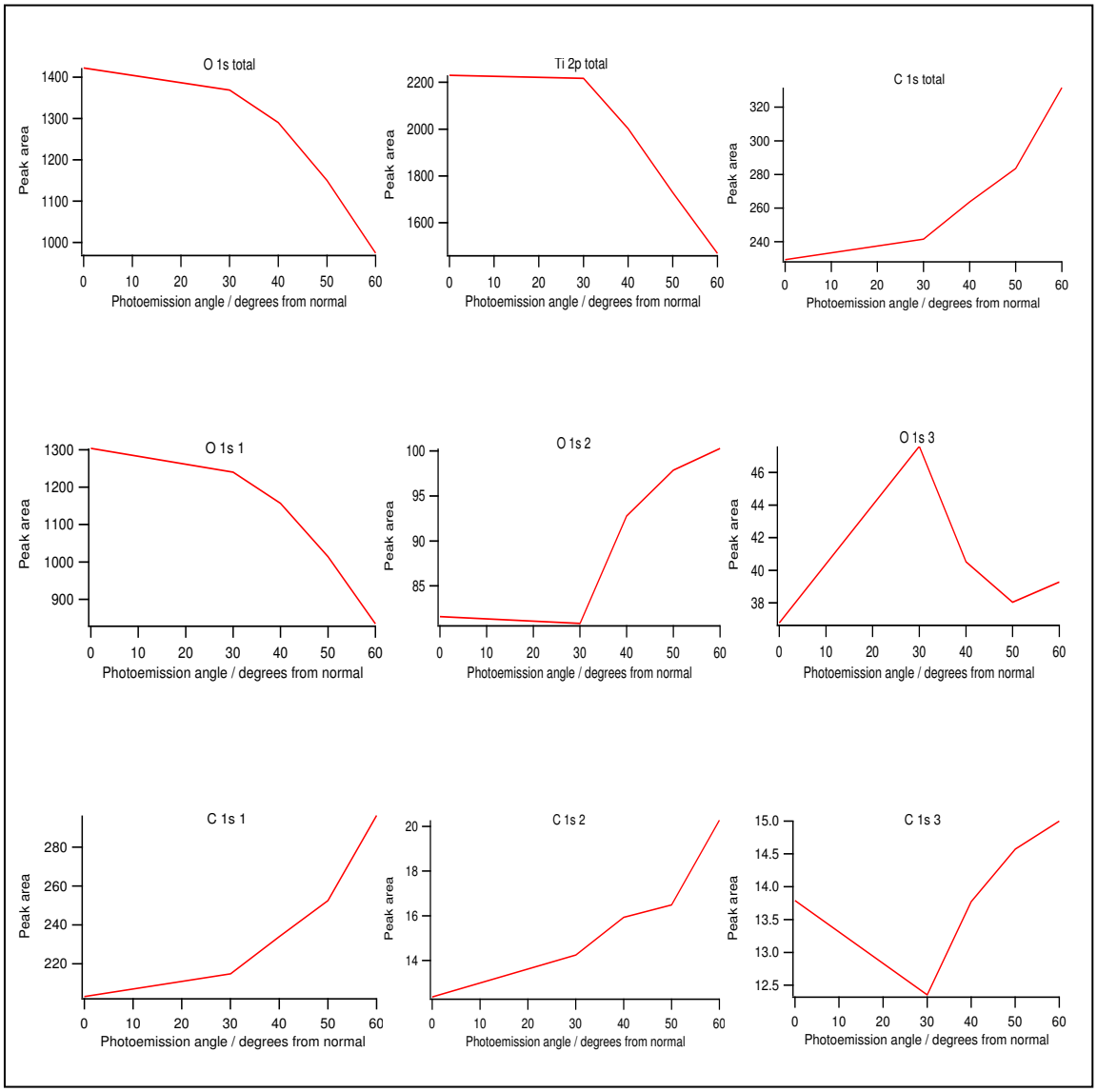

Figure 5.9. Plots of total and individual XPS intensities for O 1s, Ti 2p and C 1s transitions as a function of photoelectron emission angle for non-UHV prepared TiO_2(110).

VSFS Investigation into UV/Ozone Efficacy

The difficulties in UHV chemical analysis of the adventitious carbon brought on by its fast deposition rate is potentially compounded by additional carbonaceous contamination from oil in the vacuum pump.[33] In this case vibrational surface spectroscopies provide several advantages over vacuum chamber-based analyses, as they possess a high degree of chemical sensitivity coupled with the potential for much shorter setup times.

TiO_2(110) UV cleaning

As seen in Chapters 3 and 4, one reason VSFS has not become more widespread than it is currently relates not only to the expense and complexity of the light generation systems but also the large number of variables that must be optimised before a successful acquisition may be made. TiO_2(110) single crystal samples proved to be a particularly difficult system to probe with VSFS, as their surface electronic properties result in a non-resonant background signal several orders of magnitude smaller than the more common metallic substrates usually investigated. As the NR background is the best indicator for accurate system alignment, such weak signals can increase setup times exponentially, which is problematic when investigating chemical processes that occur over short timescales after sample preparation/cleaning. Additionally, it is desirable to suppress the NR background through visible pulse-delay techniques to better resolve vibrational resonances; this will diminish the SFG signal further requiring acquisition times of around 10-60 minutes before spectra of sufficient signal-to-noise are achieved.

Regardless, whilst long acquisition times proved necessary the high surface sensitivity of VSFS coupled with incredibly low overall background resulted in good resolution of molecular vibrations, even when total maximum photon counts were only in the double- or single-figure range.

Wet chemically prepared TiO_2(110) substrates were investigated via VSFS prior to UV exposure in both zero-delay and BG-suppressed timing configurations. The region of interest is the C-H stretching region which occurs between approximately 2750 cm^{-1} and 3150 cm^{-1}. No surface contamination was observed topographically through AFM means, but zero-delay spectra obtained through VSFS centred on $\sim$ 3000 cm^{-1} showed significant deviation from the expected Gaussian distribution, indicating surface hydrocarbon with a relatively high degree of surface ordering. Background-suppressed spectra confirmed the presence of 2-3 separate C-H vibrations, which varied in relative intensity between different samples and on different areas of the same sample, but were seen consistently on all other bare air-exposed substrates investigated.

As shown in Figure 5.10 which illustrates the effect of UV/ozone cleaning, the resonance effects from the pre-cleaned sample are particularly strong in both timing configurations, possibly due to the well-ordered nature of the underlying crystal. Apparent also from the 'dirty' TiO_2 plots is the strong effect of the phase difference between resonant and non-resonant SFG signals manifested in the zero-delay spectrum, which are much more complicated than basic signal addition.

In contrast, the background-suppressed spectra from the post-UV cleaned samples show zero signal, confirming the effectiveness of the UV/ozone cleaning and also the utility of VSFS as a C-H contamination fingerprinting technique. The UV-cleaned sample in this case had been exposed to the laboratory air for a number of weeks post-annealing/acid etching, and to achieve this subsequent level of surface cleanliness did require several consecutive UV cycles.

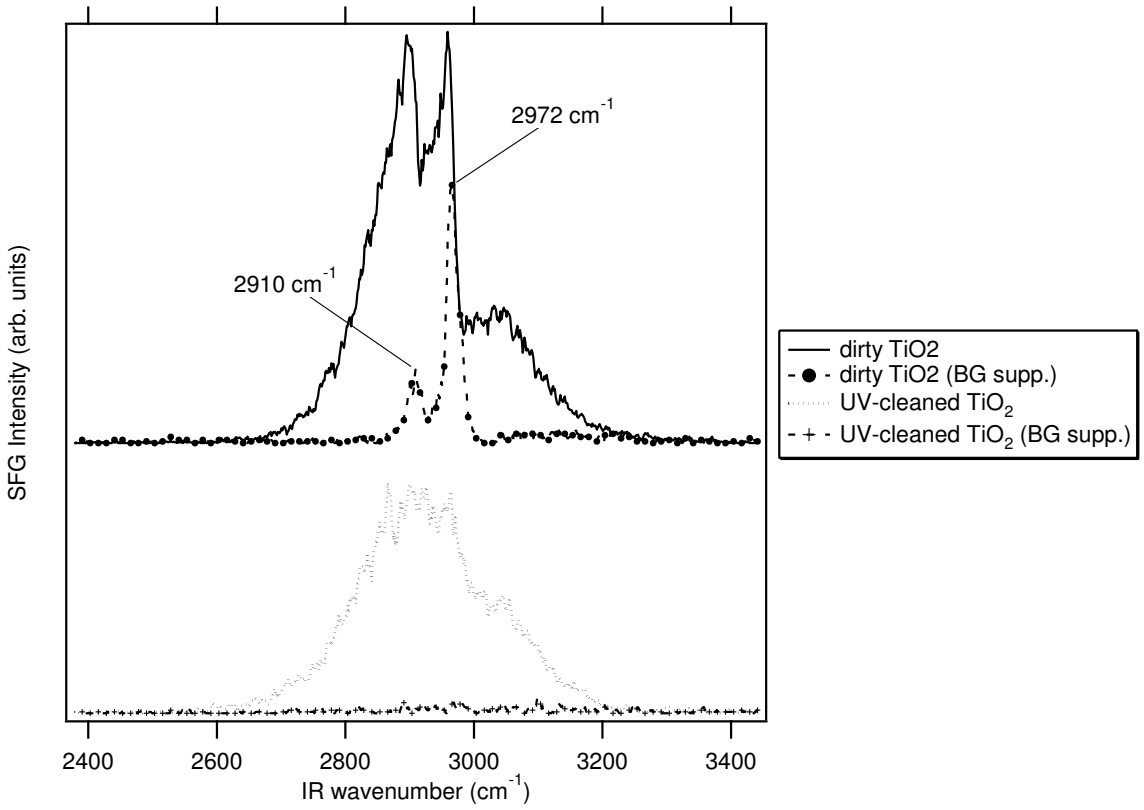

Figure 5.10. Zero-delay and background-suppressed VSFS spectra showing the effect of UV/ozone cleaning on TiO_2(110) samples contaminated by adventitious carbon. BG suppressed spectra taken with a 1 ps visible pulse delay.

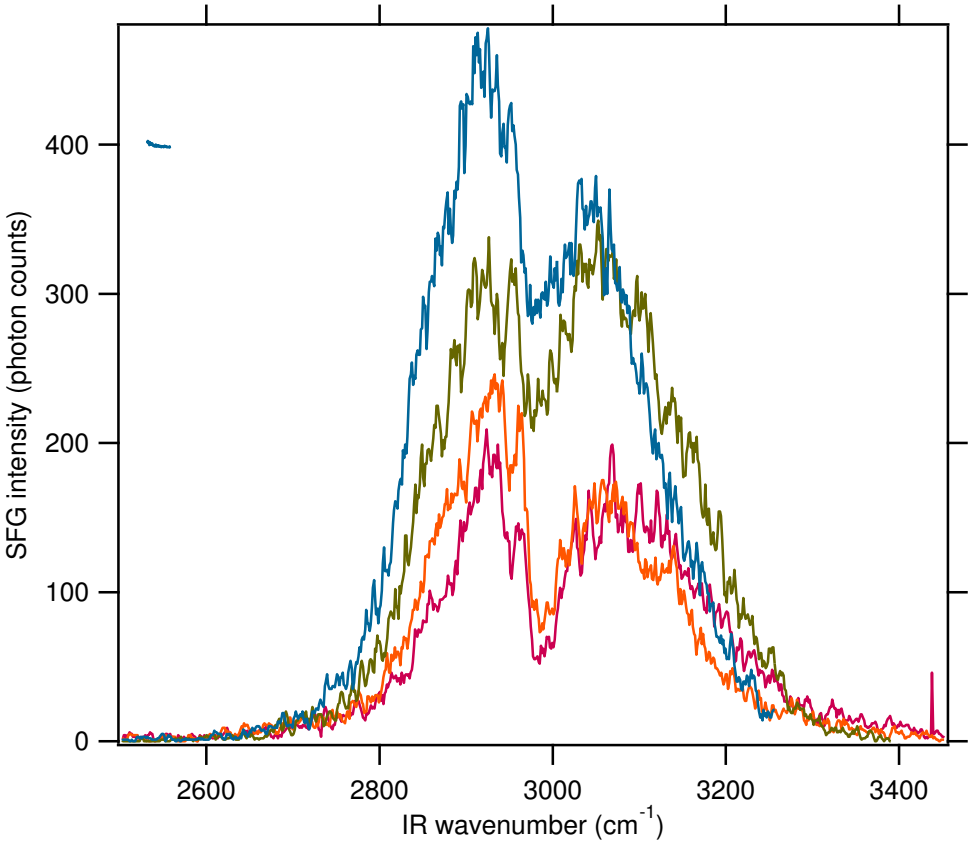

Figure 5.11. Multiple SFG spectra in the C-H stretch region of TiO2(110) substrates contaminated by adventitious carbon, to show commonalities and variation. All spectra taken at zero-delay.

A number of additional zero-delay scans of adventitious carbon on the (110) surface are illustrated in Figure 5.11, to give an idea of the variation in spectra encountered. All have been acquired with the same IR centre wavelength and the same acquisition parameters but on different days with different samples. Overall signal intensity and spectral shape is seen to vary somewhat between spectra, but resonant features appear consistently at ~ 2975, 2949 and 2907 cm^{-1} (exact wavenumbers are approximate due to slight differences in x-axis calibration).

As-yet unpublished work performed by other investigators in this author's research group included in-depth XPS analysis of the cleanliness of UV-exposed TiO_2(110) substrates, where the UV irradiation was performed in a controlled environment in a glove box above the XPS load-lock. This work also confirmed the efficacy of the UV cleaning technique.

This project necessitated the UV cleaning of TiO_2 on a regular basis, and provided care was taken not to introduce extra contaminants (e.g. solvents, greases or particulates) a 'clean' surface free from C-H resonances as observed by VSFS was consistently achieved.

Time-evolution of C-H Resonance

A brief *in situ* experiment was then performed to determine the time-evolution of the carbon deposition. An intermediate visible time delay was chosen to compromise between background suppression and acquisition time, and the results are shown in Figure 5.12. Whilst a small change between spectra can be identified, bearing in mind the background suppression and relatively long timescales this experiment suggests that in-cell recontamination is not a major concern. Scans were taken consecutively, meaning the sample was continuously illuminated by IR and Vis beams, and it is unclear how this would affect overlayer development. Additional confirmation of the UV/ozone efficacy was performed for all other VSFS investigations involving TiO_2, and from these it is estimated that trace levels of surface carbon will generally become detectable via SFG ~30 minutes post-UV irradiation; this seems to depend on sample history. As older samples could prove harder to clean, all unused samples were periodically UV cleaned to prevent the accumulation of large scale adventitious carbon deposits.

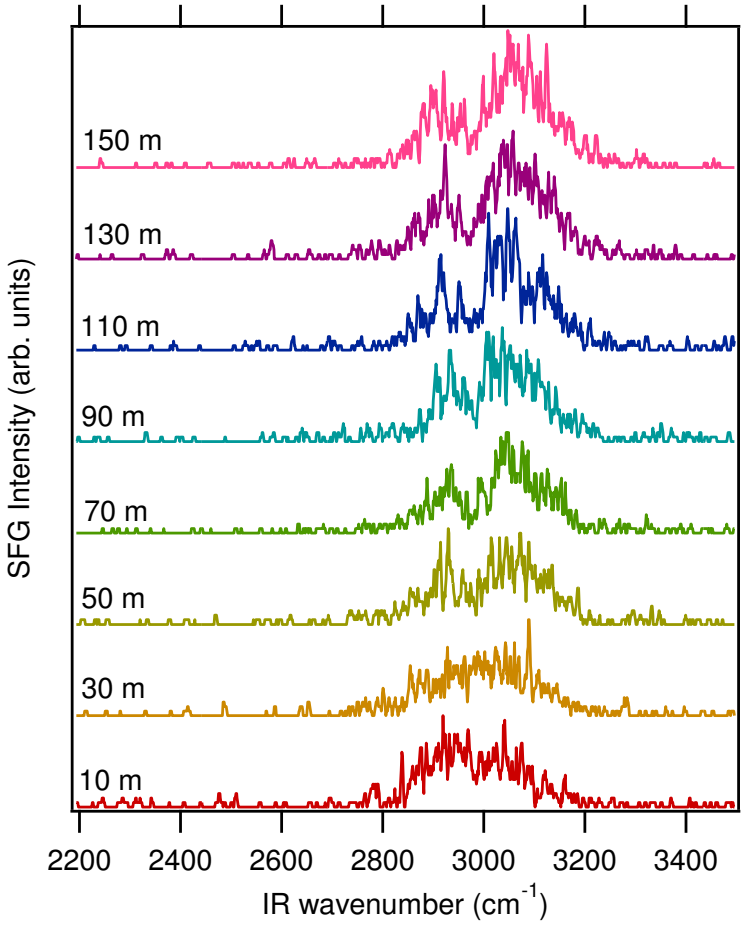

Figure 5.12. Partially background-suppressed ($\tau = 800$ fs) SFG spectra acquired continuously from UV-cleaned TiO_2(110) to chart the development of the carbonaceous overlayer. Labels indicate time in minutes since removal from ozone.

Contact Angle Confirmation

Additionally, throughout the organic-cleaning investigation, liquid contact angle techniques were used to perform quick macroscopic tests of surface cleanliness. TiO_2 is known to undergo a transition from non-wetting (hydrophobic) to wetting (hydrophilic) behaviour under irradiation by UV light.[9, 39, 40] This transition was observed and confirmed via VSFS to correlate with surface cleanliness, as small droplets of deionised water were deposited on the crystal surfaces at various points during the cleaning regime and the contact angle visually estimated. The samples found via VSFS to have detectable carbon contamination were seen to illicit a sessile droplet contact angle of approximately 60°, forming a small ($\sim$ 2 mm diameter) droplet on the 10×10 mm crystal interface. Samples showing minimal resonant signals over the C-H region via VSFS were seen to be fully wetting, with the same size and volume of droplet fully wetting the crystal surface i.e. a contact angle of 0°. An example image of the hydrophobic nature of carbon-contaminated TiO_2 is shown in Figure 5.13.

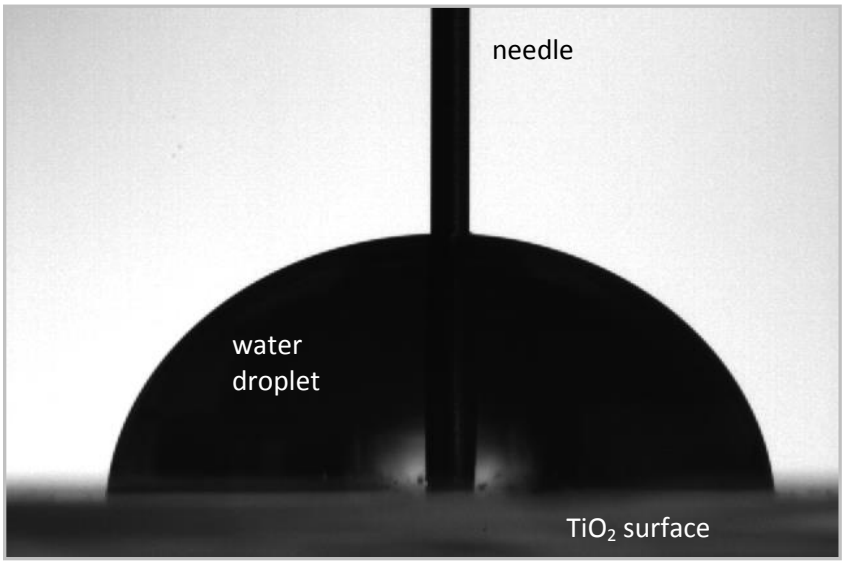

Figure 5.13. An image of the advancing contact angle from water on non-UV cleaned TiO_2(110). This advancing contact angle acquired through the captive needle technique is $\sim 80^{\circ}$ which is slightly greater than that observed for a sessile drop technique (see section 3.3.1).

Additional Comments

All scans thus far have been acquired in the **ppp** polarisation combination (see Section 5.4.2) which is sensitive to the largest variation of molecular orientations and generally achieves the highest overall signal intensities. Some experimentation was performed probing adventitious

carbon on TiO_2(110) using different polarisation combinations, but the photon count rates were so low and thus S/N too poor for results be statistically significant.

Additional confirmation of the efficacy of the wet chemical preparation technique was acquired by other members of the research group who performed UHV substrate characterisation via Low Energy Electron Diffraction (LEED) and Auger Electron Spectroscopy (AES) techniques. LEED is a crystallographic method which probes surface order, and investigation of the TiO2 showed a high degree of surface ordering with the expected (1×1) termination. Significant surface carbon contamination would result in dimmer or non-present diffraction spots but these were not observed. AES is a UHV material characterisation technique analogous to XPS, and Auger scans performed concurrently with LEED confirmed the cleanliness of the crystal surface by the lack of a significant carbon response. The Auger scans also confirmed the removal of the Mo and K responses seen in the previous XPS investigation.

5.4 Acetonitrile Adsorbed on TiO_2(110) Examined via VSFS

5.4.1. Introduction

Pictured in Figure 5.14, acetonitrile (CH_3CN) is well-characterised organic solvent molecule possessing both alkyl and nitrile functional groups, the vibrations of which are both easily observable via VSFS. Technologically it is used as a polar solvent for many applications including molecular synthesis, liquid chromatography, and several chemical extraction processes, as well as in the manufacture of batteries and pharmaceuticals amongst others.[41]

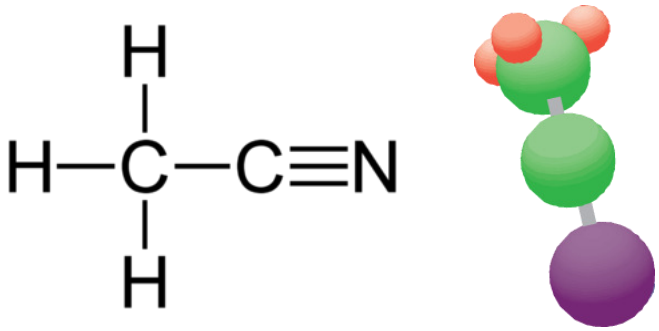

Figure 5.14. The acetonitrile molecule as represented by a skeletal formula and ball and stick diagram.

In addition to these applications, acetonitrile is also used as a solvent in the manufacture of TiO_2 based dye-sensitised solar cells (DSSCs).[42-44] As previously addressed, photons of sufficient energy may create electron-hole pairs in TiO_2. The freed conduction band electrons can then flow through an external circuit driven via a chemical potential. The ~ 3 eV band gap of TiO_2 means that only photons in the near-UV posess enough energy to drive the exciton formation, and in a solar cell application this effectively discounts the large majority of the solar spectrum. An alternative approach (DSSCs) instead utilises only the semiconductor nature of TiO_2, with electrons injected into the TiO_2 from photoactive dye molecules covering the surface, from which the electrons flow to a conducting electrode. To prevent decomposition of the oxidised dye molecule, it strips an electron from an iodide ion in solution – acetonitrile is the common solvent used, as it conveys higher overall conversion efficiencies than systems utilising ionic liquid electrolytes.[45]

Due then to its simplicity and high degree of prior characterisation, and then also its application in the development of low-cost light harvesting, the acetonitrile molecule in conjunction with the TiO_2(110) surface is a highly attractive system for fundamental investigation via SFG techniques.

Aside from functional investigations into efficiencies of DSSCs,[12] most previous work on the acetonitrile-TiO_2 interface has focussed on the catalytic photodegradation of adsorbed molecules.[46-48] The following section will instead look at the detection of adsorbed acetonitrile on the in-air prepared TiO_2(110) monocrystalline surface through VSFS, and the use of varying light polarisations in order to infer molecular orientation.

5.4.2. Electric-Field Polarisation in VSFS – Theory

For simplicity, the theory of SFG presented in Section 3.5.2 did not discuss light polarisation considerations and only lightly touched upon the generation of surface nonlinear Fresnel fields, and so this section will expand upon this as it will be necessary for orientation calculations.

Light as an EM wave

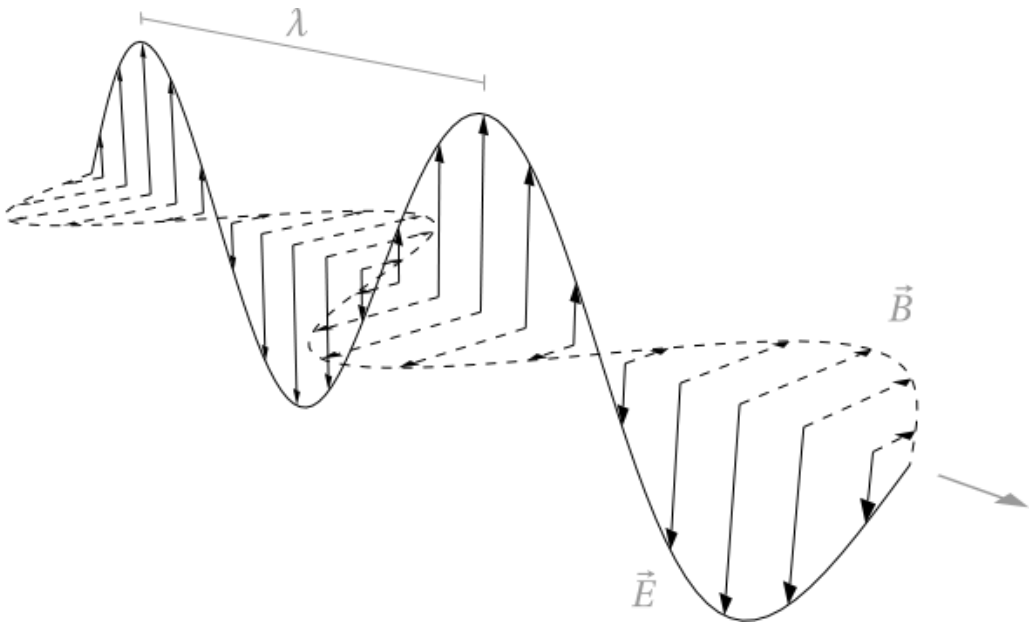

Figure 5.15. Diagram illustrating the relationship between electric $\vec{E}$ and magnetic $\vec{B}$ field vectors for a plane-polarised EM wave of wavelength λ relative to the direction of propagation.[49]

Electromagnetic radiation is a continuous spectrum although it has been arbitrarily partitioned by wavelength into such phenomena as (in decreasing wavelength) radio, microwaves, infrared, visible light, ultraviolet, X-rays and gamma rays. A monochromatic coherent light such as that generated by a laser can be treated as a two-dimensional transverse wave of fixed wavelength, with an electric and magnetic field component perpendicular to one another, and both oscillations perpendicular to the direction of propagation as illustrated in Figure 5.15. The electric dipole approximation which will be used for this derivation ignores the magnetic field component

due to its minimal interaction with dielectric media, and also assumes that any induced polarisation in a molecule is solely due to the incident electric field with no effect from the fields generated in neighbouring molecules.[50, 51]

With respect to the surface in an experimental system, two fundamental polarisation states may be defined; *p-polarised* light in which the electric field vector is parallel to the plane of incidence, and *s-polarised* light in which the incident electric field vector is perpendicular to the plane of incidence. These two scenarios are presented in Figure 5.16, which helps illustrate the wave/surface geometry relative to laboratory coordinates.

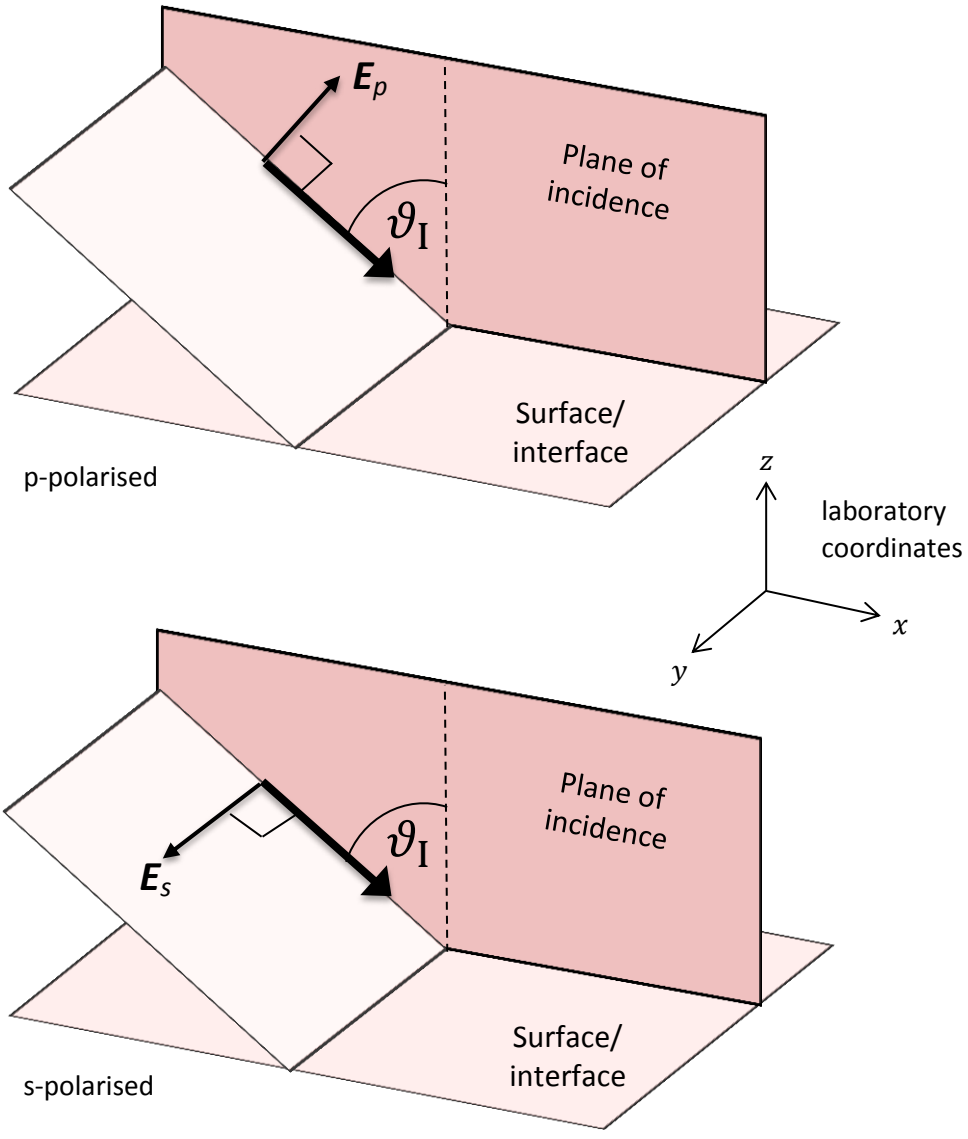

Figure 5.16. Diagram showing the electric field directions relative to surface and plane of incidence for a plane-polarised EM wave for p- and s- polarised light. Heavy black arrow represents direction of propagation and ϑ is the angle of incidence; reflected and transmitted light have been omitted for clarity.

Having defined polarisation geometry and Cartesian laboratory coordinates this section now has two objectives; firstly to derive the optimum incidence angles for sum-frequency generation off TiO_2(110) in order to maximise signal strength, and then to present a method for orientational analysis of molecular adsorbates relevant to the TiO_2-acetonitrile system. The notation of such derivations depends on chosen geometries and coordinate systems, and herein will follow the notation used by Lambert.[52]

Fresnel Optics

To calculate electric fields at the interface, these fields must be defined relative to each coordinate system. The total field at the surface is a product of the incident and reflected fields, and these can be calculated using Fresnel equations and coefficients.[50]

From purely trigonometric considerations the magnitude along the i axis ($i = x, y, z$) of the incident electric field $\boldsymbol{E}^I$ can be written as

$$E_x^{\mathrm{I}} = E_p^{\mathrm{I}} \cos\vartheta_{\mathrm{I}}$$
$$E_y^{\mathrm{I}} = E_s^{\mathrm{I}}$$
$$E_z^{\mathrm{I}} = E_p^{\mathrm{I}} \sin\vartheta_{\mathrm{I}}$$

(Eq. 22)

where E_p^{I} and E_s^{I} are the magnitudes of the p- and s- polarised E-fields respectively and ϑ_{I} is the angle of the incident beam (see Fig 5.15).

Fresnel equations can then be used to describe the behaviour of an electric field incident on an interface in terms of its Fresnel reflection coefficient r, relative to the refractive indices of the incidence and transmission media (n_{I} and n_{T}) and the angle from the interface normal of incident and transmitted beams (ϑ_{I} and ϑ_{T} respectively). This reflection coefficient, described in detail elsewhere[50, 53], is by definition the ratio between incident and reflected E-fields such that

$$r_p \equiv \frac{E_p^{\mathrm{R}}}{E_p^{\mathrm{I}}}$$

and

$$r_s \equiv \frac{E_s^{\mathrm{R}}}{E_s^{\mathrm{I}}}$$

(Eq. 23)

where r_p and r_s are Fresnel reflection coefficients for p- and s-polarised light respectively.

As the total surface field is a sum of incident and reflected fields, combining Equations 22 and 23 the total electric field E_i for $i = x, y, z$ can be written in terms of light polarisation as

$$E_x = E_x^{\mathrm{I}} + E_x^{\mathrm{R}} = E_p^{\mathrm{I}} \cos\vartheta_{\mathrm{I}}\left(1 - r_p\right)$$
$$E_y = E_y^{\mathrm{I}} + E_y^{\mathrm{R}} = E_s^{\mathrm{I}}(1 + r_s)$$
$$E_z = E_z^{\mathrm{I}} + E_z^{\mathrm{R}} = E_p^{\mathrm{I}} \sin\vartheta_{\mathrm{I}}\left(1 + r_p\right)$$

(Eq. 24)

To calculate the intensity of a sum-frequency signal generated at an interface requires a revisiting of the general SFG equation alluded to in Section 3.2.2. The SFG intensity I_{SF} is a product of the induced polarisation $P_{\mathrm{eff}}^{(2)}$ brought about by the IR and VIS E-fields and second order nonlinear susceptibility $\chi_{\mathrm{eff}}^{(2)}$ where

$$I_{\mathrm{SF}} \propto \left|P_{\mathrm{eff}}^{(2)}\right|^2 = \left|\chi_{\mathrm{eff}}^{(2)} E_{\mathrm{VIS}} E_{\mathrm{IR}}\right|^2$$

(Eq. 25)

The nonlinear susceptibility term $\chi^{(2)}$ is a third-rank tensor with 27 components, although depending on the symmetry of the surface under investigation the majority of these disappear. To simplify the description, i, j and k are defined to denote the laboratory coordinates of the SFG, VIS and IR electric fields respectively in terms of x, y and z, so Equation 25 which describes induced sum-frequency (SF) polarisation is expanded to become

$$\boldsymbol{P}_{i,\mathrm{SF}}^{(2)} = \varepsilon_0 \chi_{ijk}^{(2)} K_j \hat{\boldsymbol{j}} E_{p/s,\mathrm{VIS}}^{\mathrm{I}} K_k \widehat{\boldsymbol{k}} E_{p/s,\mathrm{IR}}^{\mathrm{I}}$$

(Eq. 26)

where ε_0 is the permittivity of free space, and K_j and K_k are known as Fresnel K-factors for the visible and IR E-fields respectively (which are themselves products of n_{I}, n_{T}, ϑ_{I} and ϑ_{T}).[52] $\hat{\boldsymbol{j}}$ and $\widehat{\boldsymbol{k}}$ are unit vectors for j and k and are generally omitted by convention. This description of the surface polarisation induced by two incident electric fields contains information regarding the strength and direction of all relevant E-fields as well as those of the surface response in the laboratory coordinate system. It also contains information regarding incident angles and polarisations, meaning the system description is almost complete. The last task is to describe the sum-frequency electric field generated as a result of this interfacial polarisation, and this requires a similar derivation that additionally accounts for the phase-matching requirements on the angle of the SF emission and also factors in continuity requirements of the electric fields over the interface.[54, 55]

Analogous to the K-factors, L-factors can be applied to the induced polarisation $\boldsymbol{P}_{i,\mathrm{SF}}^{(2)}$ to derive the electric field $\boldsymbol{E}_{i,\mathrm{SF}}$ generated as a result of vibrational dipole moments, such that

$$\boldsymbol{E}_{i,\mathrm{SF}} = L_i \boldsymbol{P}_{i,\mathrm{SF}}^{(2)}$$

(Eq. 27)

There are six L-factors, one for each Cartesian axis in reflection and transmission SFG; each consists of a scaling factor and is otherwise a function of the refractive indices and angle-from normal for the incidence and transmission sum-frequency fields, or in notation $n_{\mathrm{SF}}^{\mathrm{I}}$, $n_{\mathrm{SF}}^{\mathrm{T}}$, $\vartheta_{\mathrm{SF}}^{\mathrm{I}}$ and $\vartheta_{\mathrm{SF}}^{\mathrm{T}}$. Their derivation is given elsewhere[54, 55] but when inserted into Equations 27, 26 and 25 this yields the final summation for SFG intensities generated along the p- and s- polarisation planes presented thus:

$$\begin{aligned}
I_{p,\mathrm{SF}} &\propto \left|\boldsymbol{E}_{x,\mathrm{SF}}\right|^2 + \left|\boldsymbol{E}_{z,\mathrm{SF}}\right|^2 \\
&\propto \left|L_x \boldsymbol{P}_{x,\mathrm{SF}}^{(2)}\right|^2 + \left|L_z \boldsymbol{P}_{z,\mathrm{SF}}^{(2)}\right|^2 \\
&\propto \left| L_x \sum_{j}^{x,y,z} \sum_{k}^{x,y,z} \varepsilon_0 \chi_{xjk}^{(2)} K_j E_{p\mathrm{VIS}}^{\mathrm{I}} K_k E_{p\mathrm{IR}}^{\mathrm{I}} \right|^2 \\
&\quad + \left| L_z \sum_{j}^{x,y,z} \sum_{k}^{x,y,z} \varepsilon_0 \chi_{zjk}^{(2)} K_j E_{p\mathrm{VIS}}^{\mathrm{I}} K_k E_{p\mathrm{IR}}^{\mathrm{I}} \right|^2 \\
I_{s,\mathrm{SF}} &\propto \left|\boldsymbol{E}_{y,\mathrm{SF}}^{\mathrm{I}}\right|^2 \\
&\propto \left|L_y \boldsymbol{P}_{y,\mathrm{SF}}^{(2)}\right|^2 \\
&\propto \left| L_y \sum_{j}^{x,y,z} \sum_{k}^{x,y,z} \varepsilon_0 \chi_{yjk}^{(2)} K_j E_{p\mathrm{VIS}}^{\mathrm{I}} K_k E_{p\mathrm{IR}}^{\mathrm{I}} \right|^2
\end{aligned}$$

(Eq. 28)

where L_x, L_y and L_z are the L-factors relating to the x, y and z components respectively, and all other terms have their usual definitions.[52]

It will be further convenient in later derivation to combine all the Fresnel coefficients into a single Fresnel term F_{ijk} which results in a significant simplification to Equation 28 independent of the plane of SFG polarisation where

$$I_{\mathrm{SF}} \propto \left| \sum_{i} \sum_{j.k} F_{ijk} \chi^{(2)}_{ijk} E_{\mathrm{VIS}} E_{\mathrm{IR}} \right|^2$$

(Eq. 29)

Polarisation Convention in VSFS

Experimentally, ignoring intermediate polarisations which have both p and s components, polarisation can be set to either p or s for each of the three interacting beams (visible, infrared and sum-frequency). From Figure 5.16 which shows how the incident light is oriented relative to the laboratory coordinates, one can see that s-polarised light will only excite vibrations along the y-axis, whereas a p-polarised incident EM field will excite molecular vibrations along the x- and z-axes. There are 12 different polarisation combinations that are attainable, and by convention they are always noted in the following order; SFG, VIS and IR.

The 27 elements of the $\chi^{(2)}_{ijk}$ tensor – which ultimately contains all molecular susceptibility information – are described in terms of the laboratory coordinate system and the possible combinations are as follows:

$$\begin{array}{ccccccccc} xxx & xyy & xzz & xyz & xzy & xzx & xxz & xxy & xyx \\ yxx & yyy & yzz & yyz & yzy & yzx & yxz & yxy & yyx \\ zxx & zyy & zzz & zyz & zzy & zzx & zxz & zxy & zyx \end{array}$$

To better relate these elements back to the induced polarisation from two incident electromagnetic fields Equation 26 can be rewritten as $P^{(2)}_{i(\mathrm{SFG})} = \sum_{j,k} \chi^{(2)}_{ijk} E_{j(\mathrm{VIS})} E_{k(\mathrm{IR})}$, which when expanded to include all $\chi^{(2)}_{ijk}$ elements[81] yields the following matrix relationship in terms of lab coordinates

$$\begin{matrix} SFG \\ \downarrow \end{matrix} \quad \begin{matrix} & & & & & & & & VIS & IR \\ & & & & & & & & \downarrow & \downarrow \end{matrix}$$

$$\begin{bmatrix} P^{(2)}_x \\ P^{(2)}_y \\ P^{(2)}_z \end{bmatrix} = \begin{bmatrix} \chi^{(2)}_{xxx} & \chi^{(2)}_{xyy} & \chi^{(2)}_{xzz} & \chi^{(2)}_{xyz} & \chi^{(2)}_{xzy} & \chi^{(2)}_{xzx} & \chi^{(2)}_{xxz} & \chi^{(2)}_{xxy} & \chi^{(2)}_{xyx} \\ \chi^{(2)}_{yxx} & \chi^{(2)}_{yyy} & \chi^{(2)}_{yzz} & \chi^{(2)}_{yyz} & \chi^{(2)}_{yzy} & \chi^{(2)}_{yzx} & \chi^{(2)}_{yxz} & \chi^{(2)}_{yxy} & \chi^{(2)}_{yyx} \\ \chi^{(2)}_{zxx} & \chi^{(2)}_{zyy} & \chi^{(2)}_{zzz} & \chi^{(2)}_{zyz} & \chi^{(2)}_{zzy} & \chi^{(2)}_{zzx} & \chi^{(2)}_{zxz} & \chi^{(2)}_{zxy} & \chi^{(2)}_{zyx} \end{bmatrix} \begin{bmatrix} E_x E_x \\ E_y E_y \\ E_z E_z \\ E_y E_z \\ E_z E_y \\ E_z E_x \\ E_x E_z \\ E_x E_y \\ E_y E_x \end{bmatrix}$$

In a centrosymmetric scenario, direction is invariant ($x = -x$, $y = -y$ and $z = -z$) and thus $\chi^{(2)}_{ijk} = \chi^{(2)}_{-i-j-k}$. As a third rank tensor, a change in the sign of all three elements is equivalent to reversing the axis system and so $\chi^{(2)}_{ijk} = -\chi^{(2)}_{-i-j-k}$ must also apply, which can only be the case if $\chi^{(2)}_{ijk}$ is equal to zero and SFG is forbidden.

It can be similarly be shown that for a completely isotropic surface possessing $C_{\infty v}$ symmetry i.e. $x = -x$, $y = -y$ and $z \neq -z$, there are only seven non-zero $\chi^{(2)}_{ijk}$ terms that contribute to the sum-frequency intensity.[52, 54] Take for example the $\chi^{(2)}_{zxx}$ term, where a reversal of the x-axis would produce $\chi^{(2)}_{z-x-x}$; using the rules from the centrosymmetric example $\chi^{(2)}_{z-x-x} = -\chi^{(2)}_{zx-x} = \chi^{(2)}_{zxx}$, which means that in this particular symmetry the zxx element can be non-zero and SFG is allowed. Conversely a reversal of the x-axis on the $\chi^{(2)}_{zzx}$ term leads to $\chi^{(2)}_{zz-x} = -\chi^{(2)}_{zzx}$, which is only satisfied if $\chi^{(2)}_{ijk} = 0$ and SFG is again forbidden. The total allowed tensor elements are thus only those which are quadratic in either x or y, with the exception of zzz which is unaffected if x- or y-axes are reversed. As such the allowed $\chi^{(2)}_{ijk}$ tensor elements are

$$\begin{bmatrix} 0 & 0 & 0 & 0 & 0 & xzx & xxz & 0 & 0 \\ 0 & 0 & 0 & yyz & yzy & 0 & 0 & 0 & 0 \\ zxx & zyy & zzz & 0 & 0 & 0 & 0 & 0 & 0 \end{bmatrix}$$

For more limited surface symmetries this decreases further as geometric equivalencies make certain $\chi^{(2)}_{ijk}$ terms redundant.

The specific $\chi^{(2)}_{ijk}$ elements that are detectable with each experimental polarisation combination can be calculated using the following derivation for the effective second-order nonlinear susceptibility

$$\begin{aligned}
\chi^{(2)}_{\mathrm{eff}} = {} & \sin\sigma_{\mathrm{SFG}} \sin\sigma_{\mathrm{VIS}} \sin\sigma_{\mathrm{IR}} L_{yy}(\omega_{\mathrm{SFG}}) L_{yy}(\omega_{\mathrm{VIS}}) L_{zz}(\omega_{\mathrm{IR}}) \sin\theta_{\mathrm{IR}} \chi_{yyz} \\
& + \sin\sigma_{\mathrm{SFG}} \cos\sigma_{\mathrm{VIS}} \sin\sigma_{\mathrm{IR}} L_{yy}(\omega_{\mathrm{SFG}}) L_{zz}(\omega_{\mathrm{VIS}}) L_{yy}(\omega_{\mathrm{IR}}) \sin\theta_{\mathrm{VIS}} \chi_{yzy} \\
& + \cos\sigma_{\mathrm{SFG}} \sin\sigma_{\mathrm{VIS}} \sin\sigma_{\mathrm{IR}} L_{zz}(\omega_{\mathrm{SFG}}) L_{yy}(\omega_{\mathrm{VIS}}) L_{yy}(\omega_{\mathrm{IR}}) \sin\theta_{\mathrm{SFG}} \chi_{zyy} \\
& - \cos\sigma_{\mathrm{SFG}} \cos\sigma_{\mathrm{VIS}} \cos\sigma_{\mathrm{IR}} L_{xx}(\omega_{\mathrm{SFG}}) L_{xx}(\omega_{\mathrm{VIS}}) L_{zz}(\omega_{\mathrm{IR}}) \cos\theta_{\mathrm{SFG}} \cos\theta_{\mathrm{VIS}} \sin\theta_{\mathrm{IR}} \chi_{xxz} \\
& - \cos\sigma_{\mathrm{SFG}} \cos\sigma_{\mathrm{VIS}} \cos\sigma_{\mathrm{IR}} L_{xx}(\omega_{\mathrm{SFG}}) L_{zz}(\omega_{\mathrm{VIS}}) L_{xx}(\omega_{\mathrm{IR}}) \cos\theta_{\mathrm{SFG}} \sin\theta_{\mathrm{VIS}} \sin\theta_{\mathrm{IR}} \chi_{xzx} \\
& + \cos\sigma_{\mathrm{SFG}} \cos\sigma_{\mathrm{VIS}} \cos\sigma_{\mathrm{IR}} L_{zz}(\omega_{\mathrm{SFG}}) L_{xx}(\omega_{\mathrm{VIS}}) L_{xx}(\omega_{\mathrm{IR}}) \sin\theta_{\mathrm{SFG}} \cos\theta_{\mathrm{VIS}} \cos\theta_{\mathrm{IR}} \chi_{zxx} \\
& + \cos\sigma_{\mathrm{SFG}} \cos\sigma_{\mathrm{VIS}} \cos\sigma_{\mathrm{IR}} L_{zz}(\omega_{\mathrm{SFG}}) L_{zz}(\omega_{\mathrm{VIS}}) L_{zz}(\omega_{\mathrm{IR}}) \sin\theta_{\mathrm{SFG}} \sin\theta_{\mathrm{VIS}} \sin\theta_{\mathrm{IR}} \chi_{zzz}
\end{aligned}$$

where σ are the polarisation angles (from p-polarisation) and θ the incidence angles of the sum-frequency, visible, and infrared beams.[57] Assuming typical incidence angles e.g. not normal or

grazing incidence, and inputting angles for the various polarisation combinations allows the constituent susceptibility elements in each to be acquired e.g. for **ppp**, $\sigma_{SFG} = \sigma_{VIS} = \sigma_{IR} = 0°$. The various $\chi^{(2)}_{ijk}$ elements that each polarisation combination thereby contains are shown in Table 5.2, which follows the geometry defined in Section 5.1.2 and illustrated in Figure 5.16.

Non-zero Polarisation Combinations (SFG,VIS,IR)	Constituent $\chi^{(2)}_{ijk}$ Elements
ppp	$\chi^{(2)}_{xxz}, \chi^{(2)}_{xzx}, \chi^{(2)}_{zxx}, \chi^{(2)}_{zzz}$
ssp	$\chi^{(2)}_{yyz}$
sps	$\chi^{(2)}_{yzy}$
pss	$\chi^{(2)}_{zyy}$

Table 5.2. Showing the four possible non-zero polarisation combinations used in VSFS and their corresponding geometric second-order susceptibility components.[57]

From this description it is easy to see how controlling the light polarisation allows orientational analyses to be made, as the different polarisation combinations result in molecular excitation relative to the orientation of the incident E-fields. Also apparent is the relative magnitude of the **ppp** polarisation state, owing to it probing components of four different geometric elements; it is for this reason that VSFS investigation performed without the need for any orientational information is mostly gathered in **ppp** polarisation to maximise the signal acquired.

Typically, the type of substrate governs the observed SFG response in the various polarisation combinations. Metallic substrates for example are usually highly reflective for IR wavelengths and result in large induced surface fields in the z-direction. Accordingly, polarisation combinations which probe a z-component with the infrared [**ppp**($\chi^{(2)}_{zzz}$, $\chi^{(2)}_{xxz}$) and **ssp**($\chi^{(2)}_{yyz}$)] will often dwarf any response from the other two combinations.

Molecular Geometry and the Euler Transformation

The molecular hyperpolarisability β which was touched upon in equation 13 (Chapter 3) is the individual molecular SFG response parameter which is macroscopically averaged to obtain a $\chi^{(2)}$ value. It is also a third-rank tensor with 27 individual components, and fully describes how a molecule responds to local electric fields, although again many of these cancel out due to geometric and symmetry considerations.[58, 59] Of the 11 non-vanishing β_{abc} elements, only three are involved in symmetric stretching vibrations which are the focus of investigation with regards

to acetonitrile on TiO_2(110). Here, a, b and c are the molecular coordinate system analogous to the x, y, z of the laboratory coordinates, and the three elements pertinent to symmetric stretching are $\beta_{aac} (= \beta_{bbc})$ and β_{ccc}.

Just as the previous section showed the derivation for translating polarisation components $\left(\mathrm{SFG}_{p/s}, \mathrm{VIS}_{p/s}, \mathrm{IR}_{p/s}\right)$ into lab coordinates (x, y, z), Euler transformations in the form of three rotation matrices allow for translation from the molecular coordinate system (a, b, c) into laboratory/surface coordinates around three Euler angles, ϕ, θ and ψ, whose relationships are illustrated in Figure 5.17.

Aside from the axes mentioned above, an additional useful axis in describing the geometric transformation is the line of Nodes N which is defined as the intersection between the xy and ab planes. The angle ϕ is the rotation angle between the x and N axes, and is analogous to the rotation of a molecule around the surface normal as illustrated by Figure 5.18. Tilt angle θ is the angle between the z- and c- axes (or alternatively a rotation about the N- axis in the zc plane), and for a molecule on a surface this corresponds to the tilt of the molecule away from the surface normal (by our definition the z- axis). The angle ψ is dubbed the twist angle and is geometrically defined as a rotation around the c- axis of the ab plane from N to b (again see Fig 5.17). In the adsorbed molecular model, this corresponds to twist about the molecule's centre axis, which will generally be invariant for non-chiral molecules.

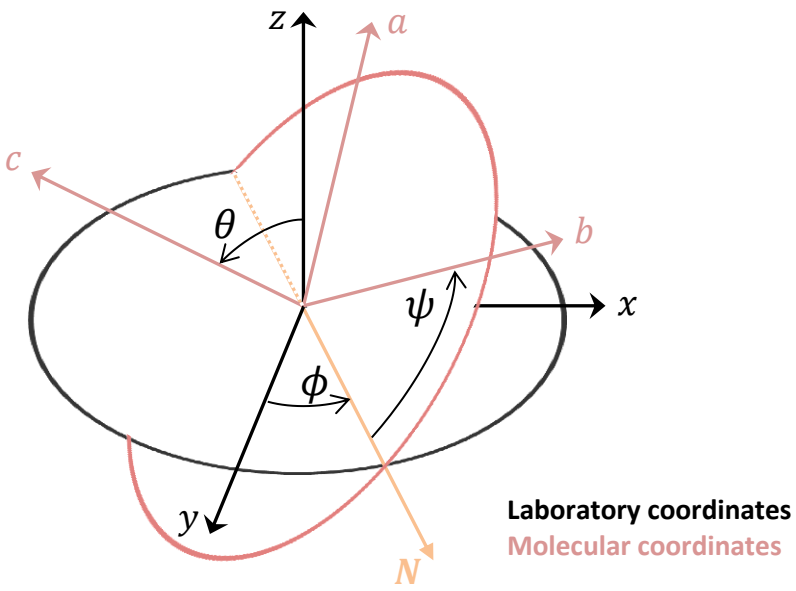

Figure 5.17. Diagram showing the Euler angles for translation between two coordinate systems. ϕ, θ and ψ correspond to rotations about the z, N and c axes respectively.

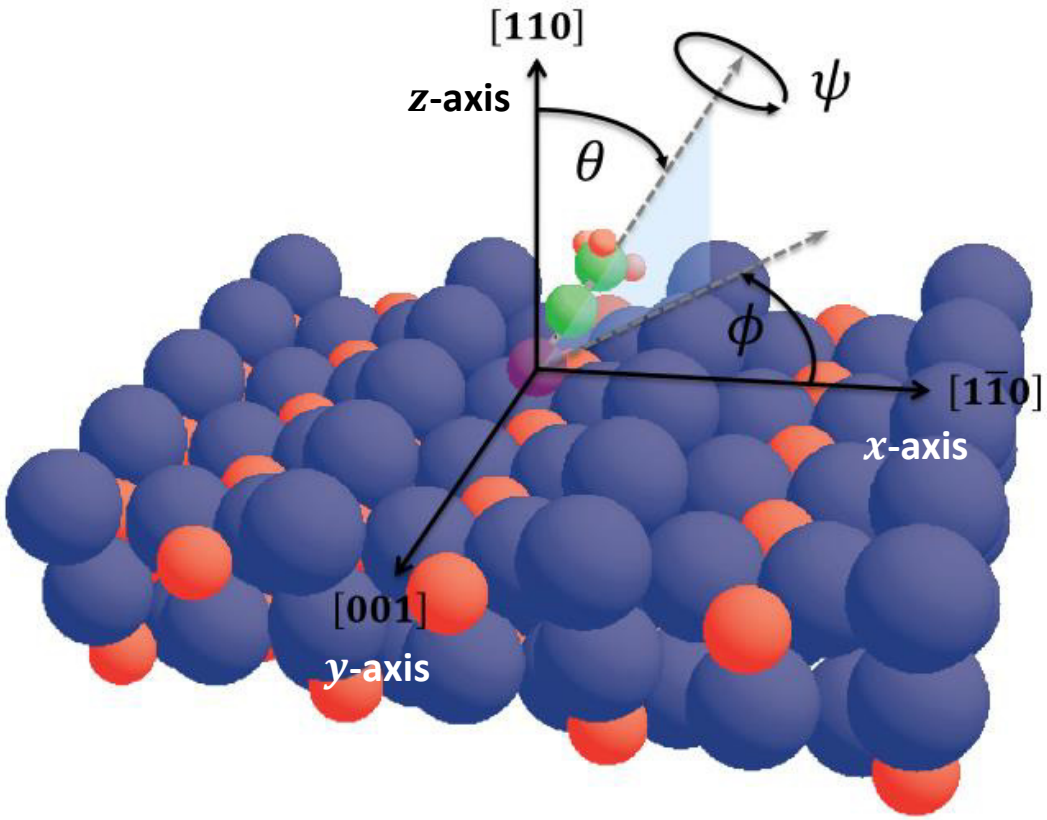

Figure 5.18. Model of the TiO_2(110) surface with adsorbed acetonitrile molecule showing real-world interpretations of Euler transformations. This also illustrates the definition of laboratory axes relative to crystal axes.

Using the Euler rotation angles one can derive terms relating the four non-zero macroscopic $\chi^{(2)}_{ijk}$ terms to their associated molecular hyperpolarisability terms,[56, 60] which can then in turn be translated into a relationship between light polarisation combinations, β terms, and the combined Fresnel function F_{ijk}:

$$\chi^{(2)}_{\mathrm{eff,R,ssp}} = F_{yyz}\big((\langle\cos^2\phi\rangle + R\langle\sin^2\phi\rangle)\langle\cos\theta\rangle - (\langle\cos^2\phi\rangle - R\langle\cos^2\phi\rangle)\langle\cos^3\theta\rangle\big)\beta_{ccc}$$

$$\chi^{(2)}_{\mathrm{eff,R,sps}} = F_{yzy}\big((\langle\cos^2\phi\rangle - R\langle\cos^2\phi\rangle)\langle\cos\theta\rangle - (\langle\cos^2\phi\rangle - R\langle\cos^2\phi\rangle)\langle\cos^3\theta\rangle\big)\beta_{ccc}$$

$$\chi^{(2)}_{\mathrm{eff,R,pss}} = F_{zyy}\big((\langle\cos^2\phi\rangle - R\langle\cos^2\phi\rangle)\langle\cos\theta\rangle - (\langle\cos^2\phi\rangle - R\langle\cos^2\phi\rangle)\langle\cos^3\theta\rangle\big)\beta_{ccc}$$

$$\begin{aligned}\chi^{(2)}_{\mathrm{eff,R,ppp}} = {} & -F_{xxz}\big((\langle\sin^2\phi\rangle + R\langle\cos^2\phi\rangle)\langle\cos\theta\rangle - (\langle\sin^2\phi\rangle - R\langle\sin^2\phi\rangle)\langle\cos^3\theta\rangle\big)\beta_{ccc} \\ & -F_{xzx}\big((\langle\sin^2\phi\rangle + R\langle\sin^2\phi\rangle)\langle\cos\theta\rangle - (\langle\sin^2\phi\rangle - R\langle\sin^2\phi\rangle)\langle\cos^3\theta\rangle\big)\beta_{ccc} \\ & +F_{zxx}\big((\langle\sin^2\phi\rangle - R\langle\sin^2\phi\rangle)\langle\cos\theta\rangle - (\langle\sin^2\phi\rangle - R\langle\sin^2\phi\rangle)\langle\cos^3\theta\rangle\big)\beta_{ccc} \\ & +F_{zzz}(R\langle\cos\theta\rangle + (1-R)\langle\cos^3\theta\rangle)\beta_{ccc}\end{aligned}$$

(Eq. 30)

where the triangular brackets ⟨ ⟩ denote an orientational average over a collection of molecules, and $R = \beta_{aac}/\beta_{ccc}$ which has been calculated previously by Hirose et al.[55]

Considerations for the TiO_2(110)-acetonitrile system

From the coordinate system in Figure 5.18, in order to get values related to molecular orientations from VSFS measurements a substrate geometry must be defined and set in terms of the laboratory coordinates. The rutile TiO_2(110) is a uniaxial birefringent crystal, presenting two different refractive indices depending on the crystal direction encountered and light polarisation. The exception to this is the crystal's optic axis, down which light travels at a speed independent of polarisation; in rutile (110) this is the $[001]$ axis. The optical axis was ascertained experimentally and set as the y-axis in the laboratory coordinate system, meaning p- and s- polarised light would experience ordinary and extraordinary refractive indices respectively – these values were parameters included in modelling and data fitting procedures. This geometry is demonstrated in Figure 5.18.

Figure 5.19 shows the magnitude of the second-order nonlinear susceptibility for a -CH_3 stretching group on the TiO_2(110) for various polarisation combinations and tilt angles, as calculated directly from Equation 30. The curves here represent the relative magnitudes of the susceptibilities and

thus of the SFG response for the four polarisation combinations over all possible molecular tilt and rotation angles (plotted directly from the terms in Equation 30), and were used to determine which polarisation combinations it would be most effective to measure in.

At all tilt angles the **ppp** and **ssp** responses are orders of magnitude greater than the **sps** and **pss** responses, and so will be the only two polarisation combinations investigated; this is due to several terms in the derivation for $\chi^{(2)}_{\mathrm{eff,R,}\mathbf{sps}}$ and $\chi^{(2)}_{\mathrm{eff,R,}\mathbf{pss}}$ cancelling one another out.[61] Also of note in the figure is the dependency on the tilt angle θ of the dominant SFG polarisation combination, with **ssp** polarisation dominating the response when the vibration is close to the surface normal, and **ppp** polarisation dominating the SFG response for moderate to large values of tilt angle. CH_3 vibrations oriented parallel to the TiO_2 surface ($\theta = 90°$) are difficult to observe via any polarisation combination.

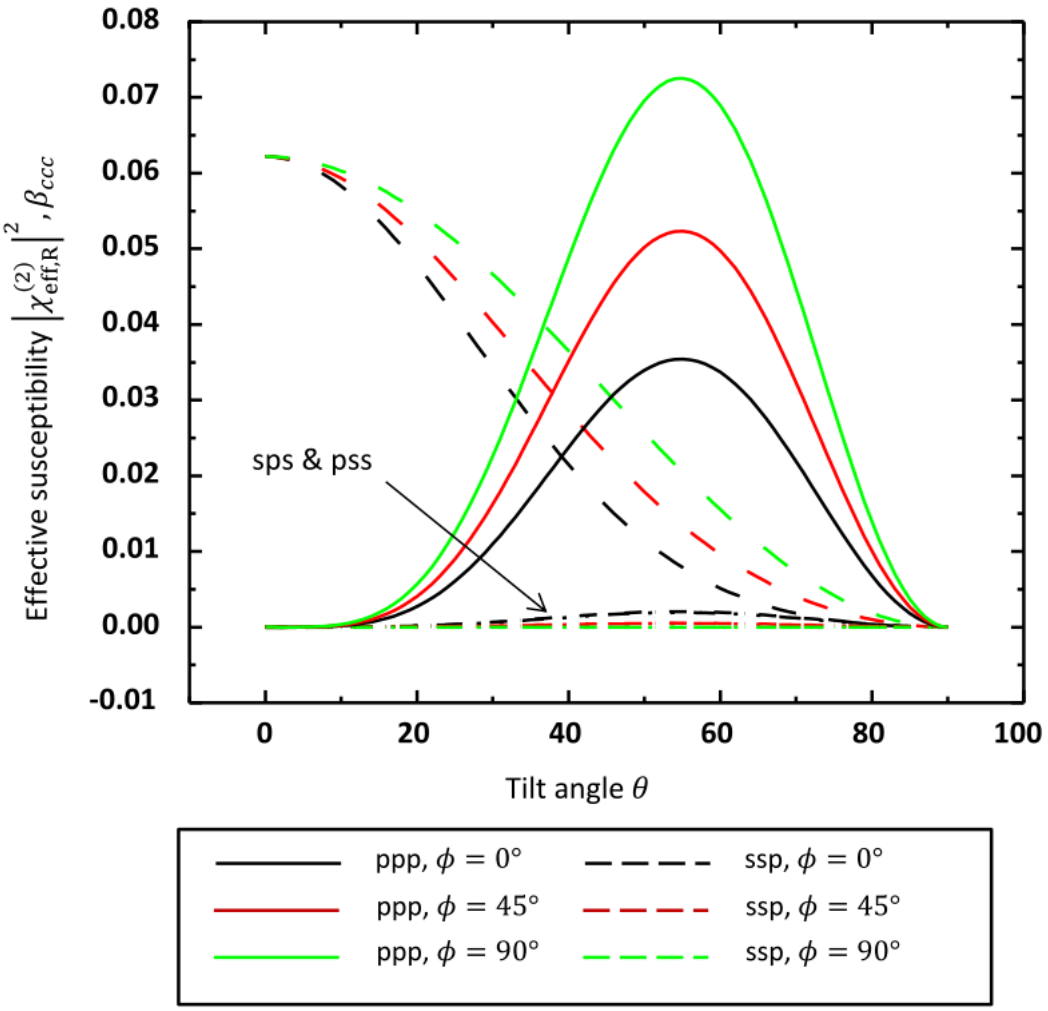

Figure 5.19. The effective susceptibility terms for ppp, ssp, sps, and pss polarisations for varying rotation angles (ϕ) as a function of the vibration tilt angle θ.[62]

The intensity differences apparent in Fig 5.19 with rotation angle ϕ for both **ppp** and **ssp** are problematic if attempting to estimate molecular tilt angles from SFG intensities. For example, at $\theta = 0°$ the $\chi^{(2)}_{eff,R}$ value in **ppp** polarisation is approximately 0.35 for $\phi = 0°$ (the black curve) and 0.73 when $\phi = 90°$ (the green curve). Unless the C-H vibration is close to normal ($\theta = 0°$), a rotation of the molecule about the surface normal may thus result in a significant variation in the observed sum-frequency intensity. To help circumvent this difficulty, the ratio between $\chi^{(2)}_{eff,R}$ values for **ppp** and **ssp** were calculated, and the resulting plot is shown in Figure 5.20. This particular variable, hereafter labelled γ, exhibits significantly less variation for different rotation angles ϕ and even converges around $\theta = 48°$, making it a more robust variable with which to attempt to measure the molecular tilt angles of $-CH_3$ groups adsorbed on our substrates.

As seen from the plot in Figure 5.20, the ratio of the effective susceptibilities from **ssp** and **ppp** polarisations exhibits much less ϕ dependence; it then follows to use this parameter,

$$\gamma = \frac{\chi^{(2)}_{\mathrm{eff,R,}\mathbf{ssp}}}{\chi^{(2)}_{\mathrm{eff,R,}\mathbf{ppp}}}$$

as the basis for orientational analysis.

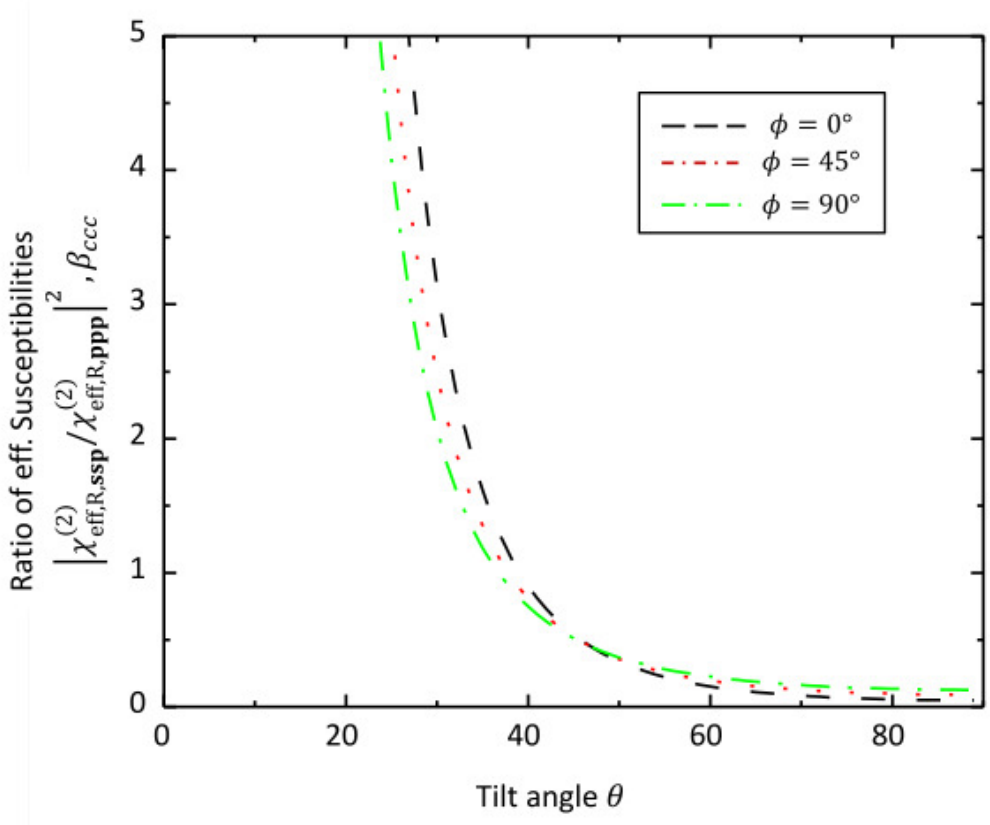

Figure 5.20. A plot of the ratio of effective second-order nonlinear susceptibilities for ssp and ppp polarisations as a function of tilt angle θ for three different Euler rotation angles (ϕ).[62]

The 'Master Equation'

To simplify the number of variables yet further and begin to develop an experimental method, one should consider a convenient special case where most parameters are kept constant; ideally a scenario where a single variable can be plotted and correlated to a tilt angle value according to Fig 5.19. It is indeed possible to quantify a single methyl stretch in both **ssp** and **ppp** polarisations and use a discrete calculation of γ to identify a molecular tilt, although there are many experimental factors which if not identified may result in erroneous comparative data. Several potential methods exist but the most convenient is to set VIS and IR polarisations to be constant and to vary only the SFG polarisation.

If the visible polarisation is conveniently set to $45°$ from p-polarisation and the IR is set to $0°$ from p-polarisation, the effective susceptibility can be described by

$$\chi^{(2)}_{\mathrm{eff,R}} = \sin\sigma \sin 45° \cos 0° \, \chi^{(2)}_{\mathrm{eff,R,}\mathbf{ssp}} + \cos\sigma \cos 45° \cos 0° \, \chi^{(2)}_{\mathrm{eff,R,}\mathbf{ppp}}$$

(Eq. 31)

where σ is the angle from p-polarisation of the SFG polariser. This can be simplified with some trigonometric relationships and the introduction of the γ term into

$$\chi^{(2)}_{\mathrm{eff,R}} = \frac{1}{\sqrt{2}}(\gamma \sin\sigma + \cos\sigma)\chi^{(2)}_{\mathrm{eff,R,}\mathbf{ppp}}$$

(Eq.32)

Returning back to Equation 14 in Chapter 3 and introducing the new expression for the susceptibility derived in Equation 32 gives a complete description of $\chi^{(2)}_{\mathrm{eff,R}}$

$$\chi^{(2)}_{\mathrm{eff,R}} = \frac{1}{\sqrt{2}} \frac{A_{\mathbf{ppp}}(\gamma \sin\sigma + \cos\sigma)}{\omega_q - \omega_{\mathrm{IR}} - i\Gamma}$$

(Eq. 33)

where $A_{\mathbf{ppp}}$ is the intensity of the molecular resonance in **ppp** polarisation, and ω_q and Γ are the resonant frequency and damping terms associated with it.

The final addition to the master equation for quantitative analysis of SFG spectra on TiO_2 with an orientational component is the interference and phase effects that come about due to so-called 'near-resonant' behaviour. Whilst sum-frequency generation is forbidden in the bulk, the incident electric fields are sufficient to partially excite the electronic structure at the surface of the

semiconductor in a less-intense but analogous fashion to the generation of the electronic non-resonant background response from metallic surfaces. The near-resonant response has been detected at all four polarisation combinations,[62] and its corresponding susceptibility term $\chi^{(2)}_{\mathrm{eff,NR}}$ is treated in a similar way to $\chi^{(2)}_{\mathrm{eff,R}}$ although with significantly fewer terms as it does not exhibit resonant-type behaviour.

When combined with the resonant description arrived at in Equation 33, the master equation can be fully set out as a function of frequency and SFG polarisation angle thus:

$$I_{\mathrm{SFG}}(\omega,\sigma) \propto \left| \frac{A_{\mathbf{ppp}}(\gamma \sin\sigma + \cos\sigma)}{\omega_q - \omega_{\mathrm{IR}} - i\Gamma} + (\gamma_{\mathrm{NR}} \sin\sigma + \cos\sigma) N e^{i\delta} \right|^2 + c$$

(Eq. 34)

Of the new parameters in this expression, γ_{NR} is a numerical weighting ratio which is derived from the effective susceptibilities of all four polarisation combinations (**ssp,spp, psp, ppp**). Experimentally, γ_{NR} is a constant that needs fixing via fitting procedures. N is the summed magnitude of the near-resonant susceptibility terms (again arrived at experimentally) and δ is the phase term, constant for all polarisation combinations, which governs the interference between resonant molecular and near-resonant sample responses. Finally, c is a constant which corrects for any additional contributions to the SFG background from such sources as fluorescence or nonlinear scattering processes which have been observed in other systems.[63, 64]

In summary then, the magnitudes of the sum-frequency response of a theoretical $-CH_3$ group have been calculated and plotted for varying light polarisations and molecular orientations. The dominant responses from **ppp** and **ssp** led to these being chosen as viable experimental combinations, and their variability under different molecular Euler rotations was somewhat negated by defining the ratio between the two, $\gamma = \frac{\chi^{(2)}_{eff,\mathrm{R},\mathbf{ssp}}}{\chi^{(2)}_{eff,\mathrm{R},\mathbf{ppp}}}$, and then using this variable to ascertain molecular tilt angles. In order to achieve this a 'master equation' was derived which integrated Equation 14 from Chapter 3 with both the γ term and a near-resonant response term, as well as introducing several necessary weighting factors and constants. Curves from this master equation will be plotted and correlated with measured SFG spectra, from which a range of likely molecular tilt angles will be extracted (see section entitled '*TiO_2(110) With Adsorbed Acetonitrile – Null Angle Method*').

5.4.3 Experimental Description

The laser system and experimental setup employed in the PSI for VSFS measurements has been described in detail in Chapter 4. Parameters that required further refinement or customisation for the TiO_2(110) measurements will be described here, as will the local sample environment for acetonitrile investigation.

Acetonitrile/TiO_2(110) Sample Environment

Preliminary acetonitrile spectra were taken prior to the introduction of the CaF_2 prism discussed in Section 4.5.9 and the prism cell was utilised for all subsequent measurements. The sample cell was designed with gas-flow capabilities in mind, but is otherwise composed of a chemically inert polymer, PCTFE, which has been machined to fit specifications. The prism cell design is illustrated in Figure 5.21 which indicates beam geometries and sample position, and also includes photographs of the experiment to demonstrate where the cell fits into the VSFS setup.

Gas-flow was not required for the acetonitrile investigation; instead a small liquid amount ($\sim$ 1-2 ml) of the solvent was introduced into the sample cell via a pipette and when sealed this created a saturated atmosphere in which the molecules would directly adsorb onto the sample (and cell) surface. Due to the high vapour pressure of acetonitrile and its tendency to escape through any available gaps into the lab atmosphere, the cell was designed with a tight seal reinforced by the use of PTFE tape as an O-ring. The window was attached to the cell front face with a low vapour pressure epoxy suitable for UHV applications so that it would not leach any solvents into the sample environment.

Work with the setup outlined here encountered issues with acetonitrile condensation on the inside face of the prism due to the temperature differential and internal partial pressure, and this condensation negatively impacted incident and output light intensities through absorption and scattering losses. To rectify this, a length of chemically inert polymeric tubing connected the in-flow and out-flow ports of the cell. The liquid acetonitrile was instead introduced into the tubing, which was kept at 0°C in an ice bath – this altered the partial pressure of the gaseous acetonitrile in the cell-tubing system and avoided any further window condensation.

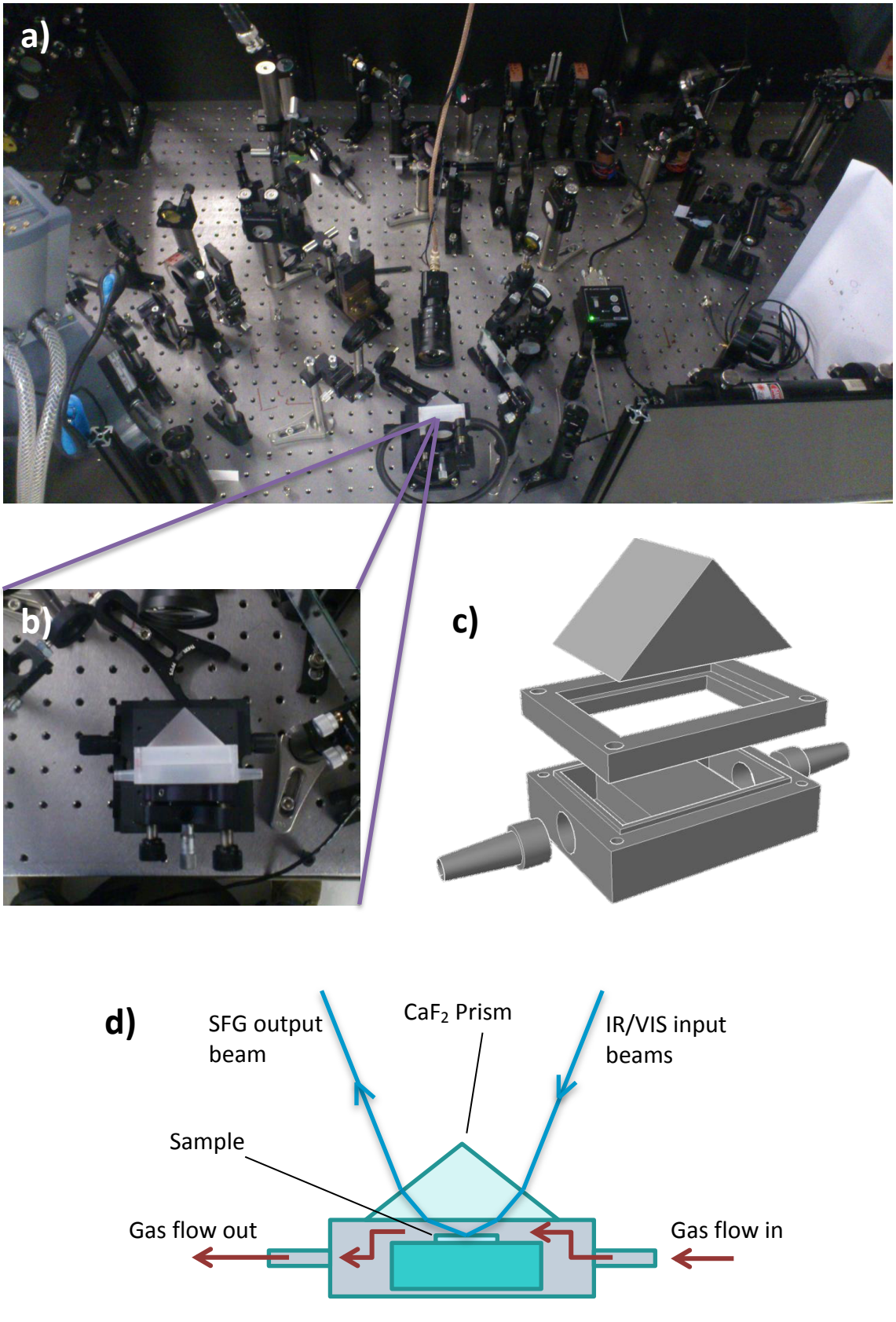

Figure 5.21. a) A photograph of the optimised VSFS setup in Manchester with b) an expanded view of the prismatic sample cell. c) shows a CAD design of the cell's internal construction, and d) is a side cross section of the cell illustrating the beam geometries, sample position and gas-flow orientation.

Specific VSFS Parameters

The infrared wavelength was occasionally shifted but left with its centre-energy around $2950\ \mathrm{cm}^{-1}$, the approximate energy of the acetonitrile symmetric stretching vibration. Incident powers were limited by the OPA efficiency, but typical energies of 15 mJ/pulse in the infrared and 20 mJ/pulse in the visible ($\sim$ 801 nm, depending on exact etalon angle) were utilised. Incident polarisations were set as defined in Equation 31 with the visible set at $45°$ away from p-polarisation (anticlockwise with respect to the beam propagation direction) and the infrared left at p-polarisation. The SFG polarisation angle σ was varied using a Glan-Taylor polarising beamsplitter cube, and the transmitted radiation was passed through a wavelength optimised quarter-wave plate to be incident on the spectrograph grating with a circular polarisation.

All spectra for TiO_2(110) were acquired in the photon-counting mode (discussed in section 4.5.4) due to the low SFG intensities experienced. Spectra were analysed at zero-delay and background-suppression pulse timings, and acquisition durations were chosen that would give sufficient signal-to-noise values. Due to the large number of variables and the sensitivity of both technique and laser system, absolute values of SFG intensity are not directly comparable between experiments. Incident powers, beam steering, temporal and spectral pulse profiles, and OPA emission frequency were all seen to vary after the regular and necessary optimisations that took place daily. Calibration procedures were performed regularly however, so the relative SFG intensities in any given experiment and the absolute resonance frequencies observed between experiments should remain rigorous and valid within error.

TiO_2(110) Incidence Angle Optimisation

In Section 5.4.2 a derivation for the sum-frequency intensities was arrived at in terms of the incident E-fields (IR and VIS) and the respective incidence angles and refractive indices contained within the Fresnel sum-frequency L-factors (Equation 28). Refractive indices for common media and those involved in this investigation were obtained and inserted into the expression, from which plots relating SFG signal and input IR/VIS incidence angles could be generated. Relative SFG maxima are seen to differ greatly between polarisation combinations as expected, and some pertinent plots are presented in Figure 5.22, which shows angle-dependent intensity maps for the air-gold and air-TiO_2 interfaces at **ppp** and **ssp** polarisations.

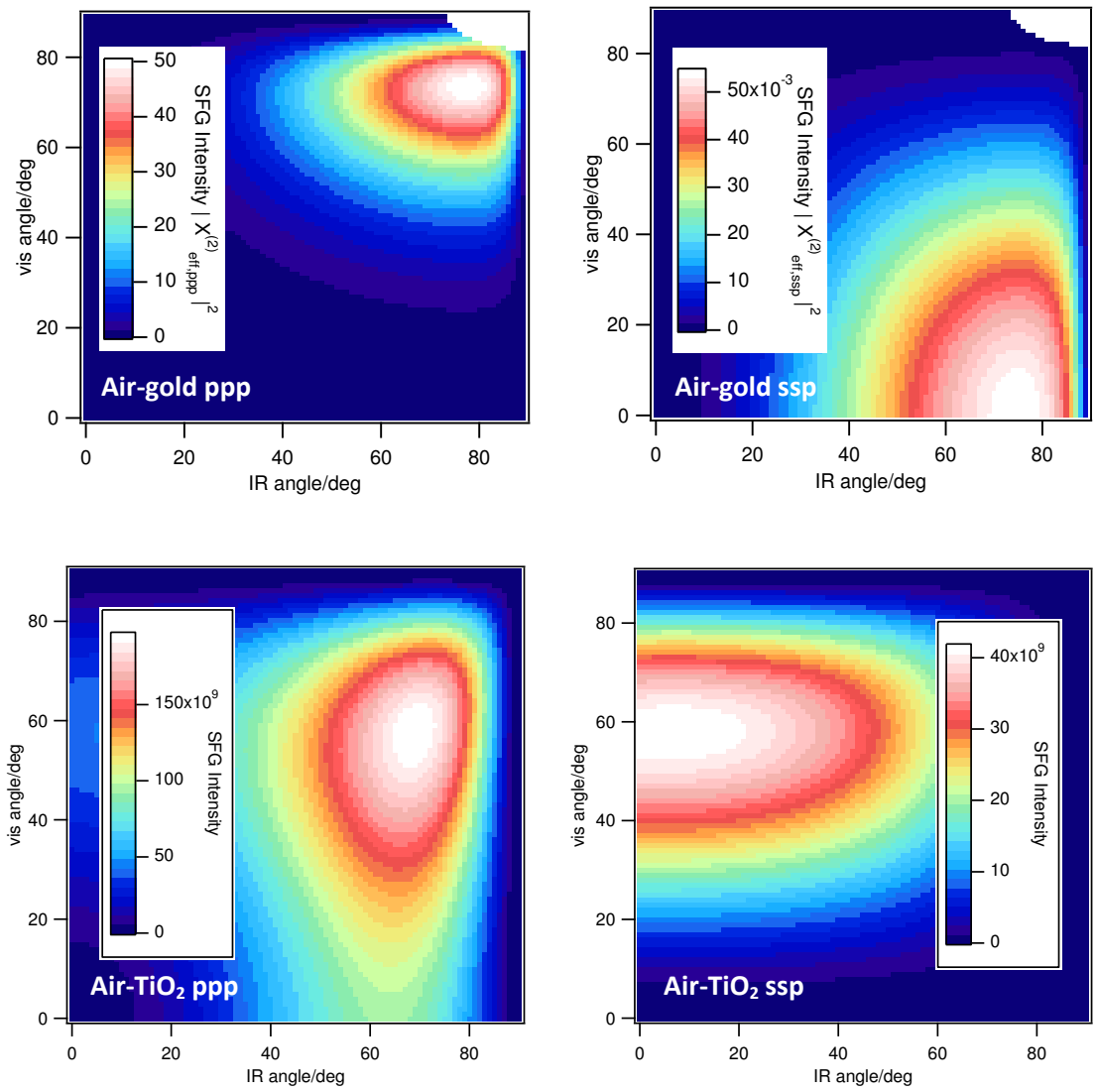

Figure 5.22. Plots of SFG intensity vs. beam incidence angles for gold and TiO2 at ppp and ssp polarisation combinations.

From Figure 5.22, it is apparent how 'optimum' incidence angles (those judged to give sufficiently high sum-frequency generation efficiencies) vary between materials and polarisation combinations and so compromise values were decided upon. The VSFS system was at the time being concurrently used to investigate metallic substrates whose ideal incidence angles would correlate more closely with those shown for gold in the above plot, and any large alterations to visible and IR incidence angles would require a not-insubstantial rearrangement of beam steering and collection optics. For theoretical and spatial reasons, angles of $\sim 55°$ for the IR and $\sim 65°$ for the visible beam were chosen for sample incidence and these were translated using the prism plot in Figure 3.31 into cell incidence angles. The system was designed so that these angles could be easily adjusted by $\pm 4°$ which after prism diffraction corresponds to an effective incidence angle adjustable range of $\pm 10°$ (see Figure 4.32).

5.4.4 Results & Discussion

TiO_2(110) Crystal Orientation

For the material refractive index to be in keeping with the modelling and data fitting parameters the crystal's optic axis had to be set as the y-axis in the laboratory geometry. To ascertain the optics axis for each crystal investigated, both optical and LEED techniques were employed.

Due to the birefringence of TiO_2, light interacting with its surface behaves differently in a macroscopically observable fashion depending on the orientation of the crystal face. It was known that the edges of the crystal corresponded to its $[1\bar{1}0]$ and $[001]$ axes but which edges required identification, and this was done by comparing measured reflectivity values with the theoretical curves derived from the Fresnel reflectance mentioned in Sections 4.5.9 and 5.4.2. Fresnel reflectivity curves for 800 nm light on TiO_2 are plotted in Figure 5.23 for the two situations in which the optic ($[001]$) axis of the crystal is parallel to the experimental x- and y- axes respectively. Included in the plot is the ratio between reflectivities of p- and s- polarised light, which will be constant independent of incident powers.

A wet chemically prepared TiO_2(110) sample was mounted on a vertical optic mount in the path of the 800 nm visible beam after pulse- shaping, intensity control, and polarisation control optics, and oriented at approximately $50°$ to the beam. The reflected 800 nm light was coupled directly with a laser power/energy meter (Orphir Optronics) and reflected intensity recorded; this was done for both p- and s- polarised light and the ratio between the two calculated. This was performed for two different sample rotation orientations **a** and **b**. Experimental values found matched closely with those predicted, within the error on angular measurement, as shown in Table 5.3.

To confirm the findings of the reflectometry investigation, the first TiO_2 sample investigated was then placed into a UHV chamber and LEED analysis was performed. The observed LEED spot pattern corresponded to a (1×1) surface termination with its long axis as predicted optically. Thus sample orientation was measured and confirmed.

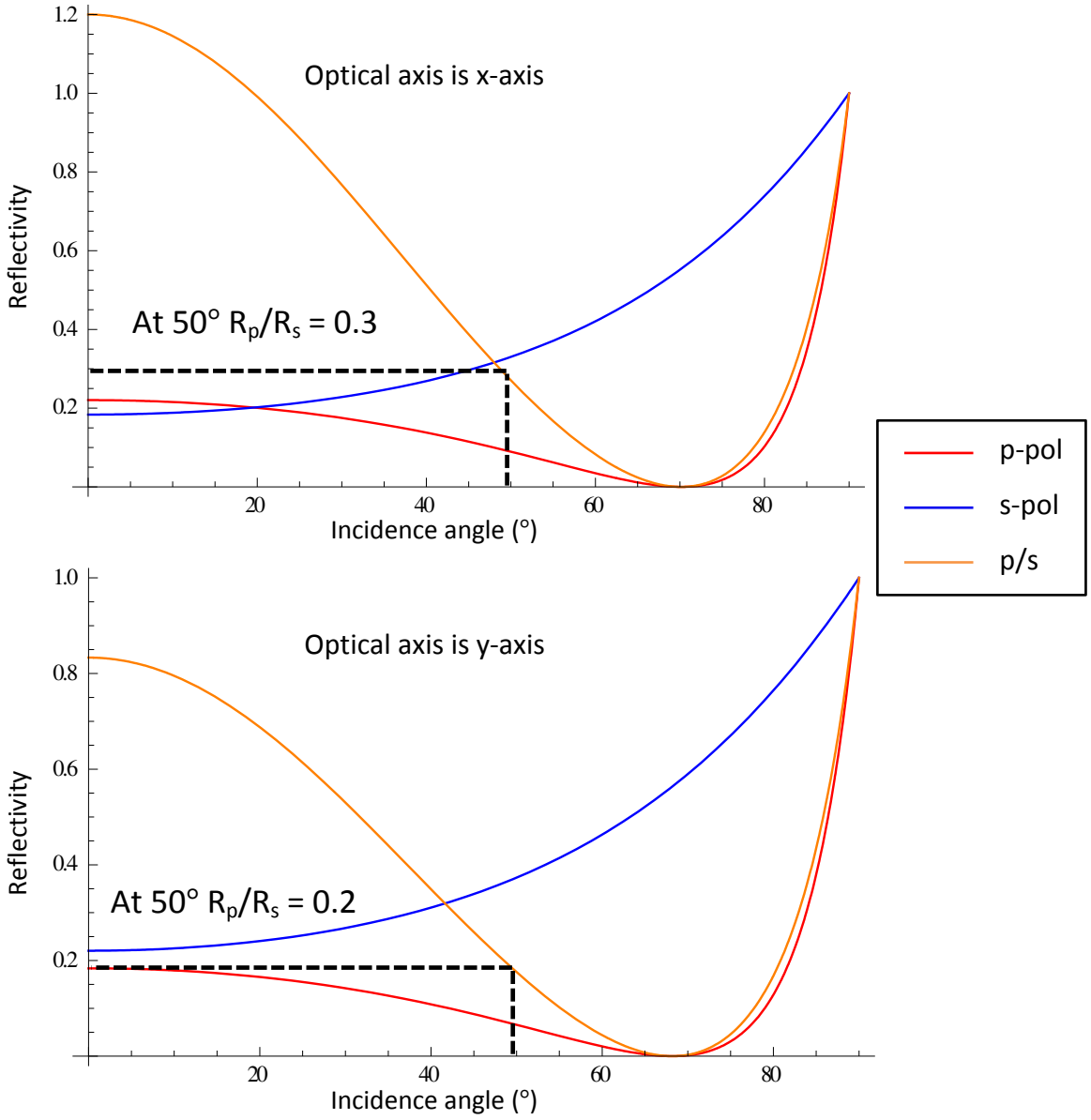

Figure 5.23. Fresnel reflectivity curves for TiO_2 at 800 nm with crystal optic axis in two different laboratory orientations.

Orientation	a	b
Reflected intensity R_p	8.21 mW	5.90 mW
Reflected intensity R_s	25.83 mw	27.31 mW
R_p/R_s	0.318	0.216
	Optical axis=X	**Optical axis=Y**

Table 5.3. Measurements of reflected power for different light polarisations off TiO_2(110), to ascertain crystal orientation.

Preliminary Work at the University of Houston

The first VSFS work involving wet-chemically prepared TiO_2(110) and adsorbed acetonitrile was performed during collaborative work at the University of Houston, Texas USA. In comparison to the Manchester system, the experimental system employed at the laboratory of Dr S. Baldelli involves much longer duration light pulses and thus is a narrow-bandwidth scanning VSFS system. The amplifier outputs 1064 nm pulsed light with pulse durations of 20 picoseconds at a repetition rate of 20 Hz; part is this is used to pump an OPA for the IR light and part is converted via second-harmonic generation into visible light at 532 nm. The two beams are similarly overlapped spatially and temporally, and generated SFG is measured from a monochromator/ photomultiplier tube (PMT) pair. To allow for the variation in IR intensity over different wavelengths and any vapour absorption, the reflected IR is picked off and mixed with visible light once more in a photoactive crystal to create a second non-resonant SFG signal for signal correction, which is measured simultaneously. Both IR and visible light are 20 ps pulses, and these give a spectral resolution of $\sim 8\ \mathrm{cm}^{-1}$ from 2000-4000 cm^{-1}.

Initially there were some significant issues with the cleaning of the surface carbon contamination, raw unprocessed spectra from which are shown in Figure 5.24. Surface contamination in the C-H region was clearly identified, but initial in-air UV exposure yielded little result. Subsequent UV exposure in a vacuum cell pumped down to 5×10^{-5} Torr as well as one flooded with pure gaseous O_2 had a minimal effect on the carbon response, as did submersion in piranha solution (H_2SO_4 and H_2O_2) which is an otherwise highly effective method for the removal of organic species.[65] A clean SFG surface response was only seen after an increase in the incident power of the UV irradiation, also performed in-air, as evidenced in Figure 5.24e). Surface cleanliness was again confirmed via sessile water droplet contact angle check.

Visual analysis of these spectra yields a helpful illustration of the nature of the adventitious carbon response and thus goes some way to informing signal expectations from the broadband system. Due to the narrow-band pulse profiles and the secondary reference SFG channel, all obtained spectra should be over an effectively flat baseline corresponding to the frequency-independent surface response (plus experimental background levels). Interestingly, other than the sharp resonance exhibited around 2970 cm^{-1} and some smaller features around 2860 cm^{-1}, 2880 cm^{-1}, 3010 cm^{-1} and 3030 cm^{-1}, there is a very broad resonant addition to the SFG response starting at 2730 cm^{-1} and ending around 3000 cm^{-1}. Such broad features could be a result of multiple C-H molecular bonds in different local chemical environments, or also indicative or the relative orientations or lifetimes of the bond present.[66, 67] Relative to the spectral

bandwidth of the incident IR pulse ($\sim 200\ \mathrm{cm}^{-1}$) this broad resonant region would be difficult to resolve via broadband VSFS and would appear as a frequency-dependant 'resonant background', which should be taken into consideration if quantitative analyses are to be made of the system.

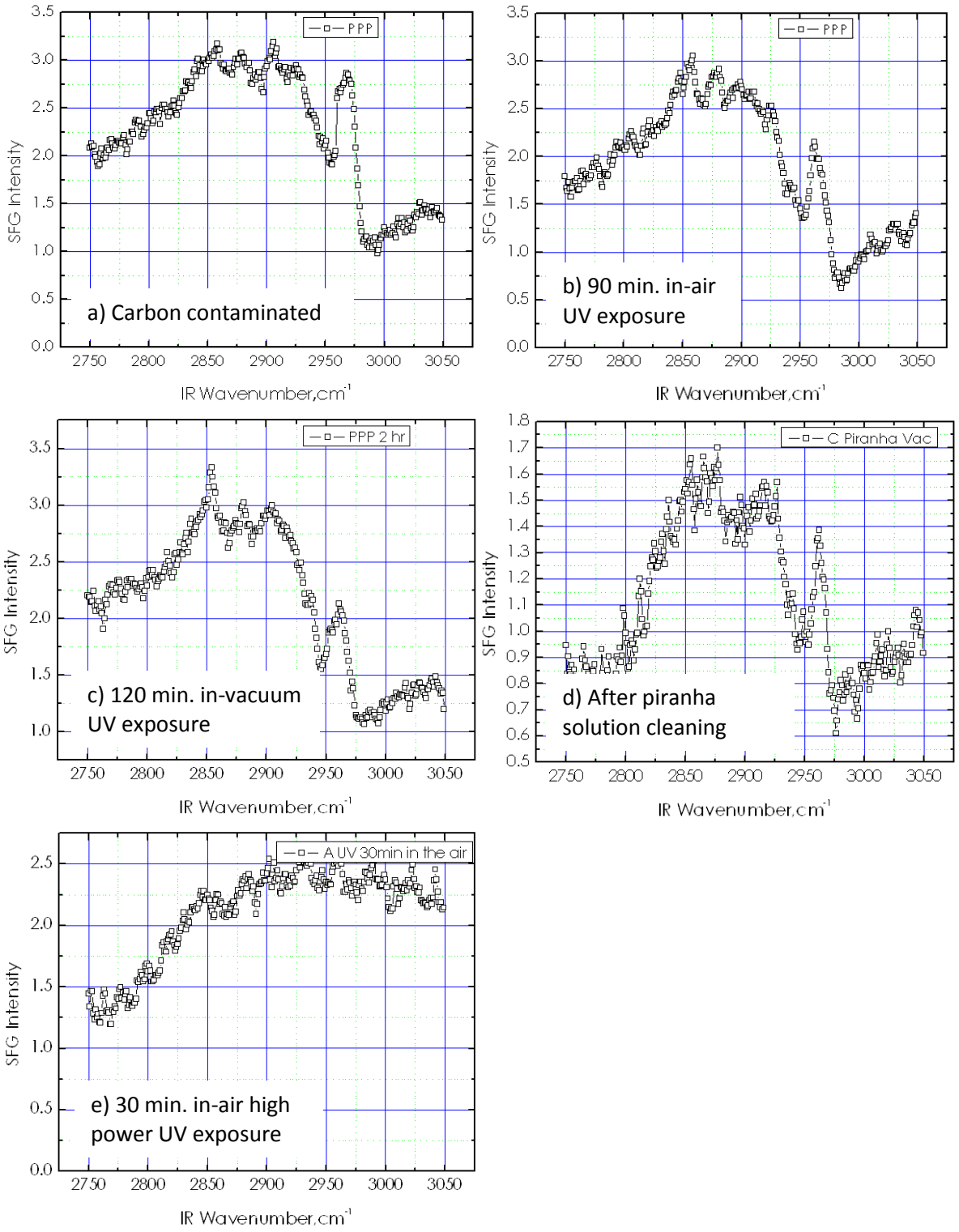

Figure 5.24. Narrow-bandwidth VSFS spectra detailing the organic cleaning attempts for carbon-contaminated TiO_2(110) examine over the C-H stretching region.

Due to the issues encountered during carbon cleaning, acetonitrile measurements were acquired via the use of a polymer sample cell at atmospheric pressure rather than the silica vacuum cell originally planned – the act of pumping down the cell seemed to consistently re-introduce surface carbon, potentially from the diffusion pumps. Liquid acetonitrile was placed in a small enclosed reservoir in the cell and this was exposed after SFG confirmation of surface cleanliness. As expected, a strong vibrational resonance was detected from at 2945 cm^{-1}, corresponding to the acetonitrile symmetric -CH_3 stretching mode. The expected antisymmetric stretching mode at 3005 cm^{-1} could not be resolved by the system, suggesting the average acetonitrile molecule orientation to be relatively close to surface normal. Initial SFG spectra for both **ppp** and **ssp** polarisations are shown in Figure 5.25, which also shows the effectiveness of UV-cleaning for removal of acetonitrile and return to a flat baseline scenario.

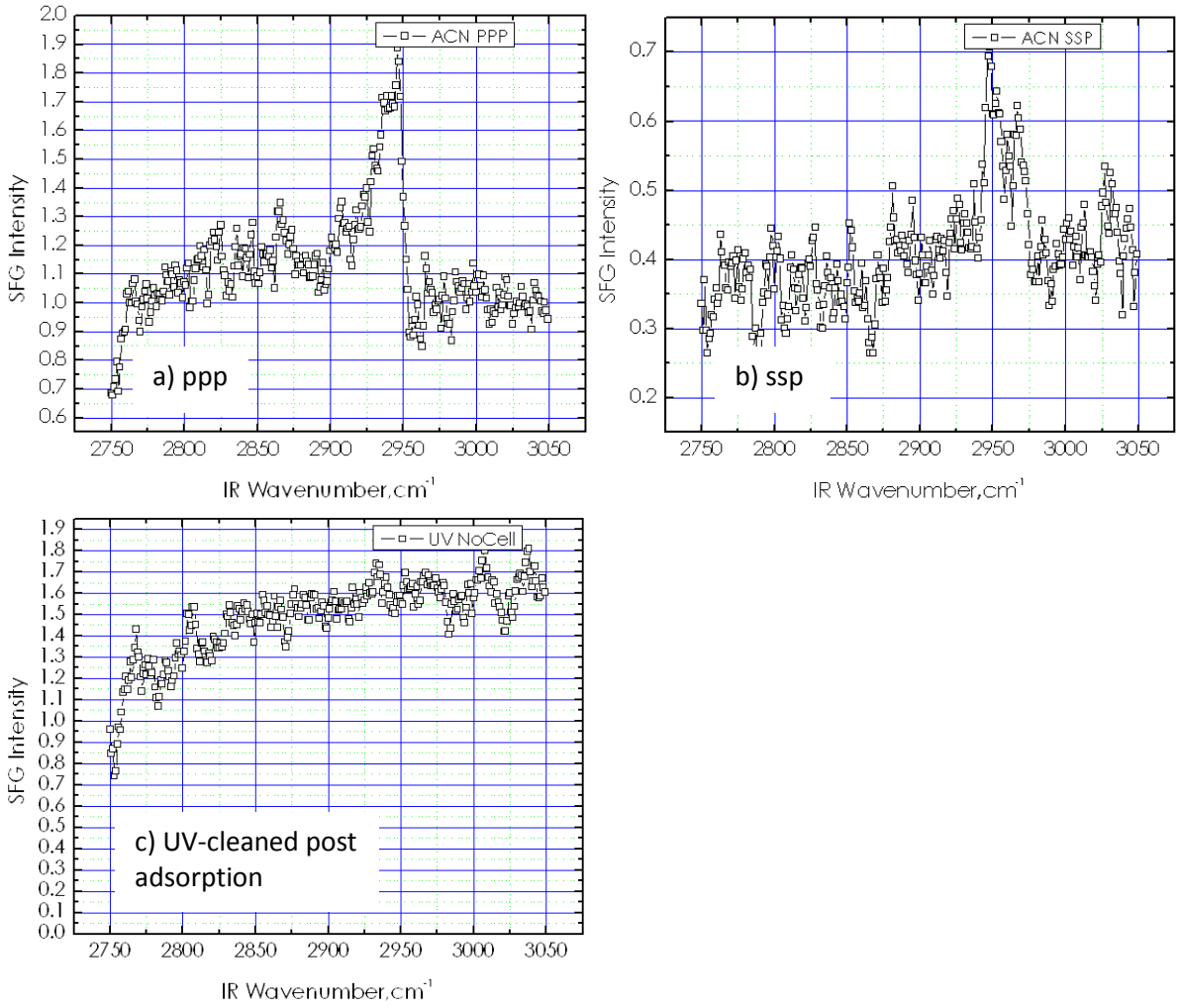

Figure 5.25. Initial observation of acetonitrile symmetric C-H stretch on TiO_2(110) from the narrow-bandwidth VSFS at the University of Houston in a) ppp and b) ssp polarisations. Subsequently UV-cleaned surface is also shown in c).

The presence of a resonant peak in the **ssp** polarisation combination confirms the feasibility of the theoretical model laid out in Section 5.4.2. It also confirms that the molecules must on average be oriented away from the surface normal, as there would be no resonance in **ssp** if the molecules were perpendicular to the surface, due to polarisation/geometric considerations – see Figure 5.19 for tilt angle $\theta = 90°$.

Scans taken of the same TiO_2/acetonitrile system to observe any time-evolution behaviour saw a decrease in the strength of the symmetric -CH_3 resonance over time, with noticeable peak reductions $\sim$ 30 minutes after solvent exposure. This was attributed in part to a poor seal on the sample cell, as the liquid in the reservoir had gone after this period, but this does not also rule out some effect from the laser energy incident on the surface over this time (which for the shorter pulses of the broadband system would involve considerably higher peak powers over much smaller durations).

TiO_2(110) With Adsorbed Acetonitrile – Initial Attempt

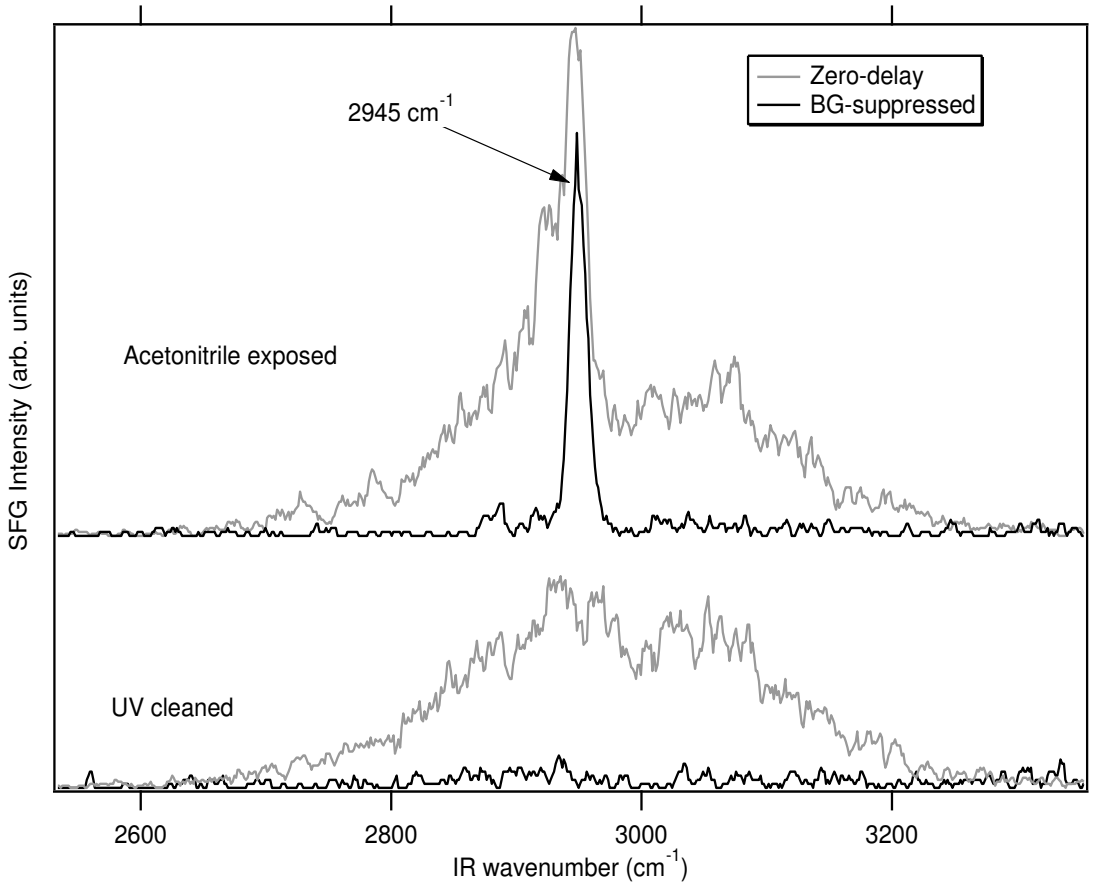

Figure 5.26. Initial ppp SFG spectra of the TiO_2(110)-acetonitrile interface at zero-delay ($\tau = 0$) and background-suppressed ($\tau = 800$ fs) timings. UV-cleaned TiO_2 substrate spectra are shown for comparison.

The symmetric -CH_3 stretching mode from acetonitrile adsorbed on TiO_2(110) was observed utilising the VSFS system at The University of Manchester, described in detail in Chapter 4. Spectra were taken initially at **ppp** polarisation in both zero-delay and background-suppressed timing modes, with an IR centre-frequency of $\sim$2950 cm^{-1}. These spectra are shown in Figure 5.26 with the UV cleaned pre-exposed spectra for comparison. Importantly the UV-cleaned sample prior to acetonitrile dosing exhibits no C-H resonance features resulting from surface carbon contamination.

Acetonitrile on TiO_2(110) Time-evolution

The initial experiment probing the symmetric acetonitrile methyl stretch on TiO_2 in the **ppp** polarisation configuration noticed some time-related reduction in the resonant signal which was a cause for some concern, especially considering the necessarily long acquisition durations. A summary of some zero-delay spectra over the first hour after molecular exposure is presented in Figure 5.27, and although possessing a poor signal-to-noise the corresponding background suppressed spectra (not shown) also suggested a similar trend. After SFG acquisition was completed, a visual inspection of the sample cell system revealed the liquid acetonitrile to have vaporised completely as also noticed in the initial work from Houston. Additionally, a small amount of beam damage was visible via a blackening of the adhesive on the rear face of the TiO_2 crystal. Aside from the overall smaller resonant peak compared to other scans, the resonance feature at 2945 cm^{-1} is seen to almost fully disappear after one hour in the sample cell.

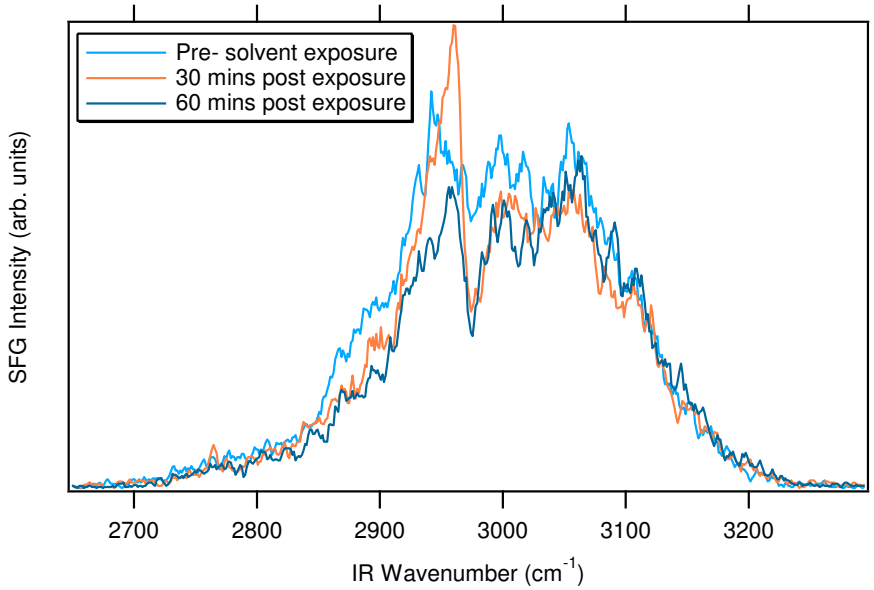

Figure 5.27. Zero delay SFG spectra showing the resonance degradation for the symmetric C-H stretch of acetonitrile on TiO_2(110) over 1 hour after solvent exposure.

Prior to the orientation analysis experiment this effect was investigated again. Whether the diminishing of the acetonitrile resonance was due to high incident powers, vapour leakage from the cell, or other unknown factors, steps were taken to utilise a more rigorous approach regarding the vapour cell system. A more intensively UV-cleaned substrate, improved cell sealing procedure, and lower incident pulse powers per unit area were employed, and the results from this experiment are shown in Figure 5.28, which shows the TiO_2 and molecular signals taken with background suppression up to four hours after solvent exposure.

Whilst some initial surface contamination is visible, the deviation from the expected Gaussian is more than acceptable for a UV-cleaned TiO_2 spectrum taken with a time delay on the visible pulse of $\tau = 800$ fs. The initial measurement of the C-H resonance first observed 30 minutes after solvent exposure and cell-sealing shows a strong and well-defined peak at 2944.5 cm^{-1} as expected, with only a slight increase in the 'resonant background' attributed to surface organics. After three and four hours in the sealed cell with the laser light continuously incident, the magnitude and shape of the symmetric resonance remained constant, with the only changes in the spectra being further increases in the additional C-H resonances from surface organics. The interpretation of this is somewhat difficult, as it would suggest a time-related evolution of the adventitious carbon response with no effect on the underlying acetonitrile adlayer. Ascertaining the relevance of these data would require a more detailed investigation to better define the physical interfacial region probed by the VSFS technique, and might necessitate the ability of the technique to resolve multilayer systems in a manner analogous to angle-resolved XPS procedures. This effect could also be explained by localisation considerations, whereby the acetonitrile molecules are present on the surface in a heterogeneous fashion, and adventitious carbon deposition is advancing on the more exposed surface oxide regions.

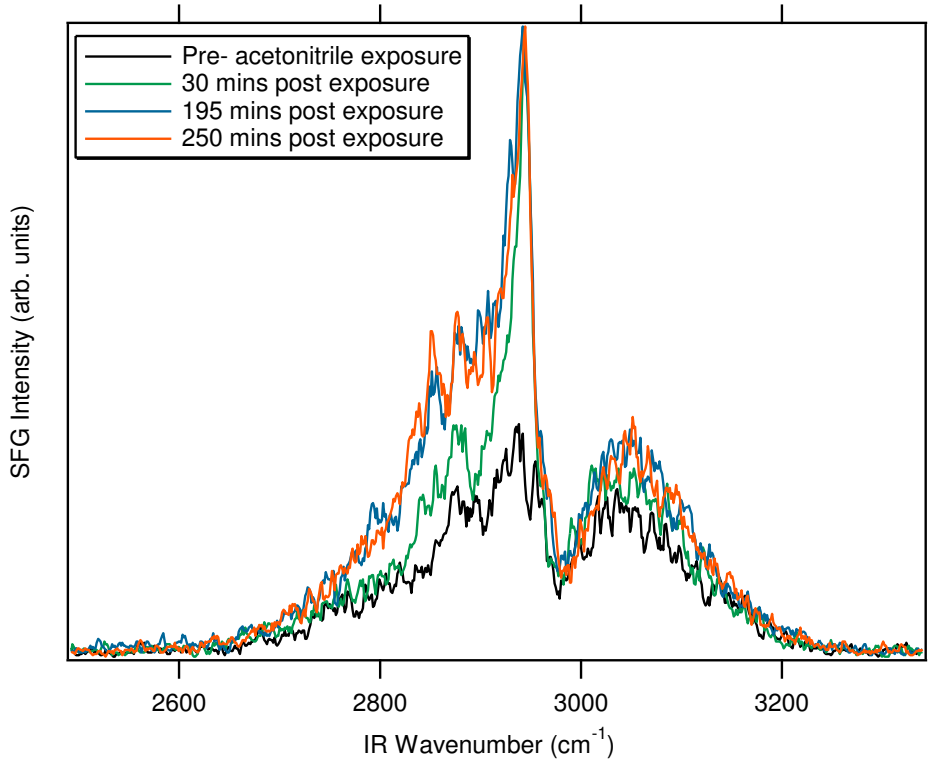

Figure 5.28. Background suppressed SFG spectra showing the time-dependent signal evolution of the -CH_3 stretch resonance from acetonitrile adsorbed on TiO_2(110).

TiO2(110) With Adsorbed Acetonitrile – Null Angle Method

Data acquisition & Analysis Procedures

Due to the obvious potential for measurement error when attempting to derive a γ value from pure **ppp** and **ssp** scans using a system with problematic polarisation control, the method chosen to obtain an estimate of molecular tilt was a 'null angle' method involving multiple scans using intermediate polarisations. This null-angle method heavily utilises fitting procedures using the 'master equation', and extracts γ values from the fit.[62]

To more accurately fit the obtained null angle scans requires resonant spectra relatively free from non-resonant contributions, and so a background subtraction technique was utilised. For every polarisation combination, scans were taken both with and without the adsorbed acetonitrile, and the spectra taken prior to molecular adsorption were treated as background scans and subtracted for the spectral fitting as illustrated in Figure 5.29. This was done both at zero-delay and with the inherent background suppression afforded by visible pulse delay, yielding two different scans for γ value comparison. The angles used for acquisition are defined in the derivation in Section 5.4.2, and following the prescribed ordering of (SFG,VIS,IR) are Combination 1 (0,45,0) and

Combination 2 (45,45,0), where numbers in the brackets correspond to degrees from p-polarisation anticlockwise with respect to beam propagation direction.

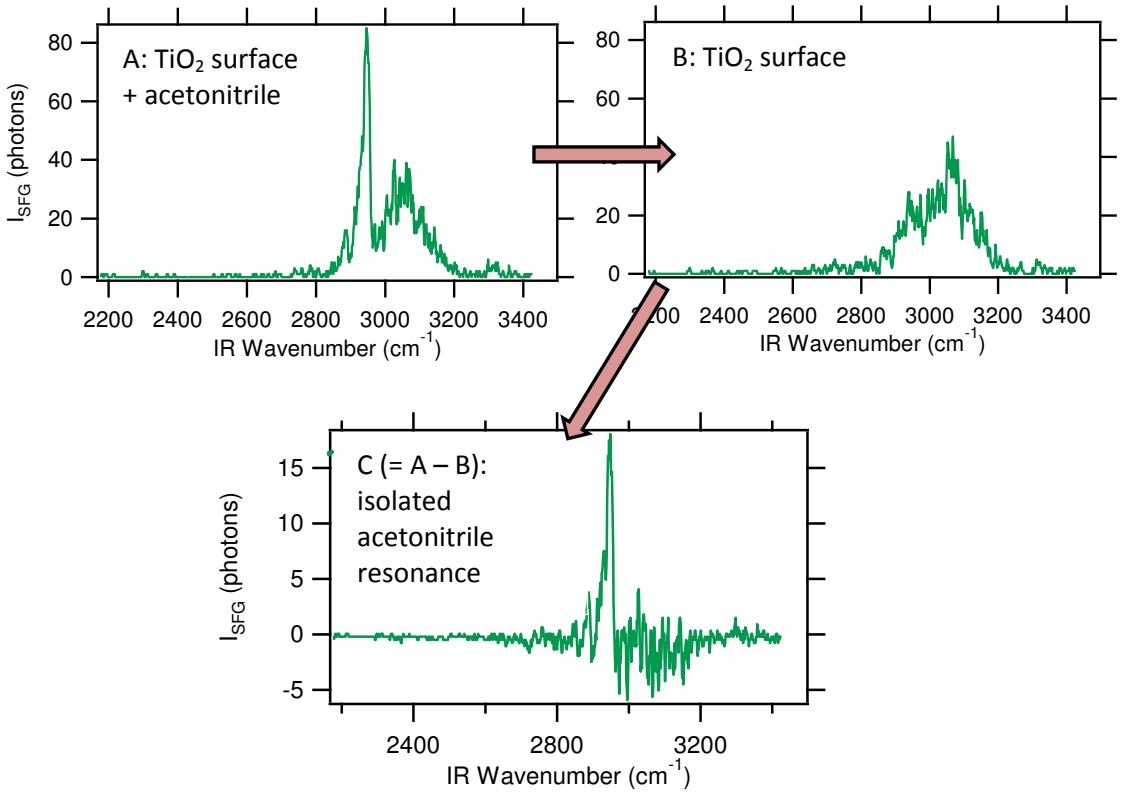

Figure 5.29. Illustrated example of the background subtraction procedure for acetonitrile-dosed TiO_2 spectra acquired with background-suppression timings. Spectral fitting is then applied to spectrum C.

The pseudo background subtraction employed prior to spectral fitting was partially used as a response to the complex adventitious carbon response. The master equation runs into complications in situations involving multiple vibrational resonances, as vibrations will interfere with one another as well as with the electronic surface response, making equation parameters derived from the spectral fitting inherently less reliable. As the antisymmetric -CH_3 stretch from acetonitrile is minimal (below detection limits), subtracting the surface spectrum prior to vapour exposure should more effectively isolate the symmetric -CH_3 stretch peak and avoid the need for a complex multi-peak fitting. As background-suppression through delaying the visible pulse further isolates resonant from non-resonant spectral information, derived master equation parameters – especially γ – should be more reliable from the background-suppressed datasets.

Figure 5.30 shows the isolated acetonitrile resonances taken via VSFS from previously wet-chemically prepared TiO_2(110), including the spectral fits for both zero delay ($\tau = 0$) and background suppressed ($\tau = 750$ fs) pulse timings. Spectral fits were acquired for both pulse timings and with an unrestricted simultaneous fit between $\sigma = 0°$ and $\sigma = 45°$ spectra. The idea of polarisation mapping (or 'null angle' analysis) is that all parameters ($A_{\mathbf{ppp}}, \gamma, \Gamma, \omega_0$ etc) are the same, and any signal change only arises due to variation of the SFG polarisation angle, σ. Hence, simultaneous fitting of a number of similar curves at various σ regards all parameters as shared or common. Thus, they are not restricted to any value but will have same value for all sets of curves (in this case just two, $\sigma = 0°$ and $\sigma = 45°$). Values for γ from each fit are summarised in Table 5.4, and presented graphically in Figure 5.31. The 'master equation (Equation 34) is restated here for convenience:

$$I_{\mathrm{SFG}}(\omega, \sigma) \propto \left| \frac{A_{\mathbf{ppp}}(\gamma \sin\sigma + \cos\sigma)}{\omega_q - \omega_{\mathrm{IR}} - i\Gamma} + (\gamma_{\mathrm{NR}} \sin\sigma + \cos\sigma) N e^{i\delta} \right|^2 + c$$

(Eq. 34)

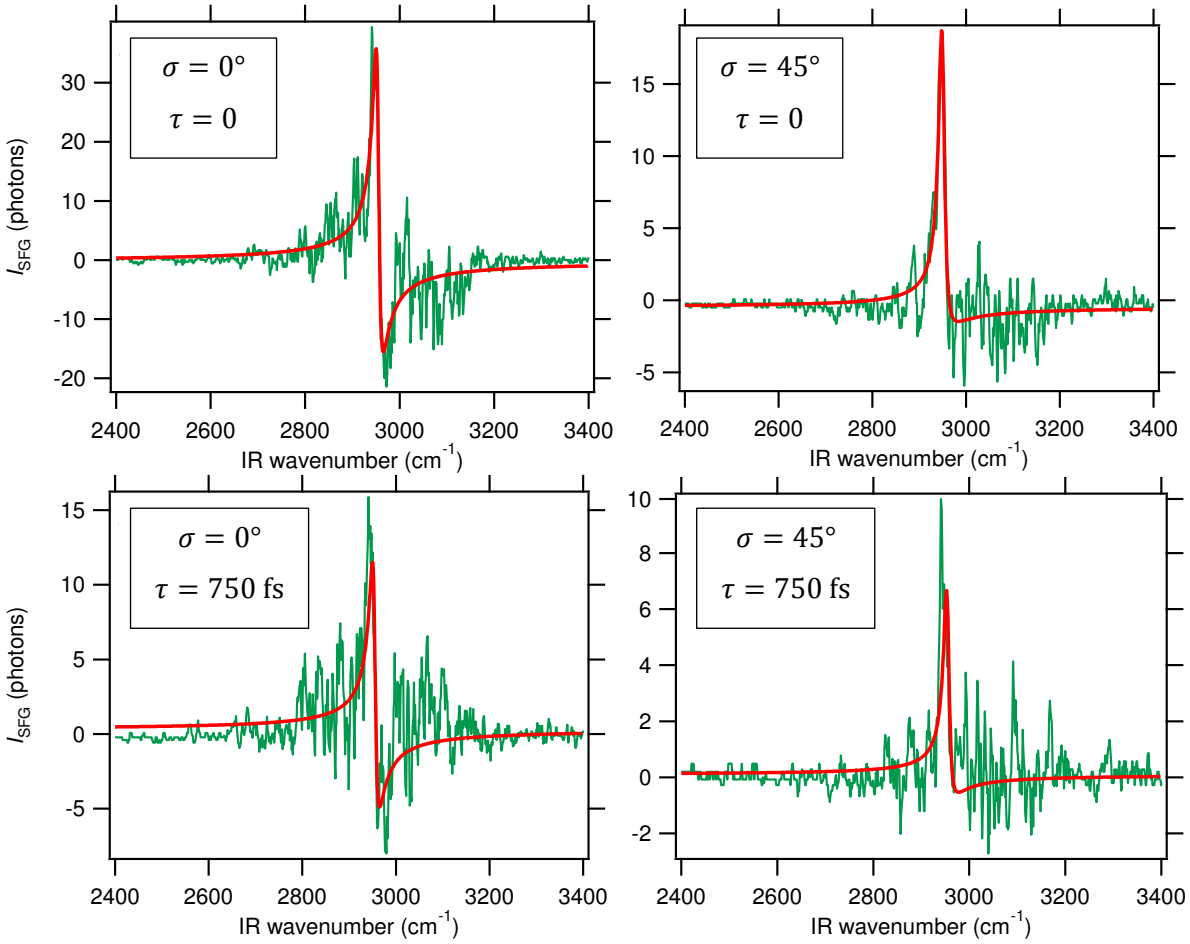

Figure 5.30. Isolated VSFS acetonitrile resonances taken off TiO_2(110) with varying SFG polarisation angle σ and visible pulse time delay τ, including spectral fitting plots.

τ (fs)	A	ω_q (cm^{-1})	Γ (cm^{-1})	N	δ(°)	c	γ (γ^2)	γ_{NR}	θ(°) (error min/max)
0	32.5	2953	7.43	1.84	22.7	-23.4	-0.477 (0.23)	2.56	**24.2 (21/27.5)**
750	10	2947	8.29	4.44	89.5	-60.2	-0.42 (0.18)	2.19	**27.7 (12.7/65)**

Table 5.4. Parameters derived from spectral fitting of acetonitrile SFG resonances. Calculated molecular tilt values have been found for $\phi = 45°$.

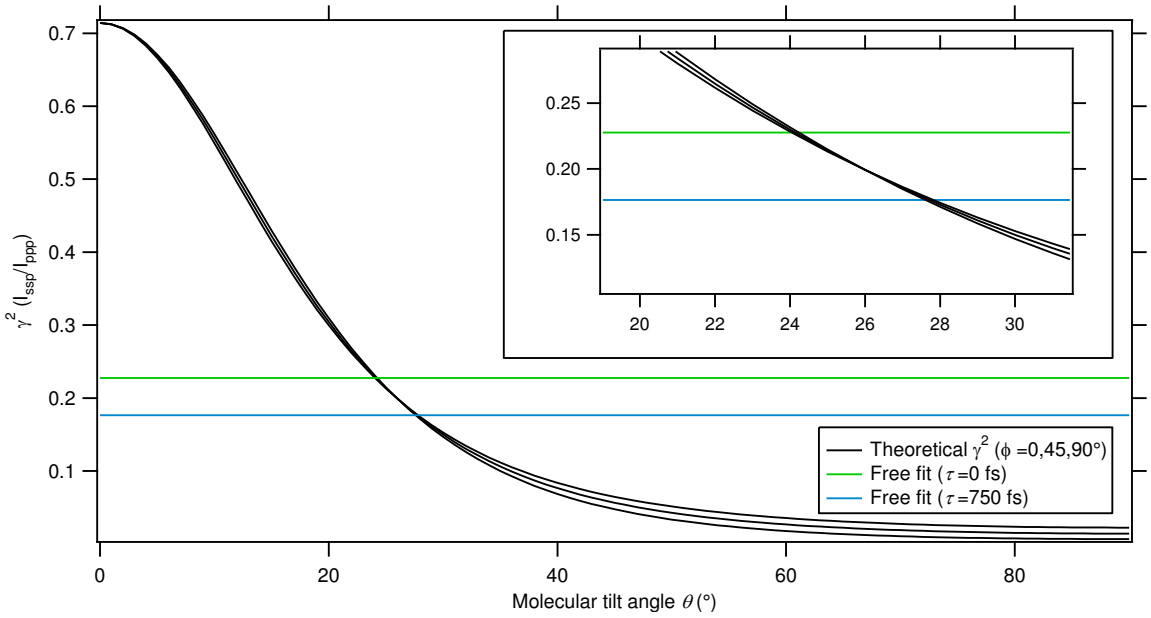

Figure 5.31. Graph of the theoretical γ^2 versus molecular tilt angle for acetonitrile on TiO_2(110) derived from Equations 30 and 34, showing the experimental intercepts taken from Table 5.4. A magnification of the region of interest is also inset.

Discussion

As seen in Table 5.4, angular tilt values from both fitting regimes fall around $\theta = 25°$. The theoretical curves show little rotational (ϕ) dependence over this range and so this investigation will only consider the central theoretical plot which corresponds to $\phi = 45°$.

The resonant frequency ω_q is seen to shift slightly from $\tau = 0$ to $\tau = 750$ fs, likely as a result of pulse distortion such as spectral chirp. Also, the summed magnitude of near-resonant terms N would actually be expected to change with polarisation owing to the heterogeneity of the TiO_2 surface electronic response which may cause some minor discrepancies with physical relevance.

The two derived values for molecular tilt are within close error of one another, but the error associated with the $\tau = 750$ fs fit is significantly larger owing to apparent feedback between fitting parameters when attempting to fit to the noisier spectrum. As such it is deemed reasonable to quote the tilt value and error for the $\tau = 0$ fitting, whilst considering the alternative angle good supporting evidence for its veracity. Thus the adsorbed acetonitrile molecules were found to possess an overall average tilt orientation of $\theta = 24° \pm 3°$.

Sources of Error

In considering experimental error several factors must be considered. Firstly the mathematics involves averaging the molecular orientations over the local area under investigation, whereas physically a small range of tilt angles are being probed; on well-ordered self-assembled monolayers for example variations in tilt angle of have been previously observed, although these were long-chain thiol molecules with more potentially for molecular distortion.[68] For the TiO_2-acetonitrile system, some variation might be expected resulting from smaller molecular vibrations/librations, which would mean a narrow distribution of orientation values. Furthermore, the fact that sample preparation and measurements were performed in-air could result in orientation variance from the inevitable localised surface contamination, which could potentially lead to small-scale topographical effects. Some error will also arise from the background subtraction process, where a more rigorous examination should include multi-peak deconvolution procedures.

Aside from some polarisation issues encountered in the initial investigation and other potential issues with the optical methods, the high light intensities and long acquisition durations required for the study could mean the system under investigation is not necessarily a static one. Any system changes in the surface molecular density or orientation of adsorbates would lead to difficulties comparing related spectra. Nonetheless, care was taken to ensure sample cleanliness and ordering, and checks throughout sufficiently minimised sources of major deviation in the results, meaning a good degree of reproducibility was maintained. Quoted values of molecular tilt agree within error with equivalent values found in our collaborative work at the University of Houston.[62]

TiO2(110) With Adsorbed Acetic Acid

Acetic acid (CH_3COOH), illustrated in Figure 5.32, is a simple organic molecule which possesses the same functional -CH_3 group as acetonitrile. It is used extensively in chemical and molecular synthesis, as well as being responsible for the common odour and characteristics of most vinegars.[69] For this study, it was investigated in addition to the acetonitrile as the same methodology and modelling could be applied to analysis via VSFS. As such it could aid in confirming the strength of the orientational SFG technique.

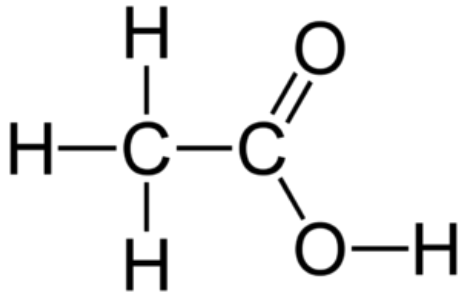

Figure 5.32. Skeletal forumal for the acetic acid molecule.

Several previous studies have investigated acetic acid adsorption on the TiO_2 surface and the acetate-rutile TiO_2(110) system is relatively well-characterised.[4, 70] Fundamental work investigating photocatalytic oxidation/decomposition of adsorbates[71-73] has complemented more applied studies regarding efficiency improvements for dye-sensitise solar cells[74, 75], or thin film TiO_2 deposition.[76] Additionally some VSFS work has been performed to investigate the orientation of the symmetric -CH_3 stretch on the surface of an acetic acid/water solution.[77]

The VSFS setup outlined in Chapter 4 was utilised with the prismatic vapour sample cell as in the acetonitrile investigation. UV/ozone cleaned TiO_2 was confirmed well-ordered and relatively free from surface contamination, and a small amount of liquid glacial acetic acid was introduced to the cell which was then sealed. The vapour pressure of the acid is such that again a liquid amount in a sealed environment should produce a vapour saturated atmosphere, and this was supported by the notable presence of the strong, characteristic odour of the acid that was present in the laboratory atmosphere after cell dosing. Initial attempts at examining the methyl stretch resonance through SFG techniques is shown in Figure 5.33, in which the expected symmetric -CH_3 stretch is seen to appear at $\sim 2944\ \mathrm{cm}^{-1}$ in the **ppp** polarisation configuration after dosing.

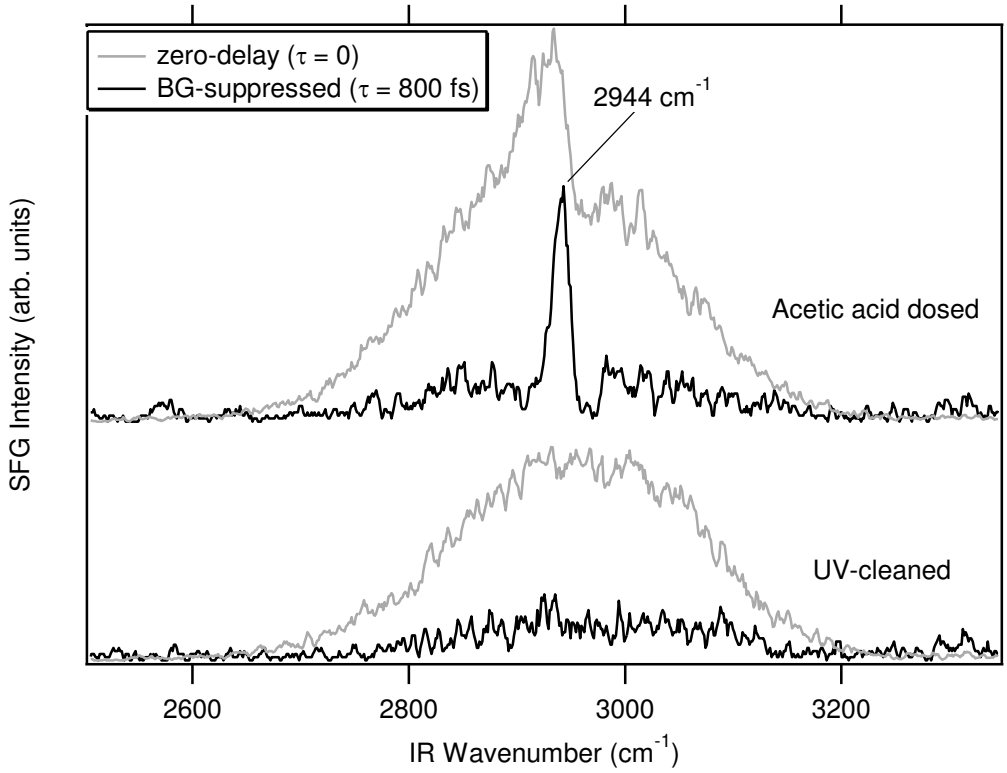

Figure 5.33. Initial ppp VSFS spectra for acetic acid adsorbed on TiO_2(110) in both zero-delay ($\tau = 0$) and background-suppression ($\tau = 800$ fs) pulse timing configurations, with clean TiO_2 surface for comparison.

In comparison to the initial results from the acetonitrile, the intensity of the vibrational resonance at zero-delay relative to the non-resonant background signal is much weaker, which is also apparent in the background-suppressed timings. Nevertheless, the spectral response was deemed sufficient to proceed with an orientational analysis using the 'null angle' polarisation combinations

The first 'null angle' polarisation configuration SFG spectra are shown in Figure 5.34, which have been taken at (0°,45°,0°) polarisations (SFG,VIS,IR). When compared to the previous acetic acid spectrum, the increase in resonant signal after introduction of the acetic acid is significantly less well-defined, and the background-suppressed pulse timings suggest a scenario involving several other integrated C-H stretch resonances at different energies. The additional polarisation configurations were acquired but as these deviate further from the intensity-optimal **ppp** configuration the associated signal strengths were weaker and the symmetric C-H stretch resonance equally less well resolved. Fitting procedures were attempted but owing to the additional resonant contributions these were unable to effectively fix the necessary fitting parameters even after background subtraction. Time constraints on the project meant a repeat investigation was not attempted.

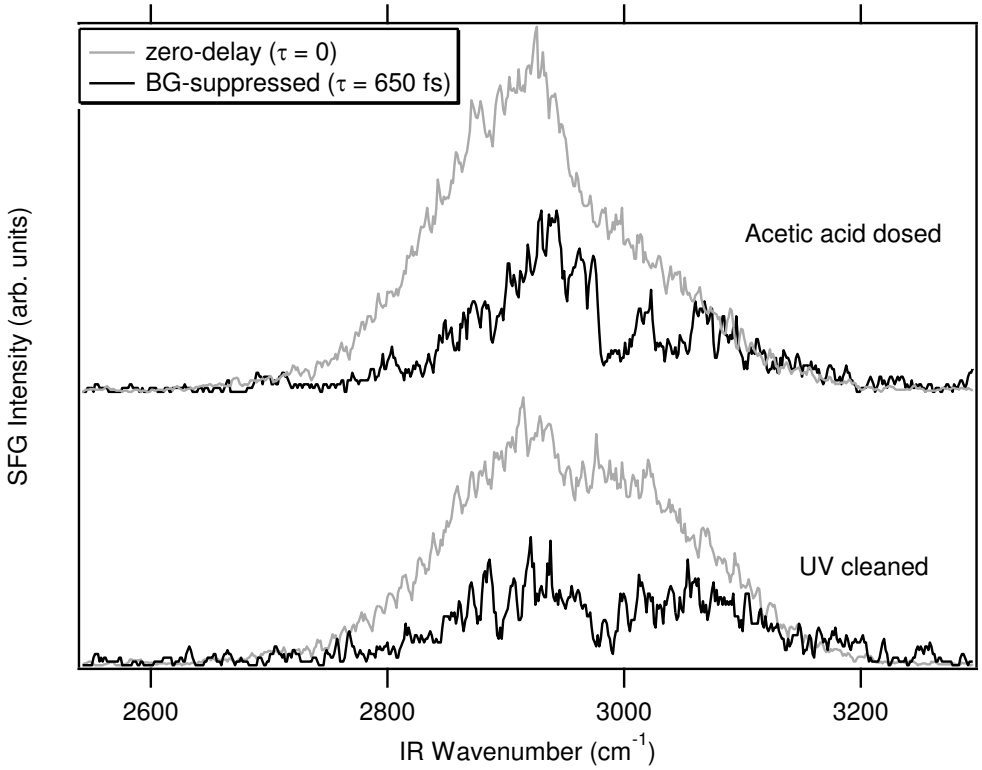

Figure 5.34. SFG spectra for acetic acid adsorbed on UV-cleaned TiO_2(110) taken with and without background suppression timings at a 'null angle' polarisation combination.

Visual analysis of the spectra in Figure 5.34 suggests a TiO_2 surface with a number of different organic species present at the surface. The signal-to-noise of all spectra are less than the previous scans owing to difficulties with pulse alignment and sum-frequency generation efficiencies, which at the time could not be improved upon without increasing the incident light intensities to levels likely to result in sample beam damage. The increase in the incident intensities which were applied relative to previous acetic acid and acetonitrile scans could be a potential reason for the diminished sharp resonant peak, as the literature reports numerous incidences of effective photo-degradation of carboxylic acids on the TiO_2 surface.[4, 78-80] Additionally, the spectra of the UV-cleaned surface prior to acid exposure shows a larger initial resonant signature from the adventitious organic contamination, and as seen previously in Houston and Manchester for the acetonitrile investigation the amount and degree of surface ordering of the molecular adsorption could be highly sensitive to surface cleanliness. In that regard, remembering that VSFS as a technique is highly sensitive to surface ordering and overall signals are dependent on average surface orientations, the prior presence of surface organics may be affecting the molecular adsorption such that induced vibrational dipoles are cancelling one another out.

A reassessment of the preliminary scans of acetic acid on the rutile surface taken at **ppp** polarisation in Figure 5.33 does however suggest that with a well aligned SFG system with better optimised overlap and pulse characteristics, the -CH_3 symmetric stretch resonance should be well resolvable and would then allow the orientational analysis to proceed.

5.5 Conclusion

A non-UHV method of TiO_2(110) surface preparation was performed and the resulting surface investigated by various characterisation techniques. Topographical analysis via AFM confirmed a flat and well-ordered interface with a resolvable monatomic step-and-terrace structure, with the (1×1) termination also confirmed via LEED[1]. Parallel chemical investigation by XPS, Auger1 and VSFS confirmed the lack of surface contamination, and thus the effectiveness of the wet chemical technique.

The TiO_2(110) non-UHV prepared surface was exposed to vapour-phase acetonitrile (CH_3CN), and the -CH_3 symmetric stretching mode was successfully detected from surface-adsorbed molecules via VSFS at $\sim$2945 cm^{-1}, a value consistent with similar investigations in the literature. The successful removal of the molecule and any accrued surface organics with a UV/ozone cleaning regimen was also confirmed spectroscopically.

Furthermore, variation of the incident light polarisations allowed for orientational determination of acetonitrile molecules on the rutile surface, an investigation which found an average molecular tilt angle of $\theta = 24 \pm 3°$ from the surface normal. This value agrees within error to derived tilt angles from a parallel investigation by S. Baldelli's group at the University of Houston.

Acetic acid (CH_3COOH) was also examined on the rutile surface and the -CH_3 symmetric methyl stretch effectively resolved via VSFS. Experimental difficulties and time-constraints prevented a full orientational analysis to be performed, but given the preliminary data this author is confident of the feasibility of such an investigation.

[1] LEED and Auger analyses were performed for work by M. Ahmed, P. Wincott, and J. Treacy, and as such have not been included in this thesis.

5.6 References

1. Cox PA, *The surface science of metal oxides*. 1994: Cambridge university press.
2. Hashimoto K, Irie H, Fujishima A. TiO2 photocatalysis: A historical overview and future prospects. *Japanese Journal of Applied Physics Part 1-Regular Papers Brief Communications & Review Papers*. 2005; **44:** 8269-85.
3. Wang CY, Groenzin H, Shultz MJ. Surface characterization of nanoscale TiO2 film by sum frequency generation using methanol as a molecular probe. *Journal of Physical Chemistry B*. 2004; **108:** 265-72.
4. Wang CY, Groenzin H, Shultz MJ. Comparative study of acetic acid, methanol, and water adsorbed on anatase TiO2 probed by sum frequency generation spectroscopy. *Journal of the American Chemical Society*. 2005; **127:** 9736-44.
5. Uosaki K, Yano T, Nihonyanagi S. Interfacial water structure at as-prepared and UV-Induced hydrophilic TiO2 surfaces studied by sum frequency generation spectroscopy and quartz crystal microbalance. *Journal of Physical Chemistry B*. 2004; **108:** 19086-8.
6. Aliaga C, Baldelli S. A sum frequency generation study of the room-temperature ionic liquid-titanium dioxide interface. *Journal of Physical Chemistry C*. 2008; **112:** 3064-72.
7. Paszti Z, Guczi L. Amino acid adsorption on hydrophilic TiO2: A sum frequency generation vibrational spectroscopy study. *Vibrational Spectroscopy*. 2009; **50:** 48-56.
8. Winkler J, *Titanium dioxide*. 2003: Vincentz Verlag Hannover, Germany.
9. Diebold U. The surface science of titanium dioxide. *Surface Science Reports*. 2003; **48:** 53-229.
10. Atkinson A, Barnett S, Gorte RJ, Irvine JTS, McEvoy AJ, Mogensen M, Singhal SC, Vohs J. Advanced anodes for high-temperature fuel cells. *Nature materials*. 2004; **3:** 17-27.
11. Linsebigler AL, Lu G, Yates Jr JT. Photocatalysis on TiO2 surfaces: principles, mechanisms, and selected results. *Chemical Reviews*. 1995; **95:** 735-58.
12. Bach U, Lupo D, Comte P, Moser JE, Weissörtel F, Salbeck J, Spreitzer H, Grätzel M. Solid-state dye-sensitized mesoporous TiO2 solar cells with high photon-to-electron conversion efficiencies. *Nature*. 1998; **395:** 583-5.
13. Pfaff G, Reynders P. Angle-dependent optical effects deriving from submicron structures of films and pigments. *Chemical reviews*. 1999; **99:** 1963-82.
14. Pang CL, Lindsay R, Thornton G. Chemical reactions on rutile TiO2 (110). *Chemical Society Reviews*. 2008; **37:** 2328-53.
15. Charlton G, Howes PB, Nicklin CL, Steadman P, Taylor JSG, Muryn CA, Harte SP, Mercer J, McGrath R, Norman D. Relaxation of TiO_ {2}(110)-(1× 1) Using Surface X-Ray Diffraction. *Physical review letters*. 1997; **78:** 495.
16. Torrelles X, Cabailh G, Lindsay R, Bikondoa O, Roy J, Detlefs B, Zegenhagen J, Thornton G. Nanoscale aqueous dissolution of TiO2 (110)(1x1), 21 edn.: The Electrochemical Society. 1926-.
17. Smyth DM. The defect chemistry of metal oxides. *The Defect Chemistry of Metal Oxides, by DM Smyth, pp. 304. Foreword by DM Smyth. Oxford University Press, Jun 2000. ISBN-10: 0195110145. ISBN-13: 9780195110142*. 2000; **1**.
18. Vickerman JC, Gilmore IS, *Surface analysis: the principal techniques*. Vol. 2. 2009: Wiley Online Library.
19. Gan S, Liang Y, Baer DR, Sievers MR, Herman GS, Peden CHF. Effect of platinum nanocluster size and titania surface structure upon CO surface chemistry on platinum-supported TiO2 (110). *The Journal of Physical Chemistry B*. 2001; **105:** 2412-6.
20. Bennett RA, Stone P, Bowker M. Scanning tunnelling microscopy studies of the reactivity of the TiO2 (110) surface: Re-oxidation and the thermal treatment of metal nanoparticles. *Faraday Discussions*. 1999; **114:** 267-77.
21. Li M, Hebenstreit W, Gross L, Diebold U, Henderson MA, Jennison DR, Schultz PA, Sears MP. Oxygen-induced restructuring of the TiO< sub> 2</sub>(110) surface: a comprehensive study. *Surface science*. 1999; **437:** 173-90.

22. Pan JM, Maschhoff BL, Diebold U, Madey TE. Interaction of water, oxygen, and hydrogen with TiO< inf> 2</inf>(110) surfaces having different defect densities. *Journal of Vacuum Science & Technology A: Vacuum, Surfaces, and Films*. 1992; **10:** 2470-6.
23. Escudero C, Salmeron M. From solid–vacuum to solid–gas and solid–liquid interfaces: In situ studies of structure and dynamics under relevant conditions. *Surface Science*. 2013; **607:** 2-9.
24. Namai Y, Matsuoka O. NC-AFM observation of atomic scale structure of rutile-type TiO2(110) surface prepared by wet chemical process. *Journal of Physical Chemistry B*. 2006; **110:** 6451-3.
25. Lu Y, Jaeckel B, Parkinson BA. Preparation and characterization of terraced surfaces of low-index faces of anatase, rutile, and brookite. *Langmuir*. 2006; **22:** 4472-5.
26. Nakamura R, Ohashi N, Imanishi A, Osawa T, Matsumoto Y, Koinuma H, Nakato Y. Crystal-face dependences of surface band edges and hole reactivity, revealed by preparation of essentially atomically smooth and stable (110) and (100) n-TiO2 (rutile) surfaces. *Journal of Physical Chemistry B*. 2005; **109:** 1648-51.
27. Assi R. Preparation of a model oxide surface for the fundamental study of a corrosion inhibitor. *Corrosion & Protection Centre*. Vol. MSc Dissertation: University of Manchester, 2006.
28. Martinez U, Vilhelmsen LB, Kristoffersen HH, Stausholm-Moller J, Hammer B. Steps on rutile TiO2(110): Active sites for water and methanol dissociation. *Physical Review B*. 2011; **84**.
29. Berkó A, Solymosi F. Study of clean TiO2 (110) surface by scanning tunneling microscopy and spectroscopy. *Langmuir*. 1996; **12:** 1257-61.
30. Piao H, McIntyre NS. Adventitious carbon growth on aluminium and gold-aluminium alloy surfaces. *Surface and Interface Analysis*. 2002; **33:** 591-4.
31. Swift P. Adventitious carbon—the panacea for energy referencing? *Surface and Interface Analysis*. 1982; **4:** 47-51.
32. Barr TL, Seal S. NATURE OF THE USE OF ADVENTITIOUS CARBON AS A BINDING-ENERGY STANDARD. *Journal of Vacuum Science & Technology a-Vacuum Surfaces and Films*. 1995; **13:** 1239-46.
33. Miller DJ, Biesinger MC, McIntyre NS. Interactions of CO2 and CO at fractional atmosphere pressures with iron and iron oxide surfaces: one possible mechanism for surface contamination? *Surface and Interface Analysis*. 2002; **33:** 299-305.
34. Barr TL. An ESCA study of the termination of the passivation of elemental metals. *The Journal of Physical Chemistry*. 1978; **82:** 1801-10.
35. Tilinin IS, Jablonski A, Werner WSM. Quantitative surface analysis by Auger and x-ray photoelectron spectroscopy. *Progress in Surface Science*. 1996; **52:** 193-335.
36. Oku M, Matsuta H, Wagatsuma K, Waseda Y, Kohiki S. Removal of inelastic scattering part from Ti2p XPS spectrum of TiO2 by deconvolution method using O1s as response function. *Journal of Electron Spectroscopy and Related Phenomena*. 1999; **105:** 211-8.
37. Walton J, Wincott P, Fairley N, Carrick A. Peak Fitting with CasaXPS: A Casa Pocket Book. 2010.
38. Vegh J. The Shirley background revised. *Journal of Electron Spectroscopy and Related Phenomena*. 2006; **151:** 159-64.
39. Hennessy DC, Pierce M, Chang KC, Takakusagi S, You H, Uosaki K. Hydrophilicity transition of the clean rutile TiO2 (110) surface. *Electrochimica Acta*. 2008; **53:** 6173-7.
40. Kim KD, Tai WS, Kim YD, Cho SJ, Bae IS, Boo JH, Lee BC, Yang KH, Park OK. Change in Water Contact Angle of Carbon Contaminated TiO2 Surfaces by High-energy Electron Beam. *Bulletin of the Korean Chemical Society*. 2009; **30:** 1067-70.
41. Dieguez C. Acetonitrile: Summary Risk Assessment Report ISPRA (VA) Italy: European Chemicals Bureau, 2002.
42. Horiuchi T, Miura H, Uchida S. Highly-efficient metal-free organic dyes for dye-sensitized solar cells. *Chemical Communications*. 2003**:** 3036-7.

43. Gao F, Wang Y, Shi D, Zhang J, Wang M, Jing X, Humphry-Baker R, Wang P, Zakeeruddin SM, Graetzel M. Enhance the optical absorptivity of nanocrystalline TiO(2) film with high molar extinction coefficient ruthenium sensitizers for high performance dye-sensitized solar cells. *Journal of the American Chemical Society*. 2008; **130:** 10720-8.
44. Hauch A, Georg A. Diffusion in the electrolyte and charge-transfer reaction at the platinum electrode in dye-sensitized solar cells. *Electrochimica Acta*. 2001; **46:** 3457-66.
45. Xu M, Wenger S, Bala H, Shi D, Li R, Zhou Y, Zakeeruddin SM, Graetzel M, Wang P. Tuning the Energy Level of Organic Sensitizers for High-Performance Dye-Sensitized Solar Cells. *Journal of Physical Chemistry C*. 2009; **113:** 2966-73.
46. Zou X-J, Ding KN, Zhang YF, Li JQ. A DFT Study of Acetonitrile Adsorption and Decomposition on the TiO2 (110) Surface. *International Journal of Quantum Chemistry*. 2011; **111:** 915-22.
47. Kislenko SA, Amirov RH, Samoylov IS. Effect of Cations on the TiO2/Acetonitrile Interface Structure: A Molecular Dynamics Study. *Journal of Physical Chemistry C*. 2013; **117:** 10589-96.
48. Sumita M, Sodeyama K, Jono R, Han L, Tateyama Y. Electronic structure of acetonitrile adsorbed on the anatase TiO2 (101) surface. *Chemical Physics Letters*. 2013; **556:** 225-9.
49. Heald MA, Marion JB, *Classical electromagnetic radiation*. 2012: Courier Dover Publications.
50. Hecht E. Optics 4th: Addison Wesley, 2002.
51. Boyd RW, *Nonlinear optics*. 2003: Academic press.
52. Lambert A, Davies P, Neivandt D. Implementing the theory of sum frequency generation vibrational spectroscopy: A tutorial review. *Applied Spectroscopy Reviews*. 2005; **40:** 103-45.
53. Shen Y-R. The principles of nonlinear optics. *New York, Wiley-Interscience, 1984, 575 p.* 1984; **1**.
54. Heinz TF. Nonlinear optics of surfaces and adsorbates. 1982.
55. Hirose C, Akamatsu N, Domen K. Formulas for the analysis of the surface SFG spectrum and transformation coefficients of cartesian SFG tensor components. *Applied spectroscopy*. 1992; **46:** 1051-72.
56. Zhuang X, Miranda P, Kim D, Shen Y. Mapping molecular orientation and conformation at interfaces by surface nonlinear optics. *Physical Review B*. 1999; **59:** 12632.
57. Wang* H-F, Gan†‡ W, Lu†‡ § R, Rao†‡¶ Y, Wu† B-H. Quantitative spectral and orientational analysis in surface sum frequency generation vibrational spectroscopy (SFG-VS). *International Reviews in Physical Chemistry*. 2005; **24:** 191-256.
58. Lambert AG. Sum frequency spectroscopy of adsorption on hydrophilic mica substrates. 2001.
59. Hunt JH, Guyotsionnest P, Shen YR. OBSERVATION OF C-H STRETCH VIBRATIONS OF MONOLAYERS OF MOLECULES OPTICAL SUM-FREQUENCY GENERATION. *Chemical Physics Letters*. 1987; **133:** 189-92.
60. Hirose C, Yamamoto H, Akamatsu N, Domen K. ORIENTATION ANALYSIS BY SIMULATION OF VIBRATIONAL SUM-FREQUENCY GENERATION SPECTRUM - CH STRETCHING BANDS OF THE METHYL-GROUP. *Journal of Physical Chemistry*. 1993; **97:** 10064-9.
61. Shen YR. Surface properties probed by second-harmonic and sum-frequency generation. 1989; **337:** 519-25.
62. Jang JH, Lydiatt F, Lindsay R, Baldelli S. Quantitative Orientation Analysis by Sum Frequency Generation in the Presence of Near-Resonant Background Signal: Acetonitrile on Rutile TiO2 (110). *Journal of Physical Chemistry A*. 2013; **117:** 6288-302.
63. McNeil LE, French RH. Multiple scattering from rutile TiO2 particles. *Acta Materialia*. 2000; **48:** 4571-6.
64. Penzkofer A, Falkenstein W. Direct determination of the intensity of picosecond light pulses by two-photon absorption. *Optics Communications*. 1976; **17:** 1-5.

65. Choi K, Ghosh S, Lim J, Lee CM. Removal efficiency of organic contaminants on Si wafer by dry cleaning using UV/O3 and ECR plasma. *Applied Surface Science*. 2003; **206:** 355-64.
66. Griffiths P, De Haseth JA, *Fourier transform infrared spectrometry*. Vol. 171. 2007: John Wiley & Sons.
67. Ye S, Osawa M. Molecular Structures on Solid Substrates Probed by Sum Frequency Generation (SFG) Vibration Spectroscopy. *Chemistry Letters*. 2009; **38:** 386-91.
68. Hernandez M, Chinwangso P, Cimatu K, Srisombat L-o, Lee TR, Baldelli S. Chemical imaging and distribution analysis of mono-, bi-, and tridentate alkanethiol self-assembled monolayers on gold by sum frequency generation imaging microscopy. *The Journal of Physical Chemistry C*. 2011; **115:** 4688-95.
69. Suresh B. CEH Report: Acetic Acid: Califomia: SRI Consulting December, 2003.
70. Liao L-F, Lien C-F, Lin J-L. FTIR study of adsorption and photoreactions of acetic acid on TiO2. *Physical Chemistry Chemical Physics*. 2001; **3:** 3831-7.
71. Muggli D, Keyser S, Falconer J. Photocatalytic decomposition of acetic acid on TiO2. *Catalysis Letters*. 1998; **55:** 129-35.
72. Mattsson A, Österlund L. Adsorption and Photoinduced Decomposition of Acetone and Acetic Acid on Anatase, Brookite, and Rutile TiO2 Nanoparticles. *The Journal of Physical Chemistry C*. 2010; **114:** 14121-32.
73. Muggli DS, McCue JT, Falconer JL. Mechanism of the Photocatalytic Oxidation of Ethanol on TiO2. *Journal of Catalysis*. 1998; **173:** 470-83.
74. Mor GK, Shankar K, Paulose M, Varghese OK, Grimes CA. Use of highly-ordered TiO2 nanotube arrays in dye-sensitized solar cells. *Nano letters*. 2006; **6:** 215-8.
75. Ito S, Chen P, Comte P, Nazeeruddin MK, Liska P, Péchy P, Grätzel M. Fabrication of screen-printing pastes from TiO2 powders for dye-sensitised solar cells. *Progress in photovoltaics: research and applications*. 2007; **15:** 603-12.
76. Blount MC, Kim DH, Falconer JL. Transparent thin-film TiO2 photocatalysts with high activity. *Environmental science & technology*. 2001; **35:** 2988-94.
77. Tyrode E, Johnson CM, Baldelli S, Leygraf C, Rutland MW. A Vibrational Sum Frequency Spectroscopy Study of the Liquid−Gas Interface of Acetic Acid−Water Mixtures: 2. Orientation Analysis. *The Journal of Physical Chemistry B*. 2004; **109:** 329-41.
78. Kim KS, Barteau MA. Pathways for carboxylic acid decomposition on titania. *Langmuir*. 1988; **4:** 945-53.
79. Sato S, Ueda K, Kawasaki Y, Nakamura R. In situ IR observation of surface species during the photocatalytic decomposition of acetic acid over TiO2 films. *The Journal of Physical Chemistry B*. 2002; **106:** 9054-8.
80. Nishijima K, Ohtani B, Yan X, Kamai T-a, Chiyoya T, Tsubota T, Murakami N, Ohno T. Incident light dependence for photocatalytic degradation of acetaldehyde and acetic acid on S-doped and N-doped TiO2 photocatalysts. *Chemical Physics*. 2007; **339:** 64-72.
81. Verbiest T, Clays K, Rodriguez V. Second-order Nonlinear Optical Characterisation Techniques: An Introduction: CRC Press, 2009.

Chapter 6. The Metal-water Interface Studied by VSFS

6.1 Introduction

Water-metal/metal oxide interfaces are highly important and prevalent systems, with implications in the fields of electrochemistry, catalysis, corrosion and biomaterials. Whilst current research has made large advances investigating the unique properties of bulk water through computational, spectroscopic, and other related techniques,[1-3] the investigation of interfacial water on metals and their oxides has overwhelmingly involved UHV conditions and low-water partial pressure environments. The unique interface sensitivity of even-order nonlinear spectroscopic techniques means that these are particularly suitable for such interfacial water studies, as the surface water responses will not be conflated with or dwarfed by signals from the bulk water. This chapter will present some initial VSFS data taken from metal/metal oxide surfaces in controlled humidity environments, together with analysis of the results.

6.2 Background

6.2.1 Water Adsorption on Metal Oxides

A large majority of investigations into interfacial water adsorption have been performed on single-crystal metal substrates, predominantly in UHV conditions. Many of the experimental techniques outlined in Section 2.4.2 have however been applied to examine the wetting behaviour of water on the more technically relevant metal oxide surface.

As the prototypical metal oxide surface, several studies have looked at water adsorption on rutile TiO_2(110). STM has been used to image molecular water dissociation on the rutile surface, pinpointing both oxygen vacancies and fivefold coordinated surface Ti as active surface adsorption sites, which have been further backed up by DFT calculations.[4, 5] High-pressure XPS has also been applied to the same system and peak analysis of the O 1s photoemission peaks was used to model water dissociation at oxygen vacancy defects, and to then observe molecular water adsorption on the resulting surface hydroxyls. This study found a water film coverage of 3 monolayers between 20% and 50% RH, rising to 8 monolayers thickness at 95% RH. The hydroxyl peak was seen to saturate at very low levels of water exposure, whilst the molecular water coverage is seen to increase constantly as a function of RH.[6] Yamamoto et al. employed this same

technique to look at wetting of Cu(111) and Cu(110) at ambient pressures up to 6 mbar, and found similar dissociation pathways, concluding that the local H_2O/OH environment on the rutile and copper surfaces at high pressure is similar to that at UHV.[7] Multilayer adsorption of water on TiO_2(110) has also been observed via HREELS, which detected molecular water adsorption and allowed for determination of H-bonding strengths.[8]

Another well-studied metal oxide is the MgO(100) surface, although currently the proposed models for water adsorption on this interface have not reached a similar consensus. Interestingly, the surface energy is such that hydroxylation and water clustering can occur simultaneously.[9] Several LEED investigations of the MgO(100)-water system have found very different surface coordinations;[10-12] it is now suggested that these result from the interface's particular sensitivity to surface preparation techniques.[13] A recent high pressure XPS analysis found experimental and DFT agreement with a water adsorption model whereby water dissociation leads to the formation of surface $Mg(OH)_2$ species, forming a passivating layer in ambient conditions.[14] AFM and FTIR techniques support this model, finding the molecular adsorption and dissociation processes to be highly localised.[15, 16]

With regards to water adsorption on ZnO, which is the main focus of this chapter, a number of studies have been reported in the literature; a combined study utilising LEED, STM, TPD, helium scattering and computational structural analysis found a stable long-range 'superstructure' on defect-free ZnO($10\bar{1}0$) as a result of a partially dissociated wetting layer. In fact, the authors suggest their data are consistent with a 1:1 ratio of H_2O:OH over the (2×1) superlattice, which is stable in vacuum up to 100°C.[17] Other low Miller-index zinc oxide surfaces, such as ZnO($000\bar{1}$) are polar and highly wetting as confirmed via LEED experiment,[18] whilst other ZnO surfaces will also partially dissociate adsorbed water in a 1:1 ratio, even when defect-free.[19]

In a more general sense, the 2002 review by Henderson lists a wealth of model oxide substrates that have been examined (via HREELS, XPS, TPD, SSIMS) in UHV with water present, and a significant proportion of those report water dissociation, many to a degree that would rule out defects as the sole activation sites.[20] For these and other surfaces, the use of computational modelling of interfacial water via density functional theory and molecular dynamics simulations has been highly utile, accurately predicting phenomena such as novel water bilayer structures[21] and hydrogen bonding clusters.[22]

6.2.2 VSFS for Water Studies

As already mentioned, the surface-specificity of VSFS makes it ideally suited for interfacial water studies. Other vibrational spectroscopies such as FTIR have examined water on interfaces relevant to this investigation, but the spectra from these are invariably dominated by the H-bonded bulk water stretching.[18, 23-25] One such example spectrum is shown in Figure 6.1, which presents infrared absorption for a ZnO-D_2O system under varying heavy water partial pressures.[26] The small feature at $2730\ \mathrm{cm}^{-1}$ is a result of the dangling free O-D at the water-vapour interface, whereas the broad asymmetric feature around $2500\ \mathrm{cm}^{-1}$ results from the aforementioned H-bonded water molecules. Water (H_2O) spectra have the same structure and shape but are instead centred around $3300\ \mathrm{cm}^{-1}$.[27] In the bulk, the molecules form a complex hydrogen-bonded network which has the effect of lowering and shifting vibration energies over a larger continuum, resulting in the singular, broad resonant feature observed.[1, 28]

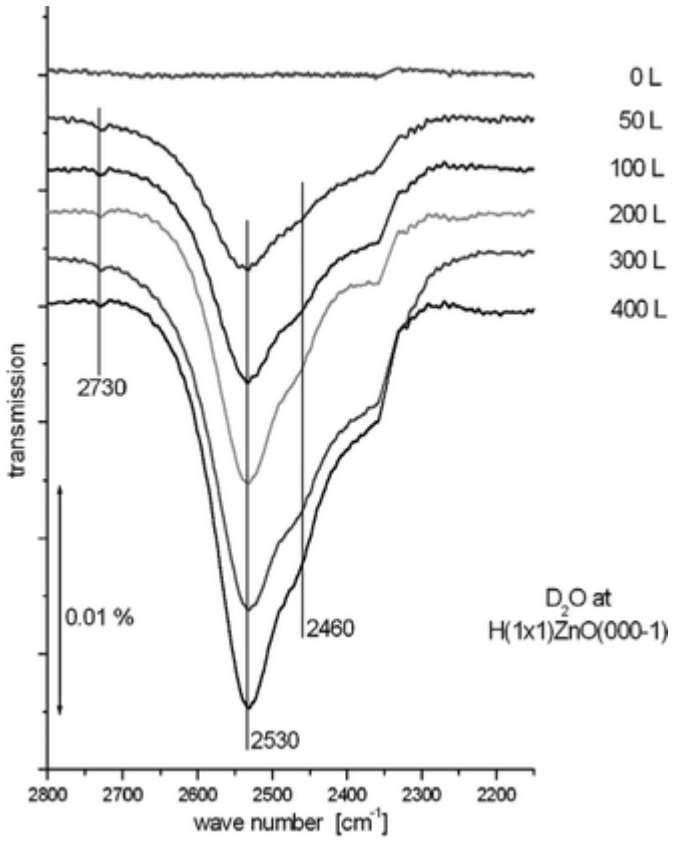

Figure 6.1. Fourier Transform Infrared Absorption spectra for D2O adsorbed on ZnO$(000\bar{1})$

The first sum-frequency vibrational spectra of a water interface were presented by Du, and examined the aqueous/air interface.[29] Other authors have used the technique to examine bond

orientations at this interface,[30-33] and the addition of hydrocarbons has allowed the interactions between water and certain hydrophilic surfactant molecules to be better understood.[31, 34-36] Additionally, computational techniques have allowed for better understanding of SFG spectra and have helped direct future experimental directions.[22, 37-39]

To a lesser extent,[40] SFG techniques have also been applied to examine the solid-aqueous interface, notably some early work on quartz which identified the presence of two major molecular water species differentiated by the strength of their local hydrogen-bonding environment; one ice-like species with tetrahedral coordination, and one more weakly bound water-like asymmetric species.[41, 42] These two species were also observed via VSFS from D_2O adsorbed on the mica interface, along with the free O-D stretch at $2740\ \mathrm{cm}^{-1}$ as reproduced in Figure 6..[43]

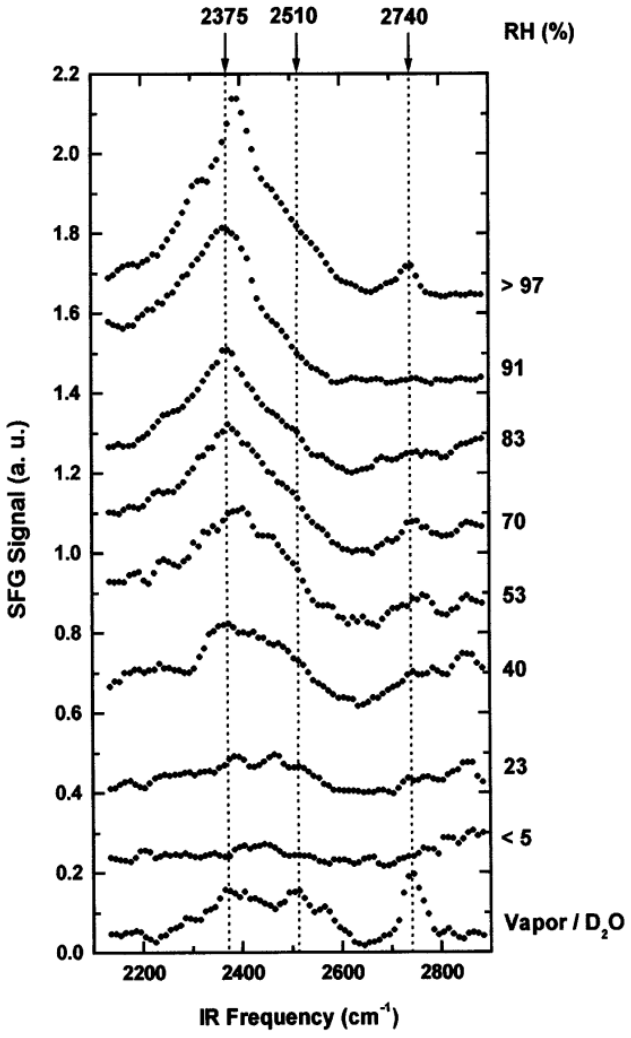

Figure 6.2. SFG spectra in the O-D stretching region for D_2O adsorbing on a mica surface at varying relative humidities. Features at $2375\ \mathrm{cm}^{-1}$ and 2510 cm^{-1} correspond to O-D stretch modes from an ordered and disordered H-bonded network respectively, whereas the feature at 2740 cm^{-1} is identified at the free O-D stretching mode.[43]

The spectrum in Figure 6.3 was taken by Hedberg et al. with a narrow bandwidth VSFS setup for an investigation into the corrosion of zinc by formic acid.[44, 45] It evaluates the metallic Zn surface at 0% and 90% RH for both H_2O and D_2O and clearly shows the free OD peak at $\sim 2730\ \mathrm{cm}^{-1}$ for the 90% RH plot. Results from this study were used as a basis for the surface water adsorption portion of this project.

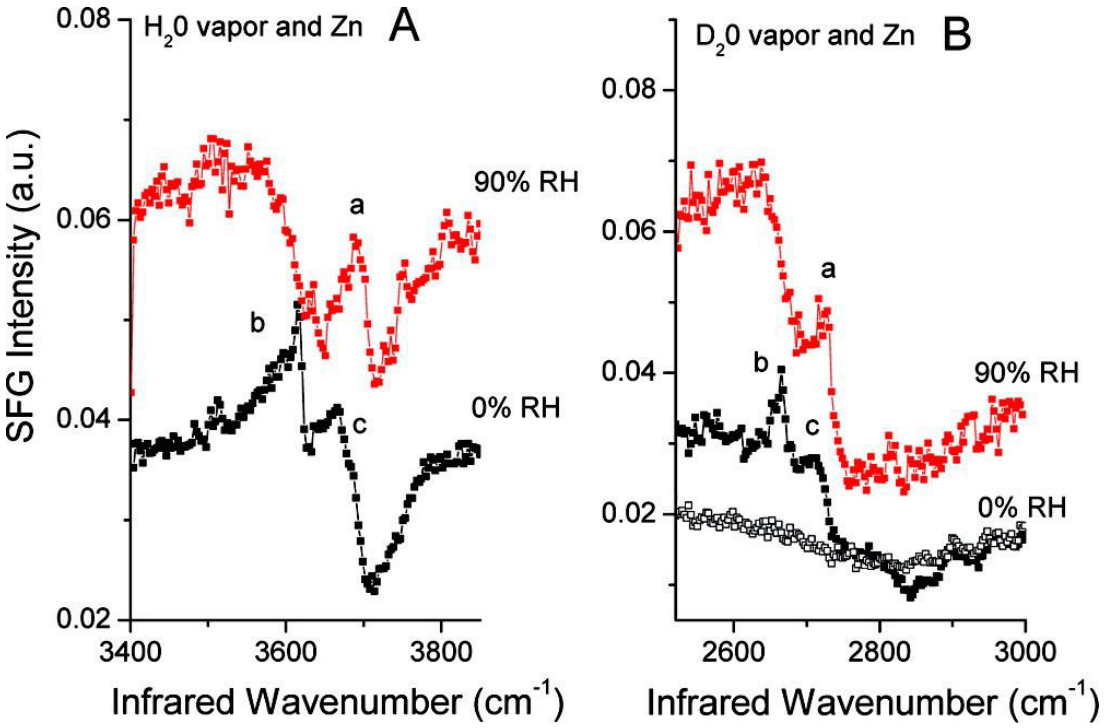

Figure 6.3. Narrow bandwidth sum-frequency spectra showing the responses for H_2O (A) and D_2O (B) on a polycrystalline zinc surface. In the original paper, the peaks labelled 'a' have been ascribed to the free O-D stretch, whilst those labelled 'b' and 'c' are identified as two different hydroxyl stretching modes.[44]

6.2.3 Measures of Atmospheric Moisture

Due to the general ubiquity of water on the planet, H_2O is present in some form or other in all but the most extreme environments, whether in solid, liquid, or gaseous form. Any experimental procedure performed outside of vacuum or a specifically controlled atmosphere must presume a certain amount of water to be present in the gas phase, and there are several different ways of describing and measuring this molecular water vapour.

The amount of water vapour present in a gas or its humidity can be described by three different measures: absolute, specific, or relative humidity. Absolute humidity (m_w) refers, as the name suggests, to the absolute amount of water vapour present in terms of mass per unit volume,

which is useful in terms of reproducibility as it does not depend on any other environmental factors. The specific humidity SH of a water air-mixture is the mixing ratio between the absolute humidity m_w and the mass of the air per unit volume (m_a) such that SH $= m_w/(m_w + m_a)$. The relative humidity (RH) is the ratio between the partial pressure of water in the water-air mixture p_w and the vapour pressure of liquid water at the temperature of the air $p_{ws}(T)$, and is usually expressed as a percentage. When the partial pressure of water in the system is equal to the temperature-specific vapour pressure of liquid water (i.e. when RH = 100%) the gas phase water vapour will condense out, but at any lower RH value there will be a dynamic situation involving continuous adsorption and desorption of molecular water on surfaces.[46] Assuming temperature and physical water content remain static, this dynamic system will operate at an equilibrium and as described in Chapter 2 will result in typical amounts of surface water coverage for any given RH value. As such this particular humidity measure can give a better impression of the amount of surface-adsorbed water in a specific system without having to explicitly state additional system variables, and will be the measure used predominantly in this study.

There are several techniques that can be used to acquire values of the humidity of a system which will be briefly outlined here. A hygrometer is the name for a generic water sensor, and each type of these is subject to inherent accuracies and variability.[47] Some techniques are more physical and utilise for example a piece of coated paper or an animal hair which changes length relative to atmospheric water content. Far more common, however, are electronic devices whereby a material's properties change as a response to the presence of water, and this change is detected and compared to calibration reference values. Materials involved are typically coated metals, ceramics and polymers, and there are commercial detectors that register changes in electrical impedance, capacitance, conductivity, and resonant frequency under an applied voltage, as all of these have been shown to vary somehow with relative humidity.[48] Additionally some devices more directly measure the water itself through detecting weight changes of hygroscopic crystals exposed to air mixtures, or a direct measure of intensity changes of infrared light due to molecular absorption.

6.3 Experimental Methodology

SFG spectra were acquired from metallic substrates as a function of relative humidity using the experimental VSFS setup described in Chapter 4. The prism sample cell was employed in a gas flow configuration in order to supply the cell atmosphere with a steady flow of air at variable humidity.

6.3.1 Humid Air control

Firstly an AD41 dry air generator (Oxford Cryosystems) containing a compressor and twin drying columns, of the sort typically used in crystallography applications, generated a continuous supply of clean, dry air at a flow rate of ~15 litres per minute – this in turn supplied the necessary input gas flow for a Sycos H (Ansyco) humid air generator, a diagram of which is shown in Figure 6.4. The Sycos H operates via water exchange between a dry and a humidified gas flow over a semi-permeable polymeric membrane. Unlike standard mixing, the amount of moisture present in the output gas flow is dependent on the humidity gradient over the membrane and the two flow rates, meaning fine control of the gas flow rates by the manual needle valves will allow fine control over output humidity whilst maintaining a constant output flow rate. The 'humid' air is humidified by being purged through a thermostatically controlled bubbler which is set just above ambient temperature, and the output flow was set at the low rate of between 15-20 litres per hour.

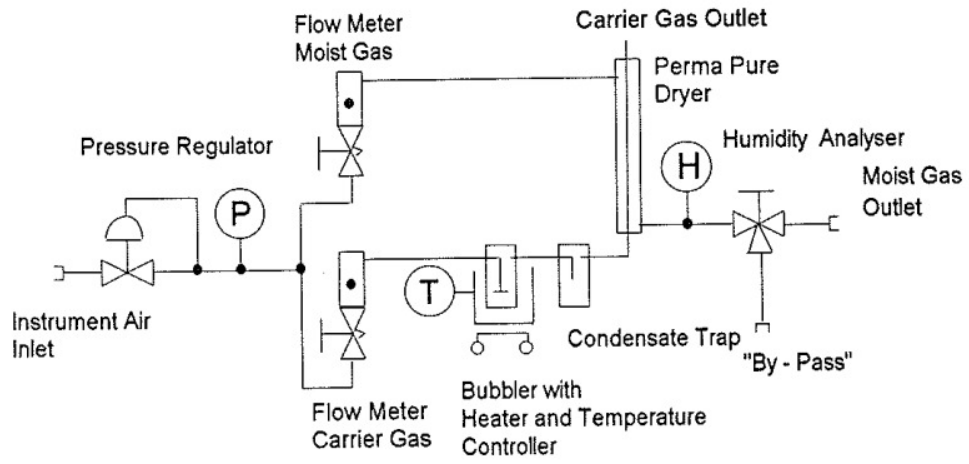

Figure 6.4. A schematic of the Ansyco humid air generator. The polymeric membrane is present in the Perma Pure Dryer component. The condensate trap is to avoid any condensate wetting of the membrane or tubing.

The humidity generator possesses a built-in humidity sensor and digital analyser unit, which can simultaneously measure the temperature, dew point and RH of the gas flow and display these

values instantaneously. The humidity probe itself is made of a silicon-based polymer which changes electrical capacitance linearly in the presence of water and is capable of measuring from 0-100% RH with an accuracy of ±2% in the range of 10% to 90% RH. The sensor specification also quotes a high repeatability value and minimal amount of observed hysteresis effects.

The humid air is then delivered via chemically inert PFA tubing to the sample cell, as illustrated in Fig 6.5. After the sample cell output port the gas flow is passed through two glass bubblers; one of which contains a secondary humidity sensor/data-logger and also acts as a backup condensate/particulate/oil trap, and one of which contains mineral oil to ensure no back-flow of gases or moisture. The secondary hygrometer/data-logger is an Easylog USB-2-LCD+ (Lascar Electronics) with an inbuilt LCD screen that refreshes the humidity reading every 60 s, and is also capable of measuring from 0-100% RH with a quoted typical accuracy of ±2% in the range of 10% to 90% RH.

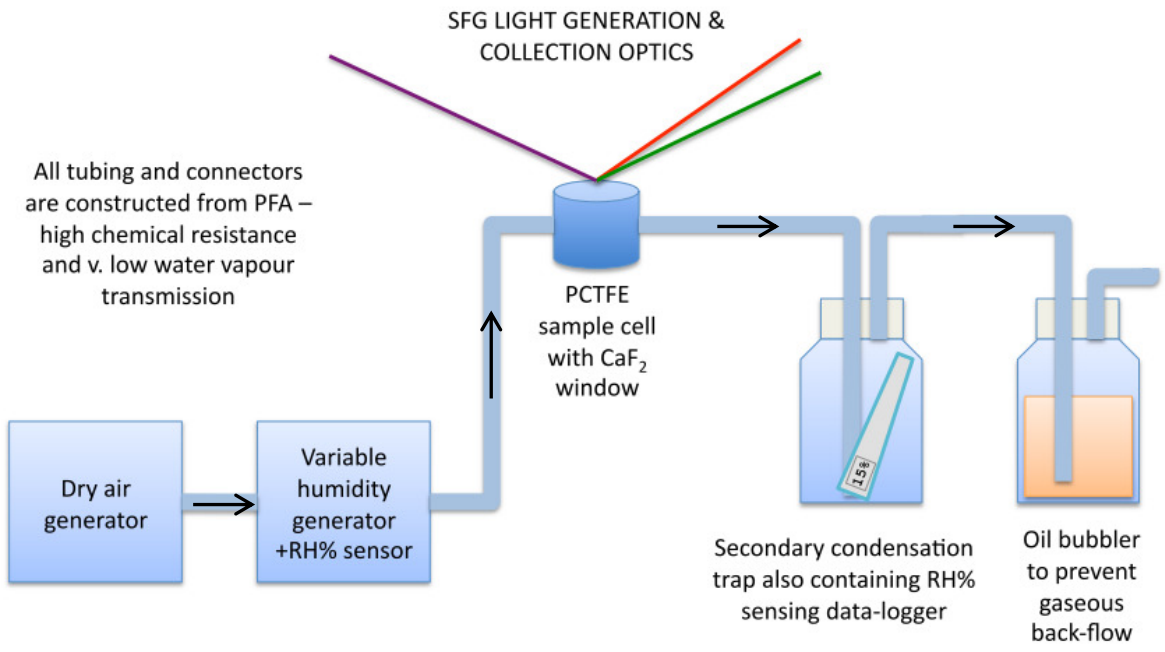

Figure 6.5. Diagram showing the humidity flow apparatus utilised in VSFS water adsorption studies, with the direction of air flow indicated by the arrows

There were initial concerns regarding leakage of the gas flow system as the air in the atmospherically controlled laboratory environment was measured to be consistently ~40% RH; any large humidity gradient between the interior and exterior of the system would equilibrate in the presence of improper gas seals. Avoiding a static sample environment by constantly

maintaining a low but steady gas flow would overcome this however as the flow creates a small overpressure within the system, ensuring any undesired gas flow is out of rather than into the cell/tubing atmosphere. Assuming no significant leakage (this was manually and aurally checked-for on a regular basis) the system overpressure could be adjusted by simply altering the depth of the submerged oil bubbler and thus the pressure that would have to be overcome before bubbling could occur.

Equilibration Times

The total internal volume of the cell and associated tubing was kept low with humidity equilibration considerations in mind. As the humid gas was maintained at a constant flow all elements of the system should reach an equilibrium level of humidity once the internal surfaces of the system had become equally wetted according to their surface energies, with a balance being achieved between molecular water adsorption and desorption processes. The cell itself was designed with a particularly open design and flow rates kept low to avoid turbulent flow. Turbulent flow of the humid air would necessarily create internal differences in pressure and as RH is also pressure-related this would result in varying local humidities, something undesirable for reproducibility and maintaining the accuracy of quoted humidity values.

The humidity generator is controlled by two manual needle valves which vary the flow rates of the dry and humid gases over the exchange membrane. Once flow rates were set a certain amount of time is required for the output humidity to reach a steady state, and the time taken for the RH to stabilise varies according the output flow rate and the magnitude of the humidity change implemented; typically this could take between 15-40 minutes before the RH was deemed stable enough for measurements to commence, setting a lower bound on the time between acquisitions and overall duration of the experiment. Additionally, a time lag was observed between the RH reading from the humidity generator and data-logger sensors, and measurements were not initialised until the two readings were within combined error of one another (a difference of $\pm$4% RH). On average, the equilibration time between acquisitions at different sequential ($\pm$10%) RH values was approximately 25 minutes.

Temperature Considerations

As previously described in section 6.2 the relative humidity of a system is a function of water vapour content, pressure and temperature, so accurate reporting of the RH at the point of VSFS beam overlap must take account of any temperature differentials in the gas flow system. Whilst the humidity generator bubbler was artificially heated, the temperature of the humid air at the generator output (and thus presumably the internal RH sensor) was measured by both a digital

thermal probe and the data-logger to be at a constant room temperature of $\sim 21°C$. In addition to this, the datalogger placed in the non-oil-filled bubbler also reported a steady atmospheric temperature of $21 \pm 1°C$. The general behaviour of a system's RH as a function of actual water content and temperature is shown below in Figure 6.6, which includes plots for 50% RH and 100% RH (the dew point at which water condenses out of the vapour phase). As can be seen from the figure, at $21°C$ it takes only 15 grams of H_2O per kilogram of air to achieve an RH of 100%.

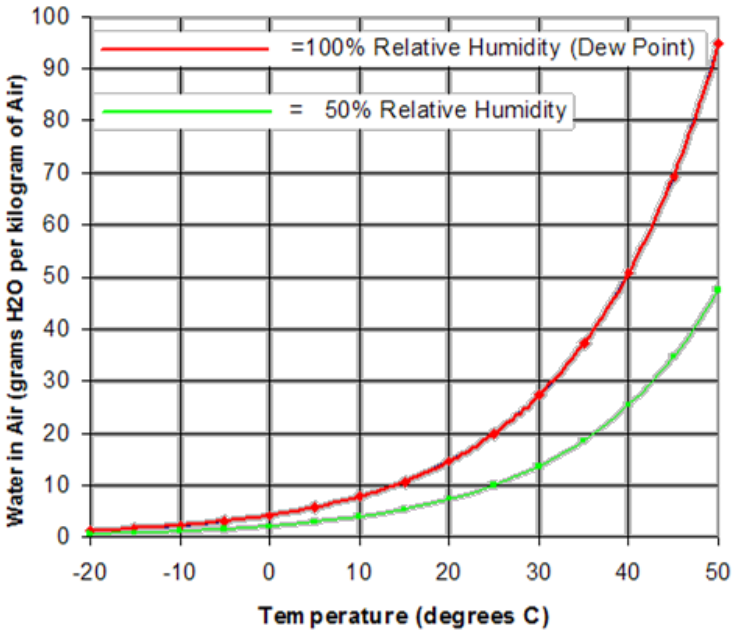

Figure 6.6. A plot of water content vs. temperature for the relative humidity of an air-vapour mixture. Plot adapted from online image.[49]

The other temperature factor not yet considered is the effect of the laser light pulses incident on the sample surface. On average there was 20-40 mW of power from both UV and Vis beams combined incident over ~ 4 mm^2 of the samples under investigation, which in a continuous wave scenario should not be a significant cause of local heating for a conductive metal sample with a relatively large volume and surface area over which to dissipate it. Slight complications arise when instantaneous incident powers are evaluated, as the majority of the power from each pulse is incident over 2-3 ps which is tiny when compared to the $1\ \text{ms} (= 10^9\ \text{ps})$ period in between successive pulses. Whilst these instantaneous high peak powers are unavoidable, average powers were minimised as much as SFG signal strengths would allow. In addition, a preliminary VSFS investigation for water on a polycrystalline metal (Zn) surface was conducted which saw no resonant signal variance between a freshly irradiated (by IR & Vis) surface at a constant RH atmosphere and the same sample after having the laser pulses incident on it continuously for a

period of 4 hours. Ideally a small thermocouple or alternate temperature sensor at the site of beam overlap would determine local heating in situ, but this was not deemed practicable due to the careful surface preparations necessary and the relatively low response time of most such sensors relative to pulse timescales.[50]

In terms of timescales it is likely that whilst the water-interface system may be perturbed by the power-limited laser pulses, any induced chemical or physical changes would only progress subsequent to SFG emission, remembering that the molecular vibrational probe is the IR pulse which has a duration of 120-150 fs. Owing then to the relatively long inter-pulse period and ready flow of water vapour, the continuous adsorption/desorption processes which are seen to rapidly hydroxylate metal oxide surfaces even in high vacuum conditions should allow the water-interface system to recover between pulses.[51-53] As an order of magnitude estimation, a Langmuir is a unit used in UHV experiments and is defined as an exposure to a pressure of $\sim 1 \times 10^{-6}$ mbar over one second, and assuming every water molecule incident on an adsorption site 'sticks',[54] i.e. an exposure to 1 Langmuir of H_2O vapour would cover 1 cm^2 with one monolayer in 1 second. A low humidity value of 10% would correspond to an H_2O partial pressure of 100 mbar, meaning it would take only 1×10^{-8} s for a full equivalent monolayer coverage as compared to the 1×10^{-3} s inter-pulse period.

Use of Deuterated Water (D_2O)

As Figure 6.7 shows, water vapour possesses a complex absorption spectrum in the IR region. Many of these absorptions are due to specific vibrational and rotational excitation, and as such may coincide energetically with the O-H resonances this project is attempting to resolve via VSFS. Owing to the laboratory atmosphere having a humidity of $\sim$40% RH, this means for any wavenumber region relevant to O-H stretching a significant proportion of the IR beam power may be absorbed by vapour phase water in the air.

Consideration of IR absorption by gaseous H_2O informed the limited length of the IR beam path (absorption will follow a Beer-Lambert law meaning an inverse exponential relationship between transmittance and path length), but in order to properly examine the vibrational response of surface water using optical techniques requires either evacuation/drying of the IR beam path up to the sample or the use of an H_2O analogue.

For this experiment deuterated water (D_2O) was used in the place of water in order to overcome the difficulties described above. D_2O is also referred to as 'heavy' water as the deuterium atoms have twice the mass of the hydrogen in standard light water (H_2O), with the consequence that all vibrational O-D resonances are shifted relative to their O-H counterparts to a region of the

spectrum minimally affected by atmospheric H_2O. The IR absorption spectrum of gaseous D_2O is also shown in Fig 6.7. The deuterated water used for all investigations is 99.8% deuterium oxide (Cambridge Isotopes) which, unless otherwise specified, has been used in the humidity generator bubbler to humidify the moist gas flow.

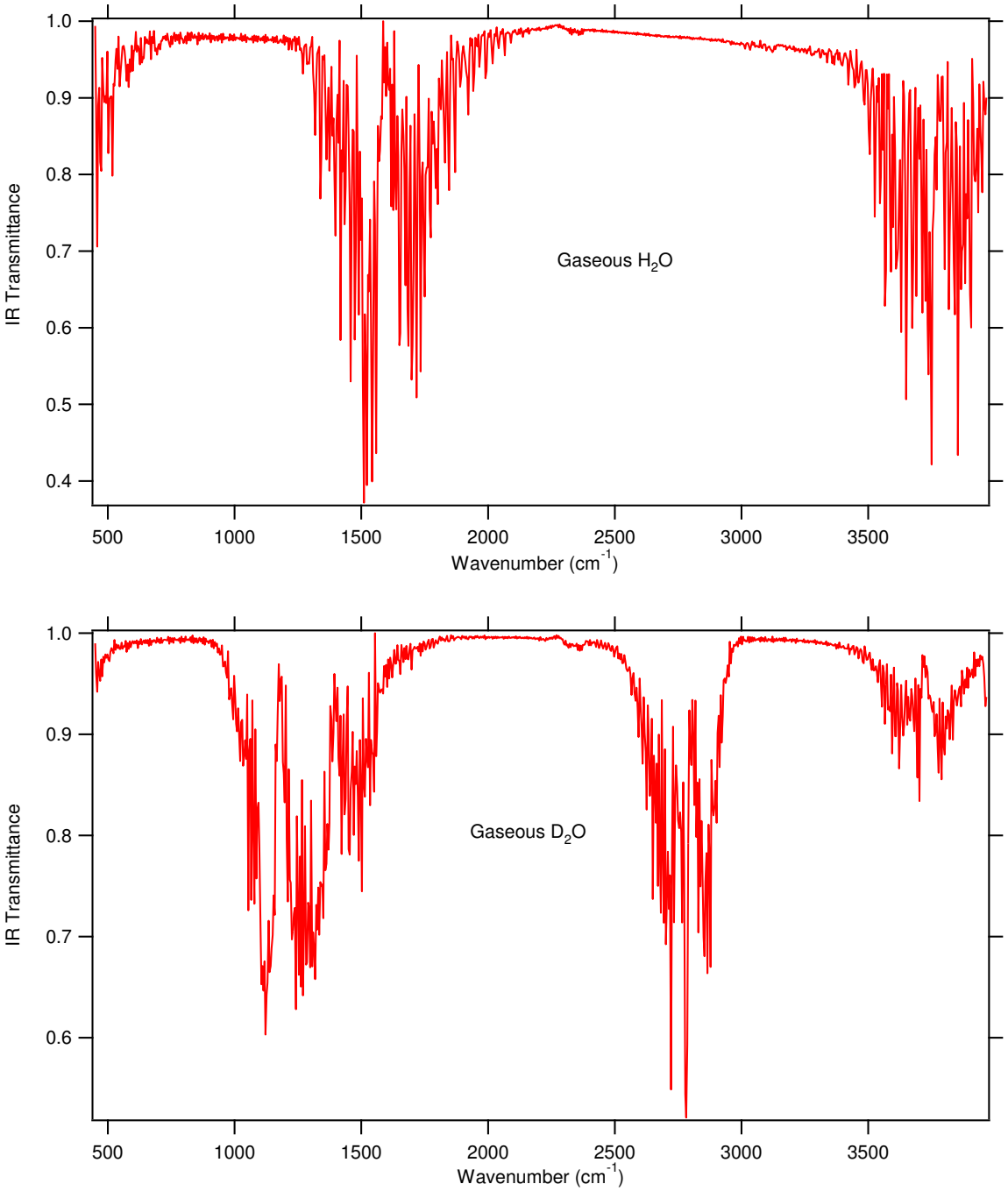

Figure 6.7. Infrared absorption spectra for gaseous H_2O and D_2O. Note the similar yet horizontally displaced absorption features. Molecular stretching regions are ~3500-3900 cm^{-1} for O-H and ~2550-2900 cm^{-1} for O-D.[55]

Physically and chemically, heavy and light water behave similarly and will interchangeably participate in a majority of the same reactions.[27] Indeed previous SFG investigation of the liquid-vapour interface found no discernible difference between the two structurally.[56] The additional mass of D_2O does however affect the strength of the internal bonds and also changes the strength of intermolecular hydrogen bonding, and so reactions sensitive to this such as those prevalent in biological systems can be negatively affected should it be substituted for H_2O.[57]

6.3.2 Sample Preparation

The initial aim of this aspect of the project was to observe the presence of adsorbed surface water on model metal oxide surfaces such as single-crystal TiO_2 and Cr_2O_3, which were prepared using the non-UHV technique outlined in Chapter 5. It became apparent during preliminary testing with these substrates however that if a resonant O-D signal was present it was too weak to resolve even with non-resonant background suppression pulse timings. The strength of molecular resonances in VSFS is amplified in the presence of large non-resonant surface signals, and both TiO_2 and Cr_2O_3 proved to have extremely low non-resonant surface susceptibilities (real-time photon count rates were several orders of magnitude lower with these than for metallic surfaces), so a decision was made to investigate polycrystalline metal surfaces which were known to elicit higher overall SFG intensities.

Several different polycrystalline metals were prepared and analysed, all using a variation of the process described here according to their general hardness. Firstly sheets and tokens were cut to an appropriate size, and rods were cut with a bench grinder into discs of ~5 mm thickness. Sample surfaces were then manually ground down using a grinding wheel and several different grades of abrasive paper from P400 up to P2500 grit (abrasive particulate sizes of ~35 µm and ~8 µm diameter respectively), until the surfaces took on a 'mirror-like' finish. After that was achieved, the samples were manually polished with a wheel-mounted high nap polishing pad, which was lubricated by solvents to help remove particulate and reduce friction. Samples were then briefly sonicated for 5 minutes each in ethanol, acetone and water, before being dried in a stream of dry air and exposed to a 45 minutes UV/ozone cleaning cycle.

The polycrystalline metals investigated were as follows:

- Zinc 99.9% (Goodfellow) 12 mm diameter rod, cut into 7 mm lengths
- Iron 99.95% (Goodfellow) 10 mm diameter rod, cut into 7 mm lengths
- Chromium 99.6% (Goodfellow) 3 mm thickness sheet, cut to 15×15 mm token

- 20Cr/25N/Nb stainless steel (obtained via NNL) 1 mm thickness foil, cut to 10×10 mm token

6.3.3 Acquisition Procedure

Initial Detection of O-D Stretch Resonances

Figure 6.8 shows the IR absorption spectrum of liquid D_2O from 200-4000 cm^{-1}. The prominent vibrational peak centred at $\sim$2450 cm^{-1} is assigned to the symmetric and asymmetric stretching vibrations of the bulk heavy water. The free O-D bonds of the interfacial water molecules are dwarfed in terms of number density by the bulk molecules, meaning in IR absorption spectroscopies their signal is minimal outside of specially selected situations.[58, 59] The surface sensitivity of VSFS allows both the higher energy free O-D bonds and those of surface-bound d-hydroxyls to become resolvable from the bulk response.

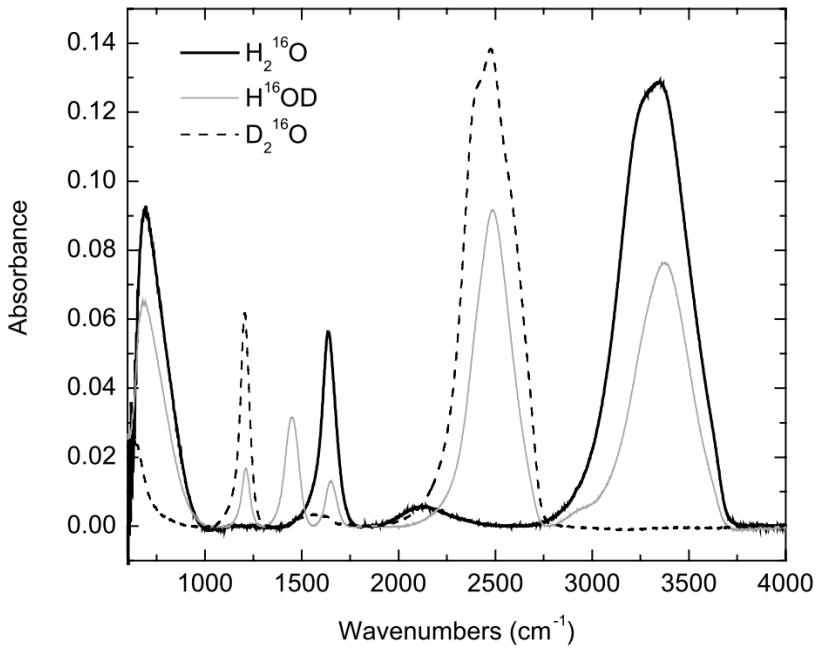

Figure 6.8. The IR absorption spectra of liquid H_2O (solid black line), D_2O (dashed line), and the isotopologue HOD (solid grey line) as measured by a commercial FTIR spectrometer.[60]

With a spectral bandwidth of $\sim$250 cm^{-1} it would be difficult to resolve the spectrally broad H-bonded O-D stretching modes with the VSFS system developed in Chapter 4, but as an initial stage

GaAs was analysed in a static D_2O cell-dosing configuration to attempt to locate any appropriate O-D resonances.

The GaAs single crystal sample was first cleaned via sonication in solvents and UV irradiation as described in Section 6.3.2, before being mounted in the prism cell and SFG spectra acquired for varying IR wavelengths. A small amount of liquid D_2O was then introduced into the cell and the input and output ports were capped which, given the water availability and its proximity to the sample, would result in a humid atmosphere at the sample face.

Pre d-hydroxylation Step (Intentional Surface Coverage with OD)

All atmospherically exposed metal surfaces will tend to have some amount of surface hydroxyls already present, but the amount will vary depending on sample history and exact surface chemistry.[61, 62] Whilst molecular D_2O will adsorb on an OH hydroxylated surface via hydrogen bonding, for reproducibility it was decided to pre-hydroxylate the surface with d-hydroxyls (OD). In the laboratory atmosphere, the surface OH will be in dynamic equilibrium with the vapour phase H_2O. Exposing this surface then to a D_2O vapour atmosphere would mean that over time surface OH should be replaced by OD at the same adsorption sites, and the large relative concentration of D_2O to any trace H_2O coupled with the gas flow would statistically diminish the chances of remaining surface OH.

Each prepared sample was fastened to the sample mount in the prism cell using adhesive, the cell was tightly sealed, and the in/out gas flow tubing attached to the cell without gas flow enabled. SFG spectra at zero-delay and background suppression timings were acquired in accumulation mode over the C-H stretch region (to check for surface cleanliness) and the O-D stretch region whilst the surface was presumably hydroxylated but at 0% RH in terms of deuterated water. The (D_2O) humidity was then increased to an arbitrarily high value (70-85% RH) which would ensure a significant coverage of water on the sample surface; once the humidity readings had equilibrated the SFG spectra were re-acquired over the O-D stretch region. After this acquisition, the flow of moist gas on the humidity generator was turned off and the generator-cell system left to dry off under a flow of 0% RH air. Thus the surface can be considered d-hydroxylated and an *experimental run* may progress once the system humidity had dropped to $\leq 4\%$ RH as measured by both hygrometers – this drying process would still take a minimum of 4-5 hours (ideally the system would be left overnight for RH values to decrease further).

Experimental Humidity Run

Once the surface has been wetted with OD/D_2O and sufficiently dried, the *experimental humidity run* may commence proper. Firstly, zero-delay and background suppressed SFG spectra were

acquired over the C-H and O-D stretch region, with the exact acquisition parameters tailored to the detected overall signal strengths; again, lower count rates will invoke the use of the photon-counting mode (as described in Chapter 4) and longer acquisition durations, whereas more intense signal strengths can proceed without these.

The humidity generator was then adjusted to a higher humidity value, and once hygrometer readings have equilibrated, the O-D spectral measurements were retaken – this was repeated in incremental steps until the humidity limit from the generator was reached, which for the slower flow rates employed was found to be ~75-85% RH (significantly faster flow rates would allow a maximum RH output of around 90% RH, although this involved longer equilibration times). Often at the high RH values spectra in the C-H region were also re-acquired to check for any carbon contamination changes, given that these seemed to inversely correlate with the system's ability to exhibit O-D resonances.

A full *humidity run* then involved a repetition of the incremental humidity steps in the opposite (high-to-low humidity) direction. The aim of this stage is to partially confirm the rough reproducibility of the low-to-high humidity spectra, but also to look for the presence of any hysteresis effects which might indicate droplet formation.[63, 64]

The final step once a near-zero humidity has been reached was to again check the C-H stretching region both to evaluate surface carbon, and also to accurately calibrate the wavenumber axis for the experiment using the absorption of a polystyrene film in the IR beam path (see Section 4.5.5).

The exact size of the humidity increments employed depended on the desired RH resolution for the particular substrate, but primarily on the surface SFG responsiveness. Surfaces with weaker non-resonant SFG susceptibilities might require 20 minute single spectrum exposure times, meaning that, coupled with humidity equilibration times, each humidity step might take 90-120 minutes.

All spectra unless otherwise specified have been acquired in the **ppp** polarisation combination.

A note on wavenumber calibration

All spectra were calibrated prior to experimentation using the polystyrene absorption spectrum as described in Section 4.5.5. Both the Ti:Sapphire amplifier and OPA were seen to wander slightly in terms of their output levels and wavelengths in response to various factors such as temperature, humidity and time since the last service but generally not over short timescales. An accidental adjustment of the spectrometer grating could knock the spectral calibration out by several wavenumbers however, and more importantly any chirp on either pulse might have the effect of changing the x-axis calibration whenever a visible time delay was applied for background suppression techniques. This effect was not fully quantified but variations of 3-4 cm^{-1} were occasionally observed between $\tau = 0$ and $\tau = 800$ fs, requiring a spectral recalibration. Thus exact quoted wavenumbers in the following section should have an implied error on them of approximately $\pm 2\ \mathrm{cm}^{-1}$.

6.4 Results and Discussion

6.4.1 Initial O-D Detection attempts (GaAs & Au(111))

Figure 6.9 shows the result of this investigation, all taken with background suppression pulse timings.

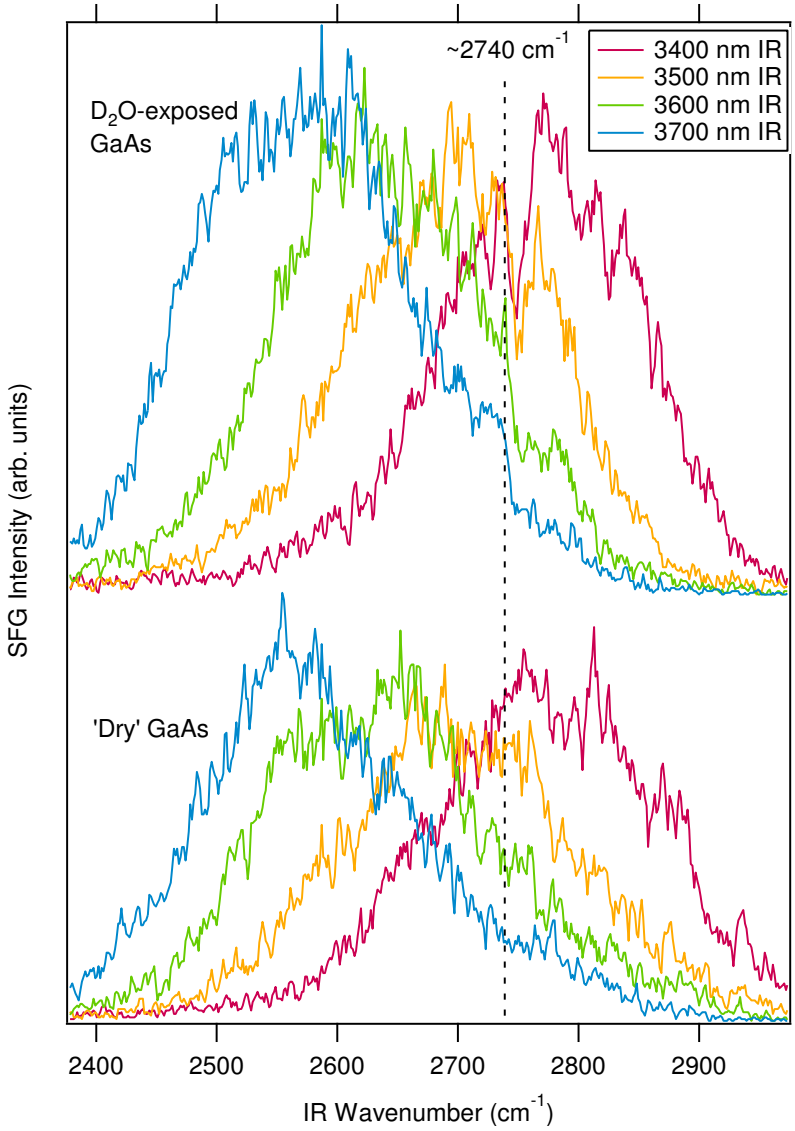

Figure 6.9. Background suppressed ($\tau = 1.1$ ps) SFG spectra of a dry and D_2O-exposed gallium arsenide single crystal sample over several different IR centre wavelengths.

Despite the long time delay on the visible pulse the differences between the dry and wet spectra are not pronounced although there is a definite discontinuity in the overall Gaussian shape across all wavelengths at ~2740 cm^{-1} which could correspond to a free O-D stretching mode. Also apparent from the figure is a noticeable increase in the SFG counts over the centre of the

3600 nm and 3700 nm plots. It is however clear from the data that the chemical and optical situation at the GaAs-water interface is not a simple one, further complicated by the resilience of the GaAs surface to the background suppression technique. Due to the structure of GaAs[65] some non-resonant signal is actually generated from the bulk which would make surface species detection difficult ; for example, despite the GaAs sample being used regularly for alignment procedures and being cleaned infrequently, very little is generally seen in the way of a surface C-H resonance despite the high probability of significant adventitious carbon build-up.

To avoid this issue, the humidity generator was used and an Au(111) substrate examined via VSFS at 0% and 70% RH, the spectra from which are shown in Figure 6.10. The subtractive element apparent in the wet GaAs scan is not present on the gold which could be due to different surface chemistry but could equally be due to a different phase relationship between surface and molecular responses. What is of some interest is the increase in amplitude of the zero-delay spectrum from 0-70% RH; the incident light intensities remain constant between the two spectra so somehow the addition of a moist atmosphere is enhancing the sum-frequency generation process.

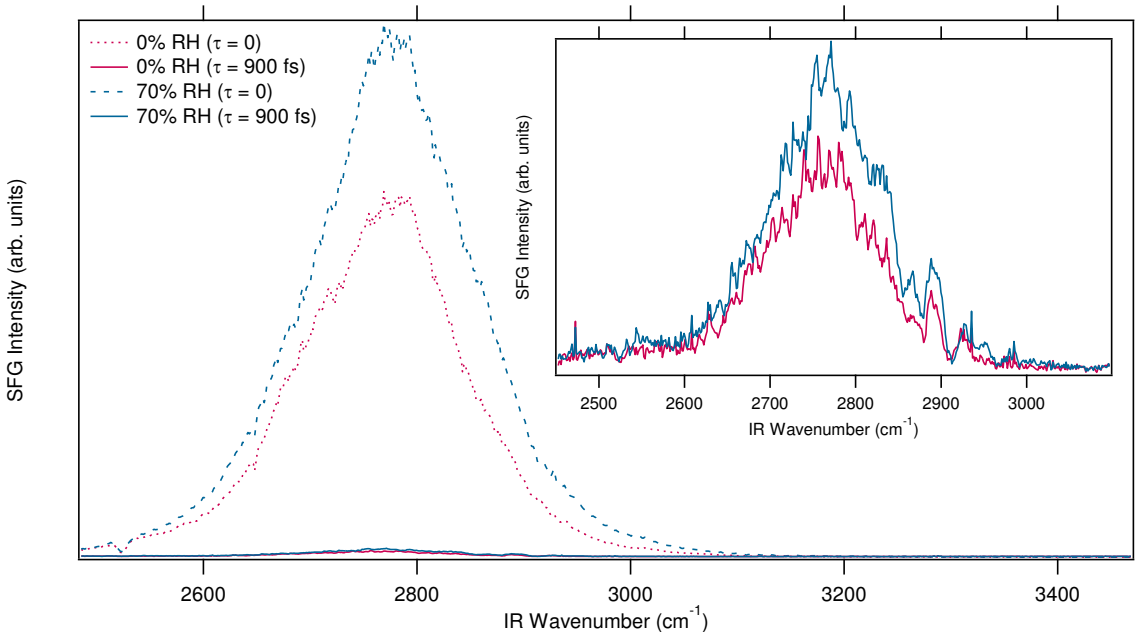

Figure 6.10. SFG spectra of Au(111) in a controlled humidity atmosphere over the O-D stretch region. A magnification of the $\tau = 900$ fs plots is presented inset.

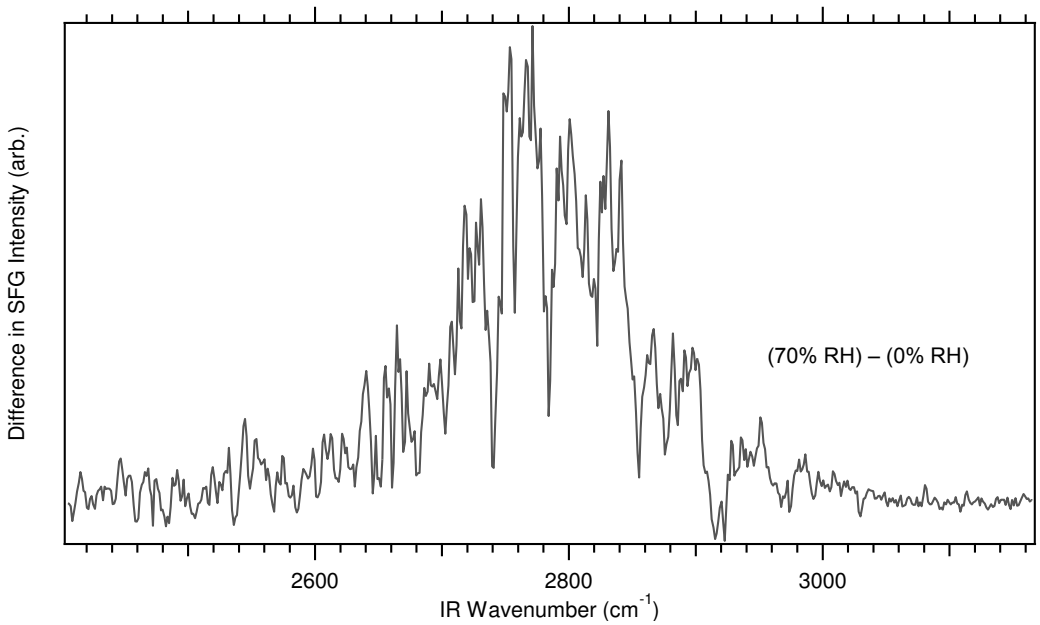

Figure 6.11. A difference spectrum subtracting the 'dry' from the 'moist' background-suppressed spectra from the previous figure (Fig 6.10).

Figure 6.11 is a difference spectrum between 0% and 70% RH spectra in Fig 6.10, but whilst there is a clear difference between signals from wet and dry samples the origin of this is not currently understood.

6.4.2 Zinc

Experimental

As seen in Figures 6.12 and 6.13, there is a well-resolved resonant element to all background-suppressed plots including the first '*pre d-hydroxylated*' spectrum. Above 40% RH there is a large peak at ~2725 cm^{-1} whose amplitude appears to rise and fall in conjunction with the humidity. Prior to this value in the 'increasing humidity' direction, there is initially a resonant peak at a slightly displaced energy which decreases slightly at ~10% and ~20% RH. To gain a more quantitative impression of the changes in resonant behaviour with humidity, some minor fitting procedures were applied.

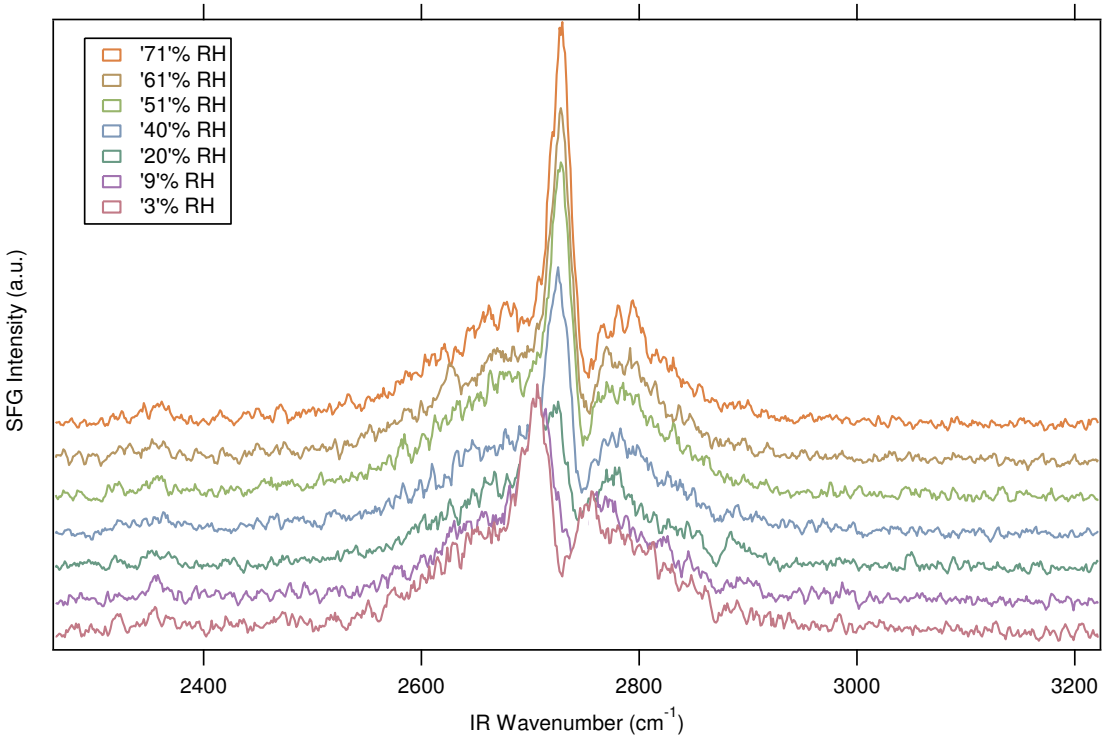

Figure 6.12. Background suppressed ($\tau = 800$ fs) SFG spectra for zinc in varying humidities. Spectra are those acquired in the increasing humidity direction (low to high), the decreasing humidity plots have been omitted for simplicity but are illustrated in Figure 6.13.

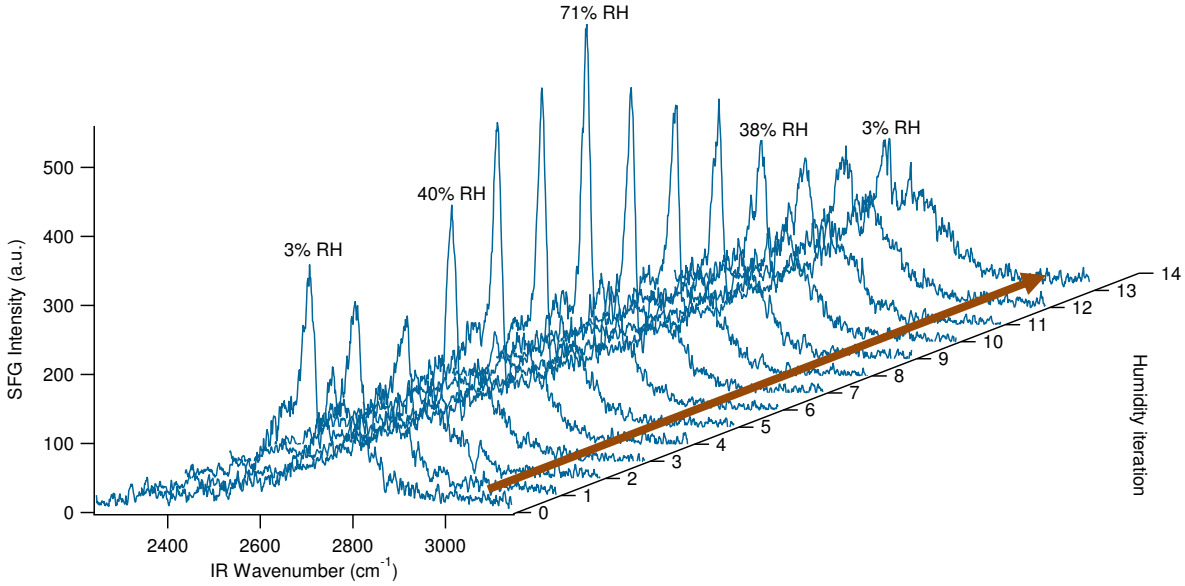

Figure 6.13. Background suppressed ($\tau = 800$ fs) SFG spectra for zinc in varying humidities plotted against 'humidity iteration, with some RH values labelled for clarity. Spectra were acquired in the order suggested by the arrow, and exact RH values for each humidity iteration are given in Table 6.1.

Humidity iteration	0	1	2	3	4	5	6	7	8	9	10	11	12	13
Relative humidity (%)	3	9	20	40	51	61	71	59	49	38	27	19	10	3

Table 6.1. The relative humidity value as given by the average of the two experimental hygrometers, correlated with the humidity iteration.

Background Subtraction

To first minimise the remains of the background signal or to remove broad underlying resonant features which would be non-resolvable, each spectrum was fitted using a selective Gaussian fitting regime which ignored the central resonance region from ~2650-3000 cm^{-1} in order to define a background without complications from the large central resonance; an example of such a fit is shown in Fig 6.14. This Gaussian curve was then treated as spectral background and was subtracted from the unprocessed spectrum.

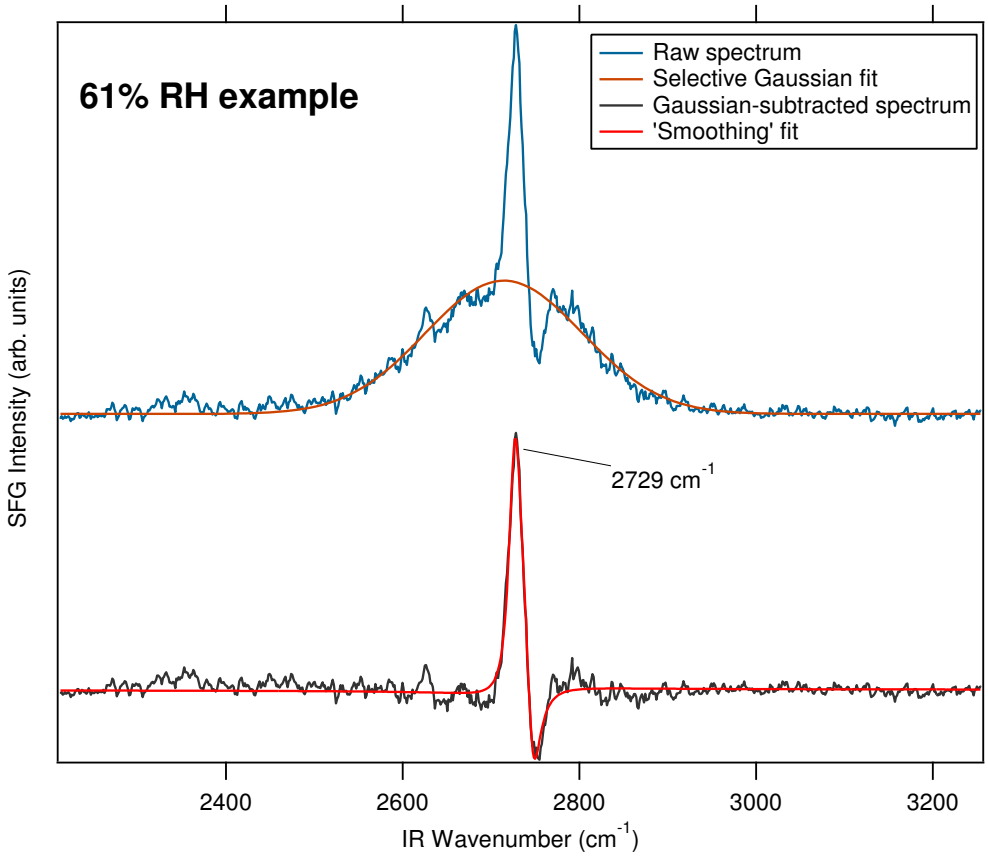

Figure 6.14. An example of the Gaussian fitting and background subtraction method utilised in analysis of the O-D stretch region on humidified zinc substrates.

The background-subtracted spectra, an example of which is also shown in Figure 6.14, were then subjected to a custom smoothing procedure in order to better extract quantitative information for the forthcoming analysis. The position and amplitude of the central resonance in the data as a function of humidity is illustrated in Figure 6.15.

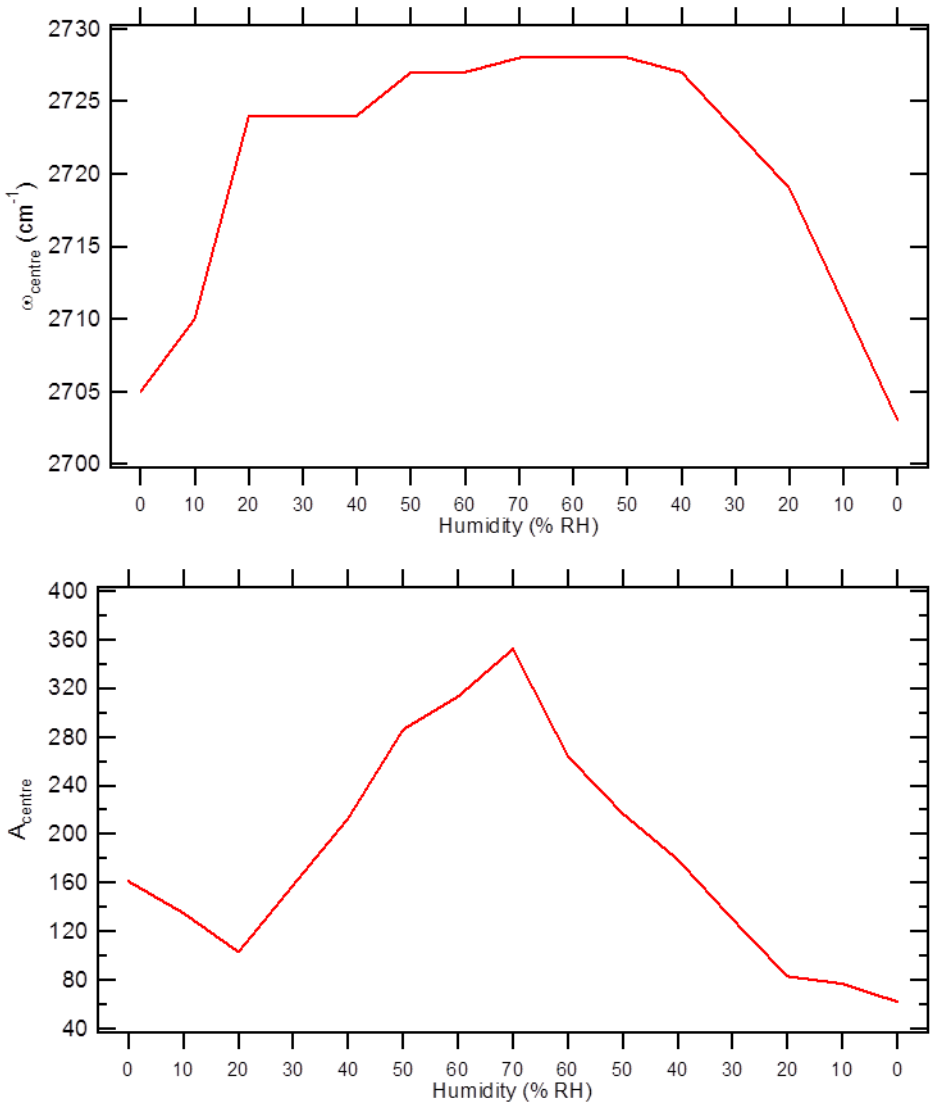

Figure 6.15. Plots of the central wavenumber ω_{central} and amplitude A_{central} of the background-subtracted data, presented as a function of relative humidity. The points on each spectrum were acquired from left to right (low RH → high RH → low RH)

Discussion of Results

Firstly, from the figures it is clear that an O-D resonant mode(s) has been detected around the expected wavenumber range.[44] Comparing the 'free OD' stretch from Fig 6.3 at 90% RH with any of those in Fig 6.12 at higher humidities illustrates the large improvements made towards the spectral resolution by the Manchester VSFS system, with peak frequencies and widths clearly measurable from the raw data without the need for complex fitting or interpolation. As an expected estimate of levels of adsorbed water, polished polycrystalline zinc at a relative humidity of 90% at 25°C should have around 8 equivalent monolayers (8 monolayers, assuming a wetting regime).[67]

Peak Identification

From Figure 6.15, at 0% RH where the surface is presumed to be d-hydroxylated, ω_{centre} is identified at 2705 cm^{-1} which would align closely with the d-hydroxyl peak detected in the Hedberg study.[44] Noting the intensity (A_{centre}) reduction in the peak for RH $= 0 \rightarrow 20\%$ coupled with a positive change in ω_{centre}, the data seems to suggest that the central feature is actually two different resonances which undergo a transition over this humidity range. At 30% RH and above, the wavenumber remains fairly constant at $\sim$2725 cm^{-1}, whilst the intensity shows a positive correlation with the cell humidity.

Physically this would correspond well with a model of a d-hydroxylated Zn(O) surface acquiring additional molecular D_2O from the vapour phase, until a sufficient coverage allows for the appearance at the water-air interface of dangling free OD.

Upon drying, ω_{centre} is again seen to fall with humidity for RH$<$ 40%, returning to 2703 cm^{-1} which displays an encouraging degree of reversibility in the system (remembering that the initial measurement of the *experimental run* is acquired after similar drying from the *pre d-hydroxylation* step).

Until a (wetting) monolayer has developed on the oxide surface one would not expect there to be a significant number of dangling O-D bonds, as the D_2O molecules which do not dissociate at high-energy adsorption sites would tend to preferentially coadsorb on surface d-hydroxyl provided there is sufficient water availability.[43, 61, 68] In this model, only once a wetting layer of D_2O/OD is present would additional water be free to hydrogen bond and orient itself with a free O-D bond, as illustrated in Fig 6.16, and this could potentially explain the emergence of the free O-D resonance in the data at relative humidities above 20% RH.

The loss of the surface d-hydroxyl resonance at $2705\ \text{cm}^{-1}$ between 0% and 30% RH could be due to the initiation of multilayer D_2O formation and the emergence of the free O-D should the latter resonant mode dominate the spectrum. The surface d-hydroxyls should persist at higher humidities as being in a state of dynamic equilibrium they now have a more plentiful supply of D_2O but the presence of molecular water structures or overlayers might act to broaden or shift the d-hydroxyl signal past the experiment's detection limits. Alternatively, in a localised island growth model (see Fig 6.18) the diminishing of the surface OD signal would correspond well with the gradual spreading out of the multilayer islands over the sites of exposed d-hydroxyls.

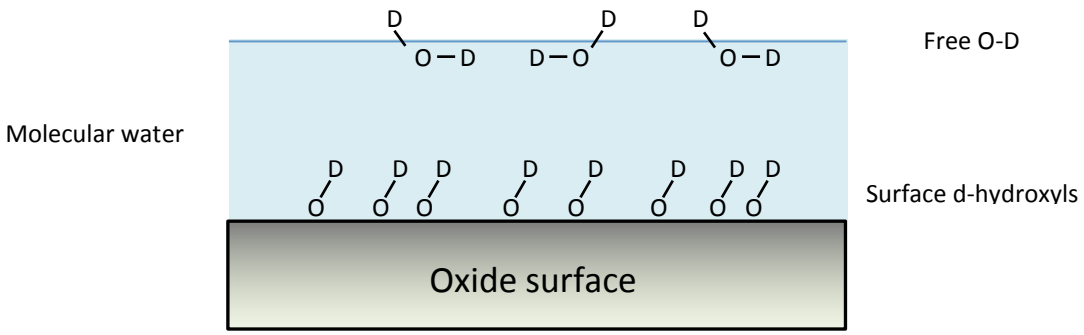

Figure 6.16. A model of molecular water adsorption on a metal oxide surface

Sub-Peak (d-hydroxyl & free O-D) Quantification

A two-peak model of d-hydroxyl and free O-D stretching was assumed and from the background-subtracted spectra the wavenumber values of $\omega_{\mathrm{d\ hydroxyl}} = 2705\ \mathrm{cm}^{-1}$ and $\omega_{\mathrm{free\ OD}} = 2728\ \mathrm{cm}^{-1}$ were allocated respectively. The symmetry of $\omega_{\mathrm{central}}$ in Fig 6.15 with respect to humidity helps to strengthen this model, with equivalent wavenumber values of the resonance at both 0% RH data points, and a constant secondary wavenumber values for moderate to high RH environments. Raw values from the data were evaluated at these wavenumbers and are plotted in Fig 6.17 as a function of relative humidity. Assuming a situation with a constant phase relationship between the components, these plots seem to support the two-resonance assertion well.

The asymmetry in the plot for the d-hydroxyl component suggests that at 0% RH prior to the initial humidity increase, there is either a greater ordering or greater surface density of d-hydroxyls when compared to the final 0% RH spectrum. Although the sample had undergone the *pre d-hydroxylation* step, it had been left to equilibrate at 0% RH for a number of hours prior to the experimental *humidity run*, so it is possible that this additional sample equilibration time could account for the d-hydroxyl asymmetry. In contrast, the free OD component shows a strong, symmetric and linear relationship with the humidity.

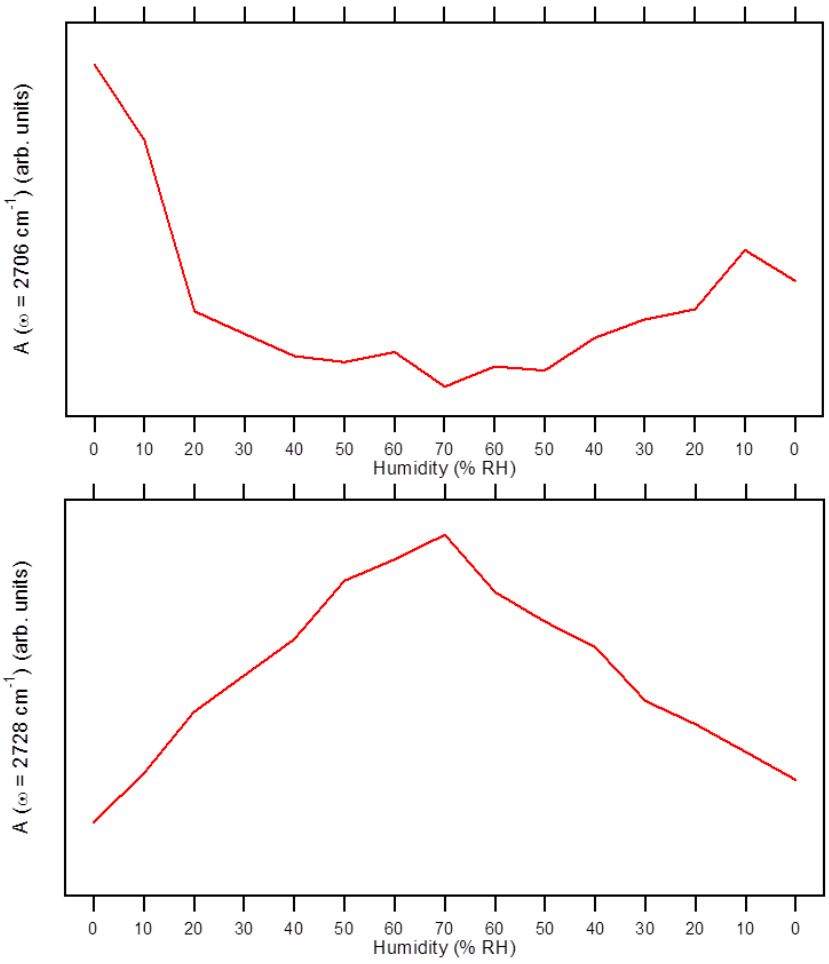

Figure 6.17. Plots showing the behaviour of the allocated d-hydroxyl (top) and free O-D (bottom) components of the zinc-D_2O vibrational resonance, plotted as a function of relative humidity. As in Fig 6.15, points were acquired from left to right (low RH → high RH → low RH)

Humidity Correlation

Ignoring trends at low humidities for a moment, the clear trend for RH as it goes from 20% → 70% → 20% is an almost linear relationship between peak amplitude and humidity, which in a simple model of sequential multilayer adsorption (wetting layer, layer 1, layer 2, layer 3 ...) seems counterintuitive. According to the basic adsorption model shown in Figure 6.16, as the humidity and thus water availability increases, at two monolayers the D_2O at the surface (layer 1) should be able to orient with a free O-D. For a layer by layer growth model, one would expect to form a maximum free O-D signal quickly which remains constant as the free OD concentration at the water-air interface is saturated with the layer growth. Any additional overlayers on top of that should not increase the free O-D resonance, as the same surface area of adsorbed water should intuitively be presenting the same surface density of dangling O-D's. In this case you would probably expect the surface OD signal to drop off quickly as the first water layer forms – a drop off is seen but an element of the surface OD signal remains in part until ~40% RH.

One explanation for the continuing rise in the free O-D peak with humidity could be localisation considerations due to inhomogeneities on the surface. If there is initially a partial wetting overlayer at localised sites it is possible that these would continue to develop into multilayer island structures which also continue to spread outward across the oxide surface with increasing humidity. In the island structure model, illustrated in Figure 6.18, free O-D is still present at the water-air interface from the lower monolayer levels, and so the occurrence of the free O-D saturation point is held off.

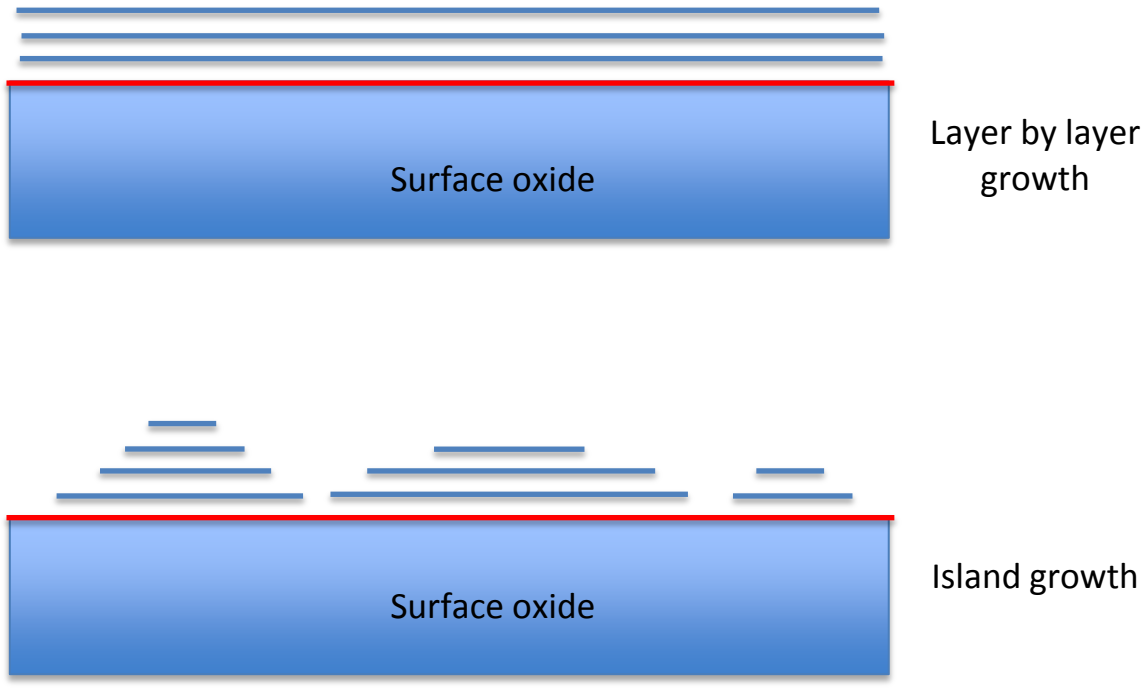

Figure 6.18. Cross-sectional illustration of two potential wetting progression mechanisms on the metal oxide surface. The red line represents the initial wetting/OD layer, and blue lines are discrete water adlayers.

As VSFS is an orientationally sensitive technique it is also possible that a thicker multilayer system could affect the water-air interfacial O-D bond orientations. Equally, a water adsorption regime consisting of microdroplet formation would mean a significant variation in free O-D bond orientation for droplets with a small radius of curvature. Continued droplet growth and aggregation would lead to larger droplets with larger radii of curvature over which there would be a smaller distribution of free O-D bond orientations, although these would still outweigh the OD concentration for a flat water layer.

6.4.3 Iron

Spectra from the d-hydroxylation step ($0\% \rightarrow 75\% \rightarrow 0\%$ RH) for polycrystalline Fe are shown in Figure 6.19, where a sharp discontinuity from the remnant non-resonant Gaussian background expected Gaussian is seen in the background-suppressed plot for a humidity of 75% RH, and to a smaller extent in the zero-delay plot. The dip at 2734 cm^{-1} corresponds closely in terms of energy with the free O-D resonance seen on zinc, and it being subtractive rather than additive would correspond to a phase difference between the resonant and non-resonant responses. Whilst the phase term becomes less important as the non-resonant background is suppressed, the 0% RH BG suppressed spectrum still shows a significant non-resonant background. Note also the less intense resonant feature at ~2870 cm^{-1} on the $\tau = 800$ fs plots which is in the C-H stretch region.

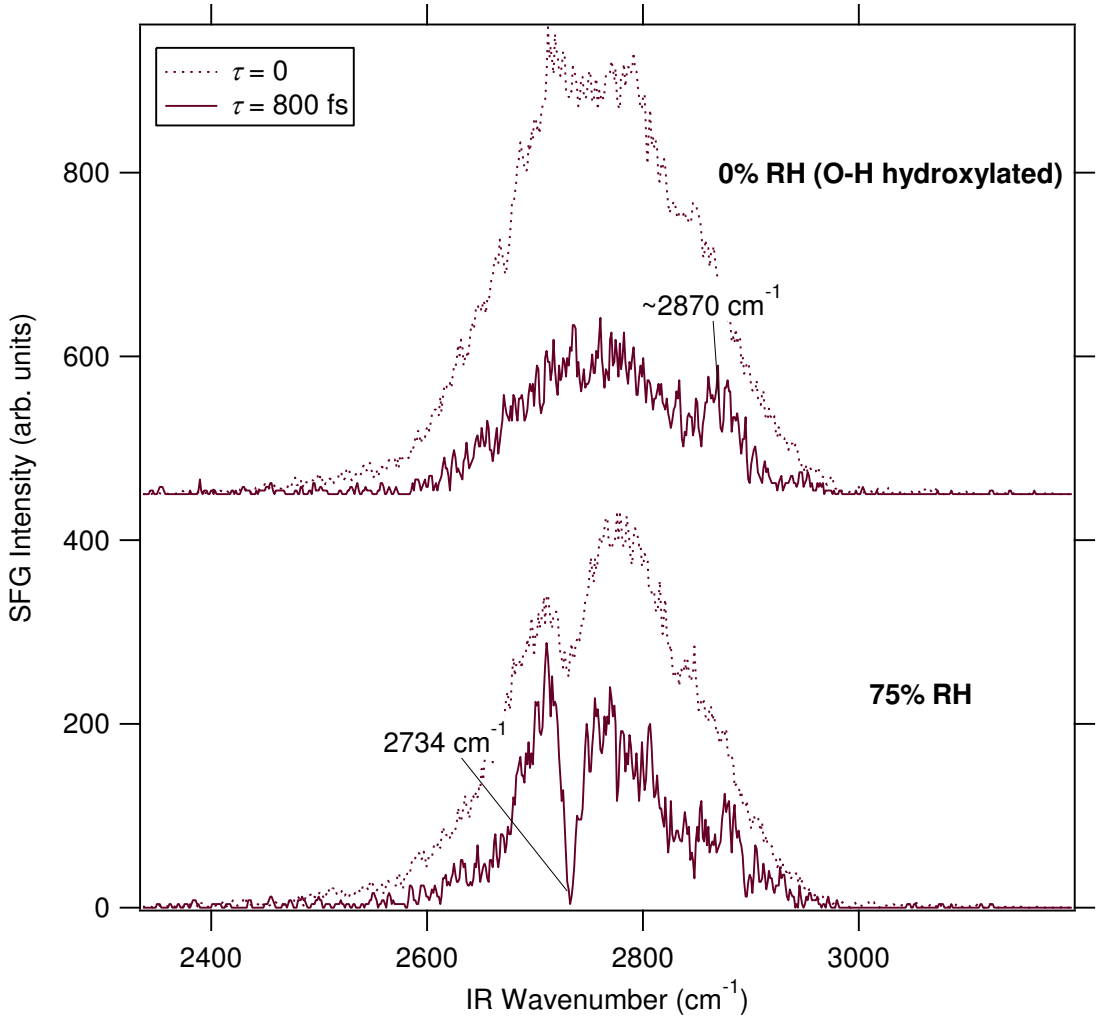

Figure 6.19. SFG spectra in the O-D stretch region for D_2O adsorbed on polycrystalline iron for two different Vis pulse timing configurations.

The system was set to 0% RH and left to equilibrate for ~24 hours. After this time a detailed *experimental run* at differing relative humidities was performed. The results from the *humidity run* are displayed in Figure 6.20 but apparent from these is a lack of the same strong subtractive resonance at 2734 cm^{-1} and an additional strong C-H resonance at ~2885 cm^{-1}. The deposition or evolution of the surface carbon by whatever mechanism coinciding with a loss of O-D resonance might suggest that the carbon is somehow preventing ordered water adsorption. Why this is the case for iron and not for zinc is unclear.

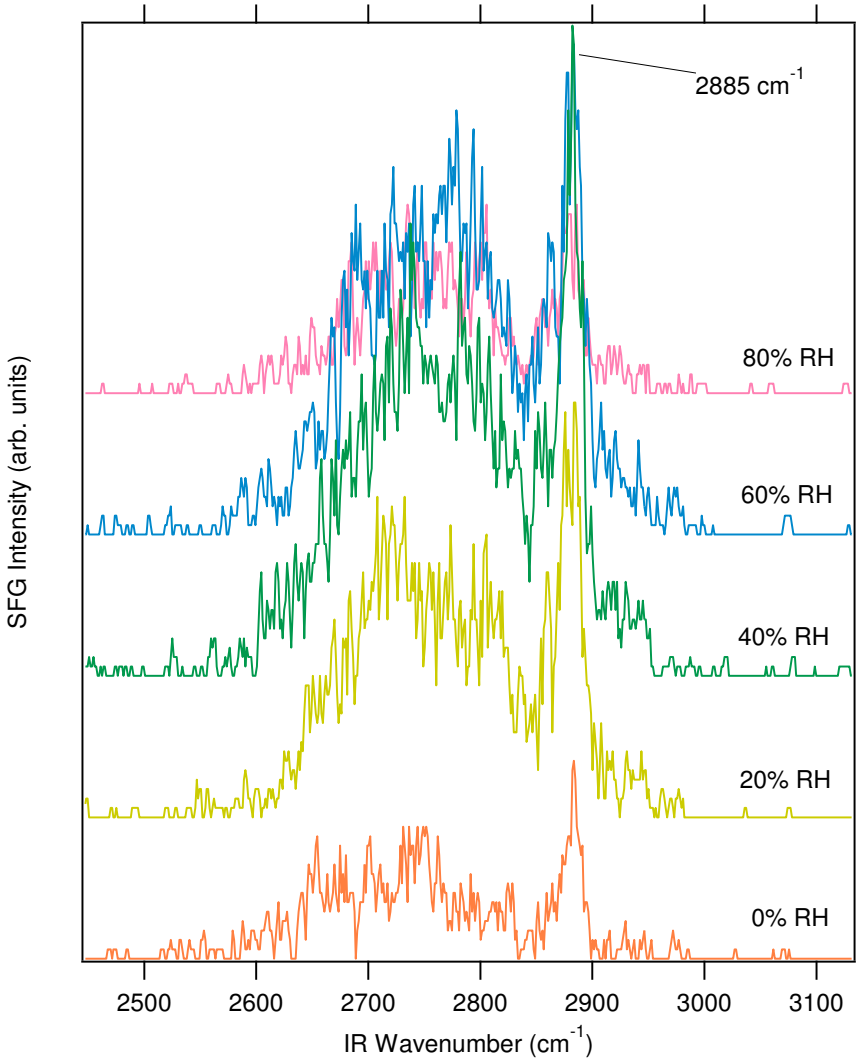

Figure 6.20. Background suppressed VSFS spectra ($\tau = 800$ fs) from iron under varying relative humidity.

6.4.4 Chromium

The spectra from the *pre d-hydroxylation* step are shown in Figure 6.21, where the energy in cm^{-1} of maxima and minima of interest have been labelled.

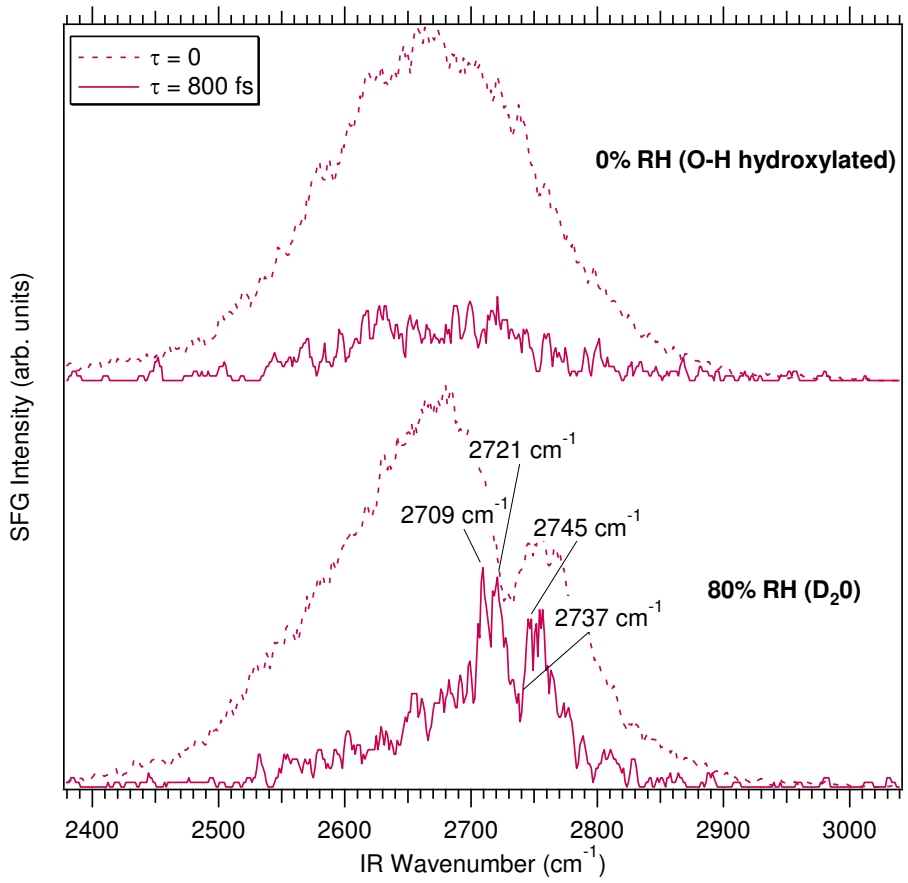

Figure 6.21. Zero delay ($\tau = 0$) and background suppressed ($\tau = 800$ fs) SFG spectra of the initial hydroxylation step on polycrystalline chromium metal. Prominent features have been labelled.

The spectra recorded from the increasing *humidity run* are shown in Figure 6.22, with the positions of the O-D features from Figure 6.3 overlaid as a visual guide. Similar to scans for GaAs, Au, and the *experimental humidity run* for Fe, the overall signal strength is seen to increase notably after the introduction of low levels of moisture. The effects of the D_2O on the resonant spectra are not easily evaluated given the signal-to-noise levels.

In spite of the poor signal-to-noise, one can distinguish steep gradients between 2710 and 2730 cm^{-1}, which are consistent to all plots where RH $\geq$ 20%, and a large, narrow feature at 2670 cm^{-1} on the 40% RH plot. A strong feature at 2900 cm^{-1} is also seen to appear at humidities above 20 % which is consistent with a saturated C-H stretch vibrational mode. With

respect to the features at 2670 cm^{-1}, 2710 cm^{-1} and 2730 cm^{-1} it is difficult to tell whether either of these are statistically significant given the quality of data, but it is worth remembering that stray light and thermal noise have been limited considerably in the experiment, such that each registered photon count has a very high probability of having originated from an SFG emission event; test background scans taken with various parameters (Vis/IR blocked, time delay set far from SFG overlap) registered as few as 5-10 photons over a 15 minute accumulation in otherwise ambient light conditions. The feature at 2670 cm^{-1} consists of raw data points that have undergone no smoothing or interpolation procedures and yet still present a smooth peak over a width of 13 points/CCD columns, making it likely that the feature has a real physical origin rather than being an effect of noise or CCD operation. Based on Fig 6.3 this could correspond to the second surface d-hydroxyl stretching mode (labelled b), which has not otherwise been observed throughout this investigation.

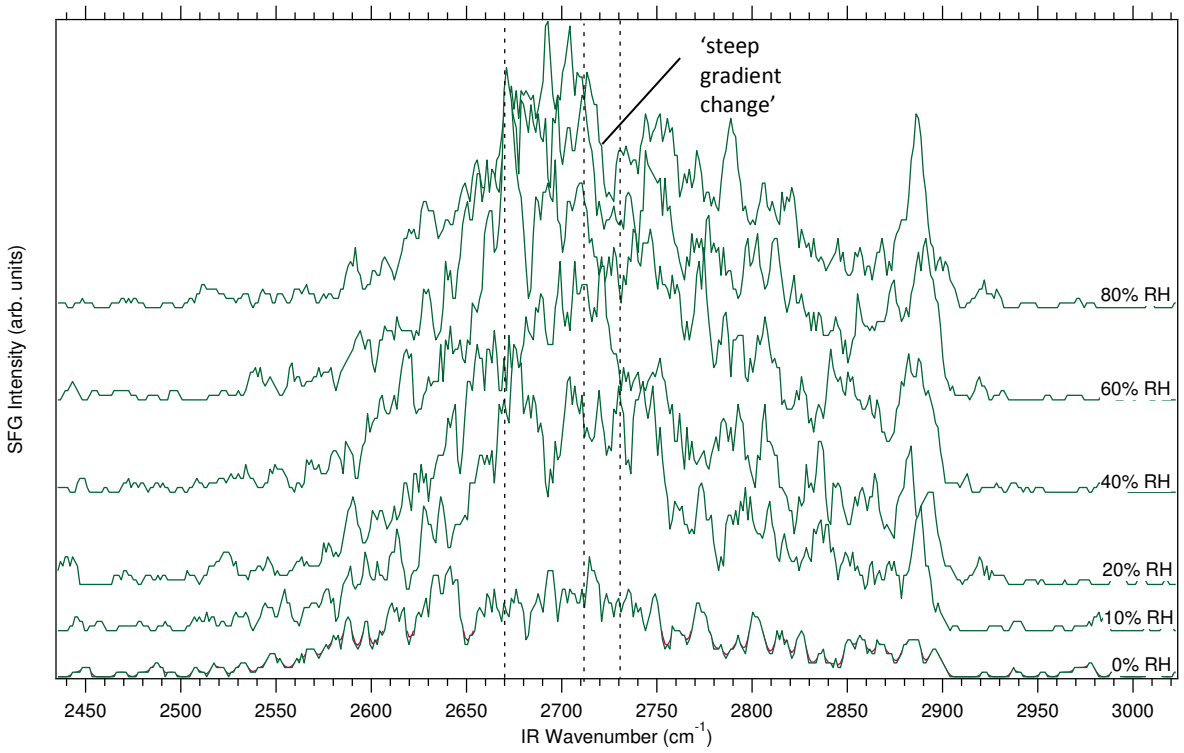

Figure 6.22. Background suppressed SFG spectra ($\tau = 800$ fs) taken off chromium metal as a function of D_2O humidity. The three vertical dashed lines are the frequencies of the three O-D resonances found by Hedberg et al.[44]

6.4.5 20Cr/25Ni/Nb Stainless Steel

A sample was procured of the 20Cr/25Ni/Nb stainless steel which is the composition of the external casing of the AGR fuel pins described in Chapter 2. The pre-hydroxylation stage is illustrated below in Figure 6.23, which has a very evident and broad resonance at 2732 cm^{-1}, even when compared with the substantial C-H region structure of the 0% RH spectrum.

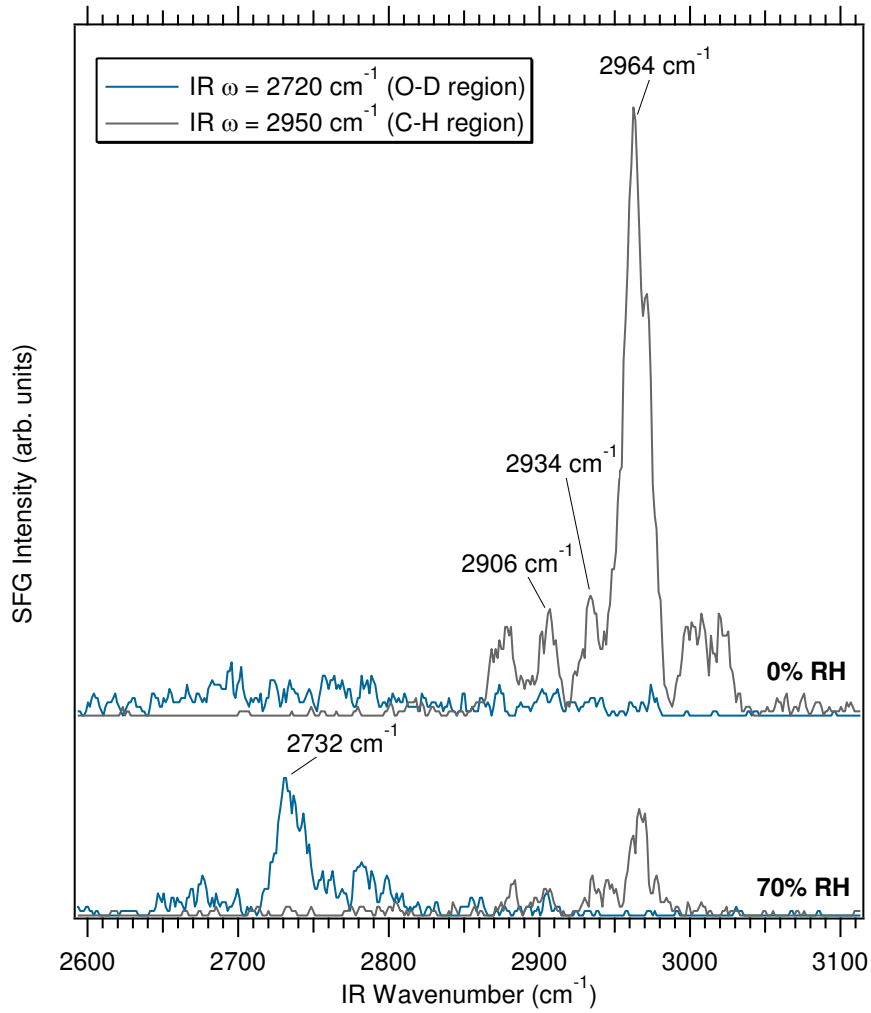

Figure 6.23. Background suppressed ($\tau = 860$ fs) SFG spectra taken from stainless steel in a controlled humid D_2O environment. Spectra from both O-D and C-H stretching regions are shown.

Focussing on the relationship between resolvable O-D stretching modes and surface carbon resonant modes, all prominent features have been labelled with their corresponding wavenumber values. As a steel there is a necessary carbon inclusion in the bulk which for this particular alloy is 0.01-0.04%.[69-71] Regardless of the large intensity of the features in the C-H region, a peak that appears to correspond to free O-D is observed in the *pre d-hydroxylation* step spectrum at 70% RH in Fig 6.23 and also in the spectra from the increasing *humidity run* shown in Figure 6.24.

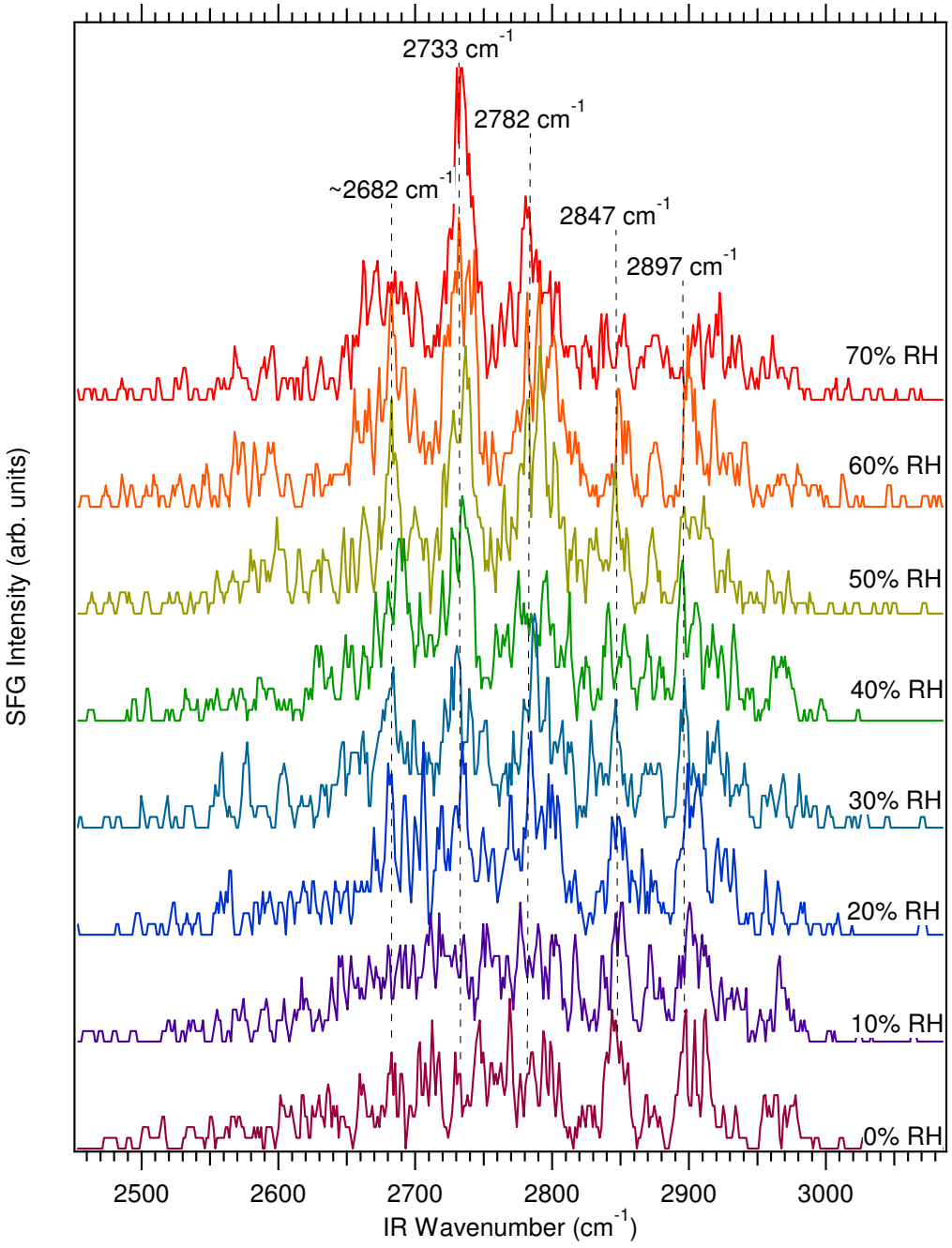

Figure 6.24. Background suppressed ($\tau = 860$ fs) SFG of the stainless steel surface under varying D_2O humidity conditions. Features common to several (greater than four) spectra have been labelled.

The resonant peak from the steel at 2733 cm^{-1} is resolvable throughout the *experimental humidity run* and one can visually identify a positive correlation with humidity for higher RH values.

The features highlighted at 2847cm^{-1} and 2897 cm^{-1} correlate with reported N-methyl and methylene symmetric stretch respectively – in fact, all C-H region resonant modes are at $\omega < 3000\ \mathrm{cm}^{-1}$, suggesting they arise from saturated C-H functional groups.[72]

A basic plot showing the raw SFG intensity for ω = 2733 cm^{-1} is shown below in Figure 6.25. No background subtraction has been attempted due to the complexity of the general spectrum and relatively low signal-to-noise levels, but the shape in the plot is similar to the equivalent plot taken from the higher resolution zinc scans, although it was not possible to observe any variation in the centre wavenumber of the resonant feature and thus determine the presence of a surface-d-hydroxyl stretch.

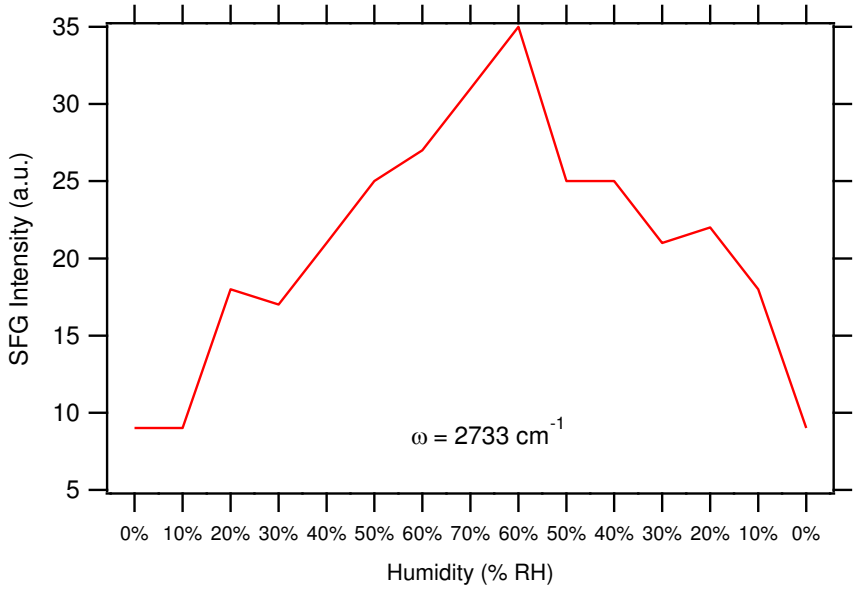

Figure 6.25. A plot of the overall SFG intensity at a stationary wavenumber value from the steel spectra in Fig 6.24. Data plotted against humidity and all are taken with $\tau = 860$ fs.

Steel Surface Carbon Investigation

To further investigate the considerable carbon response from the steel surface and whether it evolved over the course of the experiment, the C-H stretch region was also periodically scanned, the results of which are presented in Figure 6.26. Firstly, the major C-H stretching mode which is present in the initial 0% RH spectrum at 2962 cm^{-1} is practically unchanged after hydration and subsequent drying. At 70% RH it is still present but at a dramatically reduced intensity which suggests that either a conformational change has occurred in the moist environment rendering it less detectable using **ppp** polarisation, or that adsorbed surface water is nullifying the resonant signal somehow. It could simply be a case absorption of incident light by the liquid D_2O (or

organics that might have dissolved in it); however neither the infrared ($\sim$2950 cm^{-1}), visible SFG ($\sim$15850 cm^{-1}), nor visible beam ($\sim$125000 cm^{-1}) coincide with any known D_2O absorptions.[73] Scattering of light by adsorbed water on the inside prism face was considered as a possible power-loss mechanism, but the appearance of more intense zero-delay spectra in humid environments as observed with GaAs (Fig 6.9), Au (Fig 6.10), and Cr (Fig 6.21) goes some way towards discrediting that theory.

Another explanation for the reduction in the CH stretch peak intensity is the increase in the refractive index over the water-metal interface, as a change in refractive index will alter the Fresnel fields generated at the interface and thus the sum-frequency generation efficiency for a given set of wavelengths and incidence angles.

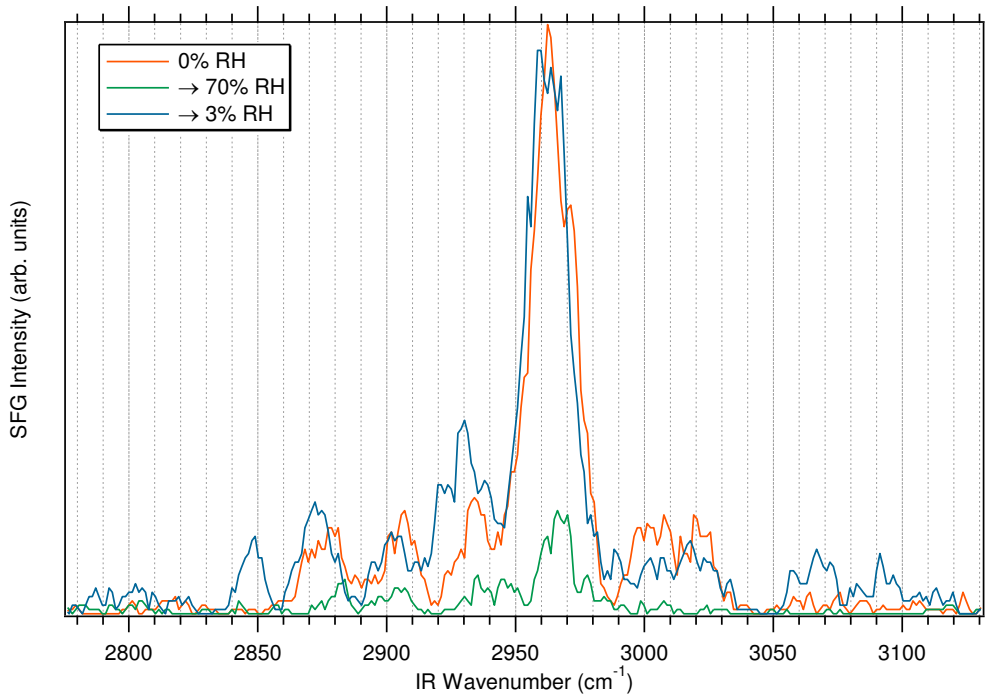

Figure 6.26. SFG spectra ($\tau = 860$ fs) over the C-H stretch region showing changes observed with the addition and subsequent desorption of adsorbed D_2O.

A quick test for this hypothesis was performed with an old ODT-coated gold substrate, which was examined with background suppression at zero and 70% RH. From this plot, shown in Figure 6.27, it is clear that some sort or attenuation process is affecting the resonant signal from metal adsorbates with a heavy water overlayer. This would depend on the inherent wetting behaviour of the substrate/adsorbate, as a highly hydrophobic surface would not necessarily experience evolution of a water overlayer, but the presence of a free O-D resonance would help support the

assertion of the presence of multilayer D_2O.

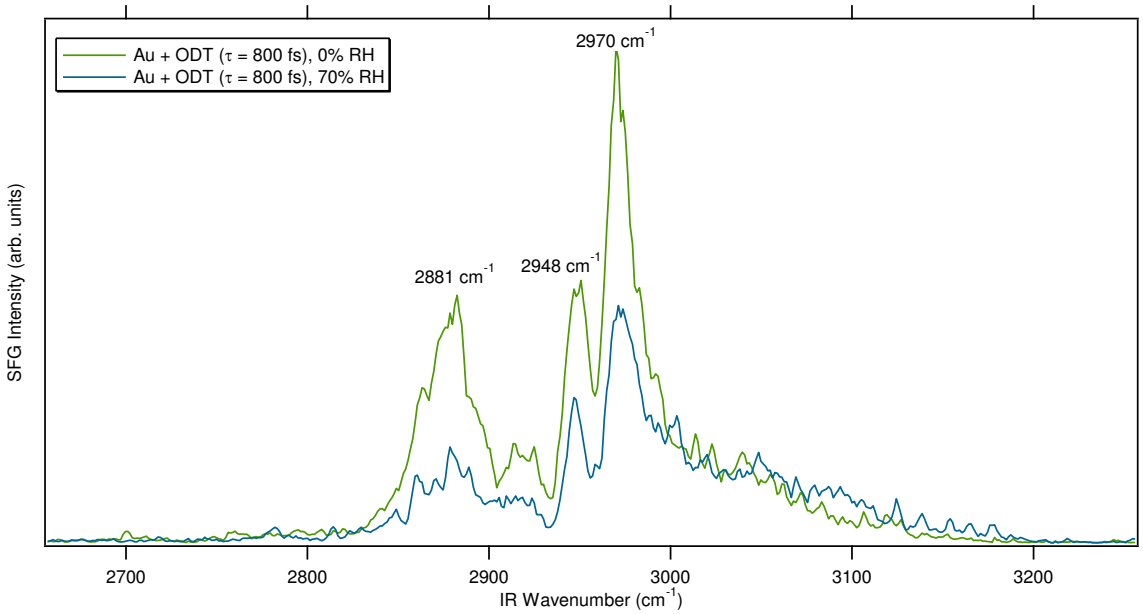

Figure 6.27. Background suppressed SFG spectra from ODT molecules adsorbed on gold, acquired under varying humidity.

6.4.6 Spectral Comparison

The four metallic spectra taken at high RH values in the *pre d-hydroxylation* step are shown together in Fig 6.28. All were acquired with similar visible pulse time delays and after having undergone equivalent preparation procedures. It was possible to resolve 'free OD' stretching modes at $\sim 2730\ \mathrm{cm}^{-1}$ on all substrates immediately after preparation, although total signal strengths depended on the nonlinear activity/electronic structure of the substrate and varied between materials. The shapes of the accumulated spectra also varied between substrates according to the phase relationship between molecular resonance and surface non-resonant background.

After leaving the cell system to equilibrate down to 0% RH however, not all samples allowed such a clear re-acquisition of molecular O-D stretch features. The cause of this change, seen especially in the case of iron and chromium, is unknown, but presents difficulties regarding spectral reproducibility. There are some indications of a correlation between the loss of O-D resonance and an increase in surface carbon, but any further analysis of this would require new data.

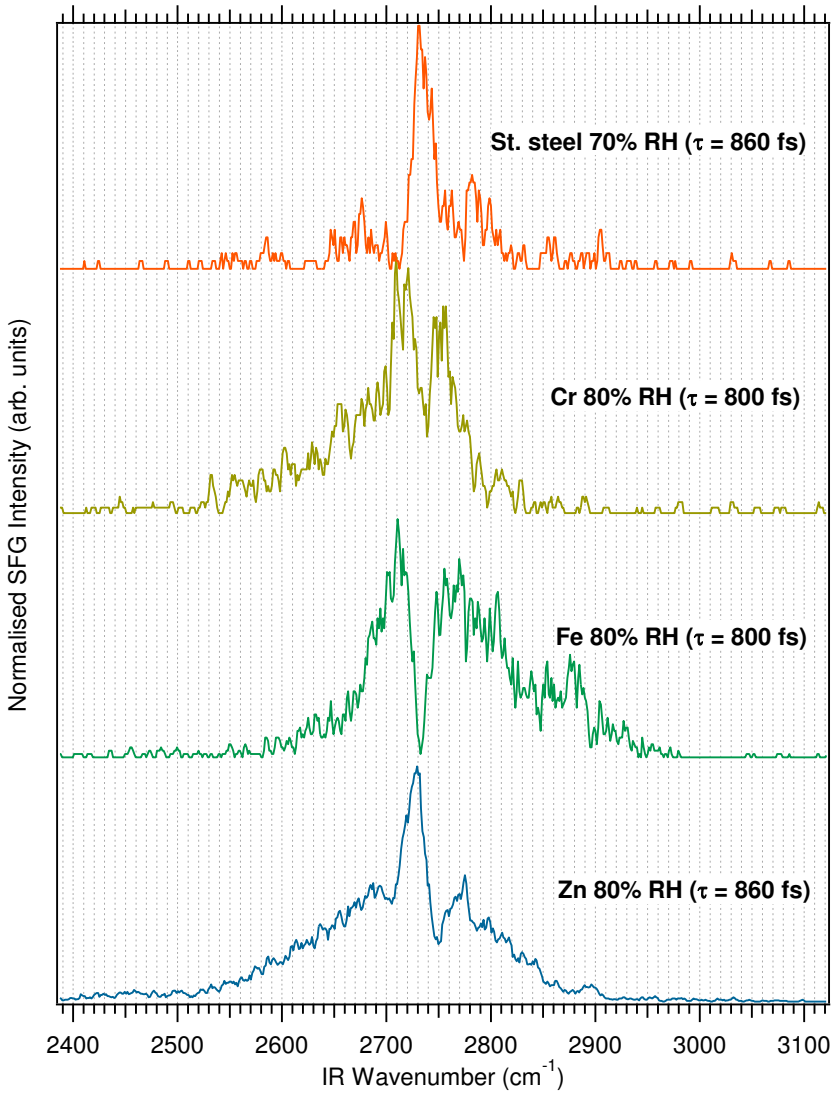

Figure 6.28. Comparison between high humidity ($\geq 70\%$ RH) SFG background-suppressed spectra for different metallic substrate materials. All normalised spectra are taken from the pre-hydroxylation step, soon after UV cleaning.

6.5 Conclusion

An experiment was carried out in an attempt to probe the O-D stretching modes of adsorbed surface water on metallic/metal oxide substrates in controlled humidity environments. The polycrystalline metals zinc, iron, chromium and stainless steel were prepared to a mirror surface finish and cleaned with solvents and a UV/ozone decontamination regime. Samples were initially 'pre d-hydroxylated' through exposure to high humidities of D_2O and were then subsequently dried *in situ*. VSFS spectra taken throughout this step were able to resolve an O-D resonance feature at $\sim$2730 cm^{-1} from all substrates.

Samples were then analysed via VSFS as a function of relative humidity in both ascending and descending humidity directions. Spectra from zinc identified a surface d-hydroxyl stretching mode at low humidities (0 → 30% RH) at $\sim$2705 cm^{-1}. This was then replaced from 30 → 70% RH by the free OD stretching mode at $\sim$2728 cm^{-1} which exhibited a positive correlation with the humidity.

SFG Spectra taken from iron and chromium as a function of humidity were unable to resolve the O-D stretching modes past the *pre d-hydroxylation* step. The stainless steel substrate, a specific alloy of relevance to the nuclear industry, exhibited a free O-D stretch at 2733 cm^{-1}, but further analysis was complicated by a significant surface carbon presence.

The VSFS setup with controlled humidity flow capabilities based at the University of Manchester was proven successful in the detection of adsorbed surface water, and the resolution and signal-to-noise levels of zinc spectra showed a significant improvement upon similar spectra in the literature.

6.6 Future Work

The work on polycrystalline zinc in a controlled humidity atmosphere shows considerable promise towards a better understanding of specific water adsorption behaviours. A more rigorous analysis of this data including complex spectral fitting procedures would allow for the development of a better quantitative model and the retrieval of molecular densities of detected species. Whilst the system at ambient temperatures is particularly energetic, VSFS acquisition with varying incident light polarisation states would be able to identify net molecular orientations – this could be further improved through the use of well-ordered single crystal substrates. Complimentary surface characterisation techniques such as AFM, XPS and gravimetric analysis performed on the substrates under varying humidities would elucidate surface topographies, micro-scale wetting behaviours, surface chemistry, and water adsorption levels/distribution which would help support adsorption models.

This holistic approach could then be translated to alternative substrate materials both for fundamental research and industrially relevant applications.

Further work should also be undertaken in an analysis of the SFG response of iron and chromium metals in varying relative humidities, and some effort should be directed towards ascertaining the mechanism behind their differing and apparently exposure/time-dependent wetting behaviours. The majority of current understanding in the field of water adsorption is based on idealised UHV investigations from model substrates or large-scale empirical corrosion/failure testing, and there is a definite need to bridge the two spheres for water-sensitive systems such as nuclear component storage or micro-electronics. The insight gained through the use of this unique, surface-specific methodology could then be used to improve predictions and direct surface preparation or modification methods in the field of corrosion control.

6.7 References

1. Ludwig R. Water: From clusters to the bulk. *Angewandte Chemie-International Edition*. 2001; **40:** 1808-27.
2. Coe JV. Fundamental properties of bulk water from cluster ion data. *International Reviews in Physical Chemistry*. 2001; **20:** 33-58.
3. Marcus Y. Effect of ions on the structure of water: structure making and breaking. *Chemical reviews*. 2009; **109:** 1346-70.
4. Brookes IM, Muryn CA, Thornton G. Imaging water dissociation on TiO 2 (110). *Physical review letters*. 2001; **87:** 266103.
5. Schaub R, Thostrup P, Lopez N, Lægsgaard E, Stensgaard I, Nørskov JK, Besenbacher F. Oxygen vacancies as active sites for water dissociation on rutile TiO 2 (110). *Physical Review Letters*. 2001; **87:** 266104.
6. Ketteler G, Yamamoto S, Bluhm H, Andersson K, Starr DE, Ogletree DF, Ogasawara H, Nilsson A, Salmeron M. The Nature of Water Nucleation Sites on TiO2(110) Surfaces Revealed by Ambient Pressure X-ray Photoelectron Spectroscopy. *The Journal of Physical Chemistry C*. 2007; **111:** 8278-82.
7. Yamamoto S, Bluhm H, Andersson K, Ketteler G, Ogasawara H, Salmeron M, Nilsson A. In situ x-ray photoelectron spectroscopy studies of water on metals and oxides at ambient conditions. *Journal of Physics: Condensed Matter*. 2008; **20:** 184025.
8. Henderson MA. An HREELS and TPD study of water on TiO2(110): the extent of molecular versus dissociative adsorption. *Surface Science*. 1996; **355:** 151-66.
9. Verdaguer A, Sacha GM, Bluhm H, Salmeron M. Molecular structure of water at interfaces: Wetting at the nanometer scale. *Chemical reviews*. 2006; **106:** 1478-510.
10. Ferry D, Picaud S, Hoang PNM, Girardet C, Giordano L, Demirdjian B, Suzanne J. Water monolayers on MgO (100): structural investigations by LEED experiments, tensor LEED dynamical analysis and potential calculations. *Surface science*. 1998; **409:** 101-16.
11. Giordano L, Goniakowski J, Suzanne J. Partial dissociation of water molecules in the (3× 2) water monolayer deposited on the MgO (100) surface. *Physical review letters*. 1998; **81:** 1271.
12. Delle Site L, Alavi A, Lynden-Bell RM. The structure and spectroscopy of monolayers of water on MgO: an ab initio study. *The Journal of Chemical Physics*. 2000; **113:** 3344-50.
13. Ewing GE. Ambient thin film water on insulator surfaces. *Chemical reviews*. 2006; **106:** 1511-26.
14. Newberg JT, Starr DE, Yamamoto S, Kaya S, Kendelewicz T, Mysak ER, *et al.* Formation of hydroxyl and water layers on MgO films studied with ambient pressure XPS. *Surface Science*. 2011; **605:** 89-94.
15. Foster M, Furse M, Passno D. An FTIR study of water thin films on magnesium oxide. *Surface Science*. 2002; **502–503:** 102-8.
16. Krueger BJ, Ross JL, Grassian VH. Formation of Microcrystals, Micropuddles, and Other Spatial Inhomogenieties in Surface Reactions under Ambient Conditions: An Atomic Force Microscopy Study of Water and Nitric Acid Adsorption on MgO(100) and $CaCO_3(10\bar{1}4)$. *Langmuir*. 2005; **21:** 8793-801.
17. Meyer B, Marx D, Dulub O, Diebold U, Kunat M, Langenberg D, Wöll C. Partial dissociation of water leads to stable superstructures on the surface of zinc oxide. *Angewandte Chemie International Edition*. 2004; **43:** 6641-5.
18. Wöll C. The chemistry and physics of zinc oxide surfaces. *Progress in Surface Science*. 2007; **82:** 55-120.
19. Hu H, Ji HF, Sun Y. The effect of oxygen vacancies on water wettability of a ZnO surface. *Physical Chemistry Chemical Physics*. 2013; **15:** 16557-65.
20. Henderson MA. The interaction of water with solid surfaces: fundamental aspects revisited. *Surface Science Reports*. 2002; **46:** 1-308.

21. Schnur S, Groß A. Properties of metal–water interfaces studied from first principles. *New Journal of Physics*. 2009; **11:** 125003.
22. Hamm P, Garrett-Roe S, Hamm P. The OH stretch vibration of liquid water reveals hydrogen-bond clusters. *Physical chemistry chemical physics*.
23. Brown GE, Henrich VE, Casey WH, Clark DL, Eggleston C, Felmy A*, et al.* Metal Oxide Surfaces and Their Interactions with Aqueous Solutions and Microbial Organisms. *Chemical Reviews*. 1998; **99:** 77-174.
24. Stumm W. Chemistry of the solid–water interface, 1992. *Willey New York*.
25. Blesa MA, Weisz AD, Morando PJ, Salfity JA, Magaz GE, Regazzoni AE. The interaction of metal oxide surfaces with complexing agents dissolved in water. *Coordination Chemistry Reviews*. 2000; **196:** 31-63.
26. Schiek M, Al-Shamery K, Kunat M, Traeger F, Woll C. Water adsorption on the hydroxylated H-(1 [times] 1) O-ZnO(000[1 with combining macron]) surface. *Physical Chemistry Chemical Physics*. 2006; **8:** 1505-12.
27. Franks F, *The physics and physical chemistry of water*. 1972: Plenum Press New York.
28. Bertie JE, Ahmed MK, Eysel HH. Infrared intensities of liquids. 5. Optical and dielectric constants, integrated intensities, and dipole moment derivatives of water and water-d2 at 22. degree. C. *The Journal of Physical Chemistry*. 1989; **93:** 2210-8.
29. Du Q, Superfine R, Freysz E, Shen YR. Vibrational spectroscopy of water at the vapor/water interface. *Physical Review Letters*. 1993; **70:** 2313.
30. Shen YR, Ostroverkhov V. Sum-frequency vibrational spectroscopy on water interfaces: Polar orientation of water molecules at interfaces. *Chemical Reviews*. 2006; **106:** 1140-54.
31. Scatena LF, Brown MG, Richmond GL. Water at hydrophobic surfaces: Weak hydrogen bonding and strong orientation effects. *Science*. 2001; **292:** 908-12.
32. Gan W, Wu D, Zhang Z, Guo Y, Wang H-f. Orientation and motion of water molecules at air/water interface. *Chinese Journal of Chemical Physics*. 2006; **19:** 20-4.
33. Watry MR, Brown MG, Richmond GL. Probing molecular structure at liquid surfaces with vibrational sum frequency spectroscopy. *Applied Spectroscopy*. 2001; **55:** 321A-A.
34. Brown MG, Walker DS, Raymond EA, Richmond GL. Vibrational sum-frequency spectroscopy of alkane/water interfaces: Experiment and theoretical simulation. *The Journal of Physical Chemistry B*. 2003; **107:** 237-44.
35. Zhang D, Gutow J, Eisenthal KB. Vibrational spectra, orientations, and phase transitions in long-chain amphiphiles at the air/water interface: Probing the head and tail groups by sum frequency generation. *The Journal of Physical Chemistry*. 1994; **98:** 13729-34.
36. Tian CS, Shen YR. Structure and charging of hydrophobic material/water interfaces studied by phase-sensitive sum-frequency vibrational spectroscopy. *Proceedings of the National Academy of Sciences*. 2009; **106:** 15148-53.
37. Morita A. Improved computation of sum frequency generation spectrum of the surface of water. *The Journal of Physical Chemistry B*. 2006; **110:** 3158-63.
38. Walker DS, Hore DK, Richmond GL. Understanding the population, coordination, and orientation of water species contributing to the nonlinear optical spectroscopy of the vapor-water interface through molecular dynamics simulations. *The Journal of Physical Chemistry B*. 2006; **110:** 20451-9.
39. Buch V, Tarbuck T, Richmond GL, Groenzin H, Li I, Shultz MJ. Sum frequency generation surface spectra of ice, water, and acid solution investigated by an exciton model. *The Journal of chemical physics*. 2007; **127:** 204710.
40. Shen YR, Waychunas GA. SFG Studies of Oxide-Water Interfaces: Protonation States, Water Polar Orientations, and Comparison with Structure Results from X-Ray Scattering. *Vibrational Spectroscopy at Electrified Interfaces*. 2013**:** 48-84.
41. Du Q, Freysz E, Shen YR. Surface vibrational spectroscopic studies of hydrogen bonding and hydrophobicity. *Science*. 1994; **264:** 826-8.

42. Ostroverkhov V, Waychunas GA, Shen YR. Vibrational spectra of water at water/α-quartz (0001) interface. *Chemical Physics Letters*. 2004; **386:** 144-8.
43. Miranda PB, Xu L, Shen YR, Salmeron M. Icelike water monolayer adsorbed on mica at room temperature. *Physical Review Letters*. 1998; **81:** 5876-9.
44. Hedberg J, Baldelli S, Leygraf C. Evidence for the Molecular Basis of Corrosion of Zinc Induced by Formic Acid using Sum Frequency Generation Spectroscopy. *The Journal of Physical Chemistry Letters*. 2010; **1:** 1679-82.
45. Hedberg J, Baldelli S, Leygraf C. Initial Atmospheric Corrosion of Zn: Influence of Humidity on the Adsorption of Formic Acid Studied by Vibrational Sum Frequency Spectroscopy. *Journal of Physical Chemistry C*. 2009; **113:** 6169-73.
46. Aastrup T, Leygraf C. Simultaneous infrared reflection absorption spectroscopy and quartz crystal microbalance measurements for in situ studies of the metal/atmosphere interface. *Journal of the Electrochemical Society*. 1997; **144:** 2986-90.
47. Kulwicki BM. Humidity sensors. *Journal of the American Ceramic Society*. 1991; **74:** 697-708.
48. Yamazoe N, Shimizu Y. Humidity sensors: principles and applications. *Sensors and Actuators*. 1986; **10:** 379-98.
49. Benson G. Relative_humidity.png: Wikimedia Commons, http://commons.wikimedia.org/wiki/File:Relative_Humidity.png, 2008.
50. Heichal Y, Chandra S, Bordatchev E. A fast-response thin film thermocouple to measure rapid surface temperature changes. *Experimental Thermal and Fluid Science*. 2005; **30:** 153-9.
51. Heidberg J, Redlich B, Wetter D. Adsorption of water vapor on the MgO (100) single crystal surface. *Berichte der Bunsen-Gesellschaft*. 1995; **99:** 1333-7.
52. Eng PJ, Trainor TP, Brown Jr GE, Waychunas GA, Newville M, Sutton SR, Rivers ML. Structure of the hydrated α-Al2O3 (0001) surface. *Science*. 2000; **288:** 1029-33.
53. Hans L, *Solid surfaces, interfaces and thin films*. Vol. 8431. 2010: Springer.
54. Stirniman MJ, Huang C, Smith RS, Joyce SA, Kay BD. The adsorption and desorption of water on single crystal MgO (100): The role of surface defects. *The Journal of chemical physics*. 1996; **105:** 1295-8.
55. Linstrom PJ, Mallard WGE. NIST Chemistry webbook; NIST standard reference database No. 69. 2001.
56. Nagata Y, Pool RE, Backus EHG, Bonn M. Nuclear quantum effects affect bond orientation of water at the water-vapor interface. *Physical review letters*. 2012; **109:** 226101.
57. Katz JJ. Chemical and biological studies with deuterium. *Am. Scientist*. 1960; **48**.
58. Gruenloh CJ, Carney JR, Arrington CA, Zwier TS, Fredericks SY, Jordan KD. Infrared spectrum of a molecular ice cube: the S4 and D2d water octamers in benzene-(water) 8. *Science*. 1997; **276:** 1678-81.
59. Shin JW, Hammer NI, Diken EG, Johnson MA, Walters RS, Jaeger TD, Duncan MA, Christie RA, Jordan KD. Infrared signature of structures associated with the H+ (H2O) n (n= 6 to 27) clusters. *Science*. 2004; **304:** 1137-40.
60. Lappi SE, Smith B, Franzen S. Infrared spectra of H216O, H218O and D2O in the liquid phase by single-pass attenuated total internal reflection spectroscopy. *Spectrochimica Acta Part A: Molecular and Biomolecular Spectroscopy*. 2004; **60:** 2611-9.
61. Grassian VH. Surface science of complex environmental interfaces: Oxide and carbonate surfaces in dynamic equilibrium with water vapor. *Surface Science*. 2008; **602:** 2955-62.
62. Hodgson A, Haq S. Water adsorption and the wetting of metal surfaces. *Surface Science Reports*. 2009; **64:** 381-451.
63. Kim J-H, Ahn SI, Kim JH, Zin W-C. Evaporation of water droplets on polymer surfaces. *Langmuir*. 2007; **23:** 6163-9.
64. Soolaman DM, Yu H-Z. Water microdroplets on molecularly tailored surfaces: correlation between wetting hysteresis and evaporation mode switching. *The Journal of Physical Chemistry B*. 2005; **109:** 17967-73.

65. Schmidt WG, Bechstedt F, Bernholc J. GaAs (001) surface reconstructions: geometries, chemical bonding and optical properties. *Applied surface science*. 2002; **190:** 264-8.
66. Busson B, Tadjeddine A. Non-uniqueness of parameters extracted from resonant second-order nonlinear optical spectroscopies. *The Journal of Physical Chemistry C*. 2009; **113:** 21895-902.
67. Farrow LA, Graedel TE, Leygraf C. Gildes model studies of aqueous chemistry. II. The corrosion of zinc in gaseous exposure chambers. *Corrosion Science*. 1996; **38:** 2181-99.
68. Salmeron M, Schlögl R. Ambient pressure photoelectron spectroscopy: A new tool for surface science and nanotechnology. *Surface Science Reports*. 2008; **63:** 169-99.
69. Powell DJ, Pilkington R, Miller DA. The precipitation characteristics of 20% Cr/25% Ni・Nb stabilised stainless steel. *Acta Metallurgica*. 1988; **36:** 713-24.
70. Smith AF, Gibbs GB. The Volume and Grain-Boundary Diffusion of Iron in 20 Cr/25 Ni/Nb Stainless Steel. *Metal Science*. 1968; **2:** 47-50.
71. Ecob RC, Lobb RC, Kohler VL. The formation of G-phase in 20/25 Nb stainless steel AGR fuel cladding alloy and its effect on creep properties. *Journal of materials science*. 1987; **22:** 2867-80.
72. Smith BC, *Infrared spectral interpretation: a systematic approach*. 1998: CRC press.
73. Gan Y, Yang X, Guo Y, Wu S, Li W, Yuyan L, Chen Y. The absorption spectra of H2O+ and D2O+ in the visible and near infrared region. *Molecular Physics*. 2004; **102:** 611-21.

- This page intentionally left blank -